Open Access Dissertations   Electronic Theses and Dissertations

2008-04-20

Angiographic Assessment of Flow Divertors as Treatment for Cerebral Aneurysms: Results in the Rabbit Elastase-Induced Aneurysm Model

Chander Sadasivan
University of Miami, c.sadasivan@umiami.edu

Follow this and additional works at: https://scholarlyrepository.miami.edu/oa_dissertations

UNIVERSITY OF MIAMI

ANGIOGRAPHIC ASSESSMENT OF FLOW DIVERTORS AS TREATMENT FOR
CEREBRAL ANEURYSMS: RESULTS IN THE RABBIT ELASTASE-INDUCED
ANEURYSM MODEL

By

Chandramouli Sadasivan

A DISSERTATION

Submitted to the Faculty
of the University of Miami
in partial fulfillment of the requirements for
the degree of Doctor of Philosophy

Coral Gables, Florida

May 2008

UNIVERSITY OF MIAMI

A dissertation submitted in partial fulfillment of
the requirements for the degree of
Doctor of Philosophy

ANGIOGRAPHIC ASSESSMENT OF FLOW DIVERTORS AS TREATMENT FOR
CEREBRAL ANEURYSMS: RESULTS IN THE RABBIT ELASTASE-INDUCED
ANEURYSM MODEL

Chandramouli Sadasivan

Approved:

_____
Dr. Baruch B. Lieber
Professor of Biomedical Engineering

_____
Dr. Terri A. Scandura
Dean of the Graduate School

_____
Dr. Brant D. Watson
Professor of Neurology

_____
Dr. Weizhao Zhao
Associate Professor of
Biomedical Engineering

_____
Dr. Ajay K. Wakhloo
Professor of Radiology
University of Massachusetts
Medical School

_____
Dr. Fotios Andreopoulos
Assistant Professor of
Biomedical Engineering

SADASIVAN, CHANDRAMOULI　　　　　　　(Ph.D., Biomedical Engineering)

Angiographic Assessment of Flow Divertors　　　　　　　(May 2008)
as Treatment for Cerebral Aneurysms: Results
in the Rabbit Elastase-Induced Aneurysm Model

Cerebral aneurysms are abnormal focal dilations of the cerebral vasculature that may rupture and cause a hemorrhagic stroke. More than a decade after seminal experimental studies showed the feasibility of successfully treating cerebral aneurysms by flow diversion, the potential of this modality is gradually being recognized in the clinical arena. A flow divertor is a metallic meshed tube that has its porosity (ratio of metal-free surface area to total surface area) and pore density (number of pores per unit surface area) optimized to facilitate occlusion of aneurysms. An appropriately designed flow divertor severely attenuates the flow exchange between the parent vessel and an aneurysm, resulting in the formation of intra-aneurysmal flow stasis zones which promote thrombosis. This study reports the results from implantation of three different configurations of a novel flow-diverting device in thirty elastase-induced aneurysm models in rabbits. Ten animals per device configuration were followed-up at 3 weeks (n=3), 3 months (n=3), and 6 months (n=4) and tissue explanted post-sacrifice was sent for histology. High-speed angiographic sequences were acquired before and immediately after device implantation, and at follow-up for each animal. Temporal variations in the angiographic contrast intensity within the aneurysms were recorded and subsequently

corrected for respiratory motion. These aneurysmal contrast washout curves were fit to a mathematical model whose parameters served to quantify device performance. Angiographic quantification was supplemented by histomorphometric data to derive composite scores of the performance of each device configuration in effecting stable aneurysm occlusion. Performance scores showed that the device with a porosity of 70%, filament diameter of 38 μm, and pore density of 18 pores/mm^2 performed better than devices with 65% porosity, 51 μm filament diameter, 14 pores/mm^2 and 70% porosity, 51 μm filament diameter, 12 pores/mm^2 with relative efficacies of 100%, 86%, and 79%, respectively. Angiographic quantification further suggested a parameter, which could be employed to estimate long-term aneurysm occlusion probabilities immediately after treatment with any flow diversion device. A value of this parameter less than 30 predicts greater than 97% angiographic aneurysm occlusion over a period of six months with a sensitivity of 73% and specificity of 82%. Larger data sets are required to improve the validity of this test. The pore density of flow divertors, rather than porosity, was seen to be a critical modulating factor of device efficacy. Refinement of the best device configuration by further optimizing the pore density may yield yet better results.

This dissertation is dedicated to my father, Sadasivan Subrahmanyam

ACKNOWLEDGEMENTS

TABLE OF CONTENTS

Chapter

LIST OF FIGURES

LIST OF TABLES

LIST OF EQUATIONS

Chapter 1. INTRODUCTION

1.1. Cerebral Aneurysms

Seven to eight percent of the fifty million deaths per year worldwide are attributed to a stroke [1, 2]. There are about 700,000 strokes in the United States each year and this incidence (~0.2% of the population per year) can be assumed to currently prevail in most parts of the world [1, 2]. About five percent of all strokes are caused by the rupture of an intracranial aneurysm [3]. This section contains a brief introduction to the epidemiology, etiology, and pathophysiology of aneurysms.

Intracranial arteries are located in the space between the arachnoid mater and the pia mater membranes covering the surface of the brain. In approximately 5% of the general population, out pouches of the arterial wall, called aneurysms, are formed at bifurcation points in the arterial structure (Figure 1-1) [4-7]. Having a thin, diseased wall, these aneurysms may rupture causing blood to leak into the subarachnoid space thereby causing a subarachnoid hemorrhage (SAH). The incidence of SAH in the general population has remained relatively constant over the past decades at around 10 per 100,000 per year [3, 4]. Regional differences in the incidence rate of SAH exist, with the Finnish and Japanese populations having twice the incidence rates (20 per 100,000) while the Central and South American populations have half the incidence (5 per 100,000) [3]. The incidence rates of aneurysms and of SAH suggest that only about 0.2% of the aneurysms carried by the population rupture every year (30,000 to 40,000 ruptures per year). Although this rupture rate is low, strong motivation exists to improve the management of this disease because the prognosis after SAH is dismal.
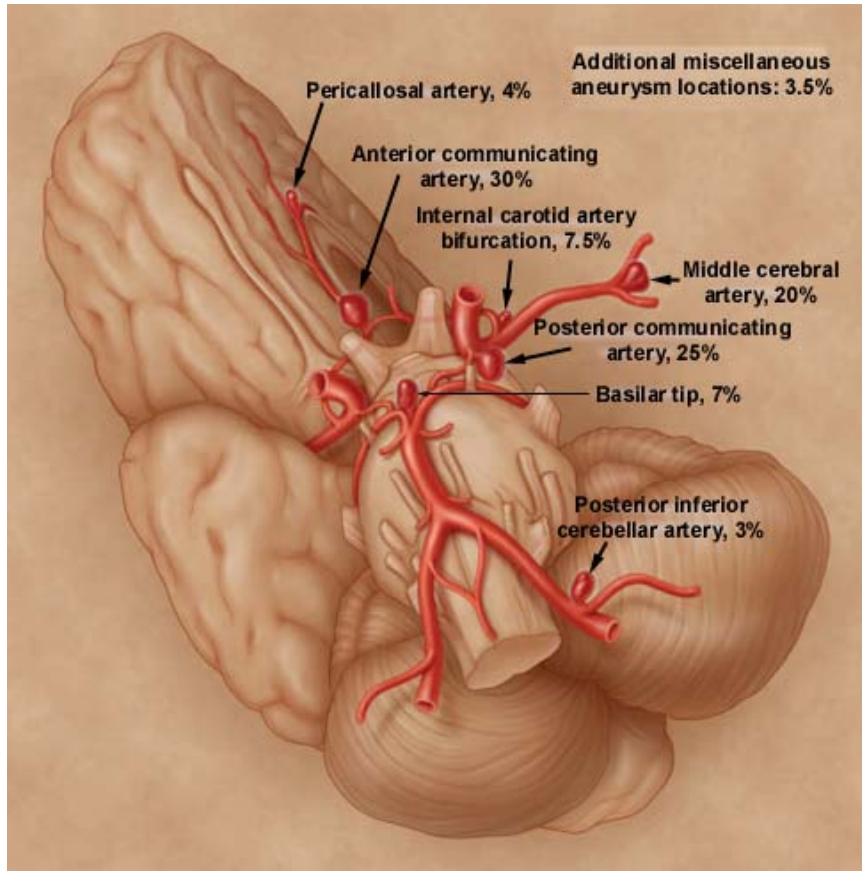
Figure 1-1. The distribution of cerebral aneurysms; modified from Brisman et al. [6]

Fatality rates due to SAH have been reported to range from 32 to 67% per calendar year and are about 45% within 30 days of the first bleed [6, 8]. Ten to twenty percent of SAH patients are either dead or comatose on arrival at an emergency department [8, 9]. The remainder may present with acute (developing over minutes to hours) excruciating headache, confusion, nausea, neck stiffness, transient loss of consciousness, epileptic seizures, or focal neurological deficits [9, 10]. Blood leaking into the subarachnoid space may cause cerebral vasospasm with concomitant ischemia within 2 to 12 days after the initial event [6, 11]. Although the initial bleed site is plugged by thrombus, the aneurysm wall remains friable and can re-bleed within 48 hours to two weeks [6, 9, 12]. Approximately 20% of SAH patients eventually become dependent with cognitive impairment and only 25-30% of patients have a relatively good functional

outcome [10, 12]. Blood present in the subarachnoid region may organize into scar tissue and prevent the proper drainage of cerebrospinal fluid causing increased pressure hydrocephalus months to years after the initial bleed [11, 12].

Various epidemiological studies have been conducted in order to ascertain the factors that contribute to the rupture of aneurysms. Three modifiable risk factors have been consistently associated with the incidence of SAH. These include current smoking, excessive alcohol intake (>100 or 150 g/week), and hypertension (>160/95 mmHg) with each carrying a relative risk of about 2 [13-15]. Other risk factors generally accepted to be associated with intracranial aneurysm rupture include aneurysm size, symptomatic aneurysms (symptoms caused by relatively large aneurysms impinging on adjacent neural structures), previous bleed from another aneurysm, aneurysms of the posterior circulation, multilobulated aneurysms, aneurysms with a large height-to-neck ratio (aspect ratio), female sex, younger age at diagnosis, and familial history [16]. Symptomatic aneurysms, posterior circulation aneurysms, and patients with previous SAH have been found to have a relative risk of rupture of about 8, 5, and 3 respectively [5, 17]. The relative risk of rupture for aneurysms having a maximum diameter of 7 to 12 mm is about 3 and for those with diameters more than 10 or 12 mm is about 15 [4, 17]. These rupture size statistics only suggest the probability of a ruptured aneurysm being a certain size and do not indicate a critical size for rupture of any given aneurysm because even 2 to 5 mm diameter aneurysms have been known to rupture [7, 18]. The aspect ratio of ruptured aneurysms has been observed to be significantly higher (1.5 to 2 times) as compared to the aspect ratio of unruptured aneurysms [19, 20]. Aneurysms with multiple lobes have been found to have a statistically higher risk of bleeding than unilobular
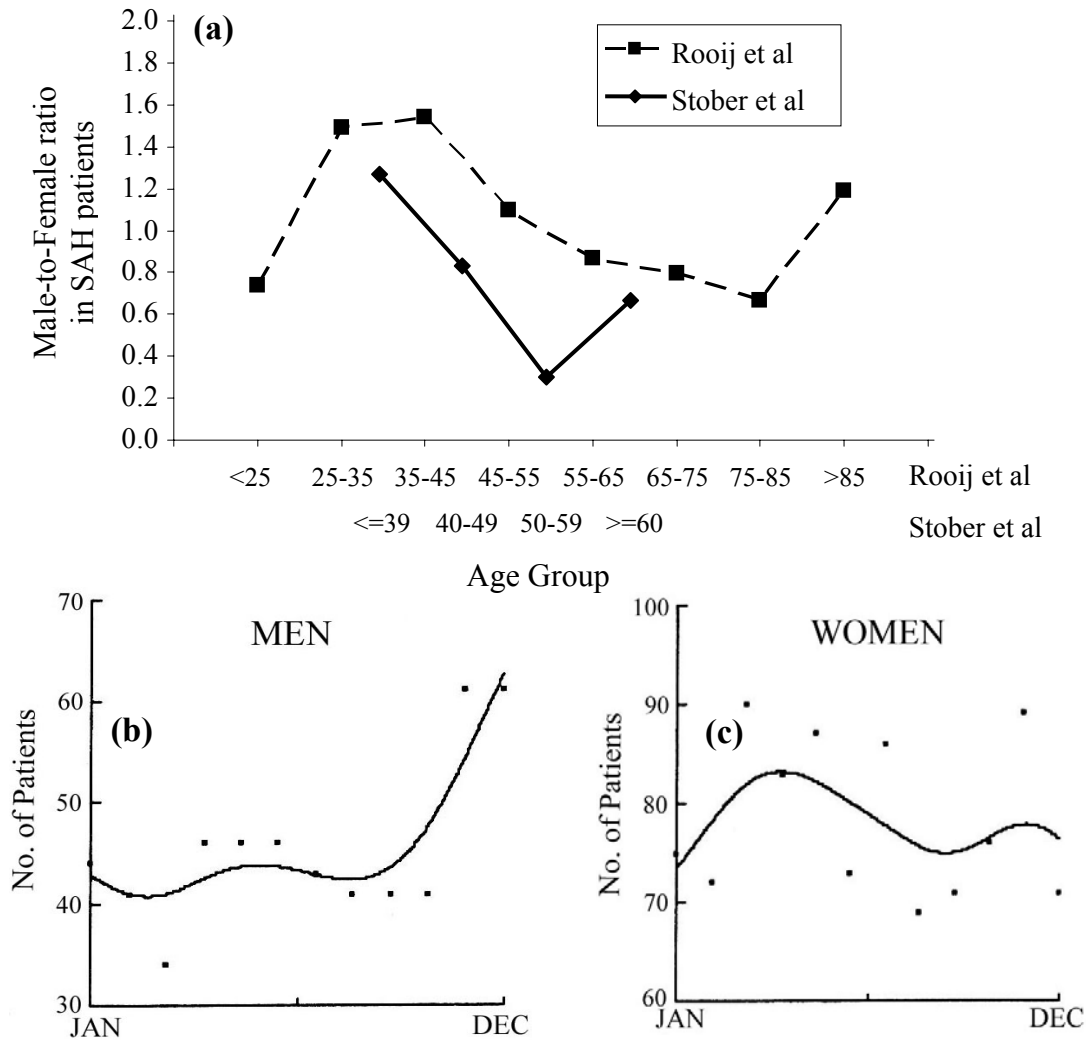
Figure 1-2. Gender differences in the incidence of SAH. (a) Variation in the ratio of men to women SAH patients with age; data from Rooij et al. [3] and adapted from Stober et al. [23]. Seasonal fluctuation in the incidence of SAH in (b) men and (c) women. The smoothed lines are a distance-weighted least-squares filter of the data points; from Chyatte et al. [24].

aneurysms; data from relatively small studies suggest that multilobular aneurysms rupture

at least twice as frequently [18]. Ten to thirty percent of all patients have more than one

aneurysm in their cerebrovasculature with higher percentages in women or in patients

with a familial bias [6, 11, 12, 21, 22]. This effect was accentuated in the case of 1

woman with an established familial bias (grandfather had aneurysmal SAH) who

developed 5 new aneurysms within a period of 9 years after being treated for SAH from

one aneurysm at the age of 24 [22]. First-degree relatives of patients are four times more likely to develop SAH with siblings being more liable than parents or children, while second-degree relatives have a relative risk of about 2 [4, 12]. A higher proportion of aneurysms is generally found among women than men (female-to-male ratio of about 1.5) and the relative risk of aneurysm rupture in women is about 2 [3, 5, 12]. Figure 1-2A shows the relative incidence in men and women with age. The fact that women have a higher incidence of aneurysms than men only when they are not in the reproductive stage suggests that there is a hormonal influence, with estrogen possibly playing a protective role [3, 22, 23]. Decreases in the skin collagen content are commonly observed in post-menopausal women. Collagen in the cerebral arterial vessel wall may also be diminished at this stage, predisposing the weakened arteries to develop aneurysms [23]. Gender differences have also been observed in seasonal fluctuations of aneurysm rupture (Figures 1-2B and 1-2C). Men seem to have a peak incidence in late fall while women have an annual peak during late spring (data from Connecticut, USA) [24]. Clustering of SAH in males occurred within 72 hours of a drop in maximum daily dew-point temperature of more than 25 °F or a drop in maximum daily barometric pressure of more than 55 mmHg; SAH in women showed no such trend [24].

Histopathological and/or immunohistochemical evaluations of the walls of human cerebral aneurysms suggest that the walls of unruptured aneurysms can be differentiated into what are possibly different stages of progression to eventual rupture. Results from three separate studies assessing a total of 74 unruptured aneurysms and 108 ruptured aneurysms provide an overall hypothesis for changes that occur in the aneurysm wall [25-27]. Nascent or initial stage aneurysms seem to have their inner surfaces completely

covered with endothelial cells with thin "smooth" walls comprised of linearly organized smooth muscle cells, regular layers of type IV collagen and very little evidence of inflammation. Possibly due to complex flow patterns being established in the diseased region, the wall undergoes injury and progresses through two different observed types. The wall thickens, being comprised of fibroblasts and disorganized smooth muscle cells (intimal hyperplasia), but eventually starts to lose its gross "regularity" and becomes hypocellular showing increased collagen content, and organizing luminal thrombosis. In what can be considered the final stage before rupture, the wall becomes irregular, extremely thin, and hypocellular with obscure layers of collagen and sparse smooth muscle cells. Figure 1-3 shows these four stages or types of unruptured aneurysm walls.

Ruptured aneurysm walls were mostly comprised of an acellular proteinacious structure (hyaline-like) with sparse smooth muscle cells and irregular layers of collagen IV with diffuse infiltration of macrophages and leukocytes. Other characteristics were suggestive of vascular remodeling attempts after a bleed. Recently bled aneurysms had open rupture points with a bulging protective layer of fibrin nets with fresh thrombus. Aneurysms maturing post-rupture showed reinforcement of the protective fibrin layer, proliferation of smooth muscle cells and capillaries within the organizing thrombus plug and intramural hemorrhage due to bleeding from these capillaries. Walls of ruptured aneurysms also express more of the basement membrane protein fibronectin (involved in early angiogenesis) as compared to unruptured aneurysms from the same patient [28]. The luminal surface of ruptured aneurysms consistently showed marked de-endothelialization [26]. Figure 1-4 shows the histomorphometric scores for the luminal
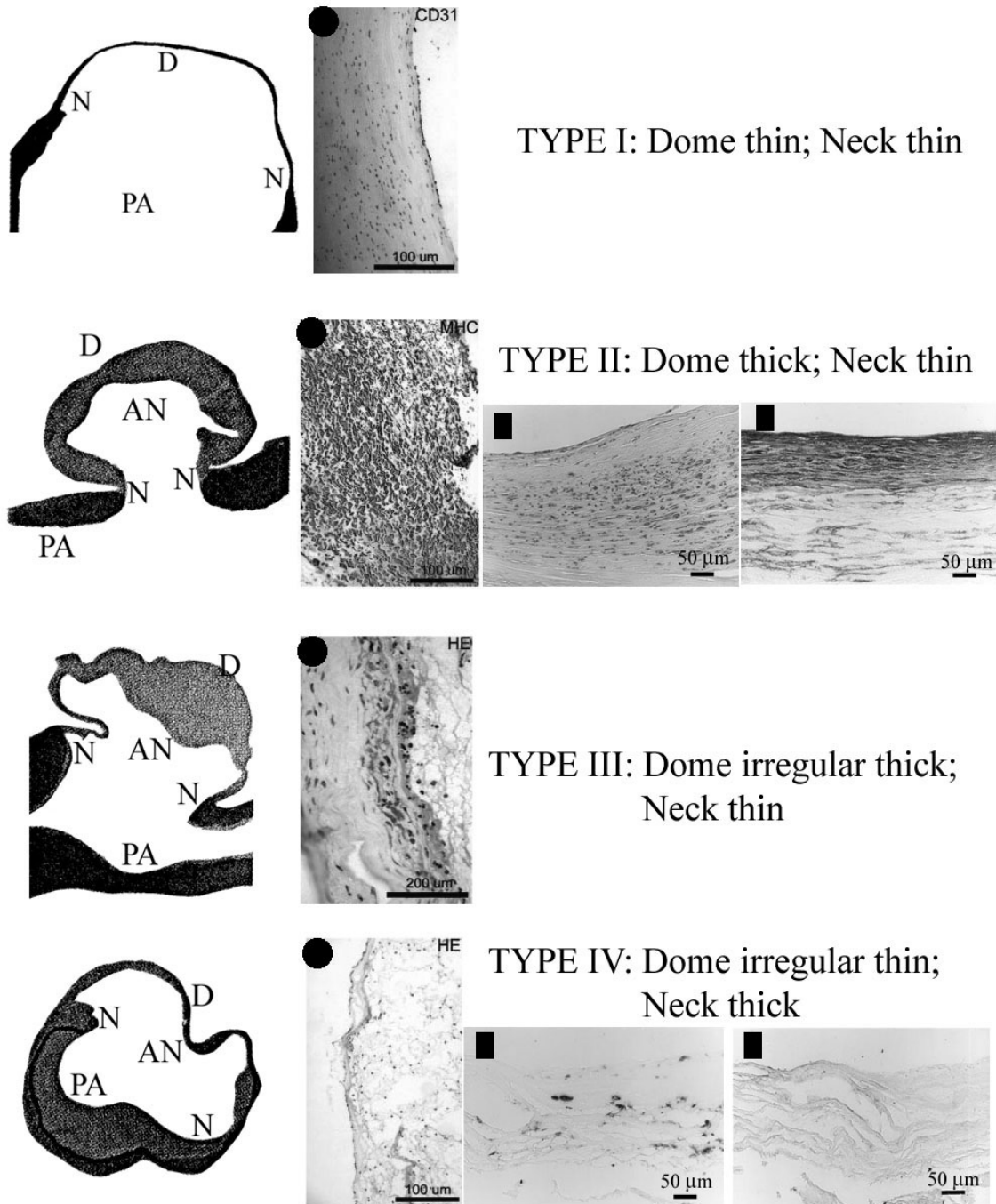
Figure 1-3. Four types of unruptured aneurysm walls suggesting progression before rupture. Left column from Suzuki et al. [25]; AN: aneurysm; D: dome, N: neck; PA: parent artery. Middle column (circular dots) – aneurysm wall sections from Frosen et al. [27]; staining method on top right, MHC: myosin heavy chain, HE: hematoxylin eosin. Right column (rectangular dots) from Kataoka et al. [26]; Type II aneurysms left: smooth muscle actin, right: collagen 4 immunostain; Type IV aneurysms left: macrophages, right: collagen 4 immunostain.
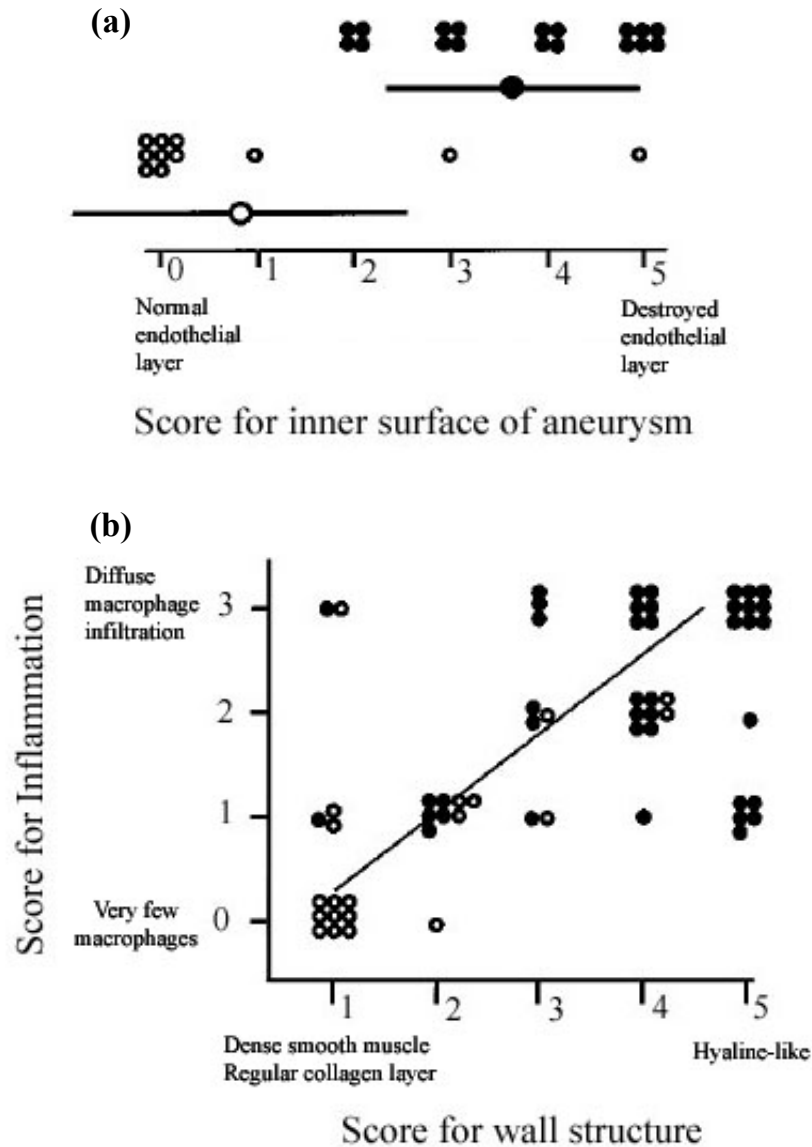
Figure 1-4. (a) Luminal surface of ruptured aneurysms (mean score 3.7±1.2) showing significantly higher endothelial cell layer destruction as compared to unruptured specimens (0.8±1.7). (b) Progressive inflammation resulting in enhanced degradation of aneurysm wall. Open and closed circles indicate unruptured and ruptured aneurysms, respectively. Adapted from Kataoka et al. [26].

surface of 29 ruptured and unruptured aneurysms and the degradation of the wall structure with progressive inflammation in 61 specimens.

It may be noted that these histopathological studies do not provide any information on aneurysm initiation or the time course of progression of aneurysms to

rupture. However, it seems safe to conclude from these data that aneurysm growth and rupture are related to abnormalities in the structure and/or maintenance of the vessel wall. This is further supported by investigations into related proteins and the genetic makeup of patients with aneurysms. The extracellular matrix (ECM) proteases matrix metalloprotease (MMP) -2 and MMP-9 have been consistently linked to cerebral aneurysms, with either patient serum or aneurysm wall tissue showing higher expression or activity of these 2 gelatinases as compared to controls [29-33]. Smooth muscle cells migrating into the organizing luminal thrombus of ruptured aneurysms [27] or the inflammatory infiltrate (macrophages) in aneurysm walls [34] would produce metalloproteases for their function, which could explain the observed increase in MMP levels. Adaptation to altered blood flow patterns in growing aneurysms might also be modulated by nitric oxide, which in itself can activate metalloproteases [35]. Patients with aneurysms also have significantly higher levels of plasma elastase (protease that cleaves elastin) as compared to controls [36, 37]. Cigarette smoking markedly reduces the inhibitory effect of α1-antitrypsin on elastase resulting in an imbalance of this protease-antiprotease interaction that predisposes smokers to aneurysm formation [38]. Aneurysm walls have been found to express less prostacyclin-stimulating factor (involved in stimulation of the synthesis of vasodilatory molecule prostacyclin) and the molecules PNUT and RAI (involved in tissue repair and arterial remodeling) as compared to control (superficial temporal artery) tissue [39]. Based on the information gained from these histopathological and molecular inferences, studies looking into variations in genes involved in the constitutive makeup of vessel walls of patients have isolated certain candidates. These include genes coding for collagens, elastin, endothelial nitric oxide

synthase, α1-antitrypsin, MMP-9, fibronectin (glycoprotein binding ECM components such as collagen, fibrin and heparan sulfate), secreted protein acidic and rich in cysteine (expressed by various cells at sites of turnover and tissue repair), polycystin (involved in protein-protein and protein-carbohydrate interactions in ECM), endoglin (component of transforming growth factor-β receptor complex expressed on endothelial cell surfaces), transforming growth factor-β receptors (involved in ECM deposition), perlecan (proteoglycan stabilizing macromolecules in basement membrane), serpin (inhibitor of active MMPs), and fibrillin (macromolecule of ECM that assembles into microfibrils surrounding elastin fibers) [40-44]. These studies have been conducted in various regions of the world with local populations and inconsistencies exist as to whether or not any particular gene (except for collagen genes) listed above induces susceptibility to aneurysm formation in any given population. A recent study has established a sequence variant in the chromosomal locus 9p21 as conferring risk for intracranial aneurysms, abdominal aortic aneurysms, and coronary artery disease [45]. Epidemiological evidence for the coexistence of these putatively disparate diseases was presented two decades previously [46]. This further suggests that an impaired response of the arterial wall in adapting to changes in blood flow patterns or to changes in blood constituents or both may be the underlying factor.

Certain investigators proffer the hypothesis that cerebral aneurysms are primarily a hemodynamically induced degenerative vascular disease [47-51]. Figure 1-5 shows the general reasoning followed in support of this hypothesis. The walls of cerebral aneurysms are known to have a complete loss of the internal elastic lamina and marked degeneration of the medial layer. In conjunction with the fact that most aneurysms are formed at
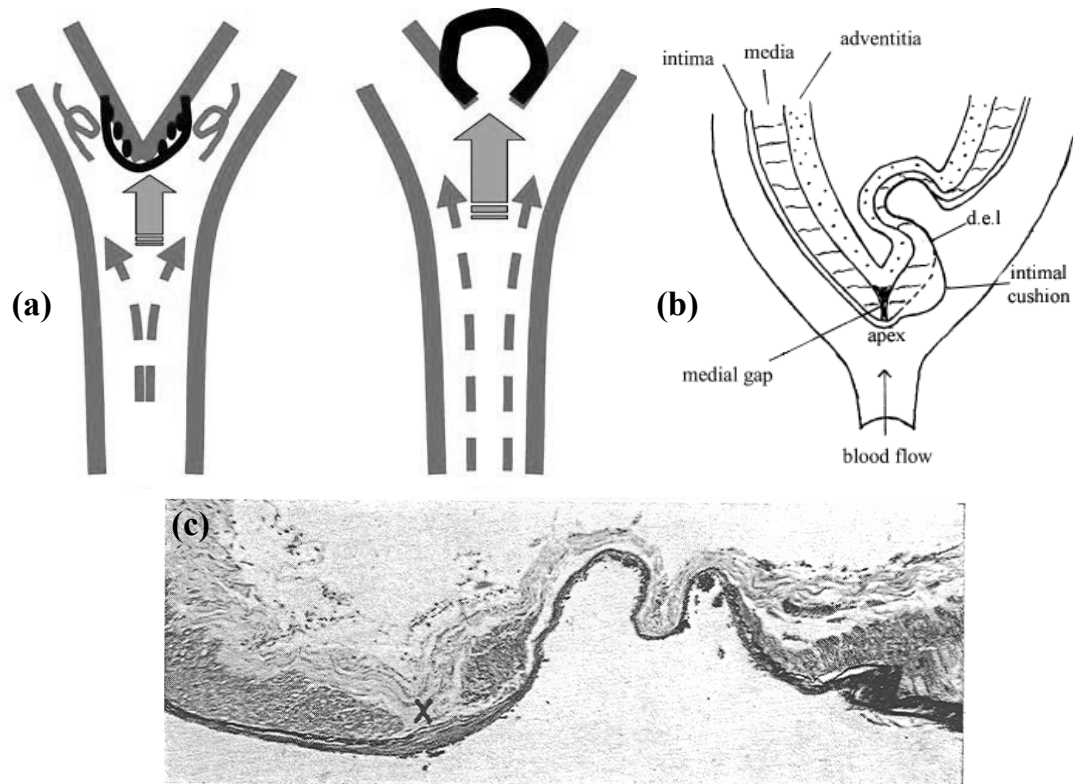
Figure 1-5. Medial gaps and intimal pads in aneurysm development. (a) Progressive hemodynamic stress at arterial bifurcations leads to intimal pad formation that reduces elasticity and disturbs flow resulting in aneurysmal dilatation; adapted from Zhang et al. [12] (b) Medial gaps at bifurcations further reduce wall strength; d.e.l: diminished endothelial layer; adapted from Krex et al. [21]; (c) histology from a human patient showing aneurysmal growth associated with similar structures, X marks the adventitial raphe (medial 'defect'); Stehbens [48].

arterial bifurcations around the fifth decade of life, it is thought that high shear rates at inner walls of bifurcations and the repetitive impingement of blood at the bifurcation apex causes changes in the structure of the bifurcation, which attempts to relieve itself of this stress by remodeling to form a cerebral aneurysm. The high elasticity of the arterial bifurcations in young ages is lost due to this repetitive hemodynamic insult, resulting in remodeling of the bifurcation to injury as intimal hyperplasia [11, 12]. These intimal pads or cushions reduce the elasticity of this region and presumably alter local flow patterns such that further hemodynamic stress causes aneurysmal dilatation. The presence of

medial gaps or adventitial raphe at bifurcation points further reduce wall strength at the apex predisposing to aneurysm formation. Medial gaps have been found in 60% of arterial bifurcations in patients between 1 and 80 years of age and the gaps widen with progressive ageing; intimal pads have been observed at 22% of bifurcations under 10 years of age and at 60% of bifurcations over 30 years [11]. If medial gaps or intimal pads predispose to aneurysm formation, these large numbers do not explain why the incidence of aneurysms is only 5% in the general population. The explanation, according to proponents of this hemodynamic injury hypothesis, seems to be that there are considerable variations in the branching structure of the cerebrovasculature around the circle of Willis and adverse flow patterns due to abnormal branching tilt the scale toward aneurysm formation in a small number of patients [11, 49]. There is no evidence yet as to what specifically these abnormalities might be. Significantly smaller area ratios (ratio of daughter branches cross-sectional area to parent artery area) have been found at bifurcations in the circle of Willis and bifurcations with aneurysms subtend larger angles than those without lesions [52]. The longitudinal axes of internal carotid, middle cerebral, and anterior communicating artery aneurysms seem to cluster around specific angles (112°, 110° & 170°, 90° & 150°, respectively) with respect to the parent artery axes [53]. There are other reports of such anatomical statistics, but a convincing geometrical argument has not yet been proposed. Surgical arterial bypass seems to generate aneurysmal dilatation at or close to the anastomosis site [54] in a small number of patients presumably due to altered flow mechanics, but it is difficult to classify these as true saccular aneurysms as found in the general population.

Hemodynamic parameters such as blood pressure (wall tension), aneurysm inflow rates, blood impingement forces, and residence time of blood within the aneurysm have been thought to play a role in aneurysm development or progression [50, 51]. The hemodynamics of cerebral aneurysms has mostly been investigated by numerical methods. The motivation of these studies has not changed since the initial reports and most of the more recent ones simply use different geometries to observe intraaneurysmal flow patterns [55-58]. Numerically computed intraneurysmal flow patterns or regions of high and low wall shear in non-complex geometries are generally similar to what may be gleaned from simple angiographic injections [59, 60] or from physical intuition based on the orientation of the aneurysm with respect to the parent vessel. It is also difficult to extract broad implications from single studies as results are specific to the geometry utilized and may not be representative of aneurysms in general. In terms of wall shear stress, however, a trend can be noted across such studies. The maximum shear stress on the aneurysm wall (generally, around the region where flow first impacts the wall, e.g., the distal neck of sidewall aneurysms) is found to be about 2-4 times the values in the parent artery, while the spatially averaged wall shear stress over the entire aneurysm is usually less than half the parent artery values [55, 56, 61]. Average shear stress over the aneurysm wall is, however, dependent on aneurysm dimensions and more or less decreases linearly with increasing aspect ratio [61]. Increased pressure within aneurysms as compared to the parent artery was thought to be a causative factor for aneurysm growth or rupture, but this pressure elevation at the site of flow impaction has been found to be only 1 to 2% of the peak intravascular pressure [62]. Numerical studies on intra-aneurysmal flow patterns and shear stress regions are in general corroborated by in vitro

studies on glass or elastomeric aneurysm models [63-66]. A recent numerical report on three paraclinoid aneurysm geometries suggests that the locations where aneurysms eventually developed may have been subjected to low and oscillatory wall shear stresses [67]. This is in contrast with the prevailing opinion that high wall shear stress may be responsible for aneurysm formation. Whether their results are artifactual or correlate with flow disturbances around intimal cushions (which presumably lead to focal flow separation regions with concomitant low wall shear) is to be determined. Numerical investigations of the aneurysm wall itself have also been conducted, but in spite of the progressive complexity of the models [68-70] changes occurring in the wall structure of human aneurysms are presently difficult to simulate in order to derive meaningful conclusions.

Experimental animal models have been consistently used to study aneurysm pathophysiology and response to various treatment methods; three general classes of these models are currently in use. Vein pouch models are the oldest of the three and are surgically constructed by suturing an explanted segment of a vein (usually jugular) onto an artery (usually common carotid). Various parent vessel-aneurysm configurations (lateral, bifurcation, terminal) can be constructed with this model by creating different anastomoses (side-to-side, end-to-side) before suturing the venous pouch at the required location [71]. This model has a short turnaround time and is preferred by companies testing deployment methodologies of devices. The limitations of this model are that the constructed aneurysm tends to thrombose spontaneously (in pigs), the aneurysm itself has a venous wall, and the parent vessel-aneurysm junction is comprised of suture lines. Another class of animal models attempts to create intracranial aneurysms based on the

hemodynamic theory of aneurysm genesis. These models utilize some combination of common carotid artery ligation to modify the flow in the Circle of Willis, high salt diet and/or renal artery ligation to induce hypertension, and diet of a lathyrogen to induce disorder in collagen cross-linking [11, 49, 72, 73]. The advantage of this model is that the lesions form on true intracranial bifurcations and could be used to study aneurysm genesis. However, the aneurysms themselves cannot be considered true aneurysms and are more aneurysm-like structures with internal elastic lamina and medial layer degradation. As a side-note, such aneurysm-like structures have also been noted to form spontaneously (effect increased with lathyrogenic diets) in the rat testicular artery due, presumably, to the hemodynamic variations produced by the vessel's high tortuosity [74, 75]. Based on initial investigations into creating saccular arterial aneurysms by elastase incubation [76], the third class of models is currently becoming the preferred mode for evaluating neuroendovascular devices and possibly even aneurysm pathophysiology [77, 78]. This model is created by incubating elastase in an isolated segment of the right common carotid artery in rabbits for a period of 10 to 20 minutes. The elastase degrades the arterial wall causing the artery to occlude while a portion of the base of the artery is maintained patent by the flow coming from the parent (innominate) artery. This results in the formation of a dilated saccular segment sitting on top of the innominate artery, thereby simulating human saccular cerebral aneurysms. The technique used to create this model has been optimized by various groups and the model is currently well characterized [79-84]. The advantages of this model are that the aneurysm wall itself is arterial, aneurysm dimensions are close to those of human aneurysms, there is no suture line at the aneurysm neck, and the aneurysm is known to remain patent for at least 2 years

[77, 85, 86]. Aneurysmal wall shear stress is similar to that experienced by human intracranial aneurysms [78]. The elastic lamina in the wall of these experimental aneurysms is markedly reduced just as it is in human aneurysms and wall thicknesses are approximately the same as human aneurysms (~50 μm) [87]. Limitations include the fact that the medial layer in the model is preserved in distinction to human aneurysms [87], the Reynolds (ratio of inertial to viscous forces) and Womersley (ratio of unsteady inertial to viscous forces) numbers in the rabbit innominate artery are about 2 to 3 times the corresponding values in human cerebral vessels, and the complication rates in working with rabbits are relatively high [88]. Figure 1-6 shows an angiogram and histological section of a rabbit elastase-induced aneurysm.
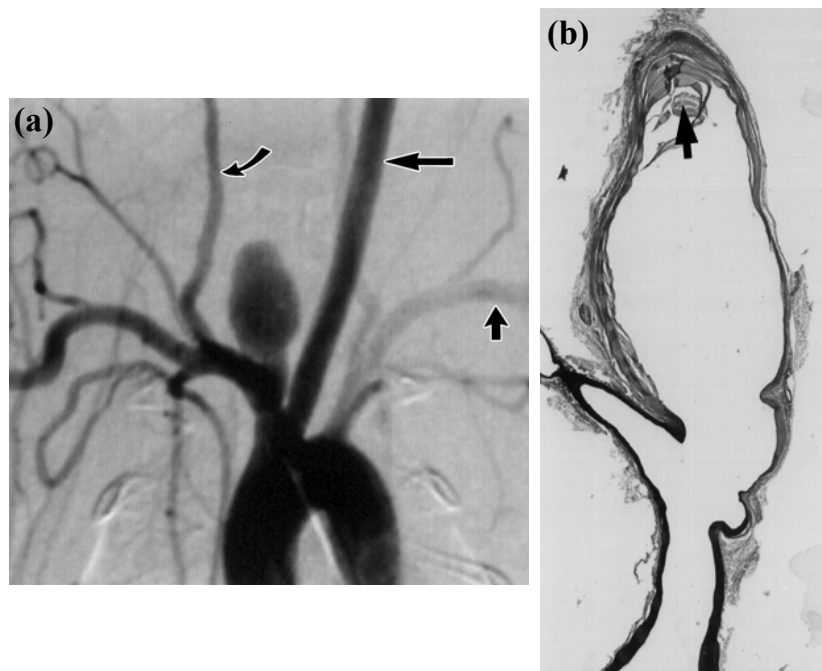
Figure 1-6. (a) Elastase induced saccular aneurysm in the rabbit two weeks after aneurysm induction; the vertebral (curved arrow), left common carotid (straight horizontal arrow), and left subclavian (vertical arrow) arteries are marked; (b) a section of the same aneurysm stained with van Gieson's stain (elastic lamina black); almost complete degradation of elastic lamina within the aneurysm cavity can be noted, laminated thrombus is present at the aneurysm dome (arrow). Adapted from Altes et al. [77].

1.2. Treatment of cerebral aneurysms by flow diversion

The treatment of cerebral aneurysms has evolved from carotid ligation in the 1930s to clipping from the surgical perspective and intraaneurysmal embolization by detachable balloons in the 1960s to coiling from the endovascular perspective [89]. Comparison between the surgical clipping and endovascular coiling treatments in the International Subarachnoid Aneurysm Trial showed a 7% absolute reduction in risk with coiling at 1 year post-treatment with the benefit being maintained until 7 years [90]. The requirement for late re-treatment is, however, as much as 7 times higher in the endovascular cohort [91]. In one long-term coiling study, complete aneurysm embolization during the procedure was achieved in only 55% of aneurysms, while aneurysm recanalization was observed in 21% of followed-up cases [92]. Intraaneurysmal coil masses are subjected to pulsatile impingement forces potentially resulting in coil compaction and aneurysm regrowth over the long term, especially in wide-necked aneurysms where it is also difficult to achieve high coil packing densities [9, 93, 94]. Initial experimental and clinical reports suggested improved success if these aneurysms were coiled with the assistance of a stent deployed in the parent artery as a scaffold [95, 96]. Flexible, intracranial stents [97, 98] have subsequently been developed to assist the endovascular coiling of wide-necked aneurysms (ratio of aneurysm height to neck less than 1.5 or 2) with better overall outcomes as compared to coil-embolization alone [99]. Current knowledge suggests that endovascular treatment can be considered for any given aneurysm, although guidelines for treatment involve consideration of conservative management of the patient and input from both interventionalists and neurosurgeons on a case-by-case basis [100]. Various improvements in endovascular

devices such as fully retrievable stents, bioactive coils, and liquid embolic agents are currently being evaluated for cerebral aneurysm treatment [91, 101].

Seminal studies in the early- to mid-90s by three independent groups introduced the notion that cerebral aneurysms could be successfully treated solely by the deployment of stents within the parent artery [102-105]. Their hypothesis was that stents would divert flow away from the aneurysm and into the parent artery and the resultant sluggish flow within the aneurysm would promote thrombus formation that would eventually organize into scar tissue and thus exclude the aneurysm from the circulation. Moreover, the stent implanted in the parent artery would, over time, be incorporated into the vessel wall thereby precluding regrowth of the aneurysm by hemodynamic mechanisms. Three different stents were implanted across twenty four sidewall venous pouch aneurysms on canine carotid arteries in these studies. Seven of nine aneurysms treated with balloon-expanded tantalum stents were stably occluded at follow-up times ranging from 1 through 9 months; 9 of 9 aneurysms treated with self-expanding nitinol stents were stably occluded at 3 through 9 months; 6 of 6 aneurysms treated with self-expanding cobalt alloy stents were stably occluded at two months [103-105]. Histological sections revealed fibrous tissue completely filling the aneurysm [105]. Angiographic injections performed immediately after device implantation showed altered intraaneurysmal flow patterns with delayed inflow and outflow and stasis of contrast within the aneurysm sac [104, 105]. Stents with higher pore densities provided higher aneurysm occlusion rates and a requirement for appropriate stent designs to optimally alter intraaneurysmal hemodynamics was noted [104]. These results have been corroborated by subsequent clinical evidence.

Figure 1-7 shows the results obtained from treating a patient with a diseased basilar artery with a Wallstent[TM] (Boston Scientific, Natick, MA). Since the introduction of stents as scaffolds to hold coil masses within aneurysms, the treatment of aneurysms with stents only has increased because clinicians may prefer to stage the coiling procedure to a later date depending on the degree of contrast stasis visualized after the stent is deployed. At least seven clinical studies treating a total of 19 aneurysms with stents alone have reported progressive thrombosis or complete occlusion of the aneurysm at follow-up (Table 1-1) [106-112]. The successful treatment of dissecting cervical internal carotid artery aneurysms and other pseudo-aneurysms solely with stents has also been consistently reported [113-116]. On the other hand, 10 aneurysms have been reported to have persistent filling at follow-up [107, 109, 117]. It is important to note that none of these devices was designed to act as a flow divertor, but instead as a scaffold for
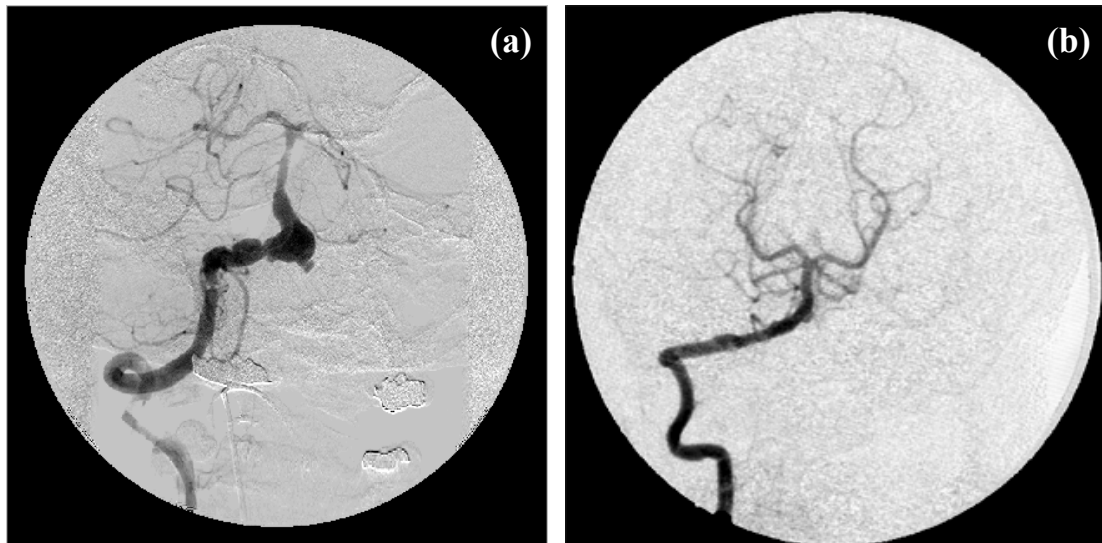
Figure 1-7. (a) Angiogram showing a fusiform vertebro-basilar aneurysm; (b) three months after treatment with a coronary stent (Wallstent[TM]), the aneurysm was completely excluded. From Sadasivan et al. [116].

Table 1-1. Clinical studies reporting treatment of aneurysms with stents only

	Publication	Stent	Aneurysm number and type	Follow-up
COMPLETE OCCLUSION	Lylyk et al. [108]	AVE inx, AVE gfx, Med X, Velocity	3 saccular sidewall, 1 dissecting, 1 fusiform, type U	CO 3-6 mo.
	Szikora et al. [109]	AVE INX	1 ICA, 2 VA	(> 90% thrombosis) ICA aneurysm occluded at 12 mo., 1 VA aneurysm recanalized at 6 mo. but stable up to 48 mo., 1 VA aneurysm shows no residual at 6 mo. based on MR angiography
	Doerfler et al. [83]	AVE INX, AVE Cerebrence	2 small wide-neck VA	CO 7 days (maintained at 6 mo.)
	Vanninen et al. [110]	Magic Wallstent, AVE S7, AVE INX	3 wide-neck aneurysms (basilar trunk, ICA)	CO 1 mo. (maintained at 6 and 24 mo.), 3 mo., and 3 mo., respectively
	Han et al. [107]	AVE S670	1 basilar trunk	~80% occlusion at 1 mo.
	Zenteno et al. [111]	Express, Express 2	3 vertebro-basilar	1 aneurysm almost CO at 15 days and CO at 3 years, 2nd and 3rd aneurysms CO 3 and 6 mo., respectively
	Zenteno et al. [112]	Velocity, Multi-link Pixel	2 superior cerebellar	CO 1 mo. (maintained at 6 mo.)
NO OCCLUSION	Lanzino et al. [117]	AVE GFX, AVE INR	2 basilar trunk, 1 VA, 1 ICA	CO 24 to 48 hours (2 cases), 48 hours to 4 days (1 case), 3 mo. (1 case)
	Szikora et al. [109]	AVE INX	3 (type U)	CO < 30 days
	Han et al. [107]	1 case AVE S670, 2 others U	1 ICA, 2 (type U)	1st case CO 2 mo., 2 others NA (probably ~2 mo. because procedure was staged for coiling)

CO: complete occlusion; mo.: month(s); ICA: internal carotid artery; VA: vertebral artery; U: not available

coils or stenotic arteries. Moreover, the follow-up time point in the clinical studies noting incomplete occlusion is less (mean ± standard deviation of 1 ± 1 month approximately) than those that found complete aneurysm occlusion (mean ± standard deviation of 4 ± 3 months approximately). These clinical reports also provide evidence of the importance of device porosity (ratio of metal-free surface area to total surface area) because sometimes two or three stents needed to be deployed concentrically at the same location to reduce the effective porosity and achieve sufficient intraaneurysmal contrast stasis [106, 118].

1.2.i. Changes within the aneurysm

Detailed evaluations of the changes in intraaneurysmal hemodynamics due to flow divertors have mostly been conducted via in vitro and numerical studies. In general, observed changes in the intraaneurysmal flow patterns have remained similar to those reported by the original studies on flow diversion [119, 120]. In non-stented sidewall aneurysms, the flow impinges on the distal neck of the aneurysm, follows the distal wall to the dome and exits the aneurysm near the proximal neck. This forms a vortex within the aneurysm that rotates in the direction opposite to the direction of flow in the parent vessel (Figure 1-8a & b). This flow pattern varies with the pulsatility and strength of the parent artery flow, aneurysm geometry, and its orientation with respect to the parent vessel. Depending on these parameters, a singular vortex with its center undulating along the distal wall and transiently entering the parent vessel may form [119, 120], or the flow may be divided after it enters the aneurysm forming regions with both clockwise and counterclockwise flow [121, 122]. Maximum velocities within aneurysms are reported to be between 10% to 50% of those in the parent vessel [120, 123, 124].
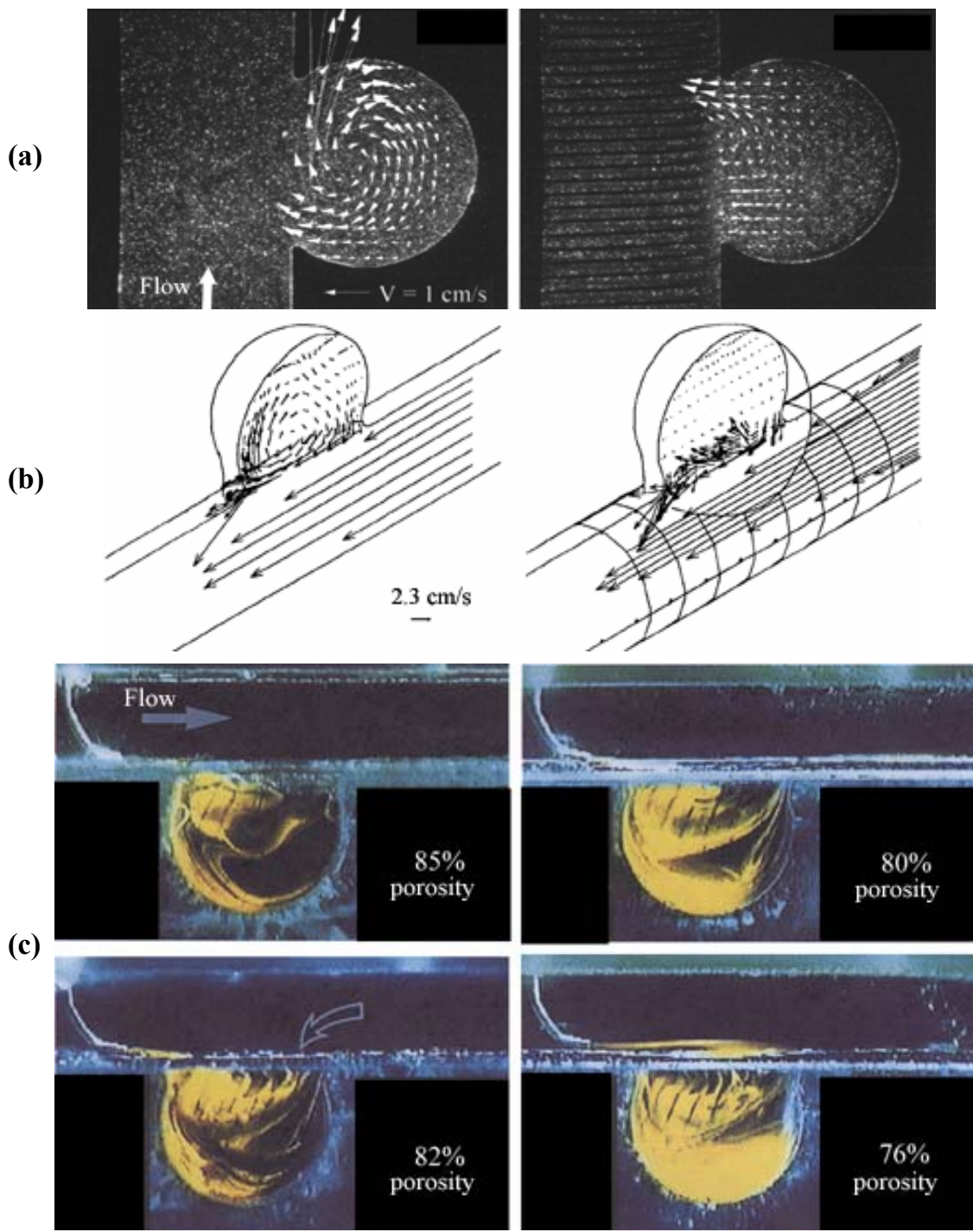
Figure 1-8. Intraneurysmal flow alterations due to flow diversion; intra-panel images are at same point in the cardiac cycle. Particle image velocimetry (a) and computational fluid dynamics (b) studies showing reduced flow activity and change in the direction of vortex rotation after stenting; left column before stent; right after stent; modified from Lieber et al. [125] and Aenis et al. [125] (c) Laser induced fluorescence study showing increasing size of flow stasis region at dome with reducing porosity of stent mesh; curved arrow shows stent layer; modified from Lieber et al. [119].

The placement of stents across the aneurysm neck breaks up the in- and out-flow patterns, with flow tending to enter the aneurysm perpendicular to the device mesh. Intraaneurysmal flow activity becomes restricted to the neck region and is in the direction of parent artery flow; flow enters at the proximal neck and exits at the distal neck (Figure 1-8a & b) [120, 122, 123, 125]. Reported reductions in maximum intraaneurysmal velocities due to stents range from 50% to 90% [123, 124, 126]. Depending on the stent configuration deployed, the maximum wall shear stress at the distal neck region of the aneurysm is reduced to 10 to 25% of non-stented cases [121, 123, 127]. Stents also mitigate the significant changes in direction of wall shear that untreated aneurysms may experience by inducing (beneficial) unidirectional shear stress on aneurysm walls [121]. A numerical simulation considering non-Newtonian effects suggests a threefold increase in blood viscosity in more than half of the aneurysm sac as compared to the non-stented case [124]. Hydrodynamic circulation, which is spatially-integrated vorticity, and mean hydrodynamic circulation, which is temporally-averaged hydrodynamic circulation, have been used as indices of intraaneurysmal flow activity [125]. The maximum and mean hydrodynamic circulation have been found to reduce to 15 to 25%, and 5 to 15%, respectively, of non-stented cases in different aneurysm geometries with device porosities ranging from 65% to 75% [121, 122, 125].

Reduction in aneurysmal flow activity due to stents is dependent on stent design. Reducing the porosity of stents from 85% to 76% progressively increased the size of the flow stagnation zone formed near the aneurysm dome (Figure 1-8c) [119]. A recent numerical study on commercially available stents showed reduced intraaneurysmal vorticity with the lower porosity stent (Wingspan, Boston Scientific/Target, 80%

porosity) as compared to higher porosity stents (Neuroform2, Boston Scientific, 84% porosity; Vision, Guidant Corporation, 89% porosity) [128]. Further simulated reductions in porosity by concentric stent deployment progressively reduced regions of high wall shear in the aneurysm [128]. Helical springs seem to significantly alter aneurysmal flow patterns under pulsatile flow [121] and reduce velocity magnitudes by 50% under steady flow simulations [123] even when both designs have the same porosities. Increasing the pore density (number of pores per unit surface area), or equivalently, decreasing the inter-strut spacing, of devices while maintaining a constant porosity reduces intraaneurysmal flow activity. A decrease in inter-strut spacing by 25% reduced the mean hydrodynamic circulation by 30% [125]; doubling the pore density reduced the maximum hydrodynamic circulation by half [122]. One study comparing different stent designs suggested that design parameters do not have any effect on intraaneurysmal hemodynamics [129], but their method of quantifying intraaneurysmal flow activity may not be amenable to stent evaluations and the high range of porosities considered (80%-93%) may not have had any measurable effect on intraaneurysmal flow.

Molecular mechanisms leading to thrombus formation within the aneurysm are not yet elucidated, but certain plausible hypotheses may be drawn. Separated flows, which have similar characteristics to intraneurysmal flow recirculation and stagnation, are known to be thrombogenic. An in vitro experiment conducted on flow around a step protrusion show increased adsorption of proteins such as fibrinogen deposited in the separated flow region resulting in high platelet adhesion specific to this zone [130]. At the low shear rates existing within the aneurysm sac, platelet adhesion is primarily mediated by fibrinogen-glycoprotein IIbIIIa linkage [131]. Platelets activated while

traversing the flow divertor struts into the aneurysm and other coagulation factors may reside for longer periods of time within the aneurysm due to the delayed washout and retarded flow induced by the device. The presence of activated coagulation factors is essential to the initiation of thrombus formation, but stagnant flow preferentially enhances the resulting thrombus burden [132]. Clinically, spontaneous thrombosis of giant unruptured aneurysms that presumably have inherent low flow or stasis zones is known to occur [133]. Histology obtained from a patient with an internal carotid artery aneurysm treated only with a high porosity (~85%) intracranial stent intended for coil-assistance (Neuroform, Boston Scientific, San Leandro, CA) showed intimal proliferation and mild endothelialization at 4 months post-treatment. Fibrocellular tissue was found lining the aneurysm walls with a central thrombus contiguous with the arterial lumen (Figure 1-9) [134].
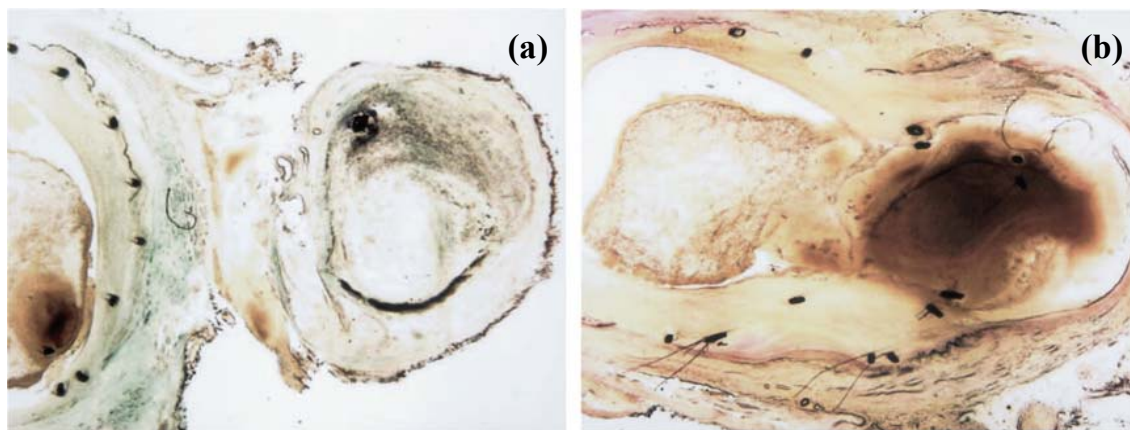
Figure 1-9. Post-mortem histological sections of an aneurysm treated only with a high-porosity intracranial stent intended for coiling procedures; 122 days post-stent implantation; parent artery on left; aneurysm on right. Proximal neck of aneurysm (a) shows fibrocellular tissue whereas central neck region (b) shows unorganized thrombus. From Lopes et al. [134].

1.2.ii. Changes in the parent artery

A sequence of molecular interactions occurs on the luminal surface of the flow divertor culminating in the formation of a new intimal lining (neointima) that covers the metallic surface. The artery is then returned to a physiological state and blood constituents are no longer exposed to a foreign body. Knowledge of the arterial response to device implantation has largely been gathered during the research and development of stents for the treatment of coronary stenoses over the past 10 to 15 years [135].

Figure 1-10 shows the phases and temporal organization of the structure of the neointimal layer. The reactivity to the deployed foreign body depends on device surface characteristics at the molecular level that are a function of the crystallographic structure, surface defects, the metal finishing process, trace contaminants, and oxidation [136, 137]. Initial interaction of the metallic surface is with serum proteins and largely depends on the water organization around the protein structure with water dipoles coupling anionic groups on the stent surface with cationic groups of the proteins [138]. This transient polar interaction may alter protein structure to expose hydrophobic regions that form more permanent nonpolar interactions with the metal surface. This further deconvolves the initial layer of proteins and they expose additional polar and hydrophobic regions to other serum proteins with intact structures and ligand sites that allow for cell-cell ineractions [136, 138]. The metal surface is thus considered "passivated". This protein layer develops over a period of seconds, as per the Vroman effect, through sequential adsorption and desorption of proteins with progressively higher affinity: albumin to globulin, fibrinogen, fibronectin, factor XII, to high molecular weight kininogen [137, 139].

(c)

(a)

(b)
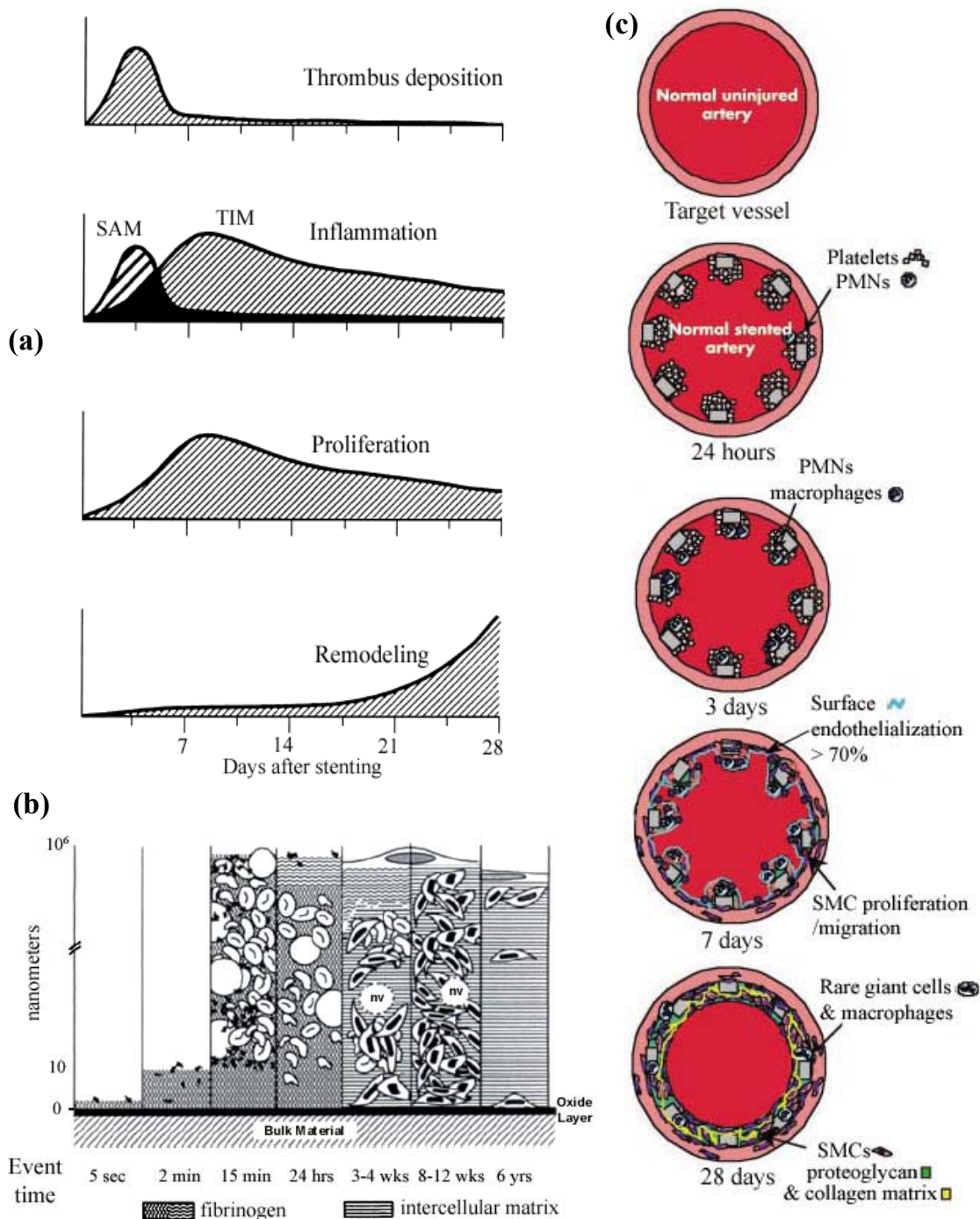
Figure 1-10. Phases in the response of arteries to stenting. (a) charts showing the activity of the four phases, SAM: surface adherent monocytes, TIM: tissue-infiltrating monocytes, from Edelman and Rogers [140]; (b) and (c) developing composition of the neointimal layer over time; (b) nv: neovessel, modified from Palmaz [136]; (c) SMC: smooth muscle cells, PMN: polymorphonuclear leukocytes, adapted from Virmani et al. [146].

Activated factor XII initiates the coagulation cascade through rapid contact-phase reactions over the next two to three minutes, which lead to common pathway ineractions on activated platelet membranes [139]. Amorphous platelet fibrin clots irregularly cover the metal surface (around the struts of the device) over subsequent minutes suggesting repeated deposition, fragmentation, and sloughing [136]. Activated platelets express adhesion molecules which attach to circulating leukocytes via platelet receptors thereby recruiting a layer of mono- (macrophages) and poly- (neutrophils) morphonuclear leukocytes to the stented region in the initial hours of the inflammatory phase of neointimal growth [140-142]. Surface adherent leukocytes infiltrate the inner regions of the developing neointima over the next 2-3 days to 2-3 weeks. During the same period, growth factors released from platelets, macrophages, and vascular smooth muscle cells initiate the proliferation and migration of smooth muscle cells from the media into the developing neointima, progressively replacing the initial thrombotic layer by fibromuscular (fibroblasts/smooth muscle cells) tissue [136, 140, 141, 143, 144]. The proliferation of smooth muscle cells with an embryonic phenotype is maximal at about a week and the phenotype of these cells in the intima is almost entirely converted to the adult type after about a month to two months signifying end of proliferation at this time point [145]. As fibroblasts proliferate in the neointima, they and endothelial cells also produce and secrete extracellular matrix constituents and by one month, the neointima also contains proteoglycans and type III collagen [145, 146]. This extracellular matrix also controls smooth muscle cell proliferation and phenotypic modulation [145]. This remodeling of the neointima continues over the next 3 to 6 months, with the fibromuscular tissue being progressively replaced by increasing type I collagen content,

leading to neointimal shrinkage and lumen enlargement [140, 146]. Neointimal thickness in experimental animal models is seen to peak at around 8-16 weeks and reduce thereafter [147-149].

Endothelialization of the luminal surface of the neointima begins within days of stent implantation and at about 1 week, the surface is incompletely covered with immature amorphous endothelial cells [148]. Coverage and maturity of the endothelial cells progressively increases showing a flat and mosaic-type appearance at 3 weeks to fully mature, elongated cells oriented in the direction of flow at 32 weeks [148]. Endothelial cell migration occurs from sites with preserved endothelial lining towards sites of injury in the direction of flow [147, 150]. Endothelialization accompanied by nitric oxide generation via endothelial nitric oxide synthase is also known to reduce the cellularity and thickness of the neointima [141, 147, 149]. Endothelial lined clefts penetrating the organizing neointima from the luminal surface have been observed at 8 days [144]. Neointimal cells in mature neointima organize around neovessels that have been shown to originate from the vasa vasorum [136]. Although the constituents of the neointima and its sequential organization are known to be the same in animals and in man, the time course to endothelialization and maturity may be significantly longer in humans (as much as 5-6 times longer, in proportion to species longevity; however, this information is based on stent implantation in atherosclerotic human coronaries) [146].
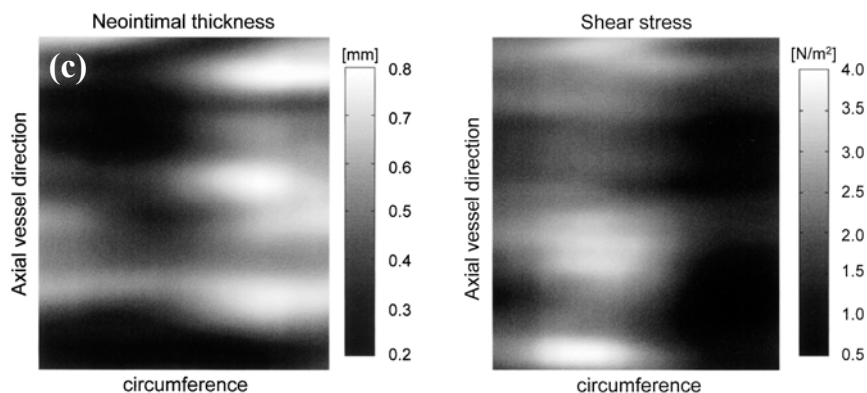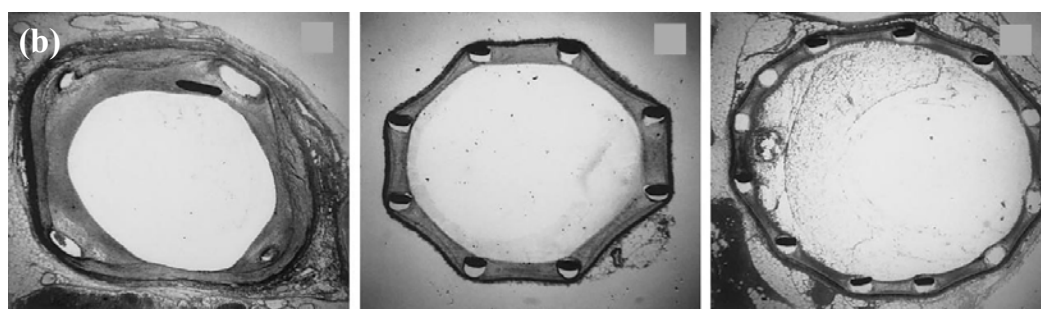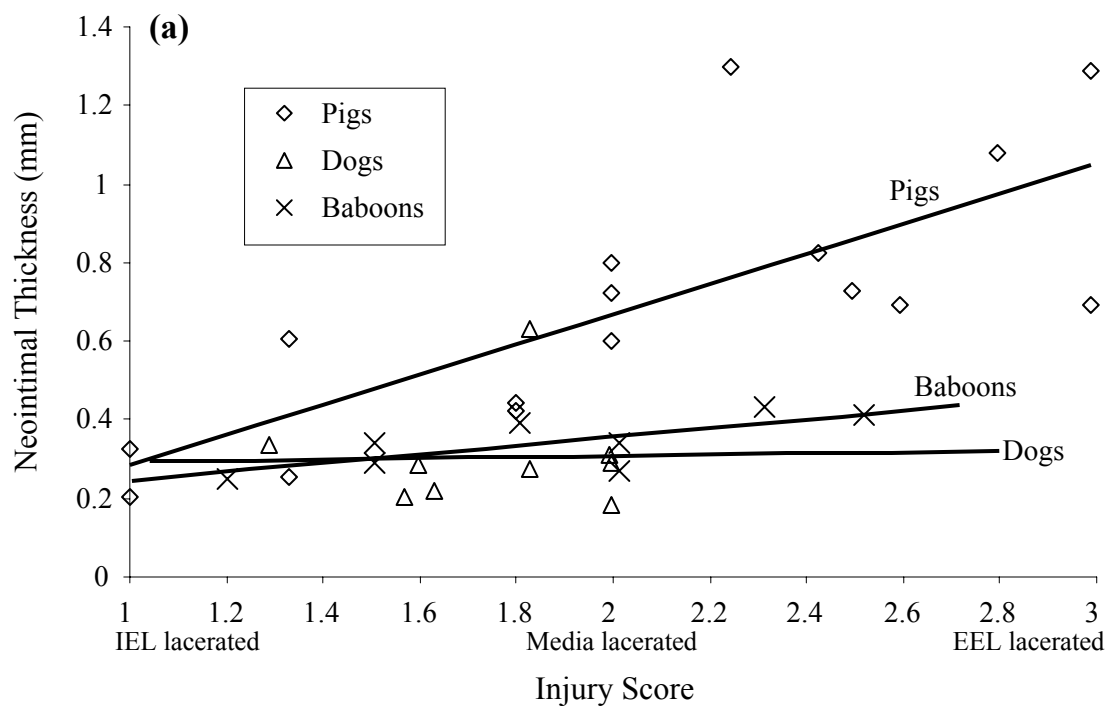
Figure 1-11. Factors modulating neointimal thickness. (a) Response to the degree of injury varies among species, but remains relatively same for mild injuries; IEL & EEL: internal & external elastic lamina, respectively; Schwartz and Holmes [151]. (b) Increased 'circularity' and lower inter-strut spacing of deployed stents in cross-section reduces neointimal thickness; Garasic et al. [155] (c) Higher neointimal thickness in regions of lower shear stress; Wentzel et al. [159].

Experimental and clinical evidence show that the degree of neointimal hyperplasia is directly dependent on the extent of injury imposed on the original artery with laceration of the internal elastic lamina by stent struts resulting in less neointimal thickness than lacerations of the medial layer (Figure 1-11a) [143, 151]. Balloon expanded stents may thus produce thicker neointima as compared to self-expanding stents [104]. Minor to no damage to the internal elastic lamina seems to produce the same degree of neointimal response across experimental species. The design of stents also modulates the neointimal response [152]. Differences in stent design produce different degrees of neointimal hyperplasia for the same degree of stent-to-artery diameter expansion ratio because of reduced disruption of the endothelial cell lining [153], or elastic or medial lamina [154], by struts of more favorable configurations. Reducing the inter-strut spacing and making the design more "circular" reduces the resultant neointimal thickness (Figure 1-11b) [155]. The vessel attempts to eliminate altered flow and low wall shear stress regions generated near stent struts by restoring circularity and normal physiological patterns [155, 156]. Reduced inter-strut spacing and stent injury must be balanced by consideration of endothelial denudation and thrombus burden. If the entire stent surface is covered by thrombus or the endothelial lining in the stented region is markedly degraded, re-endothelialization must progress from the proximal and distal non-stented regions and can take longer, resulting in greater neointimal hyperplasia [136]. Lower neointimal thickness is thus found within shorter stents [157]. The amount of thrombus deposited in the stented region is inversely dependent on parent artery flow and more thrombus generated under lower flow is correlated with higher neointimal thickness. Parent artery flow reduction by 25% has been correlated with increase in

neointimal thickness by 50 to 100% [149]. Higher neointimal thickness has been observed on the slower flow inner curvature of stented arteries when compared to the higher flow outer curvatures [157]. Increased clotting times and reduced thrombus weight have been observed in vitro at higher shear rates and the composition of the thrombus also changes with red blood cell and fibrin deposition being markedly reduced at higher shear as compared to platelet deposition [132, 158]. Regions of higher neointimal thickness within stented regions correlate with regions of low wall shear (Figure 1-11c) [156, 159]. Endothelial cell migration is also promoted under high shear rates [150]. Platelet thrombus formation on collagen surfaces under stent struts is inhibited by blocking glycoprotein IIb/IIIa function, but not by blocking glycoprotein Ibα [160], suggesting the presence of low shear regions under stent struts (between stent and artery) where platelet interaction is mediated by glycoprotein IIb/IIIa receptors only as opposed to glycoprotein Ibα receptor involvement under higher shear [131].

Poor apposition of stent struts to the vessel wall may, therefore, result in acute (<24 hours) to sub-acute (1- to 14-days) stent thrombosis [161]. Stent thrombosis is of particular concern when devices are implanted in small arteries where the increased metal-to-artery burden may overwhelm the regular process of neointima formation and excessive thrombus occludes the vessel [142, 162-165]. A higher incidence of stent thrombosis seems likely if the ratio of the open stent diameter to the artery diameter is greater than about 1.5 [142, 162, 163]. It may be noted that altering the surface properties of stents (e.g., with heparin or polymer coating) reduces the risk of stent thrombosis, but does not change the degree of neointimal hyperplasia [154]. Increased in-stent thrombus burden may increase neointimal thickness, but reduced thrombus burden does not

necessarily reduce neointimal hyperplasia [140]. Proliferation of neointima due to vascular injury does not depend solely on the amount of thrombus generated [166]. A change by more than 10° of coronary vessel angulation due to stent implantation has been shown to be a significant predictor of major adverse cardiac events [165]. Initial concerns with stent implantation included the possibility of occlusion of side branches originating from the parent vessel in the stented region. Especially in the intracranial arteries, minute side branches (called perforators) ranging in diameter from 100μm to 1 mm supply critical regions of the brain [167, 168]. Side branch occlusion by stent meshes has, however, not been observed thus far [117, 142, 157, 169, 170]. The arteriovenous pressure difference existing across the ostium of the side branch covered by the stent mesh maintains branch patency. Stent struts covering the ostium are preferentially covered by endothelial cells in continuity with the neointimal lining [148]. Side branch compromise and occlusion may occur in the case of atherosclerotic arteries due to the "snowplow" effect whereby plaque in the parent artery or side branch is pushed aside during stent implantation to occlude the side branch [171, 172].

1.3. Functional Angiography

Attempts to quantify blood flow from analysis of contrast transport have been undertaken since the advent of angiography [173]. Indicator-dilution methods that do not employ X-rays were established around the same time that X-rays were discovered. The principle of these methods relies on injecting a specified amount of dye or indicator at one location in the vascular tree and then sampling the diluted concentration of the dye at another location. Given the infusion rate (m mg/s) of the dye or the amount (M mg)

injected and measuring the dye concentration (C mg/ml) at one instant or over a period of time (t s), flow rate (Q ml/s) between the injection and sampling points could be estimated as $Q = m/C$ or $Q = M/Ct$ [174]. This method was eventually employed with angiographic acquisitions by pre-calibrating the grayscale intensity of the images against known contrast concentrations [175]. One of the more common methods used to quantify blood flow rates from angiography has been the transit time technique. The temporal variation in contrast intensity is measured at two separate locations on an artery and a measure of the time difference between the two recorded curves is used to calculate flow rate (Figure 1-12a). Various measures of the time difference such as time-to-center of gravity of curve (mean transit time) [176], time-to-peak intensity, time-to-half peak intensity, time-to-peak gradient of intensity, and time-to-maximum peak of cross-correlation between the two curves have been employed [177]. Parametric images constructed by imposing flow-related data (such as time of contrast arrival) onto image pixels have been used to analyze global regions of interest [178]. Although attempts to calculate instantaneous velocity profiles in pulsatile flow have been made [179], these methods are generally suitable for calculations of mean flow rates only. Another avenue of characterizing contrast intensity- or concentration-time curves has been to fit the curves with a suitable mathematical equation. Exponential, polynomial, log-normal, and gamma-variate functions have been used for this purpose.
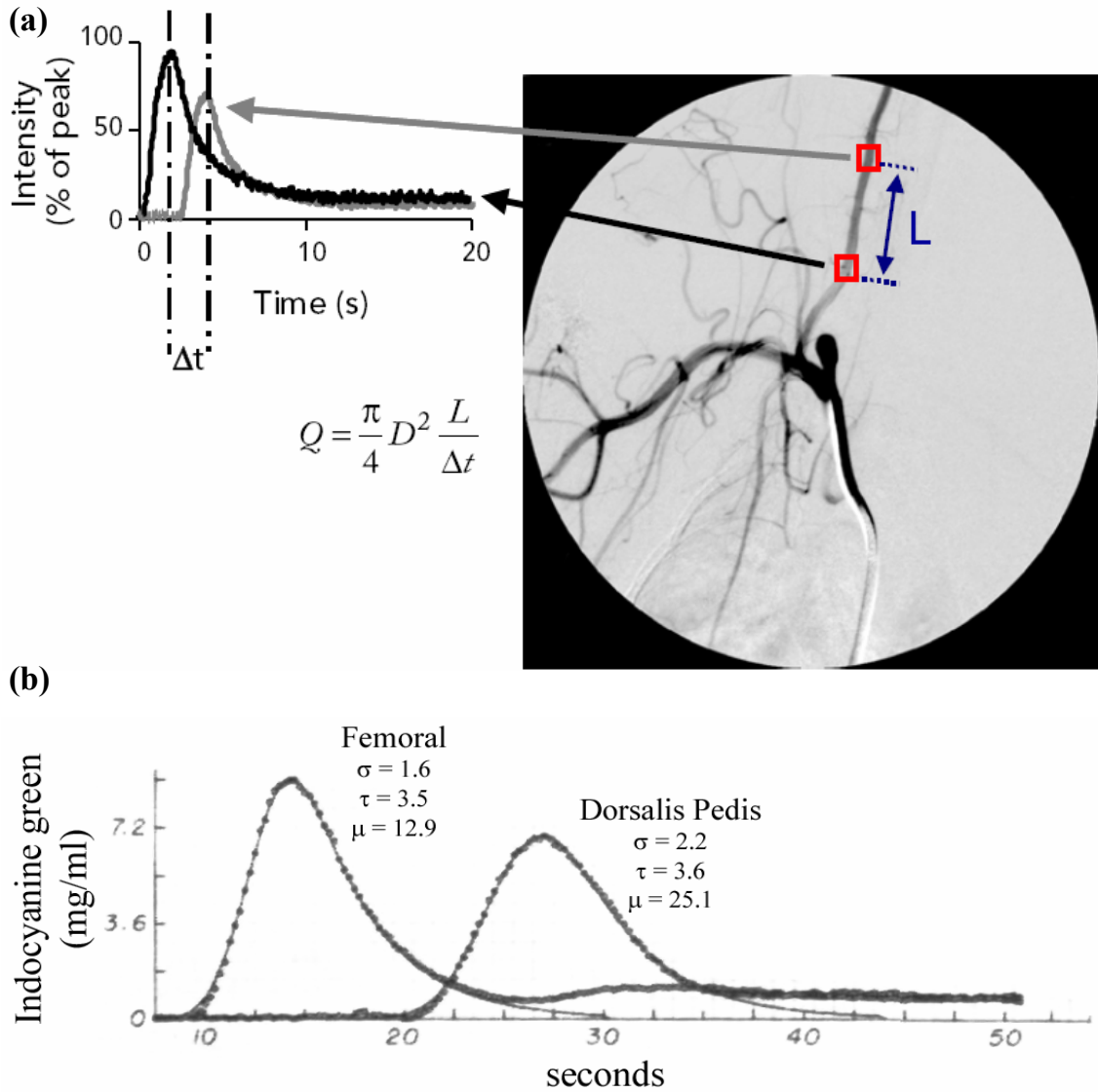
Figure 1-12. (a) Transit time estimation of flow rate based on time-to-peak intensity; D is artery diameter; from Lieber et al. [173]. (b) Lagged-normal model fit to concentration time curves of dye injected in the superior vena cava and sampled at two different locations; dotted lines are data and solid lines are curve-fits; the mean (μ) and standard deviation (σ) correspond to the Gaussian component and the time constant (τ) corresponds to the exponential decay component; modified from Bassingthwaighte et al. [180].

Based on the observation that the spatial dispersion of dye in flow through tubes was nearly Gaussian and that mixing in cardiac chambers and skewness of measured concentration-time curves seemed to follow an exponential trend, the lagged-normal function was suggested as a suitable curve-fitting equation [180]. This function, which is

a convolution of a Gaussian function and an exponential decay, could be used to represent the sequential or simultaneous effect of dispersion and mixing processes. Moreover, measures such as mean transit time, variance, area (the shape of the curve) are entirely governed by the model parameters and the curve-fit could thus be more readily translated to common physical terminology. Use of this equation to quantify concentration-time curves recorded over a wide range of conditions (different injection and sampling points, different flow rates) in five healthy men showed excellent fits over the range of curves (Figure 1-12b) [180].

As cerebral aneurysms are regions with distinct flow patterns and can be conveniently demarcated from the vasculature, the techniques mentioned above have been used to quantify intraaneurysmal hemodynamics based on angiographic acquisitions. Gamma-variate, single- and double- exponential, polynomial, and lagged-normal models have been fit to temporal variations in angiographic contrast intensity within aneurysmal regions of interest [116, 181-183]. Optimized model parameters obtained from curve-fitting were then employed to quantify treatments with stents or coils based on the changes in the contrast-intensity curves pre- and post-treatment.

1.4. Aims of the study

The primary intent of a flow divertor (as opposed to a stent) is to optimally alter the flow exchange between the parent artery and the aneurysm so as to promote complete thrombosis of the sac as rapidly as possible while eliciting minimal neointimal hyperplasia. There are no commercially available flow divertors as yet although two such devices have been recently introduced into the literature [184-186]. Based on our

laboratory's experience with flow diversion for treating cerebral aneurysms [104, 119, 120, 125, 157] and the information presented in the previous paragraphs, we have constructed a flow divertor of original design. Six potentially-optimal device configurations with varying porosities and pore densities were constructed with the intent of homing in on the optimal configuration through experimentation. Detailed particle image velocimetry [122] and preliminary in vivo [187] studies were subsequently performed on the rabbit elastase-induced aneurysm model. These studies, in combination, indicated three device configurations as having the best performance of the six.

We proceeded to implant these three devices in a large cohort of experimental aneurysms, the results of which are presented here. The primary intent of this report is to compare the performance of these three devices in the in vivo rabbit aneurysm model based on angiographic data acquired during device implantation and explantation. Alterations in the flow exchange between the parent vessel and the aneurysm due to the devices will be measured by angiographic aneurysmal washout curves. These curves will, in turn, be quantified by fitting of a mathematical model, the parameters of which serve as indices of device performance. The aneurysm occlusion rate and a device flexibility measure will be calculated from angiographic images. Angiographic quantification will be supplemented by histomorphometric data obtained externally. Statistical comparisons of these quantities will be performed at the 95% significance level. The goal is to select a single device that provides consistent and stable aneurysm occlusion in vivo in order to initiate clinical trials with the device.

Chapter 2. METHODS

The methods used in the study can be compartmentalized into procedures on animals or tissue and image processing as shown in the overall flowchart of Figure 2-1. Elastase-induced aneurysms were created in 40 rabbits and, three weeks later, 30 of these were treated with 3 flow divertors (10 animals per device), while 10 aneurysms were

Animal Experiments   Image Processing

```
Animal Experiments                              Image Processing

  ┌──────────────────────────┐              ┌──────────────────────────┐
  │ Aneurysm Creation (n=40) │         ┌──→ │ Digital Image Subtraction│
  └──────────────────────────┘         │    └──────────────────────────┘
              │ 21 days                 │       % Aneurysm │ occlusion,
              ↓                  Angio- │         Device   │ stiffness
  ┌──────────────────────────┐  graphy │    ┌──────────────────────────┐
  │Flow divertor deployment  │         │    │ Washout curve generation │
  │        (n=30)            │         │    └──────────────────────────┘
  └──────────────────────────┘         │           Notch │ filter
         │ 21, 90, or 180 days          │    ┌──────────────────────────┐
         ↓                              │    │  Mathematical modeling   │
  ┌──────────────────────────┐         │    └──────────────────────────┘
  │       Follow-up          │─────────┘          Model │ parameters
  │  Tissue explant (n=40)   │              ┌──────────────────────────┐
  └──────────────────────────┘              │    Device evaluation     │
              │                    Histo-   └──────────────────────────┘
              ↓                    morphometry      ↑
  ┌──────────────────┐──────────────────────────────┘
  │    Histology     │
  └──────────────────┘
```
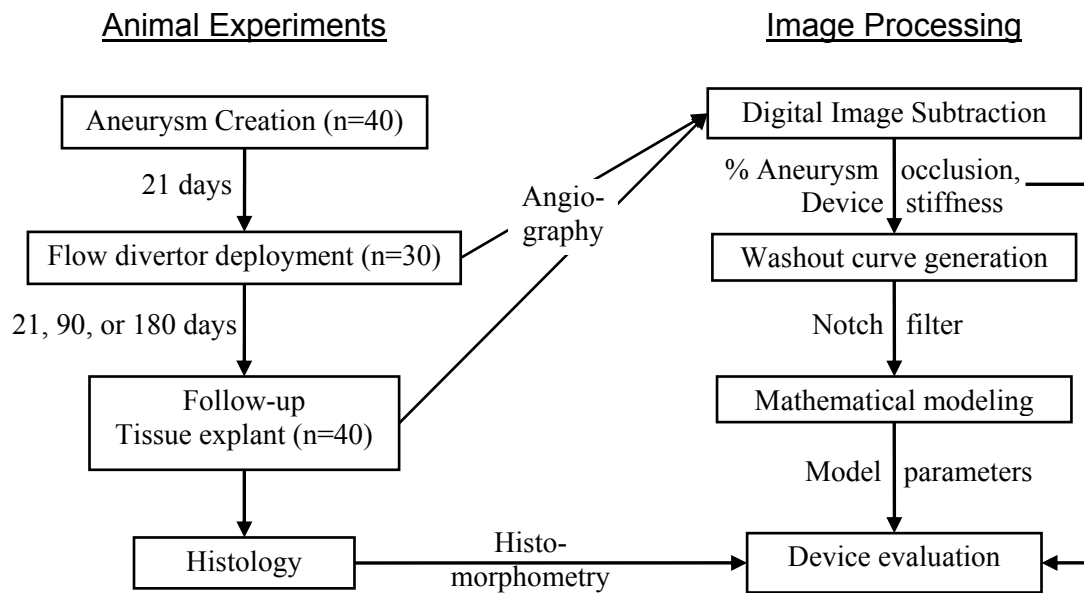
Figure 2-1. Overview of methods

used as controls. The animals were then sacrificed at the scheduled follow-up times of 3 weeks, 3 months, or 6 months post-treatment and the aneurysm-parent vessel complexes were explanted for histological processing. The image processing component of the study primarily involved analysis of three high-speed angiographic sequences acquired during experiments on each animal. Two of these sequences were acquired during the implant phase and one was acquired at follow-up before sacrifice. These angiographic sequences were logarithmically subtracted and the aneurysmal washout curves recorded. These washout curves were subsequently fit to a mathematical model after filtering. Changes in

optimized model parameters due to device implantation were then used as indices of device efficacy in conjunction with the angiographic percentage occlusion of aneurysms, a device stiffness measure, and the histomorphometric data from the histological sections. Each of the flowchart blocks are described in further detail below.

2.1. Aneurysm Creation

The procedure for creating elastase-induced aneurysms in rabbits followed the already well-established technique [77, 81, 82]. Rabbits were pre-anesthetized with an intramuscular injection of Glycopyrrolate (0.1 mg/kg) and sedated with intramuscular injections of Xylazine (5 mg/kg) and Ketamine (35 mg/kg). The neck area of the animal was shaved and the skin was prepped with iodine solution. The animal was then placed supine on the angiography table over a water-heated pad and sedation was maintained with 1-2% Isoflurane throughout the procedure.

The right common carotid artery (RCCA) of the animal was exposed. A 5 French (F) introducer sheath was inserted retrogradely through the RCCA after ligating the artery distal to the insertion point. A diagnostic angiogram was then acquired (Figure 2-2a). Under angiographic roadmap, a balloon (Endeavor, Target, Boston Scientific, Natick, MA) and a microcatheter (Prowler 10, Cordis, Miami Lakes, FL) were inserted in parallel through the sheath. The balloon was inflated at the origin of the RCCA and the tip of the microcatheter was positioned above the inflated balloon surface. The RCCA dead space between the sheath and the balloon was then filled with a solution of porcine pancreatic elastase (about 0.7 ml, 4.5 mg prot./ml) mixed with angiographic contrast (about 0.3 ml of Visipaque^{TM}, 320 mgI/ml, GE Healthcare, UK) (Figure 2-2b). The arterial segment was incubated with the elastase/contrast mixture for five to ten minutes depending on the

viability of the balloon seal as checked intermittently by fluorography. After the incubation period, the elastase mixture was drained and the microcatheter and balloon were partially extracted. Digital subtraction angiography was then performed to evaluate the dilation and washout at the base of the RCCA (Figure 2-2c). If required, second or third incubations were performed to achieve adequate results. After the procedure, the devices were extracted, the artery was ligated below the insertion point and the incision sutured. The animal was transferred to a recovery cage and its temperature and respiratory rate were monitored every fifteen minutes until recovery of the animal's alertness. The animal was given Buprenorphine (0.04 mg/kg) for pain relief and Ketoprofen (2mg/kg) as anti-inflammatory and anti-pyretic immediately after surgery and twice a day for three days post-surgery. As mentioned, aneurysms were created in this same manner in 40 rabbits.
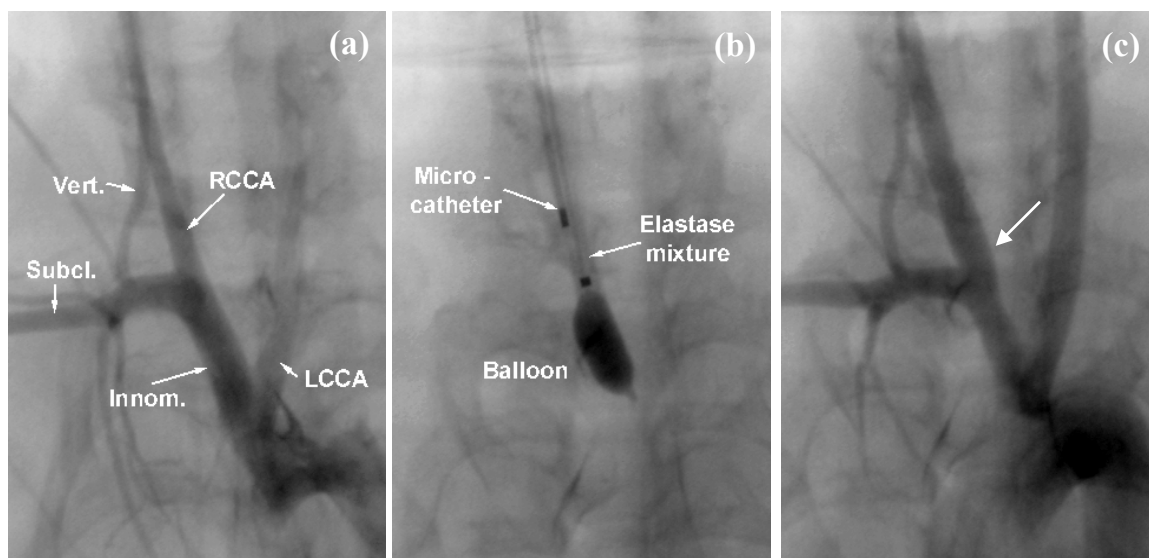

Figure 2-2. Elastase-induced aneurysm induction in the rabbit. a) Vascular structures before aneurysm creation; b) balloon occlusion of the origin of the RCCA with elastase incubated in the arterial dead space; c) post-incubation angiogram showing dilation at the root of the RCCA. RCCA: right common carotid artery; LCCA: left common carotid artery; Innom.: innominate artery; Subcl.: subclavian artery; Vert.: vertebral artery.

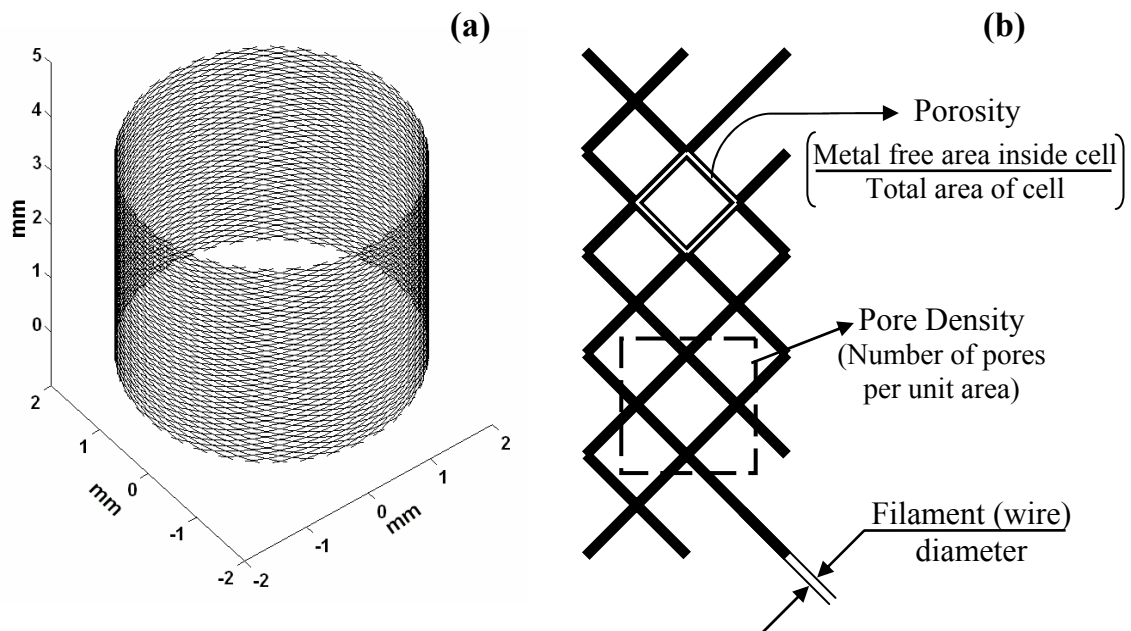## 2.2. Flow Divertor Deployment

Figure 2-3. (a) Geometrical sketch of the open configuration (4 mm diameter) of one of the flow divertors (device E) for one helical turn. (b) Sketch showing the important parameters that characterize a device.

The three devices deployed in the rabbits are labeled B, C, and E as this study is part of a larger study involving in vitro [122] and preliminary in vivo (1 animal per device) [187] evaluation of six devices that were labeled A through F. These 3 devices (B, C, and E) were judged to be the best performers based on these other study modules and were therefore selected for further evaluation in this large cohort of 30 animals (10 animals per device). Figure 2-3A geometrically shows the open configuration of device E, while Figure 2-3B explains three important geometrical parameters that characterize a flow divertor. The porosity of a device can be calculated as

$$porosity(\%) = \frac{Total\ Surface\ Area - Metal\ Surface\ Area}{Total\ Surface\ Area} \times 100 \qquad \text{(Eq. 2-1)}$$

Table 2-1. Design parameters of the 3 flow divertors used in the study.

Divertor	B	C	E
Open device diameter	4 mm	4 mm	4 mm
Filament (wire) diameter	51 μm	51 μm	38 μm
Porosity	70%	65%	70%
Pore Density (pores/mm^2)	11.7	13.9	18.3

The values of wire diameter, porosity and pore density for the 3 flow divertors are given in Table 2-1. Devices B and E have the same nominal porosity, while devices B and C have the same wire diameter. Device E has the highest pore density of the three devices. All three devices have the same open diameter and the same surface braiding pattern (2×2). The animal numbers used throughout this text contain these device labels to show the device that was implanted in that particular animal, e.g., animal #E_021_3 referenced in Figure 2-4 below was treated with device E. Control animals are marked by the letter "O" (see Table 2-2). The choice of the device to be implanted in any given animal was solely dependent on the study schedule and was otherwise arbitrary.

After allowing sufficient time for the aneurysm to mature (nominally 3 weeks after the aneurysm creation procedure), the animals were brought back to the angio-suite for flow divertor implantation. Diagnostic high-speed angiography was performed in the control animals instead of device implantation during this phase. Animal preparation and maintenance were the same as for the aneurysm creation procedures, except that the right leg area was prepped instead of the neck area. In addition, treated animals were given 20 mg of aspirin once a day beginning 2 days before the procedure and continuing till 10 days after the procedure to mitigate acute in-stent thrombotic events.

A 4F introducer sheath was inserted through the right femoral artery and a 4F catheter (Cordis Endovascular, Miami, FL) was threaded through the sheath and positioned such that its tip was in the ascending aorta. Low speed diagnostic angiograms

were performed and the C-arm orientation was adjusted such that the true (maximal)

length of the aneurysm neck could be visualized. A high-speed angiographic run was then

acquired at 30 frames/s over 20 seconds (total of 601 frames acquired) by injecting 5 cc

of angiographic contrast (Visipaque^{TM}, 320 mgI/ml, GE Healthcare, UK) at a rate of 2

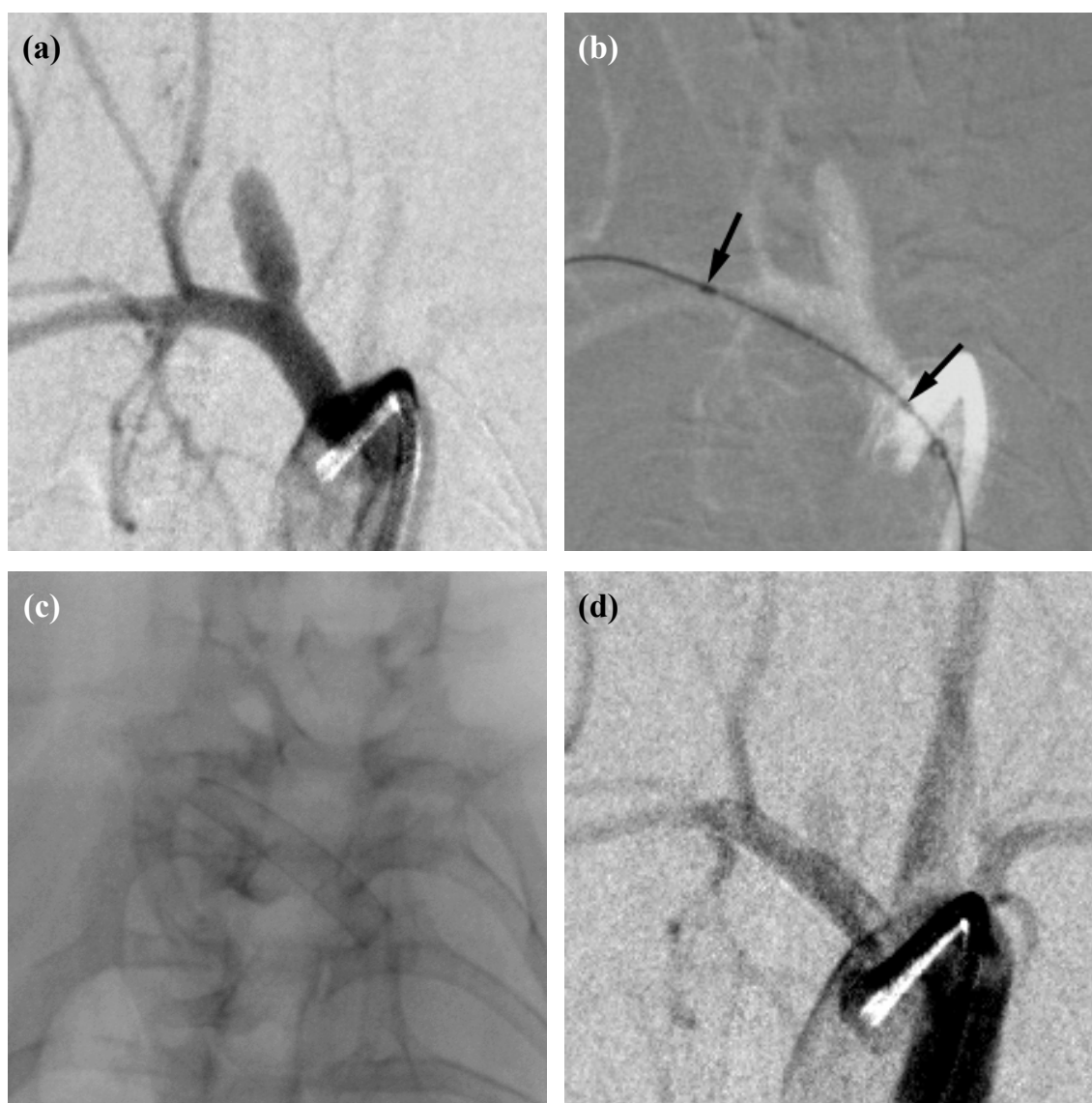cc/s (Figure 2-4a). The start of contrast injection was delayed by 2 seconds after start of

Figure 2-4. Stages in a flow divertor deployment procedure (images from #E_021_3). a) Pre-deployment angiogram; b) delivery system position with device in sheath (arrows show markers at sheath ends); c) device deployed; d) angiogram obtained immediately post-deployment.

image acquisition to obtain mask images for digital subtraction. The tip of the 4F catheter was then placed in the distal subclavian artery past the aneurysm and a 0.014" exchange guidewire was introduced through it and inserted into one of the branches of the distal subclavian artery. The 4F catheter was then removed and the flow divertor delivery system was inserted over the exchange wire and positioned such that after deployment, the device would cover the vertebral artery and span approximately equal lengths on either side of the aneurysm (Figure 2-4b). The device was then deployed and the flow divertor delivery system extracted from the animal (Figure 2-4c). The 4F catheter was inserted again into the ascending aorta and its tip was placed in the same location as before. A post-device deployment high speed angiogram (Figure 2-4d) was then acquired under identical imaging (image to source distance, C-arm orientation, acquisition mode) and injection (injection volume, injection rate, preset delay) parameters as used for the pre-deployment angiogram. The catheter was then extracted, the femoral artery ligated, and the incision sutured. Animals were monitored and cared for as after the aneurysm creation procedures.

2.3. Follow-up/Tissue Explant

Animals were followed-up at 21 days (n = 12), 90 days (n = 12), or 180 days (n = 16) after the device implantation phase of the study. The animal numbers used throughout this text also incorporate the time at which the animal was followed-up. For example, the animal number #E_021_3 mentioned previously was treated with device E and followed-up 21 days post-treatment. The number "3" at the end refers to the fact that it was one of 3 animals treated with device E and followed-up at 21 days. Table 2-2 shows the follow-up schedule used in this study and the animal numbering scheme used in this text.

Table 2-2. Distribution of follow-up times for the 40 animals and the animal numbering scheme used in this text. The order of animals within any sub-group is arbitrary.

Follow-up time Device	21 days	90 days	180 days
B	#B_021_1 #B_021_2 #B_021_3	#B_090_1 #B_090_2 #B_090_3	#B_180_1 #B_180_2 #B_180_3 #B_180_4
C	#C_021_1 #C_021_2 #C_021_3	#C_090_1 #C_090_2 #C_090_3	#C_180_1 #C_180_2 #C_180_3 #C_180_4
E	#E_021_1 #E_021_2 #E_021_3	#E_090_1 #E_090_2 #E_090_3	#E_180_1 #E_180_2 #E_180_3 #E_180_4
Control	#O_021_1 #O_021_2 #O_021_3	#O_090_1 #O_090_2 #O_090_3	#O_180_1 #O_180_2 #O_180_3 #O_180_4

Animal preparation and care for the follow-up procedures were the same as during the device implantation procedures, except for prepping the left leg area instead of the right leg area. Follow-up angiograms were then taken by accessing the left femoral artery, positioning the 4F catheter at the same location as during implantation and acquiring high-speed sequences under identical imaging and injection parameters. The catheter tip was then positioned in the entrance of the innominate artery. The animal was euthanized with an overdose of sodium pentobarbital (1 ml intravenous injection of Euthasol®, Delmarva Laboratories, Midlothian, VA). Saline was then flushed through the catheter for approximately five minutes to clear the region of any blood. Ten percent formalin was then flushed through the catheter until appropriate fixation was achieved (approximately ten minutes). The neck and chest regions of the animal were then dissected and the aneurysm-parent vessel complex including the aorta, vertebral artery,
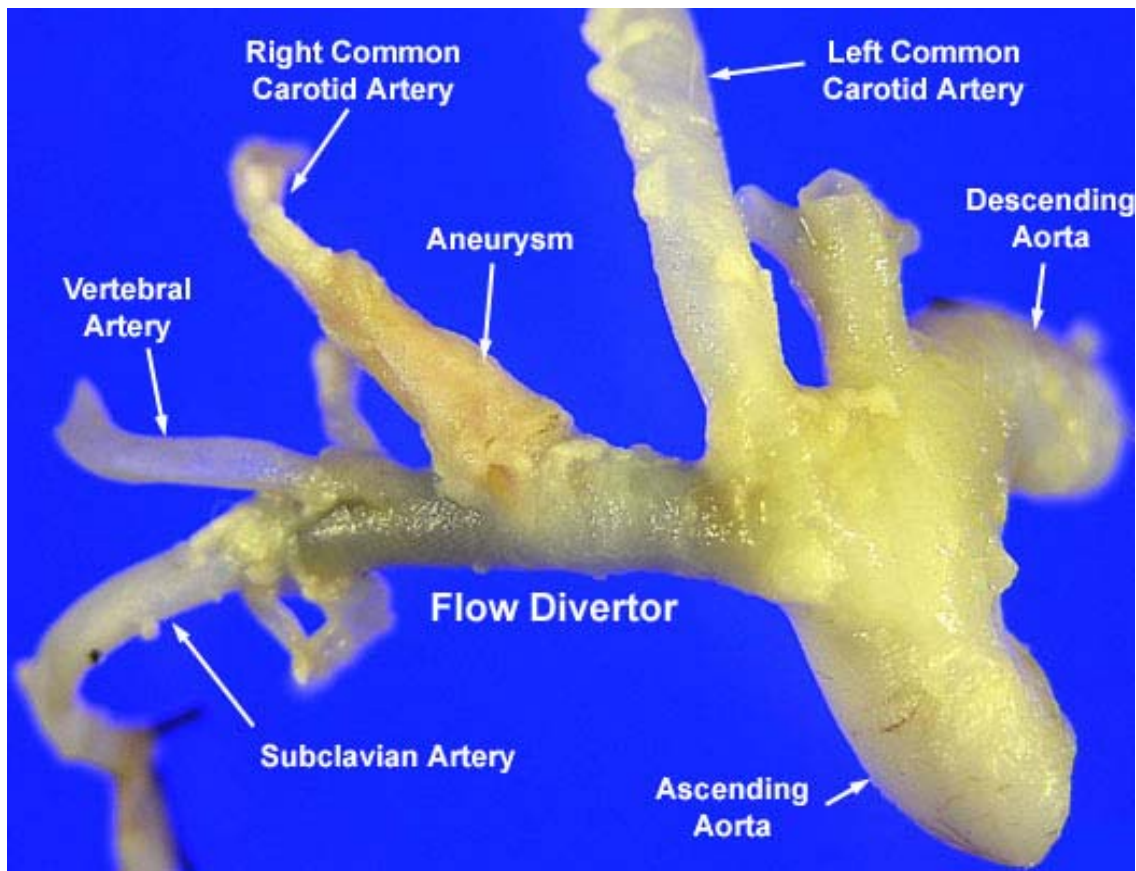
Figure 2-5. Harvested tissue sample (#E_180_1) showing the implanted flow divertor in the innominate to subclavian artery and other associated vasculature.

superficial cervical and costocervical trunk, and distal subclavian artery was explanted (Figure 2-5). The explanted tissue was then pressure-fixed with 10% formalin under approximately 50 mmHg for about 20 minutes by cannulating the ascending or descending aorta and ligating all other exit ports. The tissue was then stored in a container of 10% formalin until histological processing.

2.4. Histology

Harvested tissue was sent to Dr. Fermin Tio at the Department of Veterans Affairs, South Texas Veterans Health Care System (San Antonio, TX) for histological processing. The histological sections and histomorphometric measurements presented here were made by his laboratory. Briefly, the samples were processed through a graded
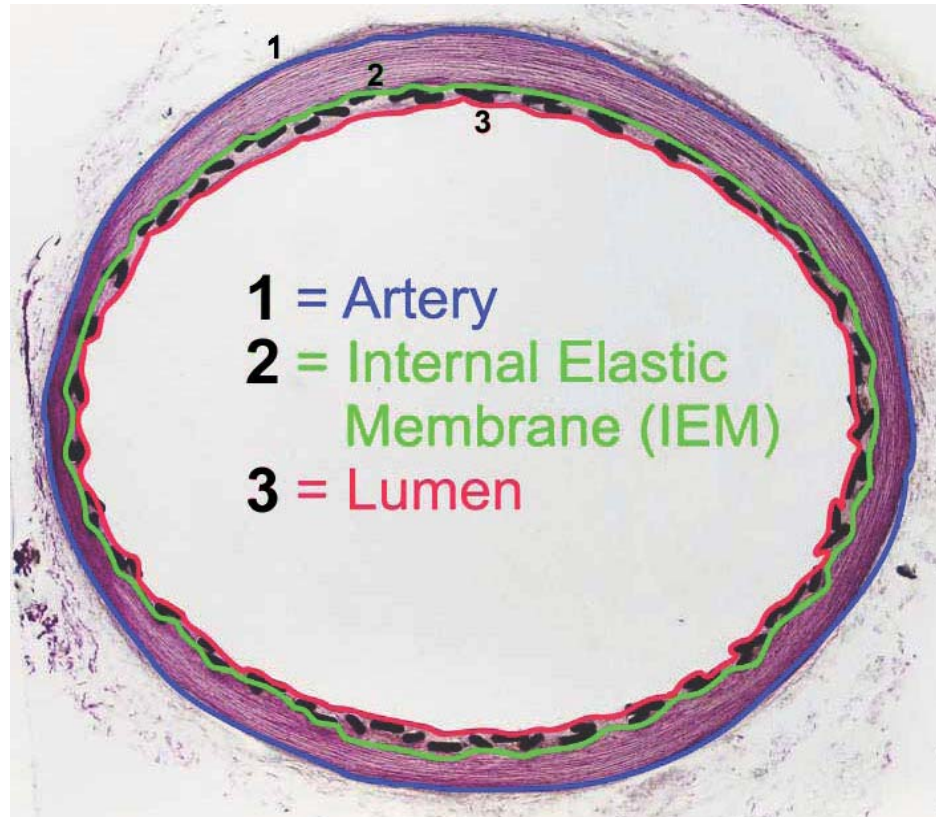
Figure 2-6. A histological section used to illustrate area measurements that were then used to calculate radii (e.g., artery radius = $\sqrt{(\text{Artery area}/\pi)}$) or neointimal thickness ($\sqrt{(\text{IEM area}/\pi)} - \sqrt{(\text{lumen area}/\pi)}$).

series of ethanol, xylene, and were embedded in methyl methacrylate. Sections were taken at approximately 600 μm intervals, polished down to 6 μm, and stained with a metachromatic (toluidine blue-basic fuchsin) stain. Values of diameters or neointimal thicknesses at any section were based on measurements of three representative areas: the artery area, internal elastic membrane area (device area) and lumen area as shown in Figure 2-6. Radii were then calculated as $\sqrt{\dfrac{area}{\pi}}$ and the neointimal thickness was calculated as device radius minus the lumen radius.

Sections of the aneurysms were graded by semi-quantitative scores of the degree of aneurysm occlusion and the degree of organization of the aneurysm sac contents as shown in Table 2-3. Performance of the three devices in terms of the histology was quantified based on the measures of neointimal thickness, extent of aneurysm sac occlusion and extent of sac organization.

Table 2-3. Semi-quantitative scoring system for the degree of aneurysm occlusion and the degree of organization of the aneurysm thrombus based on histological sections.

Degree of aneurysm occlusion
0 = Aneurysm lumen essentially empty
1 = Aneurysm lumen slightly filled
2 = Aneurysm lumen at least half filled
3 = Aneurysm lumen essentially filled

Degree of organization of aneurysm contents
1 = Clot with little organization
2 = Clot with more organization
3 = Organized with recanalization

2.5. Digital Image Subtraction

Every high-speed angiographic sequence mentioned herein and analyzed contains 601 images (30 frames/second × 20 seconds). Each image is 512×512 pixels with a grayscale depth of 8 bits and a spatial resolution of approximately 160 microns/pixel. There are 3 high-speed angiographic sequences per treated animal. The first is acquired before device implantation (called the "PRE" sequence throughout the text), the second is acquired immediately after device implantation (called the "POST" sequence), and the third is acquired at follow-up (called "FU"). There are thus 90 angiographic sequences corresponding to the 30 treated animals. The angiographic sequences were downloaded as Digital Imaging and Communications in Medicine (DICOM) files onto a compact disc

and imported into a Windows PC (Pentium 4, 2 GB RAM) for processing. All image processing described herein was done using Matlab[®] (The Mathworks, Natick, MA).

Digital subtraction angiography essentially involves the logarithmic subtraction of two images because X-ray attenuation is exponential [173]. The first image (called mask image) is acquired before the injection of angiographic contrast and the second image (contrast image) is taken after the vasculature of interest has been opacified by the injection of angiographic contrast. Subtracting the natural logarithm of the mask image from the natural logarithm of the contrast image then theoretically removes all background information (attenuation due to bone and other soft tissue) leaving only the contrast-opacified vasculature. As the innominate artery (parent artery to the elastase-induced aneurysm) is within the thoracic cavity, the aneurysm-parent vessel complex undergoes a displacement that is synchronous with the respiration of the animal (Figure
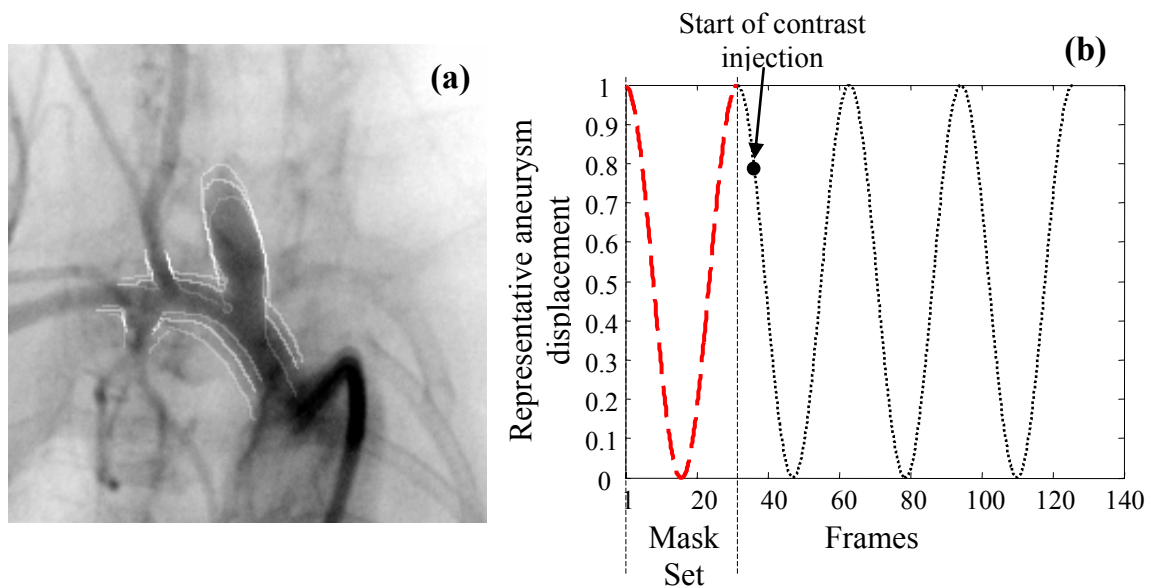
Figure 2-7. Aneurysm displacement synchronous with respiratory cycle of the animal; a) overlay of three frames showing aneurysm displacement in one case (#E_021_3); b) aneurysm displacement represented by a sinusoidal curve to show selection of mask set of frames (dashed line); every subsequent cycle (dotted line) is then subtracted from this mask set.

2-7a). To subtract the angiographic sequences obtained in these animals, therefore, each mask image must be subtracted from a contrast image that was acquired at the same point in the respiratory cycle of the rabbit. To facilitate this subtraction process, a delay of 2 seconds was introduced during the injection of angiographic contrast to allow for at least one respiratory cycle to pass by without any opacification of the vasculature. A set of images comprising one respiratory cycle of the animal could then be chosen from the angiographic sequence before start of contrast injection to form the set of mask images (Figure 2-7b). Subsequently acquired contrast images could then be grouped into respiratory cycles and the mask set of images subtracted from each set of contrast images.

In order to select the mask set of images and digitally subtract the subsequent image sequence as mentioned above, the respiratory rate must be known beforehand. Although the respiratory rate can be estimated by manually counting the number of breaths the animal takes over the 20 second image acquisition period, automatic calculation of the respiratory rate would significantly reduce the effort required. This was accomplished by adapting an algorithm published previously for determining heart rates from electrocardiogram or photoplethysmogram traces [188]. The average of 15 images from the beginning of acquisition was first calculated and used as a "static" background image. In each subsequent image, the grayscale value of pixels with values less than the corresponding pixels in the background image were summed up to record the "movement" throughout the angiographic sequence (Figure 2-8a). In most cases, the bent edge of the 4F catheter resting against the aortic arch and the dime move synchronously with the respiration of the animal and therefore move into and out of correspondence with the static background image. These two objects largely contribute to the trace after

contrast injection as shown in Figure 2-8a, where fluctuations corresponding to the respiratory rate of the animal are evident. A section of this trace from the last 10 to 12 seconds of acquisition was then selected and filtered with a 15 point median filter (Figure 2-8b). The filtered trace was then thresholded at 6 times the standard deviation to give
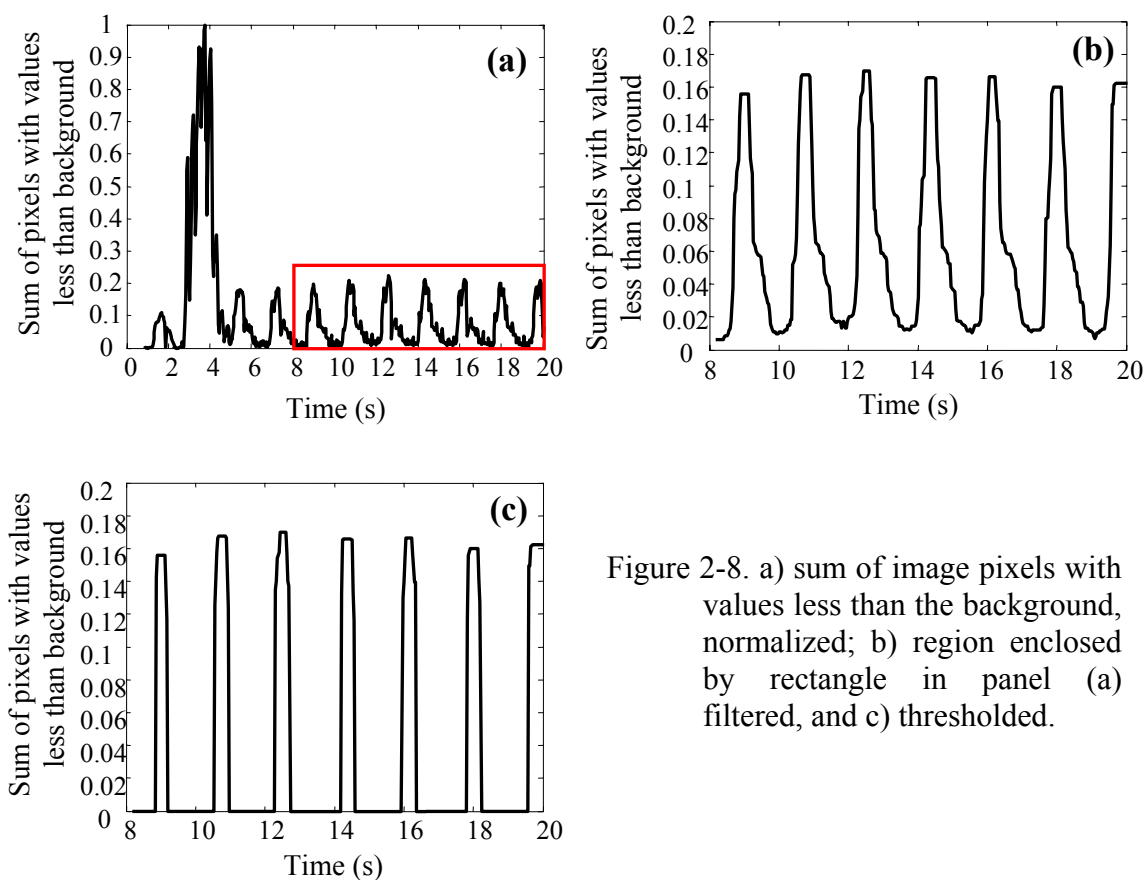

Figure 2-8. a) sum of image pixels with values less than the background, normalized; b) region enclosed by rectangle in panel (a) filtered, and c) thresholded.

spikes at approximately the maximal expiration points (Figure 2-8c). The average distance between the centers of these spikes gave the time period of respiration, from which the respiratory rate (frames per second) could be determined. By calculating the time period of the respiratory cycle for each angiographic sequence in this manner, the sequences could be automatically subtracted as described above.

As artifacts in the subtracted images occur at locations of edges in the mask and contrast images [189], the error in the subtraction process described above was quantified

based on edge detection of the rib cage of the animal (Figure 2-9a). A rectangular

window that included the rib cage (around aorta) and which was 125 pixels in length and

512 pixels in width was chosen in each angiographic sequence. A maximum intensity

projection of the vasculature opacified by contrast and the dime was thresholded and

excluded from the images to ensure that edges due to the vessels or the dime are not

accounted for (Figure 2-9b). Edges in the rest of the image were detected by the

Laplacian of Gaussian method (function "edge" in Matlab). The subtraction error was
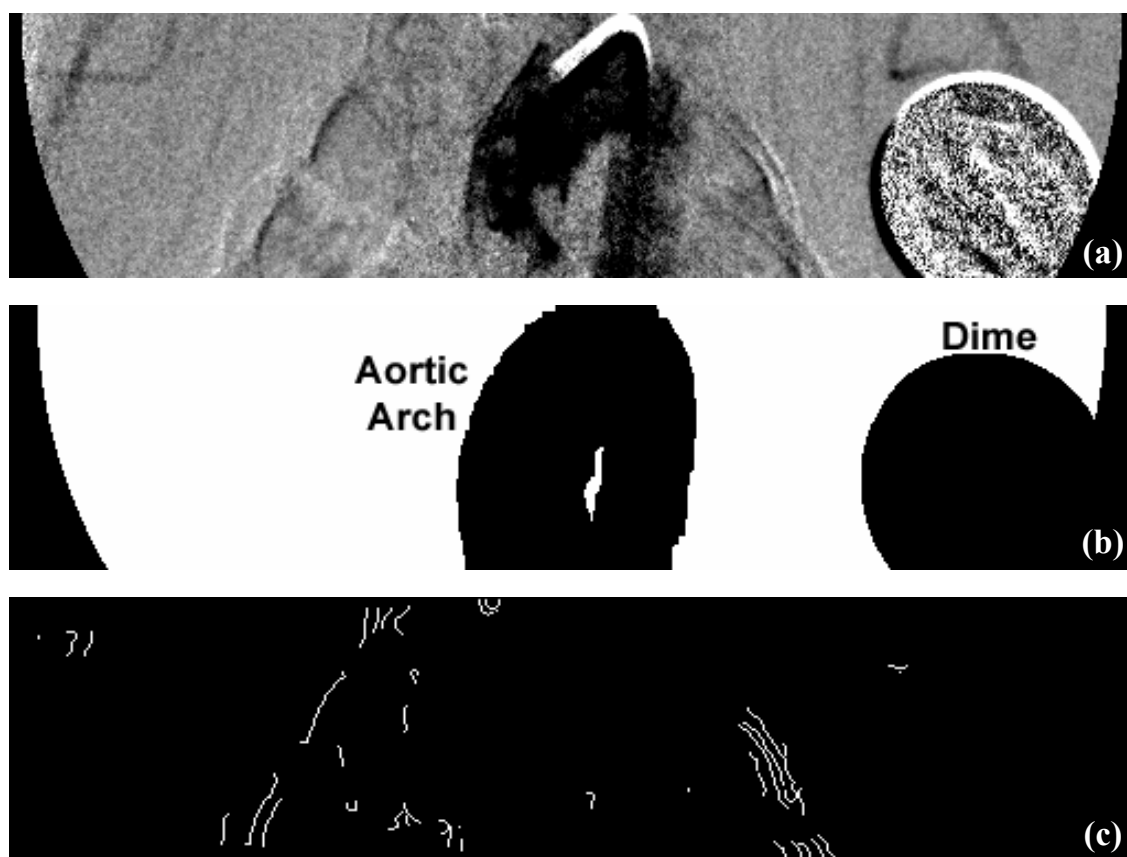
Figure 2-9. Quantification of error in the subtraction process. (a) Window of 125×512 pixels showing the edges due to the rib cage (double arrows) in the region of the aortic arch; (b) mask (white pixels) created from maximum intensity projection of contrast opacified images that excludes the aortic arch and the dime; (c) after edge detection of the region in (a) that coincides with the mask region in (b). Subtraction error was quantified as the percentage ratio of the number of white pixels in (c) to the number of white pixels in (b). Images from #B_180_3.
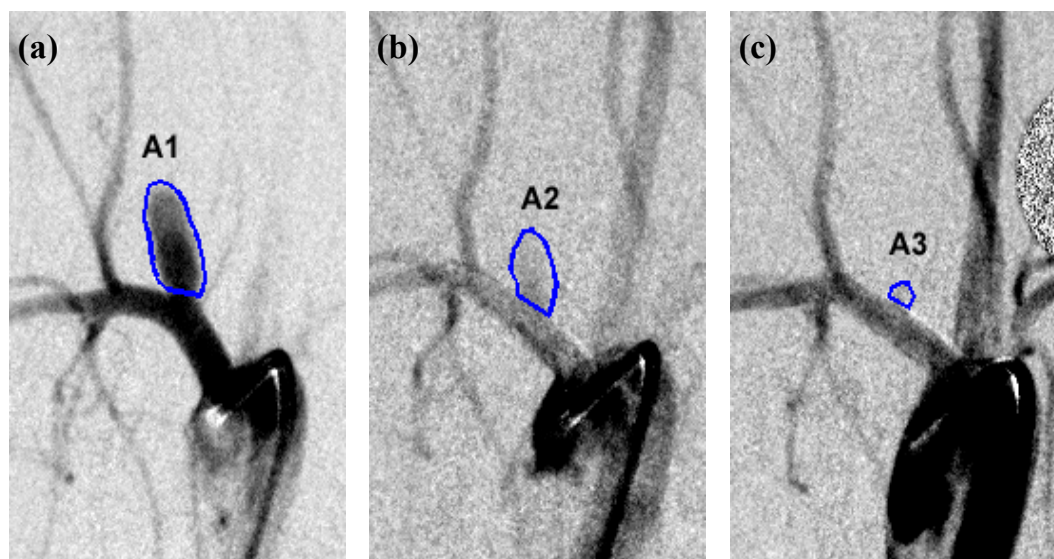
Figure 2-10. Calculation of percentage angiographic aneurysm occlusion based on measurements of the area (in pixels) of the aneurysm on frames with maximal aneurysm opacification. A1, A2, and A3 are the aneurysm areas (a) before device implantation, (b) immediately after device implantation, and (c) at follow-up, respectively. Images from #E_021_3.

then quantified as the percentage of non-zero pixels in the edge-detected images to the total number of pixels in the detection window (Figure 2-9c).

After the angiographic sequences were subtracted, the percentage angiographic aneurysm occlusion could be calculated. As the injected angiographic contrast enters the aneurysm, there is one image at which the aneurysm can be visualized to be completely filled with contrast. This image, representing maximal aneurysm opacification, was selected from the angiographic sequences of each phase (PRE, POST, and FU) for each animal. In each of these 3 images (one image per phase), the aneurysm was manually delineated as a region of interest (ROI) as shown in Figure 2-10. The area of the aneurysm in that image projection was then represented by the number of pixels in the ROI. The angiographic percentage aneurysm occlusion immediately after device implantation and at follow-up could then respectively be calculated as

$$A_{POST}\% = \frac{A1-A2}{A1} \times 100$$

$$A_{FU}\% = \frac{A1-A3}{A1} \times 100$$

(Eq. 2-2)

where, A1 was the area of the aneurysm before device implantation, A2 was the aneurysm area immediately after device implantation, and A3 was the area at follow-up (Figure 2-10). If the aneurysm could not be visualized at follow-up, area A3 was 0 and the percentage angiographic aneurysm occlusion at follow-up was 100%.
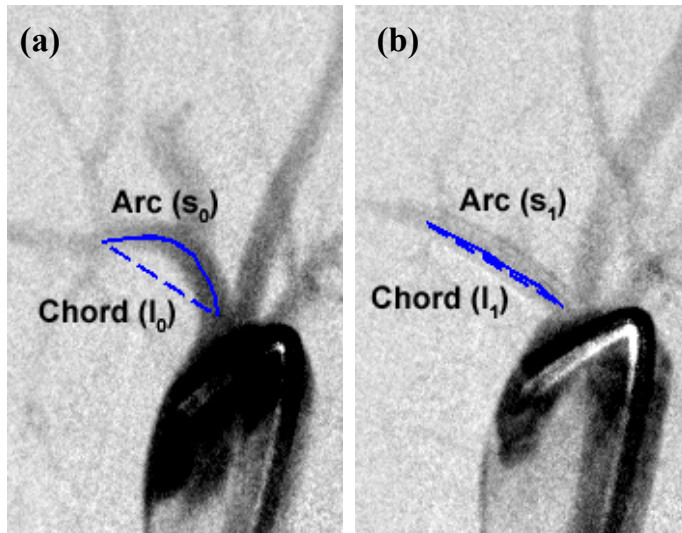
Figure 2-11. The distance metric (arc-to-chord length ratio) as a measure of the curvature of the vessel segment (a) before and (b) after treatment. Arc (solid line) length remains approximately constant, while chord (dashed line) length increases post-device deployment. Images from #E_180_1.

Implantation of the flow divertor in the parent artery reduces the curvature of the artery. This change in curvature was quantified with the distance metric [190], which is the ratio of the arc length of the treated vessel segment to the straight line distance between the segment end points (chord length). Images with maximal opacification of the parent vessel were chosen from PRE and POST angiographic sequences and the centerline of the innominate artery from its origin at the aortic arch to the origin of the vertebral artery was manually selected in both images (Figure 2-11). The change in curvature due to flow divertor implantation was then quantified as the percentage ratio of the distance metrics

$$\frac{s_1/l_1}{s_0/l_0} \times 100 \qquad \qquad \qquad \text{(Eq. 2-3)}$$

where, s_0 and l_0 are the arc and chord lengths before device implantation and s_1 and l_1 are the arc and chord lengths after device implantation, respectively (Figure 2-11). Higher values of this percentage ratio imply less change in the curvature of the artery due to the device and therefore indicate higher longitudinal flexibility of the device.

2.6. Washout Curve Generation

The flow exchange between the aneurysm and the parent vessel in any angiographic sequence is measured by recording the aneurysmal washout curve, which is essentially the temporal variation in the average grayscale intensity within the aneurysm. As noted previously, the aneurysm moves in phase with the respiration of the animal. The ROI must, therefore, also be displaced in accordance with the location of the aneurysm in any given frame so that the average grayscale intensity within the ROI can be calculated. Manually selecting the aneurysm in every frame would be practically infeasible because that would involve selection of approximately 6000 points in every angiographic sequence (approximately 10 points to define the aneurysm $\times$ 600 frames). The location of the aneurysm was therefore automatically tracked as mentioned here after manually defining it in one image per angiographic sequence.

First, the image with maximal aneurysm opacification was selected in each angiographic sequence and the aneurysm was manually delineated as a ROI (Figure 2-10) in this one image. A set of images comprising one respiratory period of the animal that included the frame with maximal aneurysm opacification was chosen. In each of these images, a segment of the parent vessel approximately 10 pixels wide and immediately distal to the aneurysm was selected by thresholding (Figure 2-12a). The average distance
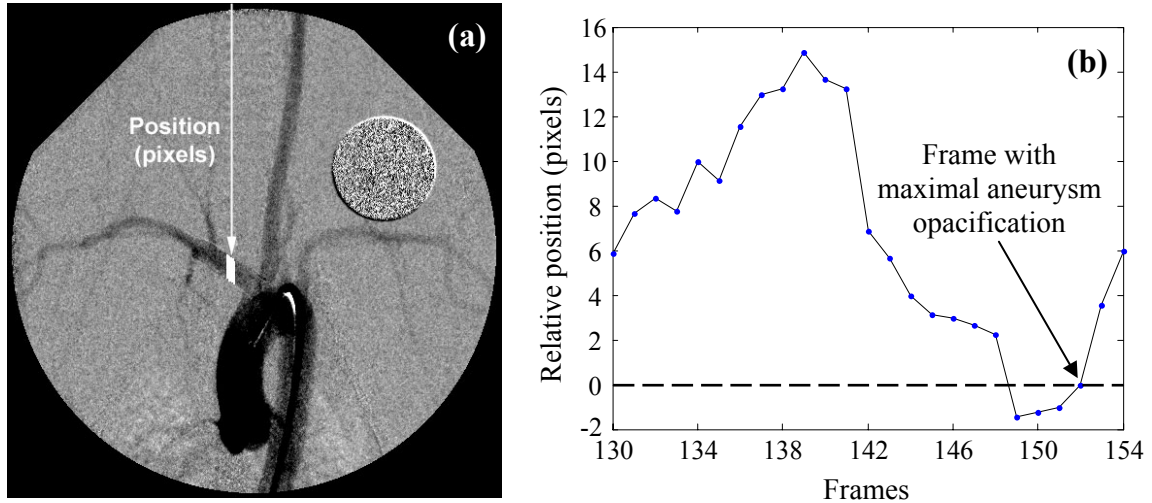
Figure 2-12. Generation of the aneurysm position vector. (a) Thresholded segment of vessel (white) immediately distal to the aneurysm and its position (length of arrow) in the given frame. (b) Position vector for this angiographic sequence. From #B_090_3 FU, respiratory period 25 frames.

(in pixels) of the superior aspect of this segment from the top of the image was then recorded (white arrow in Figure 2-12a). This set (corresponding to 1 respiratory period) of distances was then adjusted relative to the distance of the aneurysm in the frame with maximal aneurysm opacification to give the position vector for the particular angiographic sequence. Figure 2-12b shows an example of such a position vector for the FU angiographic sequence of animal #B_090_3. As the ROI is manually delineated in the frame with maximal aneurysm opacification and the position vector provides the location of the aneurysm with respect to this frame, the location of the aneurysm in the entire angiographic sequence (600 frames) can be tracked.

The average grayscale intensity within the ROI was then calculated for each frame in the angiographic sequence as

$$\text{Average Aneurysmal Intensity} = \frac{\left(\begin{array}{c}\text{sum of grayscale values of}\\ \text{all the pixels within the ROI}\end{array}\right)}{\left(\text{total number of pixels within the ROI}\right)} \qquad \text{(Eq. 2-4)}$$
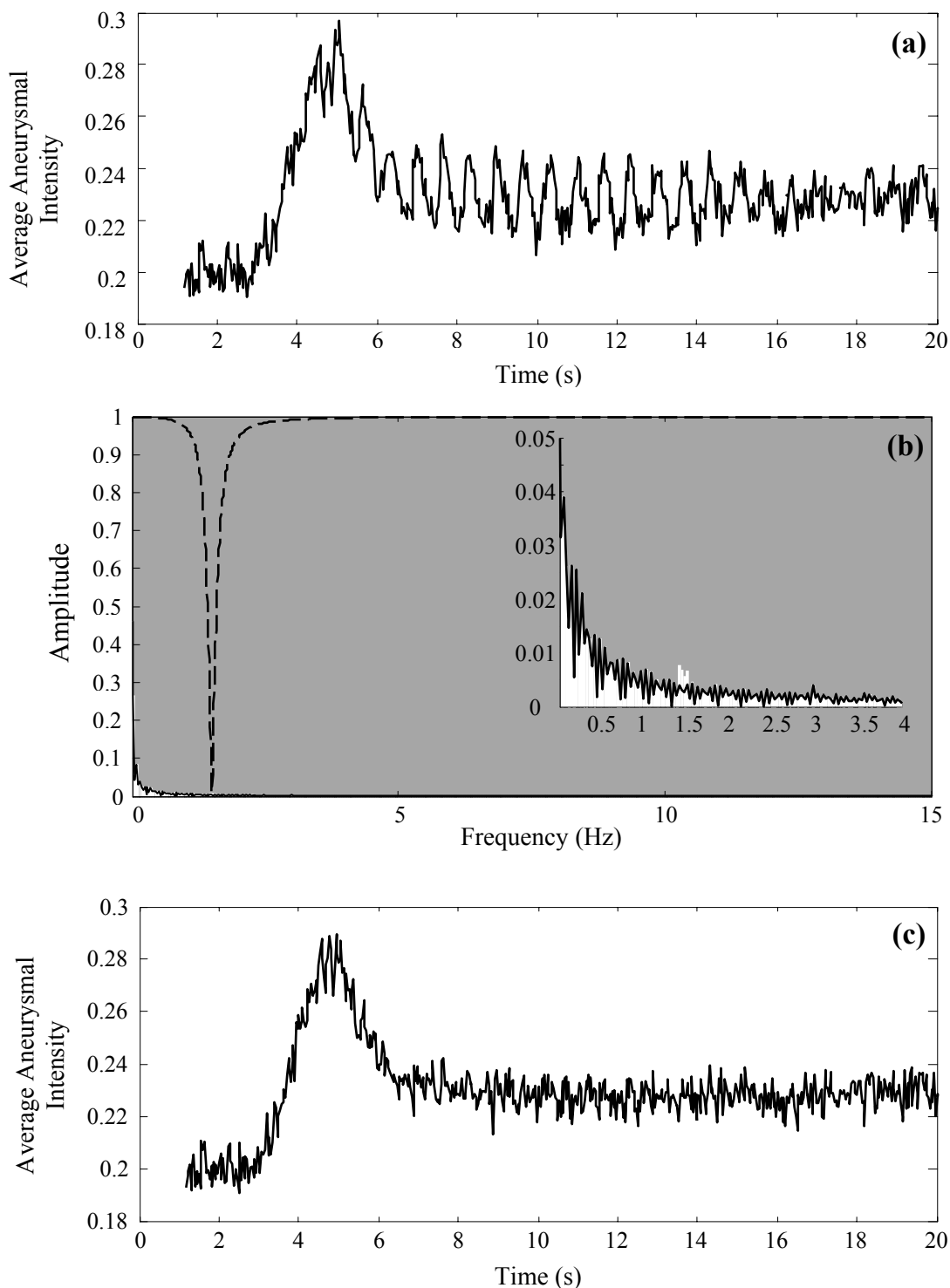
Figure 2-13. Notch filtering of aneurysm washout curves. (a) Original washout curve. (b) The frequency-amplitude plot of the original washout curve (white bars), the notch filter (dashed line) and the resulting filtered washout curve (solid line). Inset in panel (b) shows a zoomed-in view of the plot with the respiratory frequency (1.5 Hz) removed by the notch filter. (c) Filtered washout curve. Animal #E_090_1; respiratory period 20 frames (0.67 s).

The aneurysmal washout curve is the variation in the average aneurysmal intensity over the acquisition period. The aneurysmal washout curve for case #E_090_1 is given in Figure 2-13a as an example. The tracking of the ROI does not precisely match the location of the aneurysm throughout the angiographic sequence. This results in fluctuations in the aneurysmal washout curves at the respiratory frequency as can be noted in the example of Figure 2-13a. This frequency component was removed from the washout curve by a notch filter [191]. The filter had unity gain at the DC and Nyquist frequencies and a bandwidth of 0.2 or 0.3 Hz (Figure 2-13b). Washout curves were filtered if the amplitude at the respiratory frequency was within 20 dB of the fundamental frequency of the curve. In cases where the second harmonic of the respiratory frequency was also within 20 dB of the fundamental frequency, this component was also removed with a notch filter. The 20 dB value used here is only empirical and is based on the observation that there are no (or minor) respiratory rate fluctuations in washout curves with respiratory amplitudes lower than this value. A washout curve after filtering of the respiratory frequency is shown in Figure 2-13c.

2.7. Mathematical Modeling

The flow exchange between the parent artery and the aneurysm is quantified by fitting a mathematical model to the aneurysmal washout curves. The point of significant rise (estimated from the trace of sum of image pixels less than background, e.g. Figure 2-8a) in the filtered washout curves is selected as the average of 3 data points (0.1 seconds) and set to zero. Taking the average of 3 data points reduced the effect of noise fluctuations in selecting the origin. This selected point corresponds (within 5 or 6 frames, 0.2 seconds) to the time point when angiographic contrast is first visualized in the

vasculature. The washout curve is then normalized based on its maximum value and the resulting normalized curve is fit to the following mathematical model in the least squares sense [116].

$$f(t) = \rho_{conv} \int_0^t \frac{1}{\sigma\sqrt{2\pi}} e^{-\frac{(\eta-\mu)^2}{2\sigma^2}} \times \frac{1}{\tau_{conv}} e^{-\frac{t-\eta}{\tau_{conv}}} d\eta$$

$$+ \rho_{diff} \left[\int_0^t \frac{1}{\sigma\sqrt{2\pi}} e^{-\frac{(\eta-\mu)^2}{2\sigma^2}} d\eta - (1 - e^{-\frac{t}{\tau_{diff}}}) \right]$$

(Eq. 2-5)

The model has two components and six parameters. The first component, nominally the convective component, is a lagged normal distribution (convolution of a normal distribution and an exponential decay). The second component, nominally the diffusive component, is the sum of a cumulative distribution function and an exponential decay. The physical basis for this model and example plots of the 2 components are shown in Figure 2-14. The two model components attempt to model the flow exchange between two different regions that may exist in any given aneurysm. The convective component models flow into and out of a region near the aneurysm neck where the flow exchange is faster (Figure 2-14a). The diffusive component models the flow into (cumulative distribution function) and out of (exponential decay function) a region closer to the aneurysm dome that experiences relatively sluggish flow (Figure 2-14b). It is to be noted that these two regions are only conceptually distinguished and may not necessarily be physically distinct. Implantation of a flow divertor essentially increases the portion of the aneurysm that is governed by diffusive flow exchange and reduces the portion that is governed by convective flow exchange. The six parameters of the model and the
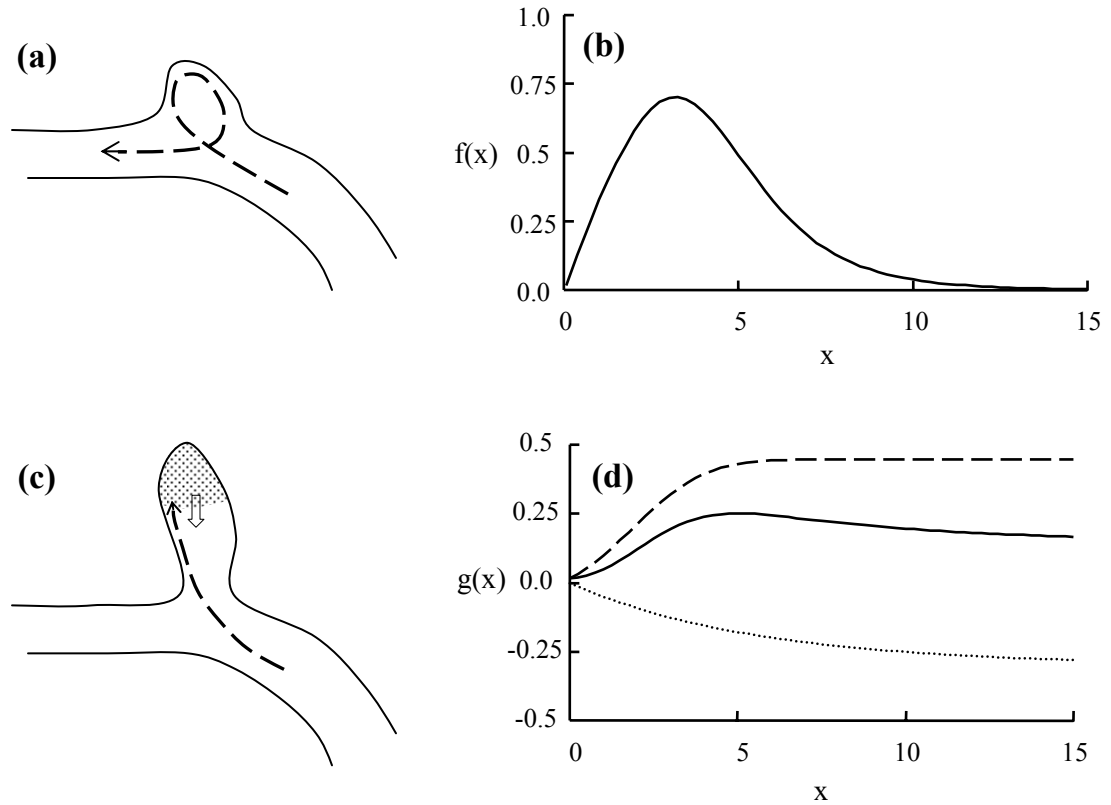
Figure 2-14. Physical basis of the mathematical model. a) The flow exchange between the parent artery and a wide neck, small height aneurysm is modeled by b) a lagged normal function that is the convective component of model. c) In a narrow neck, large height aneurysm, regions of the aneurysm near the dome (dotted) may experience sluggish flow. Flow exchange with such regions is modeled by (d) the diffusive component of the model (solid line). The cumulative distribution function (dashed line) represents the convective flow into the region (dashed line in panel c), while the exponential decay function (dotted line) represents the flow diffusing out of the region (block arrow in panel c). Amplitudes of the components shown in panels b and d are arbitrary.

implications of changes in the parameters vis-à-vis flow divertor implantation are described below:

1. ρ_{conv} and ρ_{diff}: These parameters represent the amplitudes of convective and diffusive transport, respectively. The deployment of a flow divertor should increase the "size" of the diffusive region in the aneurysm. Therefore, the

value of ρ_{diff} can be expected to increase after device implantation, whereas the value of ρ_{conv} should decrease.

2. τ_{conv} and τ_{diff}: These parameters are the convection and the diffusion time constants, respectively. The residence time of blood (angiographic contrast) can be expected to show an increase due to the deployment of the flow divertor. This increase in residence time should, therefore, be reflected in increases in the time constants, especially τ_{diff}, after treatment.

3. σ and μ: These parameters are related to the method and profile of contrast injection (rate of injection, period of injection, variations in these parameters due to manual injection, etc.) and cannot be considered to represent alterations in flow exchange due to flow divertor implantation.

In general, therefore, modeling the aneurysm washout curves obtained before and after flow divertor implantation can be expected to show a relative increase in the diffusive component (parameters ρ_{diff} and τ_{diff}) with a concomitant decrease in the proportion of the convective component (parameter ρ_{conv}). The performance of a flow divertor implanted in any given animal was quantified by the values of these 3 parameters (ρ_{diff}, τ_{diff}, ρ_{conv}) obtained by fitting the washout curve recorded after device implantation as percentages of the corresponding values obtained by fitting the washout curve recorded before device implantation. The amplitude of the aneurysmal washout curves also represents an index of device performance. This value is equal to the difference in maximum and minimum average aneurysmal intensities for a given washout curve (for e.g., this value is ~0.09 for the case shown in Figure 2-13c) multiplied by the maximum value of the model fit to the curve. As the washout curve amplitude is indicative of the amount of angiographic

contrast entering the aneurysm, the larger the reduction in this value, the better the device. The value of the washout curve amplitude obtained after device implantation as a percentage of the corresponding value before device implantation was used an index of device performance.

The optimization of the model to the washout curve data was performed using the function "fmincon" in Matlab, which uses sequential quadratic programming to minimize the objective function subject to linear and nonlinear constraints. The objective function used here returned the sum of the squares of the differences between the points of the data and the model, thus optimizing the model in the least squares sense. As the diffusive process is much slower than the convective process, τ_{diff} was constrained to be greater than τ_{conv}. The sum of the two amplitudes ($\rho_{conv} + \rho_{diff}$) was constrained to be no greater than 1 because the washout curves are normalized from 0 to 1. The area of the normal distribution in the final optimized model was constrained to be at least 0.99. Over a period of 20 seconds, the exponential decay function reduces by only 1% when the value of the time constant is 1990 ($e^{\frac{-20}{1990}} = 0.99$). Similarly, the exponential decay drops to 1% of its value at 0.033 seconds (2nd frame in sequence) when the time constant is about 7×10^{-3} ($e^{\frac{-1/30}{0.0072}} = 0.01$). Both time constants were, therefore, bound to lie between 0.007 and 1990. These values are only to restrict the time constants to reasonable values within the time period of acquisition. The goodness of fit of the mathematical model to the data was evaluated by plotting the model-fits against the data points and calculating the Pearson correlation coefficient. Goodness of fit was also assessed by testing the difference between the model-fit and data for normality based on the Kolmogorov-Smirnov statistic [192] given as

$$D = \sqrt{N} \max |F(x) - S(x)| \qquad \text{(Eq. 2-6)}$$

where, N is the sample size, $S(x)$ is the sample cumulative distribution and $F(x)$ is the cumulative normal distribution function based on the sample mean and sample variance as per Lilliefors' [193] method of estimating the D statistic when mean and variance of the population are unknown. Normality was assessed at 5% significance so that when the D value was below the critical value of 0.886 (for $N > 30$) the sample was considered to be normally distributed.

In addition to increasing the proportion and washout time of the diffusive region within the aneurysm, the flow divertor also reduces the net amount of dye entering the aneurysm, which is reflected in the washout curve amplitude. Because the diffusive process is slower than the convective process, angiographic contrast will wash out of the region of the aneurysm dominated by diffusive flow exchange much slower than the region dominated by convective flow exchange. To account for these different mechanisms in a single quantity, an index of the effectiveness of the flow divertor can be constructed. This index, called the washout coefficient here, is given as

$$W = \frac{\delta\% \times \rho_{diff}\% \times \tau_{diff}\%}{1000000} \qquad \text{(Eq. 2-7)}$$

where, $\delta\%$ is the washout curve amplitude and $\rho_{diff}\%$ and $\tau_{diff}\%$ are the proportion and time constant of the diffusive component of the model obtained immediately after device implantation (POST) expressed as percentages of the corresponding values before device implantation (PRE). With the given construction of the parameter, a control aneurysm (untreated) would result in a value of 1. W values rounding off to 1 are therefore excluded from consideration. Apart from assessing inter-device differences, such a parameter

obtained immediately after device implantation, can be used to assess whether or not any given device will occlude the treated aneurysm at follow-up. A prognostic test for aneurysm occlusion can then be developed based on a suitable threshold value for W. A threshold is chosen so as to maximize the sensitivity and specificity of the test based on the receiver operating characteristic (ROC) curve for the data and statistical significance of the test is assessed by Fisher's exact test for the resulting contingency table.

2.8. Device Evaluation

The three flow divertors were compared based on the various quantities accumulated from the data as described in the preceding pages. Statistical significance of the differences between divertors was compared by analysis of variance (ANOVA) or Student's t tests. Statistical comparisons were made with the GraphPad InStat software (version 5.1, GraphPad Software, San Diego, CA). The following table (Table 2-4) lists the indices of device performance, the source of the indices, and the trend (high or low) of each index that indicates a better device. Changes from before device implantation to immediately after device implantation (PRE-to-POST) as well as changes from before device implantation to follow-up (PRE-to-FU) were evaluated for the 4 indices relating to the washout curve analysis. The average value of each index was normalized by the maximum of the three devices to obtain a grade of the effectiveness of each device compared to the best, where the best device received a grade of 1. If lower values of the index implied a better device (neointimal thickness, washout curve amplitude, convective component amplitude), inverse of the average quantities were taken. The sum total of these grades was used as the final composite performance score.

Table 2-4. Indices of flow divertor performance.

Source of index	Performance index	Favorable trend
Histology	Neointimal thickness	Low
	Extent of aneurysm occlusion	High
	Extent of organization of aneurysm contents	High
Angiography	Percentage angiographic aneurysm occlusion	High
	Percentage arc-to-chord ratio	High
Washout analysis	Percentage washout curve amplitude	Low
	Percentage diffusive component amplitude	High
	Percentage diffusive component time constant	High
	Percentage convective component amplitude	Low

Chapter 3. RESULTS

The average dimensions (neck × width × height) at maturity of aneurysms created in the 40 animals is given in Figure 3-1. Where averages of quantities are mentioned throughout this chapter, the measure of uncertainty listed refers to the standard error of the mean unless specified otherwise. The average aneurysm dimensions in all 40 animals were 4.1(0.2) × 3.7(0.1) × 7.9(0.3) mm. The dimensions of all the aneurysms are given in Appendix 1 (Table A1.1). Differences in the neck (ANOVA p = 0.64), width (p = 0.96), or height (p = 0.22) were not statistically significant among the four groups. The average height of aneurysms treated with device E was, however, higher as compared to those treated with devices B (t test, p=0.04) and C (p=0.02). There were minimal technical difficulties in navigating the flow divertor delivery system through the aortic arch/innominate artery junction and deploying it across the aneurysms. The vertebral
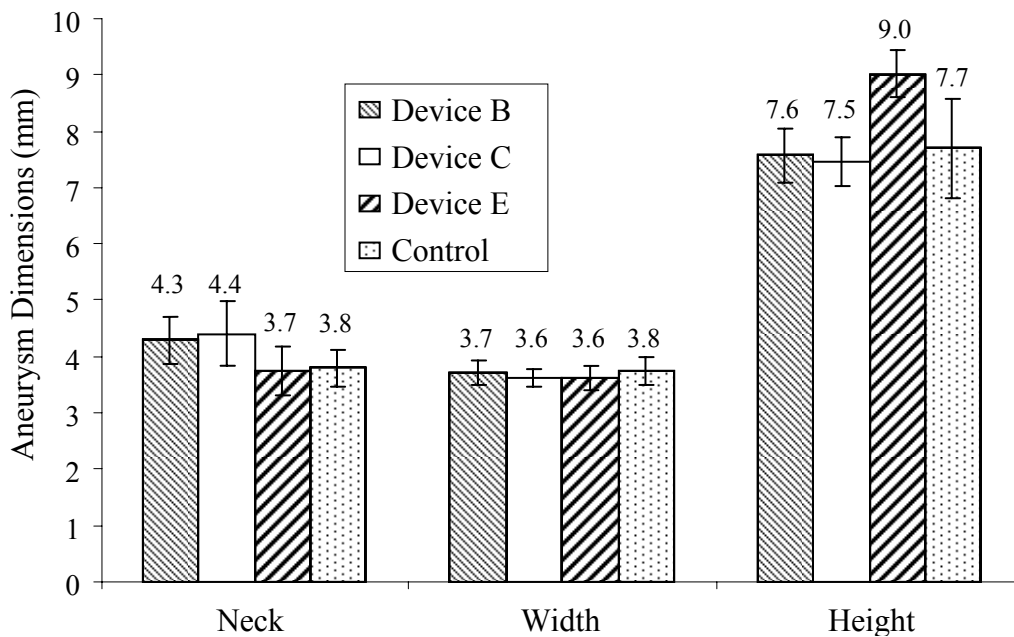
Figure 3-1. Aneurysm dimensions (mean and standard error) for the treated and control groups. There were no statistically significant differences between the four groups in any of the dimensions (ANOVA p > 0.22).

artery was covered in all animals except three (#C_021_1, #C_021_2 and #C_090_2). The vertebral artery was angiographically patent in the other 27 animals. Sample images from high-speed angiograms taken before device deployment, after device deployment and at follow-up for one animal (#E_090_2) are given in Figure 3-2. The actual number of days to follow-up after the treatment phase for each animal and the averages per group are given in Table A1.2 in Appendix 1. Overall the average follow-up times were 21.3(0.4) days, 92.8(0.6) days, and 184.1(0.7) days. There were no significant differences in follow-up times between the 4 groups (p>0.06). There were 5 cases (#B_021_1, #B_021_2, #B_021_3, #B_090_2, #E_090_1) in which mild to moderate occlusion of the parent artery near the distal tip of the device was noted during follow-up angiography, as evidenced by delayed filling of the subclavian artery. There were no cases of device migration or device fracture. At follow-up angiography in one case (#E_180_4), flow was seen to go around the device and into the aneurysm. This case was excluded from consideration for device evaluation.
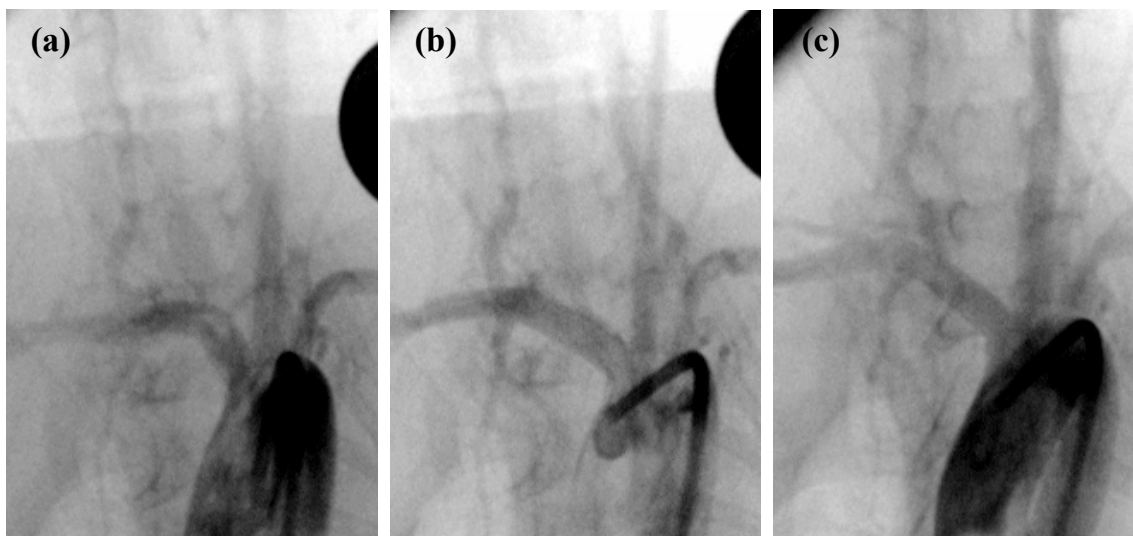
Figure 3-2. Unsubtracted angiograms obtained (a) before device implantation, (b) immediately after device implantation, and (c) at 90 days follow-up. Images from animal #E_090_2.
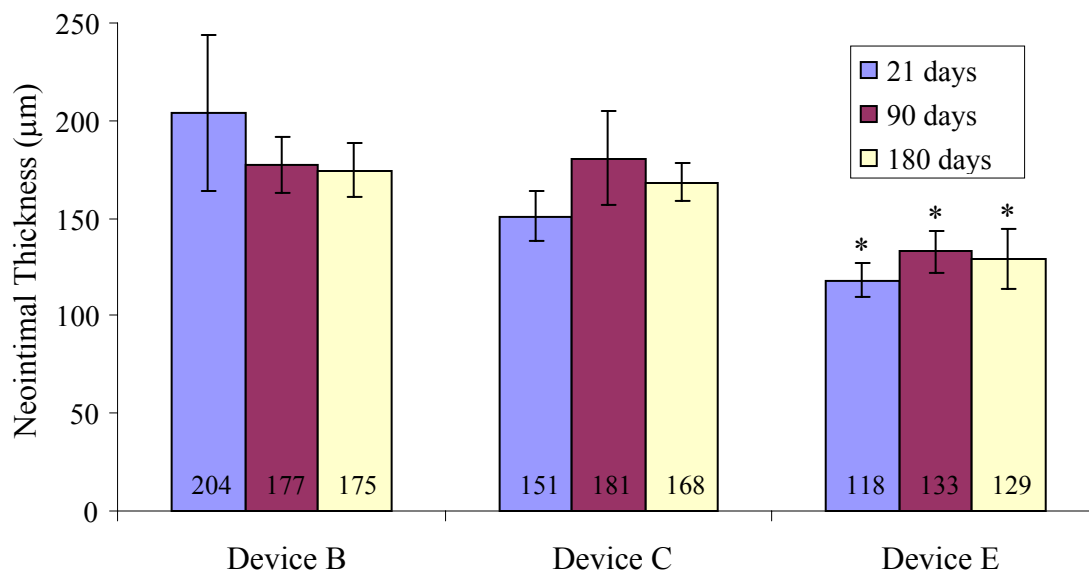
Figure 3-3. Average (standard error) thickness of the neointima formed on the luminal surface of the devices. * indicates significance (p<0.05) as compared to corresponding device B and C values. Difference between neointimal thicknesses for devices E and C at 90 days is not quite significant (p=0.055). For a given device, there were no significant differences over various follow-up times (p>0.59). Results based on 6 samples from devices B and C and 7 samples from device E. Data listed in Table A1.3, Appendix 1.
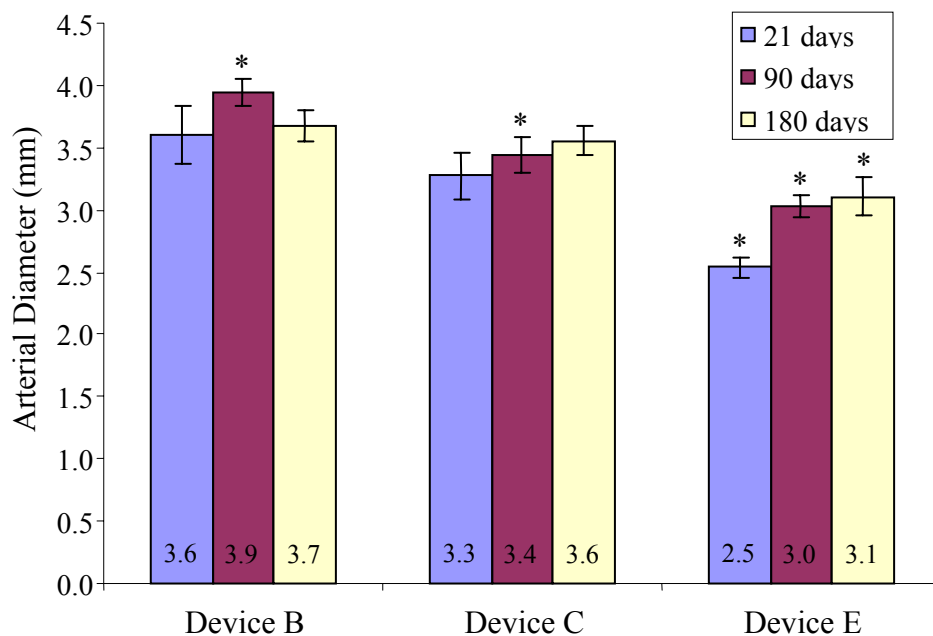
Figure 3-4. Average (standard error) diameter of the parent artery in histological sections. * indicates significance (p < 0.033) as compared to corresponding device B and C values. Arterial diameters were significantly different among all 3 devices in the 90-day samples. Results based on 6 samples from devices B and C and 7 samples from device E. Data listed in Table A1.3, Appendix 1.

Samples from 19 of the 30 treated animals have been processed by histology thus far. These include 7 animals treated with device E (#E_021_1, #E_021_3, #E_090_1, #E_090_2, #E_090_3, #E_180_1, #E_180_2), 6 animals treated with device B (#B_021_3, #B_090_1, #B_090_2, #B_090_3, #B_180_1 and #B_180_2), and 6 animals treated with device C (#C_021_3, #C_090_1, #C_090_3, #C_180_1, #C_180_2 and #C_180_3). Histomorphometric results described here are based on these samples. The neointimal thickness induced by the three devices at the different follow-up time points is shown in Figure 3-3. The neointimal thickness of the 90-day samples treated with device E was not significantly different from the thickness in the 90-day samples treated with device C (Student's t test, $p = 0.055$). At all other follow-up time points, the thickness of the neointima within device E was significantly lower than the corresponding neointimal thicknesses produced by both devices B and C (Student's t test, $p < 0.05$). There was no significant difference in the neointimal thickness at 21 days, 90 days or 180 days post-treatment for any of the three devices (ANOVA $p > 0.59$). The diameters of the parent arteries as measured on the histological sections of the samples are shown in Figure 3-4. The parent artery diameters of the samples treated with device E were significantly lower than the diameters of devices B and C ($p < 0.033$) at all follow-up time points. In the samples explanted 90-days post-treatment, artery diameters were significantly different among all 3 devices ($p < 0.02$). Values of the neointimal thicknesses and artery diameters are listed in Appendix 1 (Table A1.3).

A section at the aneurysm could not be obtained in one case (#B_180_2). Figure 3-5 (panels a, b, and c) shows histology images of the aneurysm in 3 animals that were treated with device E and followed-up at the 3 different time points. Progression of the

Figure 3-5. (a) to (c): histological sections of the aneurysm from 3 animals treated with device E and followed-up 21, 90 and 180 days post-treatment, respectively. Semi-quantitative scores of aneurysm occlusion and organization of sac contents are also listed. (d) and (e): histological sections at the vertebral artery; (d) #B_180_2, (e) #E_180_1.
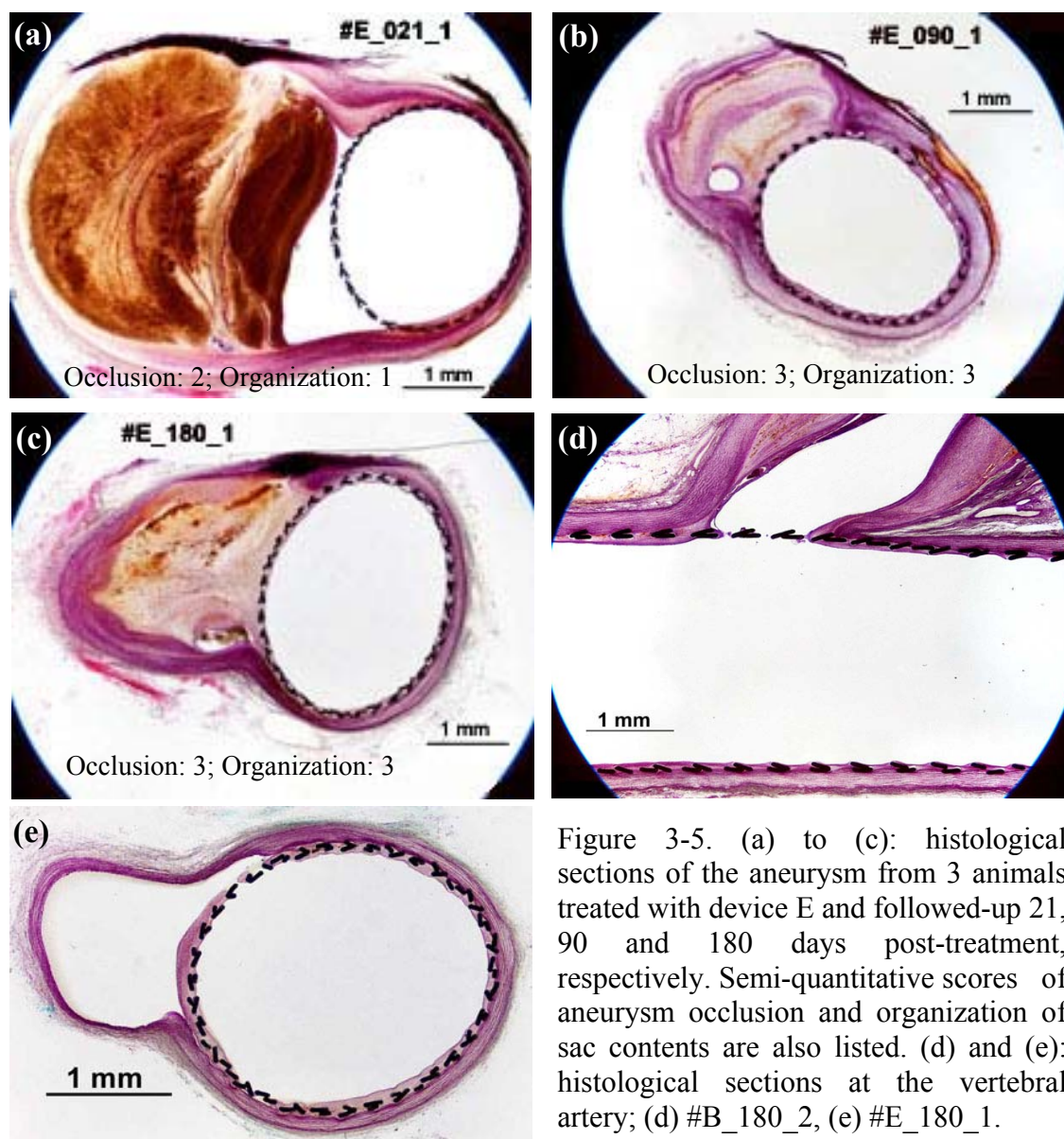
intraneurysmal thrombus from acute (darker shades) to mature (lighter areas) stages can be noted along with organization of the sac components. Histological sections at the aneurysm for all the 18 cases are shown in Appendix 3. Sample histological sections at the vertebral artery from two animals are also included in Figure 3-5 (panels d and e). Sections obtained at the vertebral artery show this artery to be patent in all animals.

The semi-quantitative aneurysm occlusion scores as seen on histological sections of specimens treated with the three devices at the different follow-up time points are
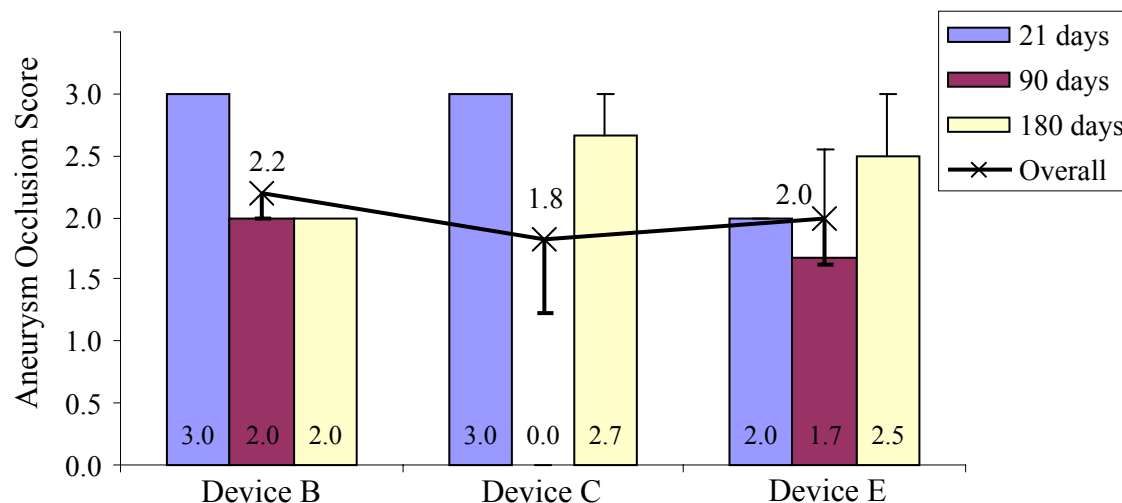
Figure 3-6. Average (standard error) semi-quantitative score of the extent of aneurysm occlusion as seen on histology. 0 – Aneurysm lumen essentially empty; 1 – Aneurysm lumen slightly filled; 2 – Aneurysm lumen at least half filled; 3 – Aneurysm lumen essentially filled. There were no significant inter-device differences in the overall extent of aneurysm occlusion (p=0.86). Results based on 5, 6, and 7 samples from devices B, C, and E, respectively. Data listed in Table A1.4, Appendix 1.

shown in Figure 3-6. Three of these sections (cases #C_090_1, #C_090_3, and #E_090_3) were devoid of any contents within the sac. The overall aneurysm occlusion score for each device is calculated as the average of the occlusion scores at the 3 different time points. Inter-device differences in the overall occlusion score were not statistically significant (ANOVA, p = 0.86). There were too few samples to test for differences between the different follow-up time points for devices B and C. There were, however, no significant differences between the aneurysm occlusion scores over the 3 follow-up times for device E (ANOVA, p = 0.74). Differences in the occlusion score between follow-up times were tested for statistical significance by grouping the occlusion scores produced by all 3 devices at any given follow-up time. The ANOVA p value in this case was 0.06, indicating no significance, with the aneurysm occlusion score at 90 days being lower than both the 21-day and 180-day scores. Figure 3-7 shows a graph of the degree of
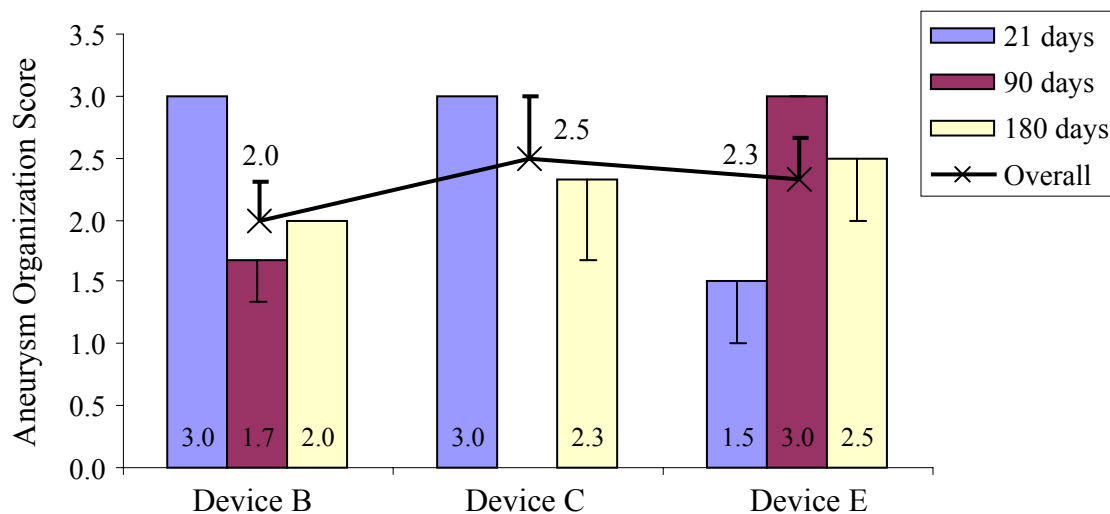
Figure 3-7. Average (standard error) semi-quantitative score of the degree of organization of aneurysm contents as seen on histology. 1 – Clot with little organization; 2 – Clot with more organization; 3 – Organized with recanalization. Aneurysm sac was empty in the two 90 day histological sections from Device C. There were no significant inter-device differences in the overall degree of organization (p=0.66). Numbers of samples were 4, 5, and 6 from devices C, B, and E, respectively. Data listed in Table A1.4, Appendix 1.

organization of aneurysm contents at the different time points for the 3 devices. Again, inter-device differences in the overall organization of the aneurysm sac contents were not significantly different (ANOVA, p = 0.66). Grouping the organization scores of the devices for a given time point also showed no statistically significant differences over the follow-up times (p = 0.97). The values of the aneurysm occlusion scores and the degree of organization of the aneurysm sac contents are listed in Appendix 1 in Table A1.4.

The respiratory periods (in number of frames) for all the animals are given in Table A1.5, Appendix 1. Digitally subtracted angiograms corresponding to the native images shown in Figure 3-2 are shown in Figure 3-8, as an example. The subtracted angiograms showing maximal opacification of the aneurysm for all 40 animals over the different phases are shown in Appendix 2. The mean subtraction error, quantified by the number of pixels in edges as a percentage of total number of pixels in the image, was
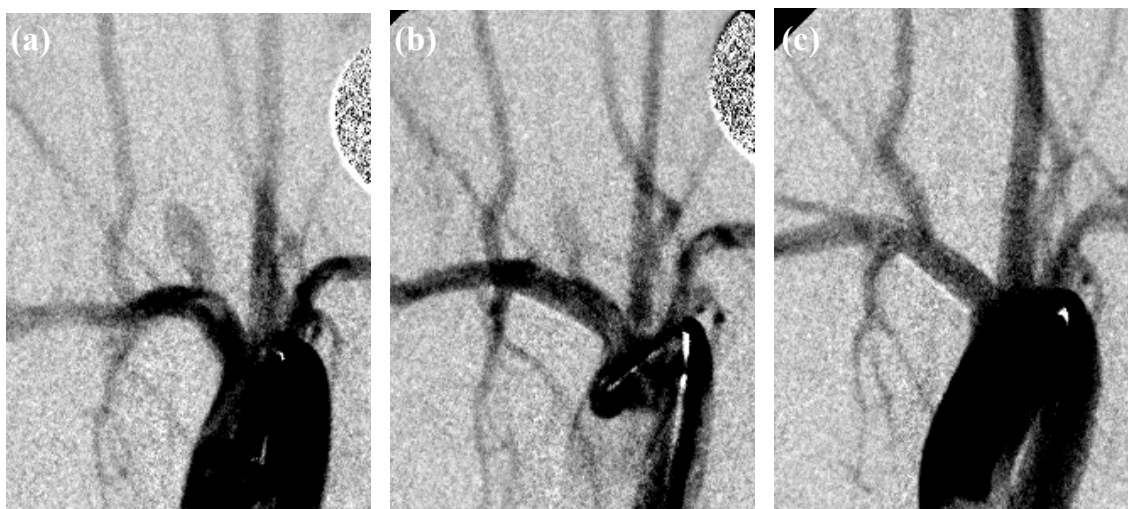
Figure 3-8. Subtracted angiograms obtained (a) before device implantation, (b) immediately after device implantation, and (c) at 90 days follow-up. Images correspond to those shown in Figure 2 (animal #E_090_2).

1.6% (0.2%) (n = 90 angiographic sequences). The percentage angiographic aneurysm occlusion measured at the different follow-up time points for the three devices is shown in Figure 3-9. Ten of the 30 animals had 100% angiographic occlusion of the aneurysm at follow-up. Twenty four, nineteen, and seventeen animals had angiographic aneurysm occlusion rates greater than 75%, 90%, and 95%, respectively, at follow-up. As can be noted in Figure 3-9, device E consistently showed high occlusion rates from 21 days through 180 days and the overall percent occlusion was highest with this device. The percentage aneurysm occlusion at 90 days in animals treated with device C was significantly lower than the occlusion rates of aneurysms treated with devices B and E at 90 days (p = 0.01). Differences in animals treated with device C were not statistically significantly at the 21, 90, or 180 days (p = 0.055). All other intra- (given device at different follow-up times) or inter- (different devices at given follow-up time point) device differences in occlusion rates were not statistically significant (p > 0.13).
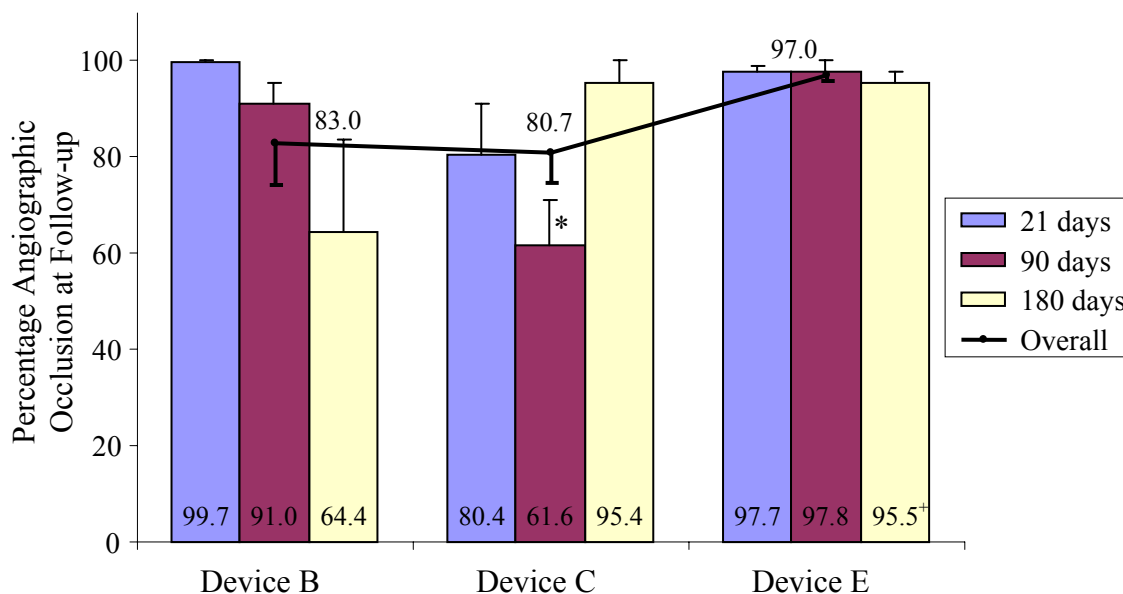
Figure 3-9. Percentage occlusion of the aneurysm measured by angiography acquired at follow-up at the different time points. *Percent aneurysm occlusion was significantly lower with device C as compared to devices B and E at 90 days post-treatment (p=0.01). There were no other significant differences between devices at the same follow-up time point or within devices at different time points. Number of cases, device B (n=10), device C (n=10), device E (n=9). All values are listed in Table A1.6, Appendix 1.
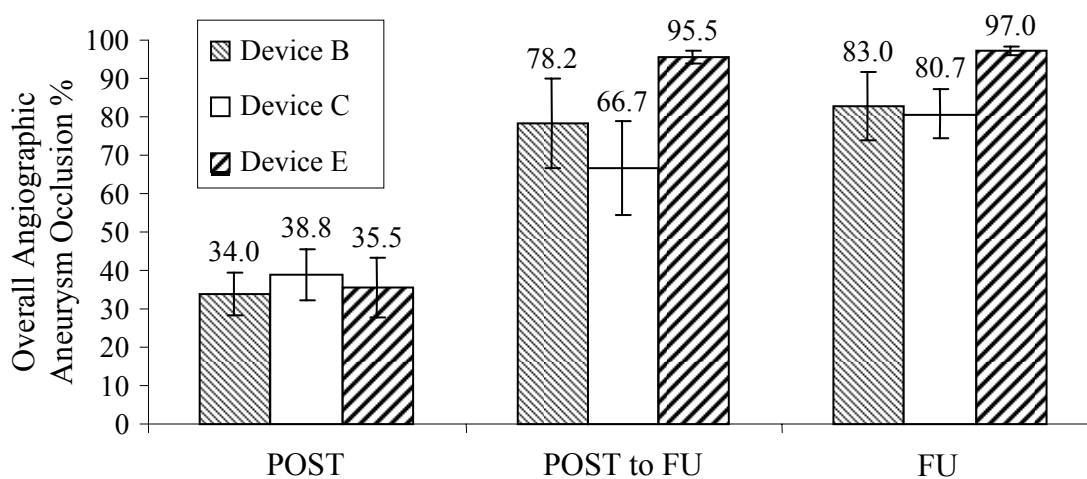
Figure 3-10. Progress in angiographic occlusion of the aneurysm. POST: angiography performed immediately after device implantation; FU: angiography performed at follow-up; POST to FU: calculated occlusion of the aneurysm during the follow-up period. Differences between devices did not reach significance at any stage (p > 0.15). Number of cases, device B (n=10), device C (n=10), device E (n=9). Values are listed in Table A1.6, Appendix 1.

Figure 3-10 shows the overall angiographic aneurysm occlusion rates for the three devices immediately after device implant (POST) and at follow-up (FU) along with the calculated POST-to-FU occlusion rates. All three devices produced an average angiographic occlusion of the aneurysm of approximately 35% immediately after device implant (ANOVA, $p = 0.87$). The overall angiographic occlusion rate produced by device E at follow-up was significantly higher as compared to device C (t test, $p = 0.03$), but not as compared to device B ($p = 0.15$). The follow-up occlusion rates of devices B and C were not statistically different ($p = 0.84$). Similar statistical trends were observed with the POST-to-FU occlusion rates; the Student's t test p value for device E as compared to device C was 0.04, for device E as compared to device B was 0.18, and for device B as compared to device C was 0.5. Although there was no statistically significant trend observed in the inter-device angiographic occlusion rates, a correlation was observed between the POST and FU degrees of angiographic aneurysm occlusion over all 3 devices combined. The average POST occlusion of cases that eventually resulted in >=97% FU occlusion ($45.1\pm17.5\%$) was significantly greater than the average POST
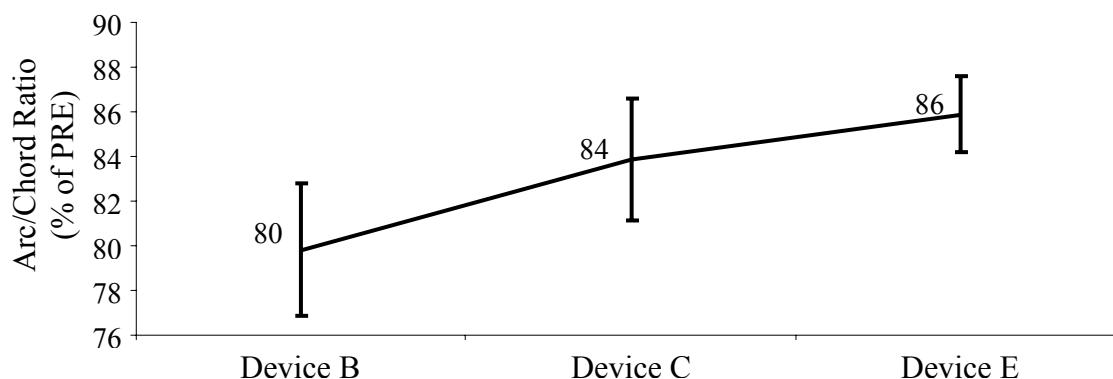
Figure 3-11. Mean (standard error) values of arc-to-chord ratios of vessel segments after implantation of a device as a percentage of the corresponding values before device implantation (PRE). Differences between devices were not statistically significant (p=0.36). Values listed in Table A1.7, Appendix 1.

occlusion of cases that resulted in <97% FU occlusion (27.1±17.7%); t test p value = 0.01. Except for 1 small control aneurysm that occluded by 51% at 21 days (#O_021_1), all control aneurysms exhibited >90% patency. The average angiographic occlusion rate of these 9 controls was 4.7±1%. Occlusion rates with all 3 devices were significantly higher than controls (t tests $p<10^{-4}$). All values of percentage angiographic aneurysm occlusion are given in Table A1.6, Appendix 1. Average changes in the arc-to-chord ratios of the treated vessel segments are shown in Figure 3-11 (values listed in Table A1.7, Appendix 1). Inter-device differences were not significant (ANOVA, p=0.26).

Washout curves were not measured in the FU sequences that had a percentage angiographic occlusion of the aneurysm greater than or equal to 97% (15 animals) because the size of the region of interest (ROI) was too small to be clearly visualized in these cases. Moreover, the washout curves from these cases would have primarily consisted of subtraction artifacts due to the device. Washout curves were thus generated from 75 (30 PRE, 30 POST, 15 FU) of the 90 sequences. The position vector tracking the aneurysm could not be automatically calculated in 9 (1 PRE, 7 POST, 1 FU) of the 75 cases because of insufficient contrast of the superior edge of the parent artery distal to the aneurysm. In these cases, the location of the aneurysm was marked manually over one respiratory period. The error in automatically generating the position vector of the aneurysm may be compared to the results from the manual selection of the aneurysm location. This error was quantified by the amplitude of the respiratory frequency in the washout curves as a ratio of the corresponding fundamental frequencies. There were no statistically significant differences in this amplitude ratio between the position vectors generated automatically or manually (t test p value = 0.84).

Three modifications that were made to some of the raw washout curves before fitting with the mathematical model may be mentioned. In washout curves where there was a large enough discontinuity between the values of the last point and the first point, the filtered washout curves showed an artifactual rise towards the end of the acquisition period (Gibbs effect). In these cases, the raw washout curve was appended by the time-domain flipped curve to get a periodic waveform. This half-range expanded curve was then filtered using the notch filter. Thirty two of the 75 curves were filtered in this way. Some of the filtered washout curves showed one or two spurious data points that appeared to not follow the trend of the rest of the curve. In such cases, a 6th order Butterworth filter or a 6th order polynomial fit was used to estimate the trend of the curves. Differences between the data points and the trend were tested for outliers using the modified three-sigma test [194]. If a point appearing to be spurious was an outlier based on this test, the value of this point was replaced by the average of the points preceding and succeeding it. A maximum of 4 points (average 2.2 points) per curve were adjusted this way in 16 of the 75 washout curves. In certain cases, the injected angiographic contrast returning through either the jugular or spinal veins was superposed on the aneurysmal ROI, adding a false rise and fall to the washout curves when the contrast within the aneurysm was in the process of washing out. A second ROI was manually selected on the vein(s) producing this artifact, the average grayscale intensity within this second ROI was measured, and the trend of this venous return artifact was obtained by fitting a 6th order polynomial to it. This venous return component was then removed from the aneurysmal washout curve by subtraction. Eleven of the 75 washout curves were corrected for venous return in this manner.

Figures 3-12a and 3-13a show the filtered washout curves from the PRE and POST sequences of one animal (#E_090_1), as an example. The filtered washout curves from the PRE, POST and, if measured, FU sequences for all the animals are shown in Appendix 2. Figures 3-12b and 3-13b show the corresponding model fits to these washout curves after normalization. Plots of the convective and diffusive components of the model are superposed in the figures and the optimized model parameters are listed. Values of the optimized model parameters for all cases are listed in tables A1.8 through A1.10 in Appendix 1. The model-fits to all the washout curves are shown in Appendix 2.

Changes in the 6 optimized model parameters (ρ_{conv}, ρ_{diff}, τ_{conv}, τ_{diff}, σ and μ) due to implantation of each of the 3 devices are shown in Figures 3-14, 3-15, and 3-16. In two cases (#B_021_2 and #E_021_3), the catheter was close to the entrance of the innominate artery during the PRE acquisitions, which resulted in an increase in the concentration of angiographic contrast entering the aneurysm. As a result, the washout curve amplitudes for these two cases were higher than the amplitudes in all other cases (only these two amplitudes of 0.47 and 0.57 were more than 2.7 standard deviations from the mean of all amplitudes, mean = 0.17, standard deviation = 0.11). The washout curve amplitudes from the POST sequences of these 2 cases are, however, similar to the POST amplitudes of all other washout curves (the two amplitudes were within half a standard deviation of the mean), suggesting that the concentration of contrast reaching the aneurysm was similar in these two POST sequences to other cases. For this reason, the change in model parameters from PRE to POST in these 2 cases could not be included in the overall results and they were excluded from consideration for device evaluation.
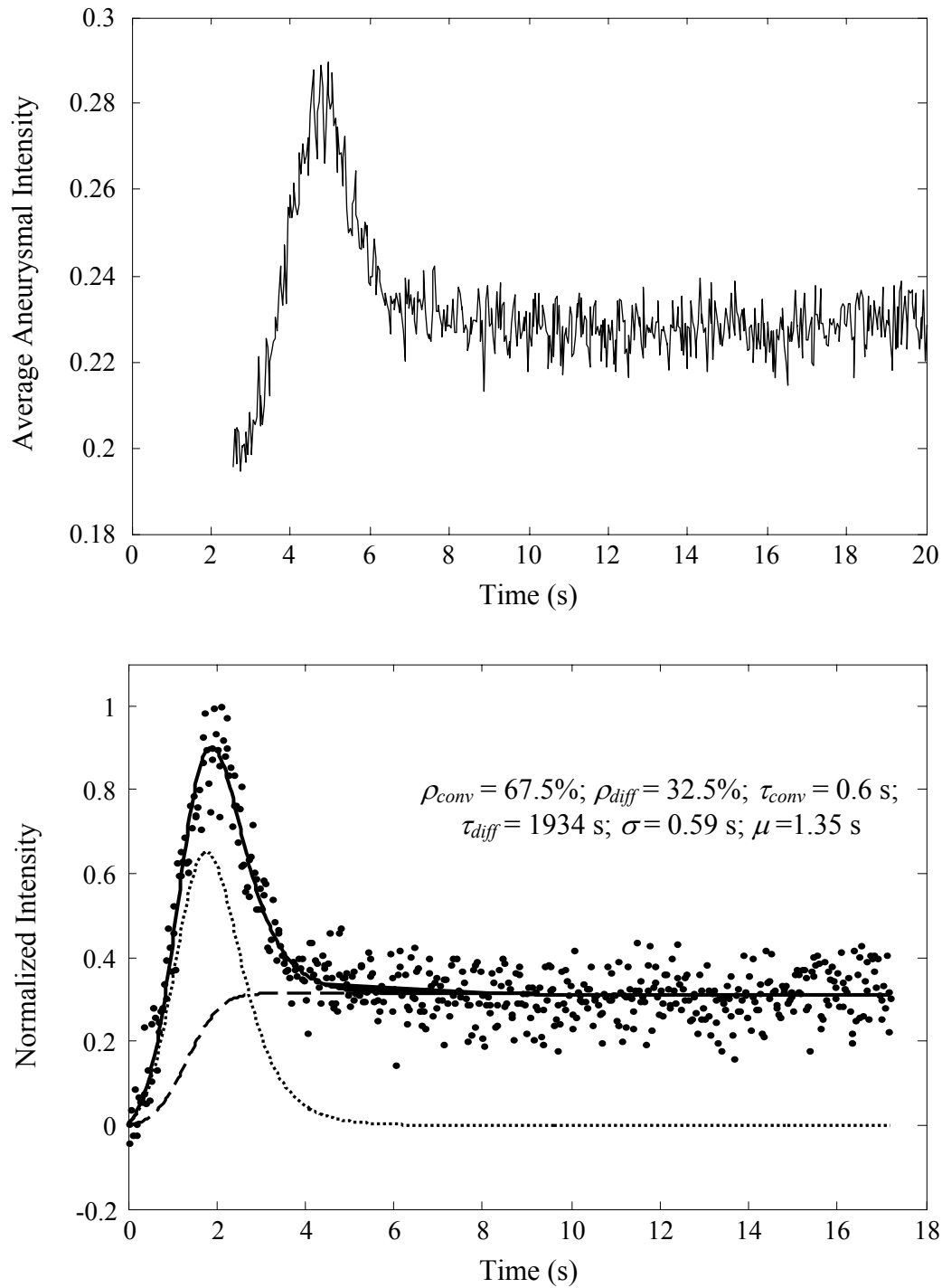
Figure 3-12. (a) Aneurysm washout curve before device implantation for one animal (#E_090_1). (b) Model-fit (solid lines) to the normalized washout curve (dots). The values of the optimized model parameters are provided along with plots of the convective (dotted lines) and diffusive components (dashed lines).
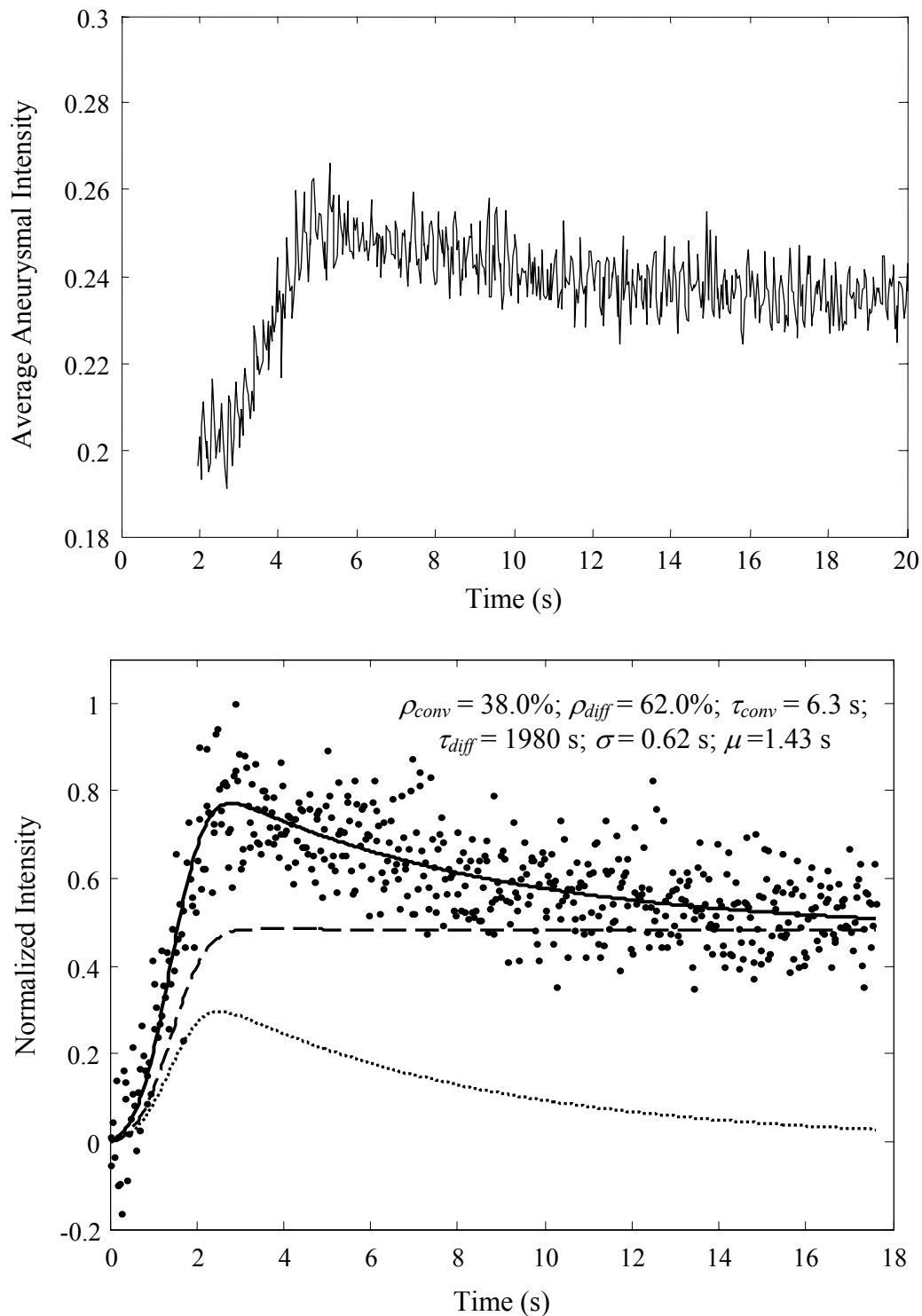
Figure 3-13. (a) Aneurysm washout curve immediately after device implantation for one animal (#E_090_1). (b) Model-fit (solid lines) to normalized washout curve (dots). The values of the optimized model parameters are provided along with plots of the convective (dotted lines) and diffusive components (dashed lines).
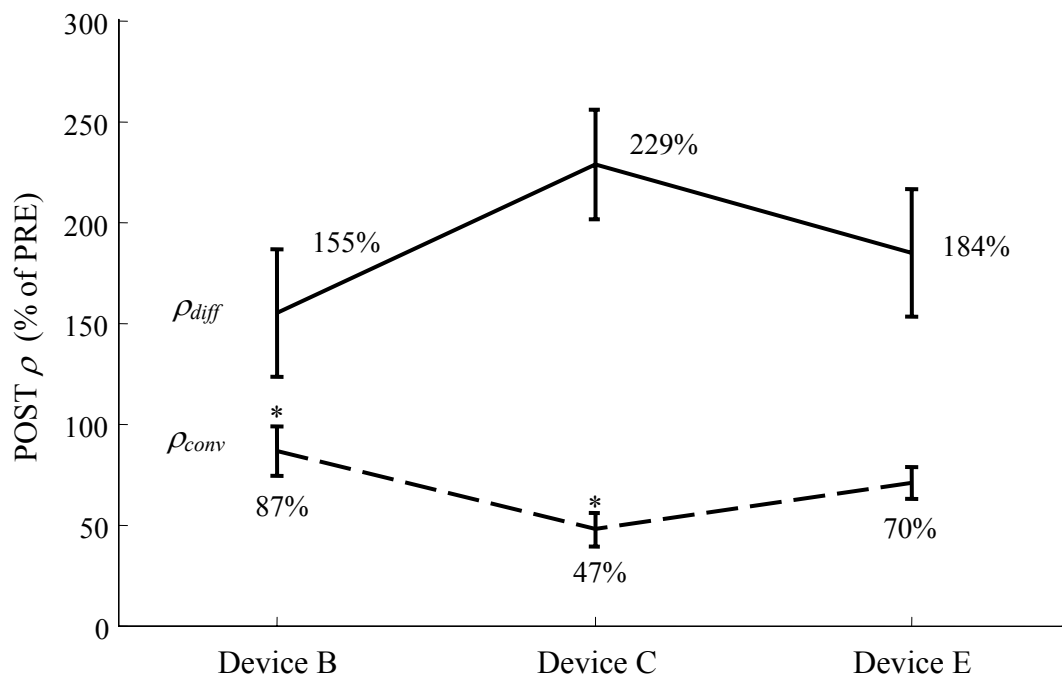
Figure 3-14. Mean (standard error) values of amplitudes of the convective (dashed line) and diffusive (solid line) components immediately after device implantation (POST) as a percentage of the corresponding values before device implantation (PRE). * The ρ_{conv} value for device C was significantly lower than that for device B (p = 0.016). Number of samples; device B (n=9), device C (n=10), device E (n=8).

Figure 3-14 shows the relative amplitudes of the diffusive and convective components of the model obtained immediately after device implantation (POST) as a percentage of the corresponding values before device implantation (PRE). In so far as increases in the diffusive component amplitude and concomitant decreases in the convective component amplitude indicate a better device, the trend in Figure 3-14 shows device C to be better than device E, which in turn was better than device B. Values of ρ_{diff} were not significantly different among the 3 devices (ANOVA p = 0.22). The ρ_{conv} value for device C was significantly lower than that for device B (t test p = 0.02), but not significantly lower than the device E value (t test p = 0.07). The ρ_{conv} values for devices B and E were not significantly different (t test p = 0.3).
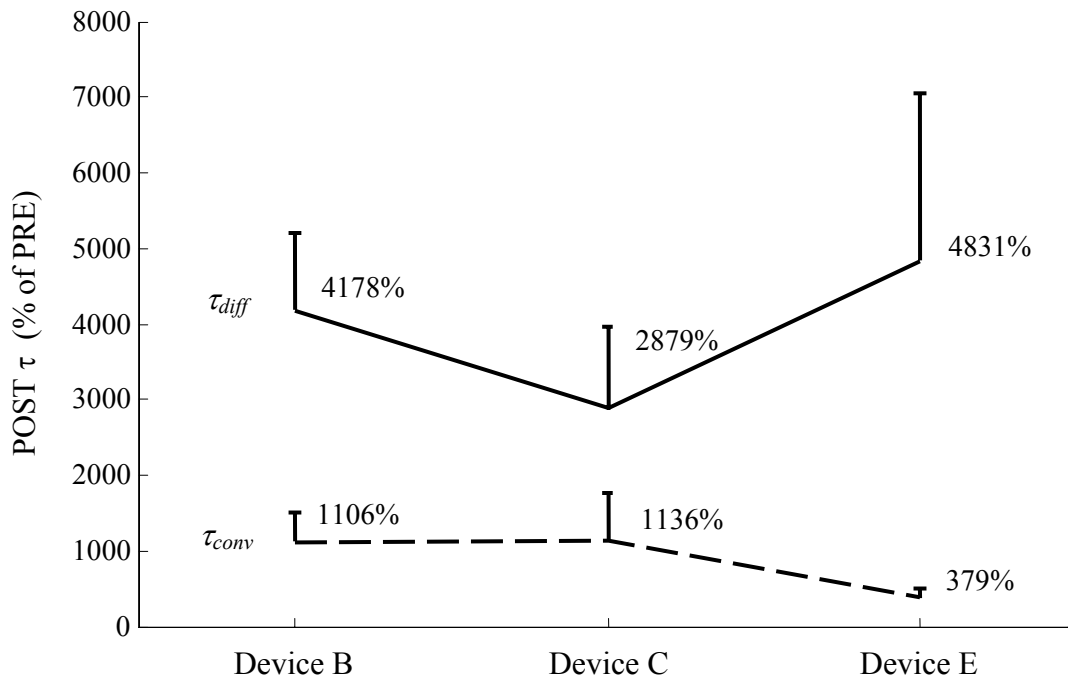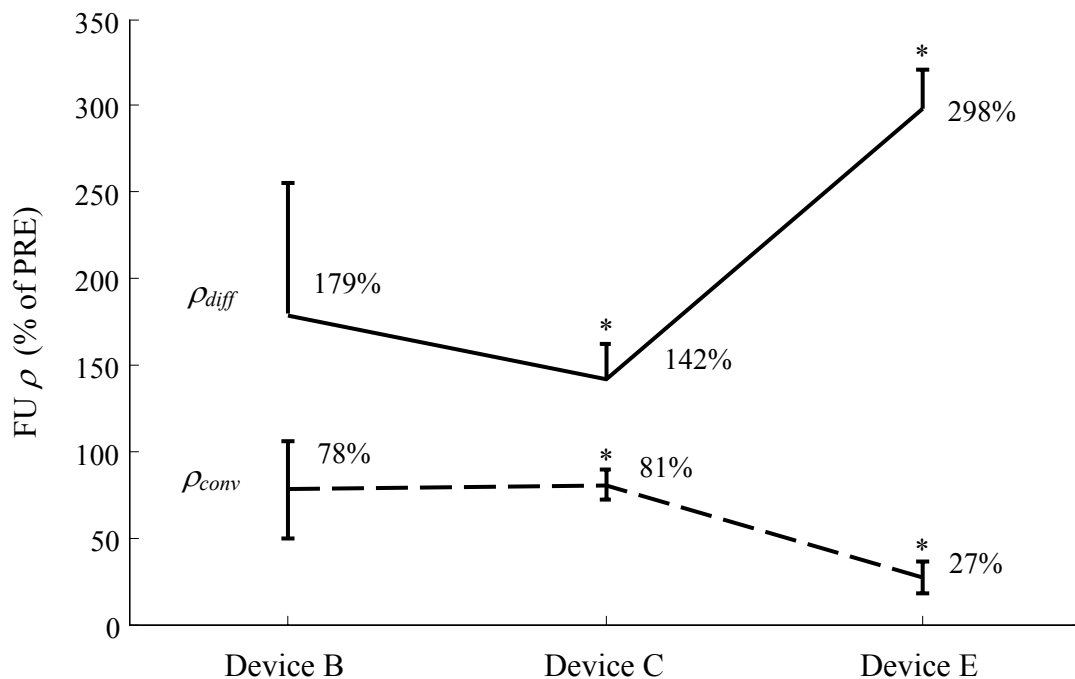
Figure 3-15. Mean (standard error) values of time constants of the convective (dashed line) and diffusive (solid line) components immediately after device implantation (POST) as a percentage of the corresponding values before device implantation (PRE). Inter-device differences were not significant for either parameter (τ_{diff}, p = 0.63; τ_{conv}, p > 0.11). Number of samples; device B (n=9), device C (n=10), device E (n=8).

Figure 3-15 shows the variation in the percentages of the diffusive (τ_{diff}) and convective (τ_{conv}) time constants immediately after implantation of the three devices. Inter-device differences were not significant for either parameter (τ_{diff}, ANOVA p = 0.63; τ_{conv}, Student's t test, Welch corrected p > 0.11). Device E was the best device in terms of increasing the diffusive time constant, which is the more important of these two parameters inasmuch as the diffusive process is slower than the convective process. The trend for τ_{diff} shows device E to be better than device B (higher residence time), which was better than device C. Device C, however, effected a larger increase in the convective time constant (τ_{conv}) as compared to devices B and E.
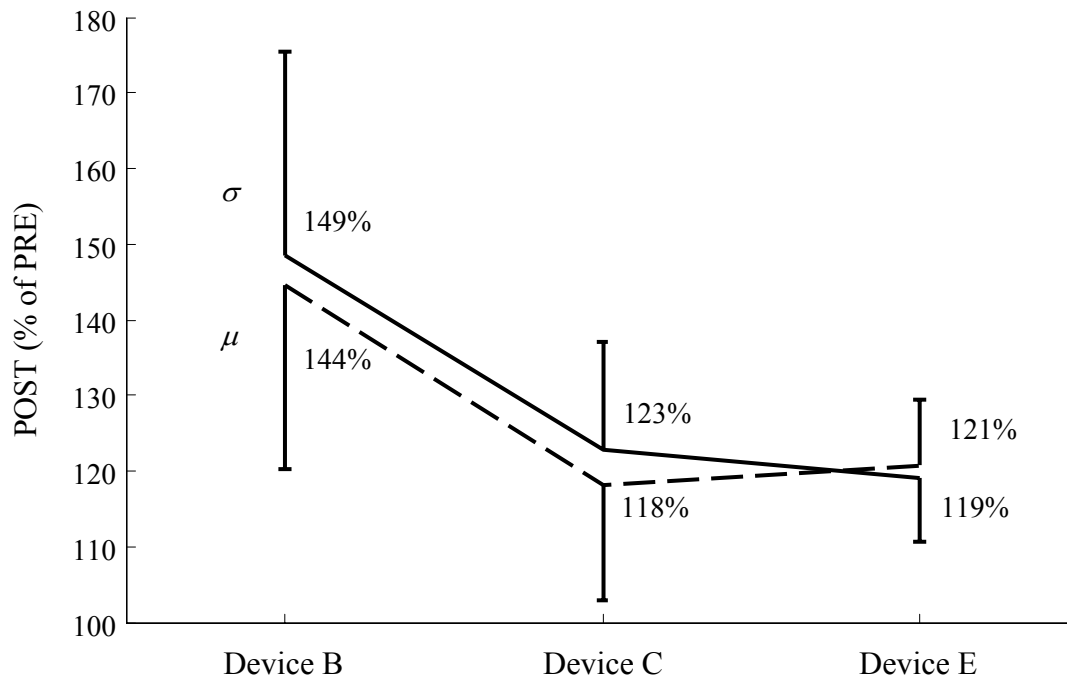
Figure 3-16. Mean (standard error) values of optimized model parameters μ (dashed line) and σ (solid line) immediately after device implantation (POST) as a percentage of the corresponding values before device implantation (PRE). Inter-device differences were not significant for either parameter (σ, p > 0.32; μ, p > 0.37). Number of samples; device B (n=9), device C (n=10), device E (n=8).

Figure 3-16 shows the changes in the parameters σ and μ after device implantation for all 3 devices. Inter-device differences were not significant for either parameter (Welch corrected t test p > 0.32 for σ and p > 0.37 for μ). Both these parameters changed by approximately the same amounts for each device (145% for device B and 120% for devices C and E). The reductions in the amplitudes of the washout curves due to device implantation are shown in Figure 3-17. The differences between devices were not significant (Welch corrected t test p > 0.19). In terms of changes in the washout curve amplitude, device C performed the best, with device E ranking second and device B effecting the least change.
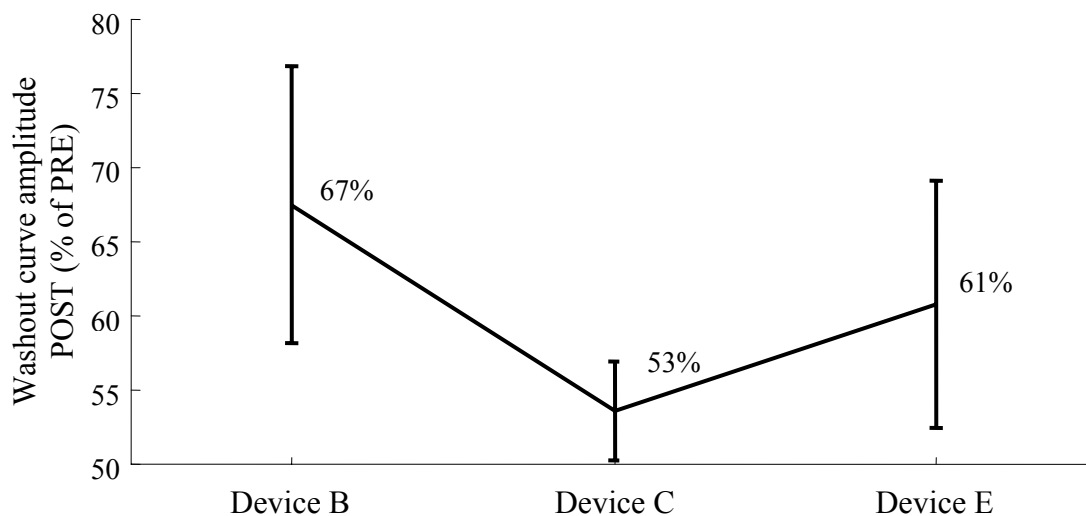
Figure 3-17. Mean (standard error) values of washout curve amplitudes immediately after device implantation (POST) as a percentage of the corresponding values before device implantation (PRE). Inter-device differences were not significant (p > 0.19). Number of samples; device B (n=9), C (n=10), E (n=8).
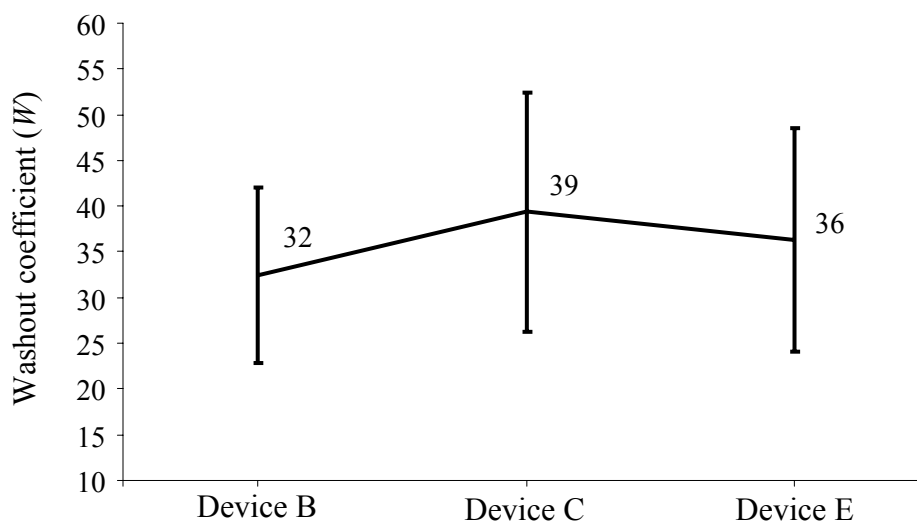
Figure 3-18. Mean (standard error) values of the washout coefficients immediately after device implantation. Inter-device differences were not significant (p=0.91). Device B (n=8), device C (n=8), device E (n=6).

A comparison of the washout coefficients based on the parameters obtained from angiographic sequences acquired immediately after device implantation is shown in Figure 3-18. The differences between the devices were not significant (ANOVA p =0.91). There was, however, a statistically significant difference in the washout

coefficient values when correlated with the angiographic aneurysm occlusion at follow-up. The average W value for cases with $>= 97\%$ angiographic occlusion of the aneurysm at follow-up (21±5) was significantly lower than the value for cases with $< 97\%$ angiographic aneurysm occlusion at follow-up (51±10); Welch corrected t test p value = 0.02. There was no significant difference in any of the parameters constituting W ($\delta\%$, $\rho_{diff}\%$, $\tau_{diff}\%$) when considered individually and grouped by $>=97\%$ or $<97\%$ aneurysm occlusion (t test p values > 0.2).

The threshold value of W which gave the maximum sensitivity and specificity for the prognostic test was 30. Figure 3-19 shows the ROC curve for the washout coefficient data with the inset showing the contingency table based on a threshold value of 30. The sensitivity and the specificity of this test were 73% and 82%, respectively. The Fisher's exact test two-sided p value was 0.03, suggesting that the row-column association was statistically significant.

	FU Occlusion		
	>=97%	<97%	Totals
1< W <= 30	8	2	10
W > 30	3	9	12
Totals	11	11	22
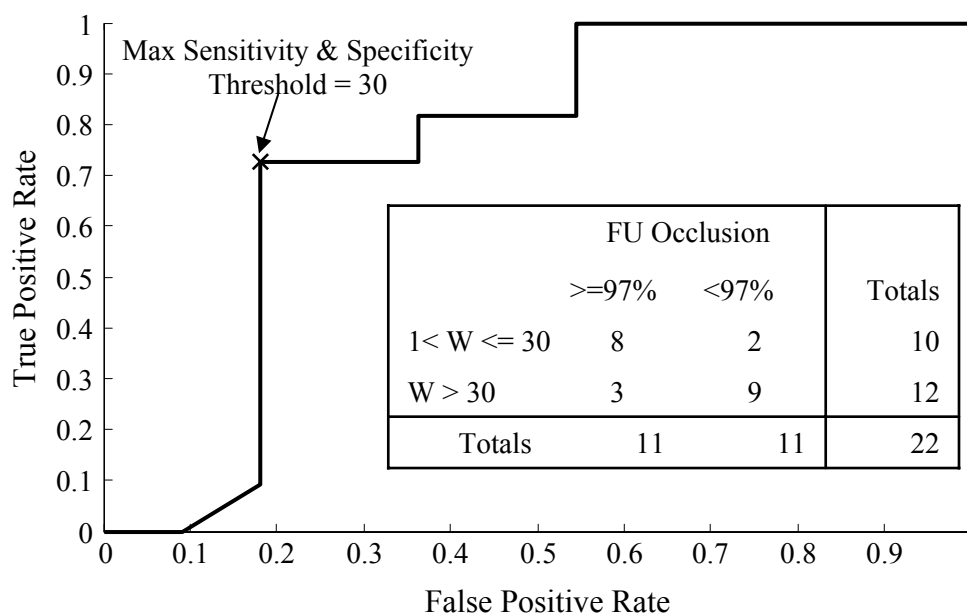
Figure 3-19. The receiver operating characteristic curve for the washout coefficient data grouped based on angiographic aneurysm occlusion at follow-up greater or less than 97%. Inset shows the contingency table based on the threshold value of 30.

The changes in the model parameters, washout curve amplitudes and washout coefficients mentioned above quantify flow exchange alterations immediately after the devices were implanted (PRE to POST). Similar comparisons can be made to quantify changes that occur over the follow-up period by evaluating the percentage ratios of parameters obtained in the FU sequences to the corresponding values in the PRE sequences. Changes in the 3 important model parameters (ρ_{conv}, ρ_{diff}, τ_{diff}), washout curve amplitudes, and washout coefficients are plotted in Figures 3-20 through 3-22. The FU washout curves that were analyzed included 4 sequences from device B (#B_090_2, #B_090_3, #B_180_3 and #B_180_4), 6 from device C (#C_021_1, #C_021_2, #C_090_1, #C_090_2, #C_090_3 and #C_180_4), and 3 from device E (#E_090_3, #E_180_2 and #E_180_3). As the number of samples is small, the parameter values were grouped per device without distinguishing between follow-up time points.

Figure 3-20 shows the changes in the amplitudes of the diffusive (ρ_{diff}) and convective (ρ_{conv}) components of the model from PRE to FU. Changes in the ρ_{diff} values of device C were significantly different from the ρ_{diff} values of device E (t test p = 0.003), while the other pairs show no statistical significance (device B vs. device E, p = 0.25; device B vs. device C, p = 0.67). Changes in the ρ_{conv} values show the same trend (device E vs. device C, p = 0.007; device B vs. device E, p = 0.19; device B vs. device C, p = 0.91). The general trend in device performance was E > B > C based on these two parameters.

Figure 3-20. Mean (standard error) values of amplitudes of the convective (dashed line) and diffusive (solid line) components obtained at follow-up (FU) as a percentage of the corresponding values before device implantation (PRE). $*\rho_{conv}$ and ρ_{diff} values for device E significantly different from those for device C (p=0.007 and 0.003, respectively). Number of samples; device B (n=4), device C (n=6), device E (n=3).

Figure 3-21 shows the variation in the diffusive time constants and the washout curve amplitudes from PRE to FU. Inter-device differences in τ_{diff} values were not statistically significant (ANOVA p = 0.83). The trend in device performance from best to worst was C > B > E based on this parameter. The change in the washout curve amplitude produced by device E was significantly lower than that produced by device C (t test p < 0.001). Differences between devices B and C (p = 0.72) and between devices B and E (p = 0.19) were not statistically significant. In terms of the washout curve amplitudes obtained at FU, device E performed better than device C, which in turn performed better than device B.
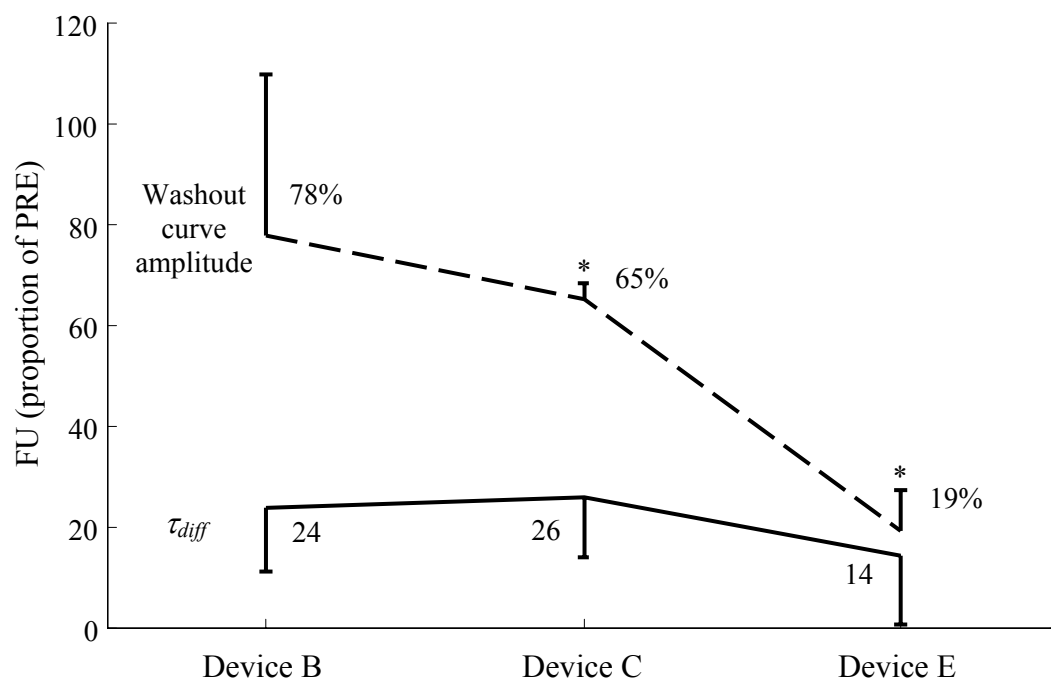
Figure 3-21. Mean (standard error) values of the washout curve amplitudes (dashed line) and time constants of the diffusive components (solid line) obtained at follow-up (FU) as a proportion of the corresponding values before device implantation (PRE). Values for τ_{diff} are in multiples instead of percentages. *Washout curve amplitude for device E significantly lower than that for device C (p<0.001). Number of samples; device B (n=4), C (n=6), E (n=3).

Figure 3-22 shows the goodness of fit of the mathematical model to the washout curve data by plotting the model-fits against the data points. All curves and curve-fits are grouped by treatment phase; PRE (n = 27), POST (n = 27), and FU (n = 13). The line of identity is superposed on the plots along with the 95% confidence intervals. The Pearson correlation coefficient (*r* value) for each of the plots is also included.
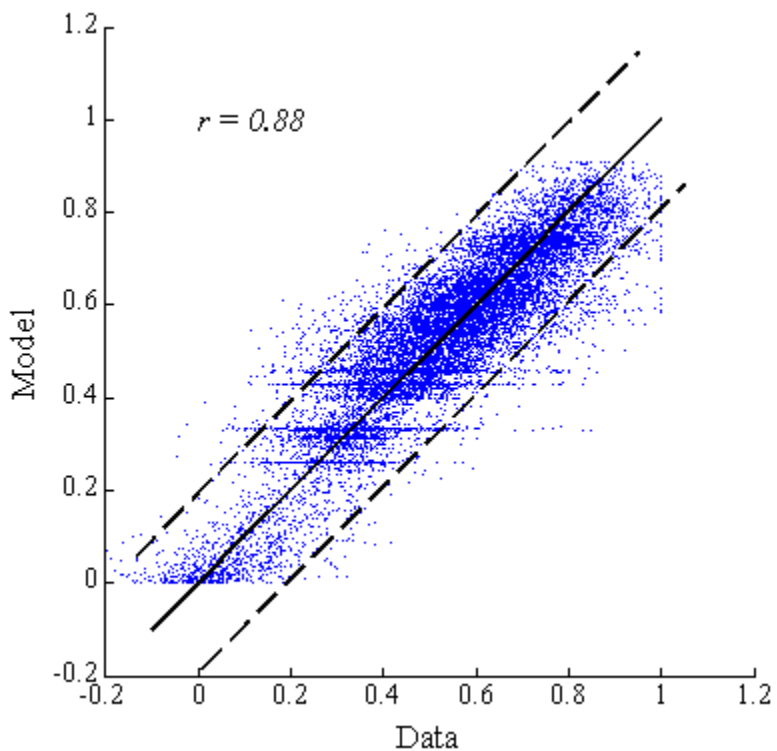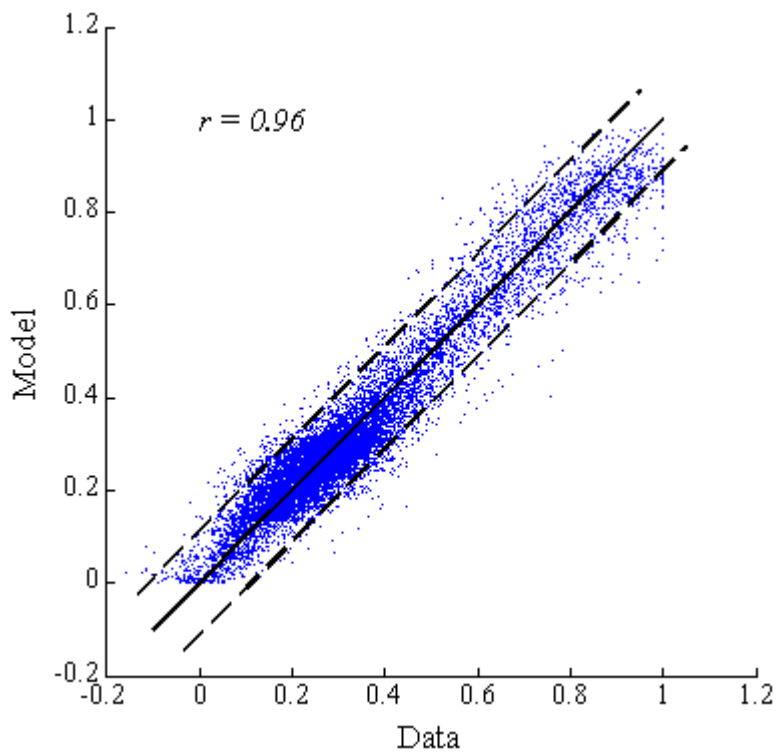
Figure 3-22. Washout curve data versus model-fit (dots) for 27 pre-implant cases (top) and 27 post-implant cases (bottom). The Pearson correlation coefficient between the data and model is given along with the line of identity (solid line) and the 95% confidence intervals (dashed lines).
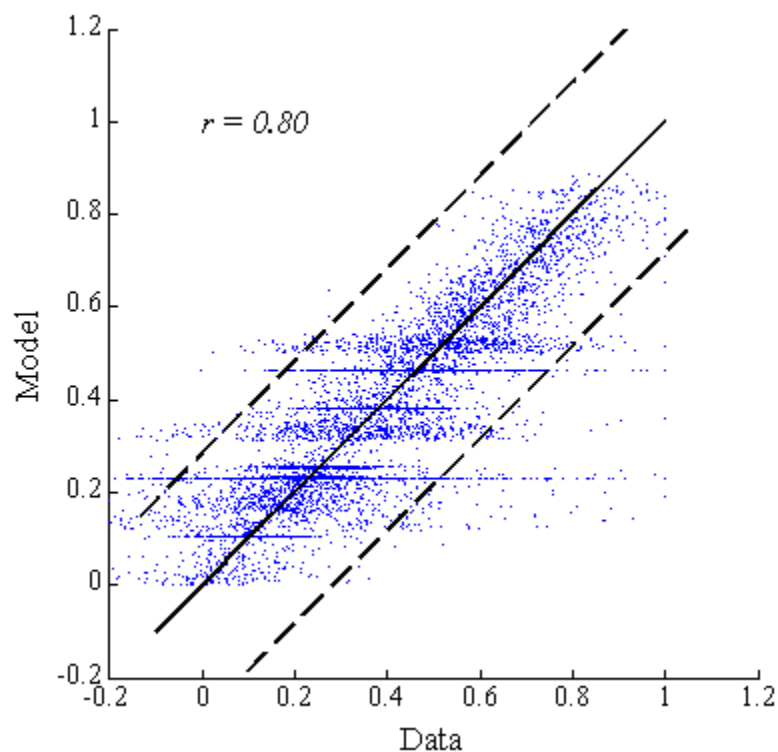
Figure 3-22 (continued). Washout curve data versus model-fit (dots) for 13 follow-up cases. The Pearson correlation coefficient between the data and model is given along with the line of identity (solid line) and the 95% confidence intervals (dashed lines).

Figure 3-23 shows the values of the Kolmogorov-Smirnov statistic (bars) and the Pearson correlation coefficient (lines) of the model-fits for the three treatment phases. The filled bars for the D statistic indicate data-model differences that could not be considered normally distributed at the 5% significance level (15 of 67 curve-fits). All the r and D values are included in Table A1.11 in Appendix 1. The time taken for the computations was highest in those processes requiring the entire angiographic sequence to be processed. Table 3-1 lists the average number of seconds taken to process one angiographic sequence for such steps and the number of sequences on which the averages are based.
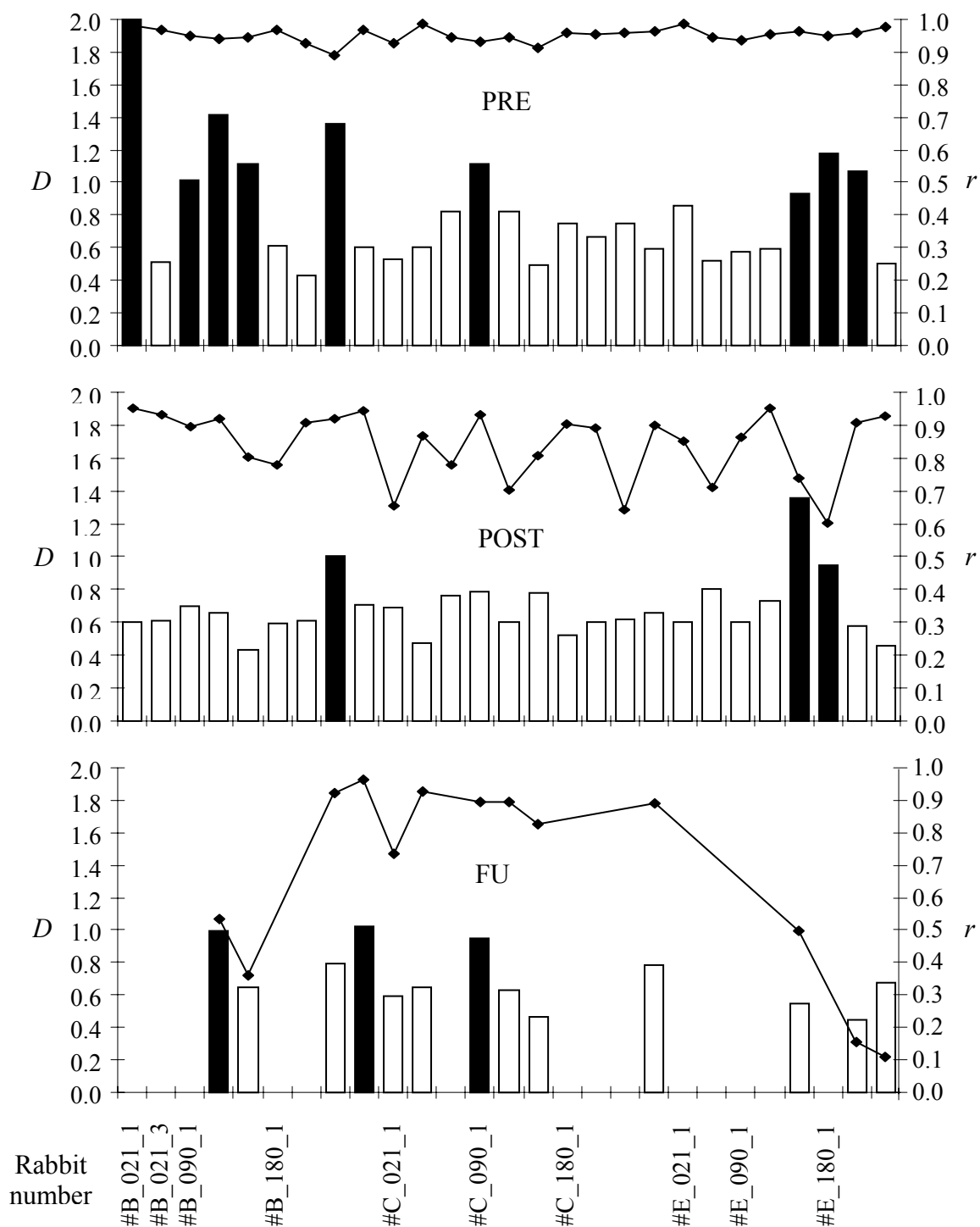
Figure 3-23. Goodness of fit of the mathematical model to the data sets assessed by the Kolmogorov-Smirnov statistic (D, bars) and the Pearson correlation coefficient (r, lines). Cases grouped by treatment phase. Filled bars indicate cases in which the error between the data and model can not be considered to be normally distributed at the 5% level of significance. Rabbit numbers are the same for the 3 plots; sequential numbers are deleted for clarity. Values missing in the follow-up plot indicate cases with no washout curve at this phase (>97% angiographic occlusion of aneurysm).

Table 3-1. Time taken for some of the image processing steps on a 2 GB RAM, 3.2 or 3.4 GHz, Pentium 4, Windows personal computer running Matlab®.

Process	Time taken per sequence (s); mean; standard deviation (S.D.); number of sequences (n)
Image conversion from DICOM to 'tiff'	50.1 s; S.D. ~ 5 s; n = 31
Respiratory rate calculation	~14 s; S.D. ~ 2 s; n = 60
Digital subtraction	141.7 s; S.D. ~ 6 s; n = 22
Calculating subtraction error	88.9 s; S.D. 5 s; n = 75
Washout curve generation	35.1 s; S.D. 1.5 s; n = 53

Table 3-2 lists the indices of device performance and the grades assigned to each device. Highlighted cells indicate the best performing device for the particular index. As can be noted, Device E had the best composite score based on these indices. The performance of the other 2 devices may be expressed relative to the performance of device E. The overall results thus suggest that device E was the best performing device, that device C was about 86% as effective as device E, and that device B was about 79% as effective as device E in treating this set of in vivo aneurysms.

Table 3-2. Composite score of device performance based on 13 indices.

Results group	Performance index	Device B	Device C	Device E
Histology	Neointimal thickness	0.71	0.75	1.00
	Extent of aneurysm occlusion	1.00	0.83	0.91
	Extent of organization of aneurysm contents	0.80	1.00	0.93
Angio graphy	Percentage angiographic aneurysm occlusion	0.86	0.83	1.00
	Percentage arc-to-chord ratio	0.93	0.98	1.00
Washout analysis PRE-to-POST	Percentage washout curve amplitude	0.79	1.00	0.88
	Percentage diffusive component amplitude	0.68	1.00	0.81
	Percentage diffusive component time constant	0.86	0.60	1.00
	Percentage convective component amplitude	0.55	1.00	0.67
Washout analysis PRE-to-FU	Percentage washout curve amplitude	0.25	0.29	1.00
	Percentage diffusive component amplitude	0.60	0.48	1.00
	Percentage diffusive component time constant	0.93	1.00	0.55
	Percentage convective component amplitude	0.35	0.34	1.00
	Total	9.30	10.10	11.75
	Relative Percent Effectiveness	79%	86%	100%

Chapter 4. Discussion

The endovascular treatment of cerebral aneurysms has progressed enough to consider it as the first line of defense against any given aneurysm [100]. The phrase "endovascular treatment of aneurysms" currently implies the deposition of micro-coils into the sac with the goal of establishing complete thrombosis and exclusion of the aneurysm. As long-term results are gathered, however, the initial promise of substantial improvement with coiling as compared to surgical methods has dampened [91, 92] primarily because of two inherently related phenomena. The repeated pulsatile impingement of blood flow against the embolic mass tends to compact it and/or the aneurysm recanalizes as its neck remains exposed to parent artery flow. The placement of a stent within the parent vessel and across the aneurysm neck was proposed as the next treatment measure in order to overcome these drawbacks. Intracranial stents were consequently developed and marketed and short-term results with these devices are now considered promising [97, 98, 195]. The benefit of stents (in addition to the effect of coils), it is noted, is that they reduce the flow within the aneurysms while providing a matrix for neointimal formation [101, 196]. The aneurysm becomes occluded, the stent gets encapsulated within the vessel wall, the aneurysm neck is not "open" to flow any further, and thus successful exclusion of the sac is effected. As the burden of treatment seems to be largely carried by the stents in this conceptual argument, it may be reasonable to question the need for coil deposition within the sac. This line of reasoning (treatment by stents only) was followed by seminal reports in the literature approximately fifteen years ago [103-105]. Preliminary testing of the hypothesis in experimental animals and arbitrarily gathered clinical data suggested that stents could indeed effect successful

aneurysm exclusion of their own accord [103-105, 107-109, 197]. Through the course of these results being accumulated, it has been consistently remarked that commercially available stents did not have the capacity to induce a large enough flow modification within the aneurysm to promote complete aneurysm thrombosis [196]. This is supported by the fact that sometimes, two or three prevalent stents needed to be deployed in order to approach the intra-aneurysmal flow modifications that the ideal device would engender [106, 118]. The characteristics expected of this ideal device have been listed [198]. In contrast to an ideal stent, such a device has low porosity and high pore density values optimized to promote intra-aneurysmal thrombosis while maintaining the parent vessel and perforators patent. Moreover, lower radial forces are required of this device as compared to a stent, which facilitates the optimization of other device characteristics such as longitudinal flexibility, trackability, and conformability. As mentioned, this device would primarily act by diverting flow away from the aneurysm and into the parent artery such that intraaneurysmal flow stasis zones with markedly diminished mass and momentum exchange with the parent artery are created. We have chosen to call such devices "flow divertors" in order to underline the crucial differences in the ideal characteristics of these two treatment approaches (flow divertors and stents). As also mentioned, reports of aneurysm treatment by flow diversion have been sparse and based on stents acting as flow divertors; there are currently no commercially available flow divertors.

The phrase "endovascular treatment of aneurysms" also implies the use of X-ray angiography. Angiography is the gold standard for diagnosing cerebral aneurysms and endovascular treatment is feasible only because of visualization of the vasculature by

injections of angiographic contrast under X-ray radiation. The prognosis of an endovascular treatment for an aneurysm is also currently based on the visualization of angiographic contrast behavior within the aneurysm. Increased intraaneurysmal residence time of blood, which can be considered a true indicator of treatment effectiveness, is qualitatively estimated by increased contrast stasis as visualized within the aneurysm. It is again reasonable to expect that if any such increase in intraaneurysmal flow stasis could be effectively quantified via the imaging method already in employ, a more reliable prognosis could be delivered to the patient. Seminal reports have also appeared over the past decades in the arena of flow quantification via dye-dilution, which suggested that fitting an appropriate mathematical equation to temporally recorded dye-dilution curves can effectively quantify the behavior of the dye and, by inference, of flow [175, 180, 199].

This report attempts to take the next logical step arising from the combination of arguments presented in the previous two paragraphs. An original device intended to act as a flow divertor for the treatment of cerebral aneurysms was implanted in a large cohort of in vivo aneurysms. Three different device configurations filtered through from in vitro [122] and preliminary in vivo [187] studies were employed and the efficacy of the devices was quantified by mathematical modeling of angiographic information. Over all, the results suggest that flow divertors can effectively promote intraaneurysmal thrombosis and stably exclude aneurysms from the circulation over the six month period of assessment. Angiographic quantification allowed for the scoring of device performance and, supplemented by histological data, suggest that the device with the highest pore density performed the best of the three configurations tested. Angiographic

quantification further allowed for the construction of a parameter (the washout coefficient) that could potentially be used as a prognostic indicator of the success of endovascular treatment immediately after the treatment has concluded.

It may be noted here that because only changes in the behavior of intraaneurysmal contrast were modeled, and no absolute conclusions on hemodynamic parameters were drawn, this method of angiographic quantification of device efficacy could be used in any clinical situation involving treatment of aneurysms by flow diversion. Aneurysmal washout curves were normalized and only changes in the model parameters from pre- to post-treatment were used as indices of treatment efficacy. The prerequisite is that injection (catheter position, amount of contrast injected, time for injection) and imaging (source-to-image distance, patient position, C-arm orientation) parameters be kept constant for pre- and post-treatment angiographic sequence acquisition. High-speed acquisitions also improve the validity of the model-fit [116]. These parameters can easily be controlled in current clinical angiographic suites. Angiographic quantification of device performance also requires that contrast enters the aneurysm after device deployment. Clinically, however, if no dye enters the aneurysm after treatment, the prognosis of the treatment is considered to be extremely good. Quantification of device efficacy may not be necessary in these situations. Certain studies have suggested that, especially in cerebral aneurysms, the transport of contrast does not follow the transport of blood. Due to its higher density, contrast is said to settle out of the blood in the gravity direction within aneurysm sacs [200, 201]. This notion has not been borne out by experiments conducted to specifically investigate the mixing of angiographic contrast with blood under conditions similar to most cerebral angiographic acquisitions [202]. The

conclusions drawn in this report based on angiographic information may thus be assumed to reflect changes in blood flow patterns.

The lagged-normal equation was introduced in the literature four decades ago as an appropriate tool for the quantification of dye-dilution curves in the arterial system [180]. Acquisition of angiographic data with high sampling rates imposes a capacity limit on the time period for which images may be acquired and especially in low flow chambers like aneurysms the dye may not completely wash out of the region of interest at the end of the acquisition period. The contrast intensity curve then has residual non-zero amplitude at the end of the sampling period. In the case of aneurysms, this residual amplitude is caused by slow washout of dye possibly due to intraaneurysmal flow zones that exchange dye by mechanisms that approach the process of diffusion in terms of the time. As the lagged-normal distribution does not allow for a nonzero residual at the end of the modeling time period (e.g., dorsalis pedis dye-dilution curve and lagged-normal fit in Figure 1-12b), a second component (diffusive component) was added to account for the different characteristic of aneurysmal washout curves. The average diffusive time constant (approximately 800 seconds) optimized from the washout curves also suggests that this model component represents the process of diffusion. Based on this value of the time constant, the time taken for 95% of the dye to wash out of the aneurysm is about 2400 seconds ($-\log(0.05)\times800$). The diffusion coefficient for liquids ranges from 10^{-8} to 10^{-10} m^2/s [203]. The diffusion length for this process is then about 1.5 mm ($\sqrt{10^{-9}\times2400}$), which is of the same order of any diffusive exchange zone existing within aneurysms. The composite mathematical model used here faithfully captured the trend of all measured aneurysmal washout curves. The goodness of fit of the model was

also good to excellent in most cases (Figure 3-22). In cases where the spread of the error in the data with respect to the model was high (low Pearson correlation coefficient), the Kolmogorov-Smirnov test showed that the data points were randomly distributed about the model. Conversely, in cases where the Kolmogorov-Smirnov test suggested a non-random distribution of the error in data, the Pearson correlation coefficient was high implying a small spread.

The lack of significant differences in the model parameters across the three devices (Figures 3-14, 3-15) may be because of variability inherent in the rabbit elastase-induced aneurysm model. As these are braided self-expanding devices, they adjust to parent vessels with diameters below the device open diameter (4 mm) by elongating. The implanted device porosities may therefore be different from the nominal porosities listed in Table 2-1. An estimation of the implanted device porosities based on angiographic measurements of the device diameters at the aneurysm necks is shown in Figure 4-1. The porosities across the aneurysm necks (B: $68.9\pm0.4\%$; C: $62.8\pm0.4\%$; E: $66.9\pm0.7\%$) are significantly different among the devices, but multiplication with the aneurysm neck area nullifies the significance. The aneurysm dimensions in this study are in the range of dimensions obtained by other investigators [84]. It is possible that a much larger number of animals per group would have been able to detect this effect size and show significant differences across the devices.
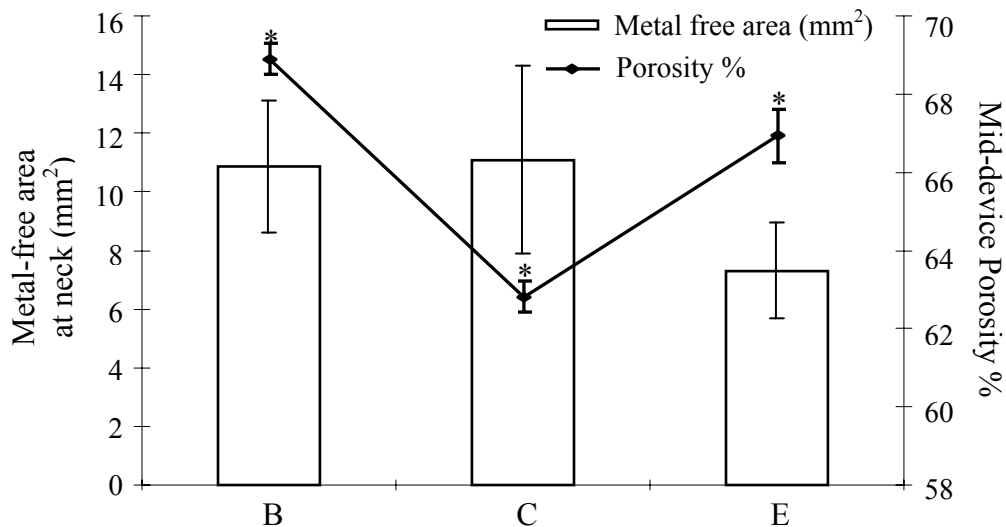
Figure 4-1. Estimates of the porosity of the devices at the neck of the aneurysm and the resulting metal-free area through which flow interacts with the aneurysm. The porosity of the devices at the neck is significantly different across devices (*, $p < 0.03$), but the metal-free area is not ($p > 0.23$).

It may be noted that the porosities and filament diameters used for these devices are not arbitrary and were based on previous experience. Reducing the porosity from 85% to 75% progressively increased the size of the flow stasis zone formed within a sidewall aneurysm [119]. Maintaining the porosity at 75% and increasing the pore density reduced the mean hydrodynamic circulation within the aneurysm [125]. Decreasing the porosity increases the metal-to-artery burden and very low porosities may result in neointimal hyperplasia and in-divertor stenosis. In parallel, very high pore densities may delay re-endothelialization by mitigating endothelial cell migration from between the device struts. There is, therefore, an extent to which porosities may be minimized and pore densities maximized. An empirically observed ratio of device open diameter to artery diameter of < 1.5 seems to protect against hyperplasia [142, 162]. A five to ten percent oversizing of device open diameters ensures proper apposition of the device against the arterial wall and mitigates device migration. Side branches that are "jailed" by meshes are

known to remain patent as long as less than half the branch entrance diameter is covered by the device strut [169]. Perforators, which are side branches of intracranial arteries, range in diameter from about 100μm to 1 mm [167, 168]. Reducing the filament diameter can improve the longitudinal flexibility of a flow divertor. Taking these varied results, the average rabbit innominate artery diameter, and manufacturing capabilities into consideration, the initial flow divertors used in this study were constructed of porosities ranging from 65% to 75% with filament diameters of 1.5 and 2 mil at an open device diameter of 4 mm.

The jailing of perforators by device struts was simulated by implanting the devices across the vertebral artery ostium. This entrance diameter is probably on the higher side of actual perforator ostia, but none of the vertebral arteries were occluded angiographically or histologically through 180 days after device implantation. An in vitro study with these device configurations (same nominal porosity) quantified the maximal reduction of vertebral artery flow to be 15% [122]. The extent to which a coronary stent reduces the curvature of the artery has been found to be a predictor of major adverse cardiac events (death, acute nonfatal myocardial infarction, or revascularization required by angioplasty or bypass grafting) [165]. More sophisticated measures of vessel tortuosity have been defined [190, 204], but the distance metric was judged sufficient for quantifying changes in the single curvature of the rabbit innominate artery due to device implantation. The maximal change in tortuosity that can be withstood by the neurovasculature is not known, but some intracranial stent implantations (Figure 1-7) suggest that, depending on the parent artery, significant alterations in curvature can be safely induced. The percent changes in the distance metric caused by two stents

(Wallstent in Figure 1-7 [116] and Express [111]) implanted in the vertebrobasilar region without any complications were approximately 75% and 89%. The changes induced by all three flow divertors in the rabbit innominate artery are within this range (Figure 3-11). Moreover, a recent study reports the deliberate use of coronary stents to straighten out superior cerebellar arteries that carried aneurysms in order to treat the aneurysms by flow diversion [112].

The sensitivity of the prognostic test for success of aneurysm treatment based on the washout coefficient (73%) is probably not high enough to guide clinical course of management. The true negative rate (82%) is less crucial because if the aneurysm actually occludes after the test predicts that it will not ($W > 30$), there is negligible loss in patient care. The physician may choose to take additional treatment steps (multiple divertors or coiling) if the test is negative. In either case, the test can at least supplement the physician's experience in evaluating the next course of action. As mentioned previously, the optimization of the washout curves and calculation of the washout coefficient can easily be performed immediately after device deployment, while the patient is on the angiographic table. This test is also based on a data set of experimental aneurysms and its validity will have to be evaluated on large sets of clinical data. In its current form, the test cannot predict success rates for cases with the washout coefficient value at or below 1 although 3 out of 5 cases with $W <= 1$ had greater than 97% angiographic occlusion at follow-up. Because occlusion percentages are grouped over the follow-up times, the test only predicts treatment success at 180 days (longest follow-up time). Computational fluid dynamics studies simulating flow alterations due to divertor treatment of minimally-idealized aneurysm geometries [128] can be used to improve the

success rate of the test. Angiographic aneurysmal washout curves obtained from 2 clinical cases suggest the feasibility of this test and the importance of the availability of such a test. Aneurysmal washout curve quantification of 1 vertebro-basilar aneurysm immediately after coronary stent placement shows the W value to be about 5. At 3 months follow-up, this aneurysm was completely occluded (Figure 1-7) [116]. The W value for another case with a similar aneurysm and similar stent was around 2, suggesting that the aneurysm may have thrombosed after stent deployment. Under visual observation of the stasis of contrast, however, a single stent was deemed to be not sufficient and the implantation of a second, concentric stent was attempted. The patient died during the course of implantation of the second stent [116].

The average percentage angiographic occlusion immediately after device implantation (A_{POST} %, Eq. 2-2) that resulted in >=97% aneurysm occlusion at follow-up (A_{FU} %, Eq. 2-2) was also significantly higher than the A_{POST} % that resulted in <97% A_{FU}. This suggests that this parameter might in itself provide a prognostic test for long-term treatment success. The threshold value of such a test was 37% (A_{POST} >= 37% results in >= 97% aneurysm occlusion at follow-up) based on this data set with low sensitivity and specificity of 70%. Fisher's exact test also suggested that the row column association was not significant (p=0.06). Again, the relative superiority (or inferiority) of this test (A_{POST} >= 37%) over the test based on the washout coefficient ($1 < W <= 30$) will have to be judged based on large sets of clinical data or benchtop and numerical studies. At the very least, these two thresholds can be currently employed as estimates of the long-term success of flow divertors being tested in the rabbit elastase-induced aneurysm model.

In one animal (#E_180_4), the parent artery was dilated past the open device diameter and this case had to be excluded from the analysis. Such fusiform dilations of the parent artery (innominate) are known to occur during the creation of elastase-induced aneurysms in the rabbit, presumably because of trace elastase leakage around the occlusion balloon [205]. Fusiform dilation at the aneurysm was also observed in three other cases (#B_180_3, #C_090_2, and #C_090_3), where the flow divertors effected 25% to 50% angiographic occlusion of the aneurysm at follow-up. In one of these cases (#C_090_2), the parent artery was also dilated, and this fusiform shape was completely occluded at follow-up. Experimental [197] and clinical [116] evidence suggest that fusiform aneurysms can be successfully treated with flow divertors. Further testing of these flow divertors in fusiform aneurysms is required in order to draw conclusions as to their effectiveness in these geometries.

In 5 cases (#B_021_1, #B_021_2, #B_021_3, #B_090_2, #E_090_1) mild to moderate delayed filling of the subclavian artery was noted. Calculation of the proximal to distal diameter ratios of all implanted devices showed that these 5 cases had amongst the highest ratios (Table A1.12, Appendix 1). A histological section at the aneurysm treated with the device with the highest "conicity" (proximal to distal diameter ratio = 2.13; Figure 4-2) showed sub-total thrombosis of the parent artery [206]; angiographically, the distal subclavian was noted to be filling even in this case. As mentioned, increased thrombus burden and subsequent neointimal hyperplasia are known to occur when the stent-to-artery diameter ratios are high [162]. It may be noted that the divertors were sized to fit the innominate-to-subclavian artery of the animals, but the rabbit subclavian artery is known to taper significantly towards the distal portion. There
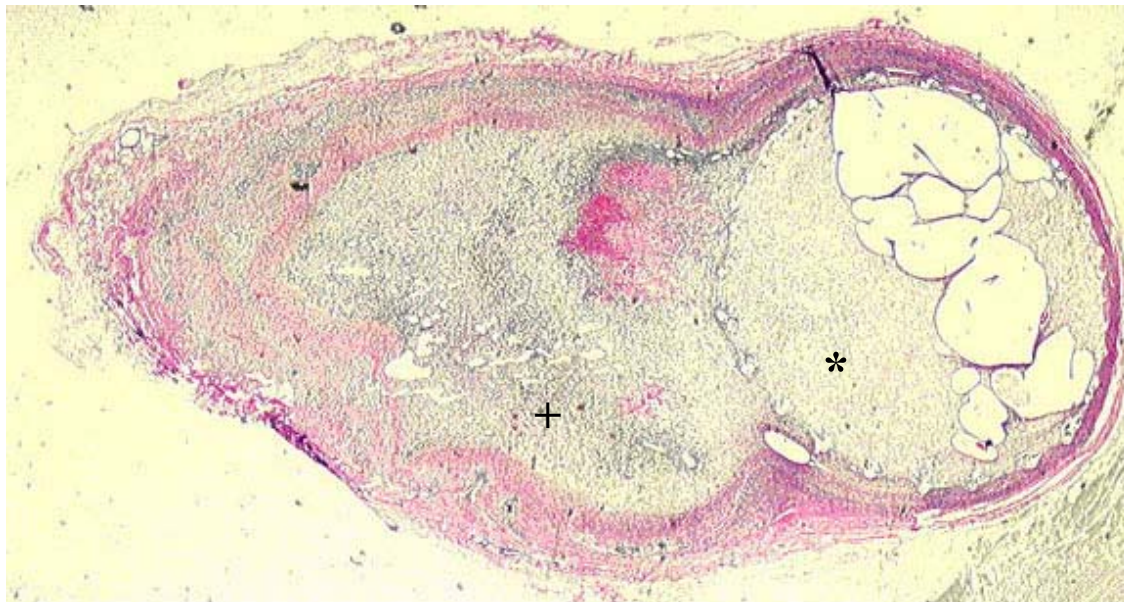
Figure 4-2. Section at the aneurysm for the case (#B_021_1) with the highest proximal-to-distal device diameter ratio (2.13) showing subtotal occlusion of the parent vessel. Delayed filling of the subclavian artery was angiographically noted at follow-up time. * Parent artery; + aneurysm; from Rakian A [206].

were no notable complications from parent vessel occlusion in any of these animals. Cerebral arteries, however, have less elastica and thicker media, making them stiffer and their response to high stent-to-artery ratios may be different than that of the subclavian artery. Such delayed filling or ischemic complications would also be of much greater concern in the intracranial vasculature. One of the commercially available intracranial stents (Neuroform) has been noted to induce moderate to severe stenosis of parent vessels in about 6% of cases [207].

Angiographic quantification was supplemented by histological results to assess device performance. In essence, the histomorphometric aneurysm occlusion score matched the percentage angiographic aneurysm occlusion rates except for one case (#C_180_2). The angiographic occlusion was noted to be 100% in this case, whereas the histology showed a sac that was only more than half-filled (occlusion score of 2). Although there were no significant differences in the degree of organization of the

aneurysm samples processed thus far, the sections from the 90 and 180 day samples show further maturity of the intraaneurysmal thrombus as organized connective tissue when compared with the 21 day samples. This organized connective tissue is maintained by a network of neovessels (e.g., sections from #C_180_1 and #E_090_2 in Appendix 3). Neovascularization of organized neointima is thought to originate from the vasa vasorum [136] and a similar process may be presumed to occur within aneurysms. Unless the process of aneurysm initiation is solely via the interaction of biochemical mediators transported by the blood and the local vessel wall, it seems unlikely that these neovessels make the organized aneurysm contents susceptible to recanalization. In other sections, however, there were channels formed within the aneurysm that seemed to be endothelialized (e.g., sections from #E_090_1, #E_090_2, #E_180_1 in Appendix 3) suggesting that these channels were connected to the parent vessel flow. Such formations have been noted before during the embolization of experimental aneurysms and are believed to occur by the migration of cells from the original endothelial layer covering the aneurysm wall [208]. The formation of endothelialized slits between the wall of the aneurysm and the embolic material within a week of embolization [209] bears a striking resemblance to endothelial lined clefts seen to extend from the luminal surface into developing mural thrombi 8 days after intimal abrasion [144]. The process seems to require the presence of the fibrin matrix within an immature clot and once the clot organizes into connective tissue, such channels do not form [208]. Although the role of circulating endothelial progenitor cells trapped within the initial thrombus [210] cannot be excluded, the fact that endothelial denudation of the aneurysm wall by mechanical scraping precludes the formation of these channels strongly suggests that cell migration
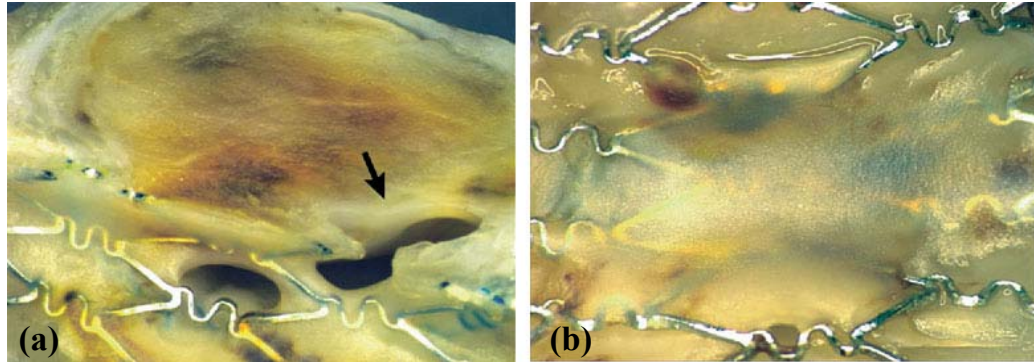
Figure 4-3. En face views of the necks of venous pouch aneurysms after stent implantation with (a) and without (b) endothelial denudation of the aneurysm wall. Channels from the parent artery into the aneurysm are seen in the former case (arrow), but not in the latter; from Darsaut et al. [211].

from the wall is the underlying cause [208, 209]. Scraping the endothelial lining of venous pouch aneurysms before parent vessel stenting has also shown a 4 times greater aneurysm occlusion rate as compared to stenting only without denudation [211]. The aneurysm contents with denudation were more organized than without and there were no channels into the aneurysm from the parent vessel in the former cases, whereas these channels were observed in the latter cases (Figure 4-3) [211]. Further studies will have to be conducted to characterize the intraaneurysmal channels observed in this report, but these channels were always adjacent to the aneurysm walls.

The intraaneurysmal thrombus near the walls of the aneurysm seemed to be further organized as compared to the central regions (e.g., section from #E_021_3 in Appendix 3) similar to observations by others [212]. More than three-quarters of the luminal surface of all devices was noted to be lined with endothelial cells on all histological sections at all follow-up time points, which is evidence of minimal injury to the arterial wall produced by these self-expanding devices. The neointimal thicknesses (100-200 μm) were similar to those obtained with a stent in the rabbit carotid artery [213]

and in the lower ranges of those observed in other experimental species [151, 157]. Further, the neointimal thickness did not change significantly over the follow-up period of three weeks to six months. These results suggest stable incorporation of the flow divertor within the arterial lumen within a few weeks.

A group of investigators from Aachen, Germany have investigated the treatment of rabbit elastase-induced aneurysms using a laser cut high grade stainless steel balloon-expandable stent (Aachen Resonance Flex). They report complete angiographic occlusion of 14 out of 20 aneurysms immediately after stent implantation, and 2/5, 4/5, and 1/5 complete angiographic occlusions at 1 month, 3 months, and 6 months, respectively [214-216]. Histological results showed up to 40% in-stent stenosis at 6 months [215]. The porosity and filament diameter of the device are not provided, but the image provided [216] suggests a high porosity (~80%), thick filament (~150 μm) device. The relatively poor occlusion rates obtained may thus be because the device was not intended to be a flow divertor and the requirement for balloon-expansion may explain the relatively high neointimal thicknesses. The treatment of rabbit elastase-induced aneurysms with two new devices that are intended to act as flow divertors has been recently introduced in the literature. The first device (JOTEC Gmbh, Hechingen, Germany) is braided out of 24 Nitinol filaments of 48 μm diameter and has a central zone (~70% of stent length) with much tighter braiding and pore areas of approximately 4×10^{-3} mm^2. Implantation of this device in 1 animal is reported to have caused angiographic occlusion of the aneurysm at 45 minutes, 2 weeks, and 1 month post-treatment [186]. Histology on the tissue at 1 month shows thrombus filling the aneurysm and side-branch patency. It is not noted whether the patent side branch was jailed by the tighter mesh portion of the device.

Moreover, the dimensions of the aneurysm in their study seem to be approximately the same as the small control aneurysm that spontaneously thrombosed by 51% at 21 days in this report. Further experimental evidence is required to evaluate the efficacy this device. The second device (Pipeline Neuroendovascular Device, Chestnut Medical Technologies, Menlo Park, CA) consists of 16 platinum and 16 stainless steel filaments that are braided to a 70% porosity. The filament diameter is not available. The treatment of 17 rabbit elastase-induced aneurysms with this device showed complete to near-complete angiographic occlusion in 5 of 6, 5 of 5, and 5 of 6 aneurysms followed-up at 1 month, 3 months, and 6 months, respectively [185]. Jailed vertebral arteries were patent in all cases. Average neointimal thicknesses were 100 μm to 200 μm at all follow-up time points. Histological sections of the aneurysm showed acute unorganized thrombus at the dome in all animals at 1 month, poorly organized thrombus in 3/4 animals and organized connective tissue in 1/4 animals at 3 months, and poorly organized thrombus in 4/6 and organized connective tissue in 2/6 animals at 6 months. Aneurysm contents were thus completely organized in 0%, 25%, and 33% of animals at 1, 3, and 6 months, respectively. By comparison, the flow divertors used in this report resulted in complete organization of aneurysm contents in 50% (2/4), 40% (2/5), and 50% (3/6) of cases at 3 weeks, 3 months, and 6 months, respectively. The flow divertors seem to perform better than the Pipeline device based on these numbers. Neointimal thicknesses within both devices (flow divertor and Pipeline) are in the same range. The authors of the Pipeline study, however, report cartilaginous and bone-like transformation of tissue around device struts; no such formations were observed around the flow divertor struts. Further studies specifically aimed at device comparisons are required to judge the equivalency of these

flow divertors and the Pipeline device, but the reduced organization of the aneurysm contents with the Pipeline device may be explained by differences in pore density. To note, the authors report organization at the aneurysm dome, but not all histological sections with the flow divertor were at the aneurysm dome. Initial clinical results with the Pipeline device have also been reported [184]. In treating 9 aneurysms successfully, 2 overlapping devices were used in 2 patients, 3 overlapping devices were used in 1 patient, 4 overlapping devices were used in another patient, and additional loose coil packing was performed in 6 patients. Immediately after treatment, the angiographic occlusion rate was 56% (5/9 cases). Presumably, additional coiling was performed through the stent struts, which again suggests that the pore sizes of the Pipeline device are much larger than what would be expected of an optimal flow divertor. Further, because angiographic quantification was not performed like in this report, the placement of additional devices may have been unnecessary. If prognosis could be established with sufficient precision based on angiographic quantification, repeated device implantations to force 100% angiographic occlusion at the time of treatment would not be required.

The pore density of flow divertors seems to be an important factor modulating the efficacy of the devices. Presumably, the finer meshes implied by

Figure 4-4. Pore density of the three devices plotted against the composite performance score (see Table III-2).
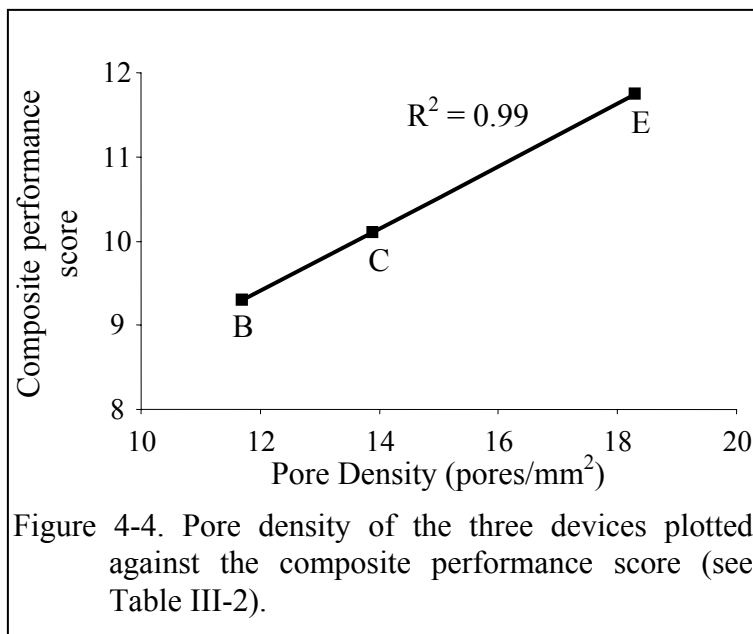
higher pore densities further stratify the flow exchange (flow movement perpendicular to the mesh) between the parent vessel and the aneurysm, which leads to delayed washout of blood and increased probability of intraaneurysmal thrombosis. Although there were only three different pore densities used in this report, Figure 4-4 shows a strong linear correlation between device pore density and the device composite performance score (Table 3-2).

In this report, the flow divertor with a porosity of 70%, filament diameter of 38 μm, and pore density of 18 pores/mm^2 (device E) was found to perform better than devices with 70% porosity, 51 μm filament diameter, 12 pores/mm^2 (device B) and 65% porosity, 51 μm filament diameter, 14 pores/mm^2 (device C) in successfully and stably occluding elastase-induced aneurysms in rabbits. However, two factors that act to confound these results should be mentioned. First, histological sections show a significantly lower parent artery diameter in the samples implanted with device E as compared to the other 2 devices (Figure 3-4) and the average ratios of the intimal to medial areas were not statistically significant across the three devices (device B: 0.7±0.1; device C: 0.7±0.05; device E: 0.7±0.05; ANOVA p=0.9). Thus, although the thinner filament diameter of device E may be expected to cause lesser local flow disturbances and result in lower thrombus formation, the results from the samples processed suggest that it does not produce a much lower neointimal burden given the same degree of arterial wall exposure. Device E also exerts lower radial forces than devices B and C due to it construction; arteries implanted with devices B and C may thus have expanded to a larger diameter compared to those implanted with device E. Second, the average height of the aneurysms treated with device E was longer than the height of the aneurysms treated with

devices B and C while the respective neck widths were not statistically different. With the overly-dilated parent artery case (#E_180_4) removed, the p values from the Student's t tests comparing the heights were 0.06 (device E versus B) and 0.03 (device E versus C). Larger aneurysms are known to have a higher possibility of thrombosis due to increased sizes of flow stasis zones and the higher aspect ratio may thus have helped produce the higher aneurysm occlusion rates seen with device E. This increase in height was, however, only 20% and its effect on promoting thrombosis is difficult to quantify.

If the neointimal thicknesses and the aneurysm occlusion rates were removed from consideration in generating the composite performance score (Table 3-2), device E still performs the best, with device B being 76% as effective as device E, and device C being 87% as effective. In a particle image velocimetry study conducted to assess the initial six flow divertor configurations [122], changes in intraaneurysmal flow dynamics due to the divertors were quantified by using four parameters: peak hydrodynamic circulation, mean hydrodynamic circulation, peak kinetic energy, and mean kinetic energy. A composite score of performance could be generated based on those results similar to the one used here to compare devices B, C, and E. Even in that study, device E performed better in reducing intra-aneurysmal flow activity, with both the other devices being 73% as effective as device E. Therefore, the overall results strongly suggest that the device E configuration is superior to all other configurations considered and should be the flow divertor chosen to proceed with any further trials or experimentation.

Chapter 5. CONCLUSIONS

Treatment modalities for cerebral aneurysms are currently far from optimal. Endovascular treatment methods are rapidly growing in sophistication whereas surgical methods have more or less reached maturity. The concept of successful cerebral aneurysm treatment by flow diversion was proffered more than fifteen years ago, but clinical implementation of this method is still in its incipient stages. Driven by the recent availability of flexible stents for the intracranial vasculature, the past couple of years have seen increasing clinical device implantations across pseudo- and small aneurysms with the intent of treatment by flow diversion. In so far as the design of flow divertors has to optimize the induction of flow stasis zones within aneurysms and not be concerned about scaffolding strengths, devices available in the clinical arena thus far are lacking. The experimental testing of two new devices designed to be flow divertors over the past year indicates a growing acceptance of this treatment method. Due to their mechanism of action, flow divertors may not induce complete angiographic occlusion of aneurysms immediately after deployment; yet, they may favorably alter the prevailing hemodynamics and cause complete aneurysm thrombosis over a period of days to weeks that eventually stabilizes the parent vessel to physiological states.

In this report, three novel flow divertor design configurations developed based on past experience were tested in a large cohort of experimental aneurysms. Successful and stable aneurysm occlusion was effected by the flow divertors over the study period of six months. Quantification of device performance via angiographic means allowed for the selection of the best device configuration tested. Results suggest that the device with a porosity of 70%, filament diameter of 38 μm, and pore density of 18 pores/mm^2

112

performed better than devices of 65% porosity, 51 μm filament diameter, 14 pores/mm^2

and 70% porosity, 51 μm filament diameter, 12 pores/mm^2 with relative efficacies of

100%, 86%, and 79%, respectively. The pore density of flow divertors was seen to be a

critical factor modulating treatment success. Further refinement of the best device by

decreasing its filament diameter and concomitantly maximizing its pore density to an

optimum value may lead to yet superior success rates. Angiographic quantification

further suggested a parameter, called the washout coefficient here, which could be

employed to estimate aneurysm occlusion probabilities immediately after the treatment

and thus preclude unnecessary additional treatment manipulations. Based on the

aneurysms treated and the devices used, a value of this parameter less than 30 predicts

greater than 97% angiographic occlusion of the aneurysm over a period of six months.

Generalization of this threshold value to the treatment of any given aneurysm by flow

diversion requires further testing.

REFERENCES

1. Rosamond W, Flegal K, Friday G, Furie K, Go A, Greenlund K, Haas N and et al. Heart Disease and Stroke Statistics - a 2007 update. A report from the American Heart Association Statistics Committee and Stroke Statistics Subcommittee. Circulation. 2007; 115:e69-e171

2. Mackay J, Mensah GA, Mendis S and Greenlund K. The atlas of heart disease and stroke. 2004

3. de Rooij NK, Linn FH, van der Plas JA, Algra A and Rinkel GJ. Incidence of subarachnoid haemorrhage: a systematic review with emphasis on region, age, gender and time trends. J Neurol Neurosurg Psychiatry. 2007 Dec; 78: 1365-72

4. Wardlaw JM and White PM. The detection and management of unruptured intracranial aneurysms. Brain. 2000 Feb; 123 (Pt 2): 205-21

5. Rinkel GJ, Djibuti M, Algra A and van Gijn J. Prevalence and risk of rupture of intracranial aneurysms: a systematic review. Stroke. 1998 Jan; 29(1): 251-6

6. Brisman JL, Song JK and Newell DW. Cerebral aneurysms. N Engl J Med. 2006 Aug 31; 355(9): 928-39

7. Wiebers DO. Unruptured intracranial aneurysms: natural history and clinical management. Update on the international study of unruptured intracranial aneurysms. Neuroimaging Clin N Am. 2006 Aug; 16(3): 383-90

8. Hop JW, Rinkel GJ, Algra A and van Gijn J. Case-fatality rates and functional outcome after subarachnoid hemorrhage: a systematic review. Stroke. 1997 Mar; 28(3): 660-4

9. Wijdicks EF, Kallmes DF, Manno EM, Fulgham JR and Piepgras DG. Subarachnoid hemorrhage: neurointensive care and aneurysm repair. Mayo Clin Proc. 2005 Apr; 80(4): 550-9

10. Al-Shahi R, White PM, Davenport RJ and Lindsay KW. Subarachnoid haemorrhage. BMJ. 2006 Jul 29; 333(7561): 235-40

11. Weller RO. Subarachnoid haemorrhage and myths about saccular aneurysms. J Clin Pathol. 1995 Dec; 48(12): 1078-81

12. Zhang B, Fugleholm K, Day LB, Ye S, Weller RO and Day IN. Molecular pathogenesis of subarachnoid haemorrhage. Int J Biochem Cell Biol. 2003 Sep; 35(9): 1341-60

13. Ruigrok YM, Buskens E and Rinkel GJ. Attributable risk of common and rare determinants of subarachnoid hemorrhage. Stroke. 2001 May; 32(5): 1173-5

14. Feigin VL, Rinkel GJ, Lawes CM, Algra A, Bennett DA, van Gijn J and Anderson CS. Risk factors for subarachnoid hemorrhage: an updated systematic review of epidemiological studies. Stroke. 2005 Dec; 36(12): 2773-80

15. Juvela S. Prehemorrhage risk factors for fatal intracranial aneurysm rupture. Stroke. 2003 Aug; 34(8): 1852-7

16. Findlay JM. Editorial comment--Prehemorrhage risk factors for fatal intracranial aneurysm rupture. Stroke. 2003 Aug; 34: 1857-8

17. White PM and Wardlaw J. Unruptured intracranial aneurysms: prospective data have arrived. Lancet. 2003 Jul 12; 362(9378): 90-1

18. Hademenos GJ, Massoud TF, Turjman F and Sayre JW. Anatomical and morphological factors correlating with rupture of intracranial aneurysms in patients referred for endovascular treatment. Neuroradiology. 1998 Nov; 40: 755-60

19. Nader-Sepahi A, Casimiro M, Sen J and Kitchen ND. Is aspect ratio a reliable predictor of intracranial aneurysm rupture? Neurosurgery. 2004 Jun; 54: 1343-7

20. Ujiie H, Tamano Y, Sasaki K and Hori T. Is the aspect ratio a reliable index for predicting the rupture of a saccular aneurysm? Neurosurgery. 2001 Mar; 48: 495-502

21. Krex D, Schackert HK and Schackert G. Genesis of cerebral aneurysms--an update. Acta Neurochir (Wien). 2001; 143(5): 429-48

22. Leblanc R. De novo formation of familial cerebral aneurysms: case report. Neurosurgery. 1999 Apr; 44: 871-6

23. Stober T, Sen S, Anstatt T, Freier G and Schimrigk K. Direct evidence of hypertension and the possible role of post-menopause oestrogen deficiency in the pathogenesis of berry aneurysms. J Neurol. 1985; 232: 67-72

24. Chyatte D, Chen TL, Bronstein K and Brass LM. Seasonal fluctuation in the incidence of intracranial aneurysm rupture and its relationship to changing climatic conditions. J Neurosurg. 1994 Oct; 81: 525-30

25. Suzuki J and Ohara H. Clinicopathological study of cerebral aneurysms. Origin, rupture, repair, and growth. J Neurosurg. 1978 Apr; 48: 505-14

26. Kataoka K, Taneda M, Asai T, Kinoshita A, Ito M and Kuroda R. Structural fragility and inflammatory response of ruptured cerebral aneurysms. A comparative study between ruptured and unruptured cerebral aneurysms. Stroke. 1999 Jul; 30(7): 1396-401

27. Frosen J, Piippo A, Paetau A, Kangasniemi M, Niemela M, Hernesniemi J and Jaaskelainen J. Remodeling of saccular cerebral artery aneurysm wall is associated with rupture: histological analysis of 24 unruptured and 42 ruptured cases. Stroke. 2004 Oct; 35: 2287-93

28. Kilic T, Sohrabifar M, Kurtkaya O, Yildirim O, Elmaci I, Gunel M and Pamir MN. Expression of structural proteins and angiogenic factors in normal arterial and unruptured and ruptured aneurysm walls. Neurosurgery. 2005 Nov; 57(5): 997-1007

29. Chyatte D and Lewis I. Gelatinase activity and the occurrence of cerebral aneurysms. Stroke. 1997 Apr; 28(4): 799-804

30. Todor DR, Lewis I, Bruno G and Chyatte D. Identification of a serum gelatinase associated with the occurrence of cerebral aneurysms as pro-matrix metalloproteinase-2. Stroke. 1998 Aug; 29(8): 1580-3

31. Bruno G, Todor R, Lewis I and Chyatte D. Vascular extracellular matrix remodeling in cerebral aneurysms. J Neurosurg. 1998 Sep; 89(3): 431-40

32. Caird J, Napoli C, Taggart C, Farrell M and Bouchier-Hayes D. Matrix metalloproteinases 2 and 9 in human atherosclerotic and non-atherosclerotic cerebral aneurysms. Eur J Neurol. 2006 Oct; 13(10): 1098-105

33. Kim SC, Singh M, Huang J, Prestigiacomo CJ, Winfree CJ, Solomon RA and Connolly ES Jr. Matrix metalloproteinase-9 in cerebral aneurysms. Neurosurgery. 1997 Sep; 41(3): 642-66

34. Aoki T, Kataoka H, Morimoto M, Nozaki K and Hashimoto N. Macrophage-derived matrix metalloproteinase-2 and -9 promote the progression of cerebral aneurysms in rats. Stroke. 2007 Jan; 38(1): 162-9

35. Lehoux S, Tronc F and Tedgui A. Mechanisms of blood flow-induced vascular enlargement. Biorheology. 2002; 39(3-4): 319-24

36. Gaetani P, Rodriguez y Baena R, Tartara F, Messina AL, Tancioni F, Schiavo R and Grazioli V. Metalloproteases and intracranial vascular lesions. Neurol Res. 1999 Jun; 21(4): 385-90

37. Connolly ES Jr, Fiore AJ, Winfree CJ, Prestigiacoma CJ, Goldman JE and Solomon RA. Elastin degradation in the superficial temporal arteries of patients with

intracranial aneurysms reflects changes in plasma elastase. Neurosurgery. 1997 May; 40(5): 903-8

38. Gaetani P, Tartara F, Tancioni F, Klersy C, Forlino A and Baena RR. Activity of alpha 1-antitrypsin and cigarette smoking in subarachnoid haemorrhage from ruptured aneurysm. J Neurol Sci. 1996 Sep; 141: 33-8

39. Kassam AB, Horowitz M, Chang YF and Peters D. Altered arterial homeostasis and cerebral aneurysms: a molecular epidemiology study. Neurosurgery. 2004 Jun; 54(6): 1450-60

40. Nahed BV, Bydon M, Ozturk AK, Bilguvar K, Bayrakli F and Gunel M. Genetics of intracranial aneurysms. Neurosurgery. 2007 Feb; 60: 213-25

41. Krischek B and Inoue I. The genetics of intracranial aneurysms. J Hum Genet. 2006; 51(7): 587-94

42. Ruigrok YM, Rinkel GJ and Wijmenga C. Genetics of intracranial aneurysms. Lancet Neurol. 2005 Mar; 4(3): 179-89

43. Ruigrok YM, Rinkel GJ, van't Slot R, Wolfs M, Tang S and Wijmenga C. Evidence in favor of the contribution of genes involved in the maintenance of the extracellular matrix of the arterial wall to the development of intracranial aneurysms. Hum Mol Genet. 2006 Nov 15; 15(22): 3361-8

44. Peters DG, Kassam AB, Feingold E, Heidrich-O'Hare E, Yonas H, Ferrell RE and Brufsky A. Molecular anatomy of an intracranial aneurysm: coordinated expression of genes involved in wound healing and tissue remodeling. Stroke. 2001 Apr; 32(4): 1036-42

45. Helgadottir A, Thorleifsson G, Magnusson KP, Gretarsdottir S, Steinthorsdottir V, Manolescu A and et al. The same sequence variant on 9p21 associates with myocardial infarction, abdominal aortic aneurysm and intracranial aneurysm. Nat Genet. 2008 Feb; 40: 217-24

46. Norrgard O, Angqvist KA, Fodstad H, Forssell A and Lindberg M. Co-existence of abdominal aortic aneurysms and intracranial aneurysms. Acta Neurochir (Wien). 1987; 87: 34-9

47. Stehbens WE. Pathology and pathogenesis of intracranial berry aneurysms. Neurol Res. 1990 Mar; 12(1): 29-34

48. Stehbens WE. Histopathology of cerebral aneurysms. Arch Neurol. 1963 Mar; 8: 272-85

49. Stehbens WE. Etiology of intracranial berry aneurysms. J Neurosurg. 1989 Jun; 70(6): 823-31

50. Ferguson GG. Physical factors in the initiation, growth, and rupture of human intracranial saccular aneurysms. J Neurosurg. 1972 Dec; 37(6): 666-77

51. Burleson AC and Turitto VT. Identification of quantifiable hemodynamic factors in the assessment of cerebral aneurysm behavior. Thromb Haemost. 1996 Jul; 76(1): 118-23

52. Ingebrigtsen T, Morgan MK, Faulder K, Ingebrigtsen L, Sparr T and Schirmer H. Bifurcation geometry and the presence of cerebral artery aneurysms. J Neurosurg. 2004 Jul; 101(1): 108-13

53. Steiger HJ. Pathophysiology of development and rupture of cerebral aneurysms. Acta Neurochir Suppl (Wien). 1990; 48: 1-57

54. Kurokawa T, Harada K, Ishihara H, Fujisawa H, Kato S, Kajiwara K and Suzuki M. De novo aneurysm formation on middle cerebral artery branches adjacent to the anastomotic site of superficial temporal artery-middle cerebral artery bypass surgery in two patients: technical case report. Neurosurgery. 2007 Nov; 61: E297-8

55. Perktold K, Gruber K, Kenner T and Florian H. Calculation of pulsatile flow and particle paths in an aneurysm-model. Basic Res Cardiol. 1984 May-Jun; 79(3): 253-61

56. Gonzalez CF, Cho YI, Ortega HV and Moret J. Intracranial aneurysms: flow analysis of their origin and progression. AJNR Am J Neuroradiol. 1992 Jan-Feb; 13(1): 181-8

57. Castro MA, Putman CM and Cebral JR. Patient-specific computational modeling of cerebral aneurysms with multiple avenues of flow from 3D rotational angiography images. Acad Radiol. 2006 Jul; 13(7): 811-21

58. Liou TM, Li YC and Juan WC. Numerical and experimental studies on pulsatile flow in aneurysms arising laterally from a curved parent vessel at various angles. J Biomech. 2007; 40(6): 1268-75

59. Strother CM, Graves VB and Rappe A. Aneurysm hemodynamics: an experimental study. AJNR Am J Neuroradiol. 1992 Jul-Aug; 13: 1089-95

60. Kim C, Cervos-Navarro J, Patzold C, Tokuriki Y, Takebe Y and Hori K. In vivo study of flow pattern at human carotid bifurcation with regard to aneurysm development. Acta Neurochir (Wien). 1992; 115(3-4): 112-7

61. Shojima M, Oshima M, Takagi K, Torii R, Hayakawa M, Katada K, Morita A and Kirino T. Magnitude and role of wall shear stress on cerebral aneurysm: computational fluid dynamic study of 20 middle cerebral artery aneurysms. Stroke. 2004 Nov; 35(11): 2500-5

62. Shojima M, Oshima M, Takagi K, Torii R, Nagata K, Shirouzu I, Morita A and Kirino T. Role of the bloodstream impacting force and the local pressure elevation in the rupture of cerebral aneurysms. Stroke. 2005 Sep; 36(9): 1933-8

63. Roach MR, Scott S and Ferguson GG. The hemodynamic importance of the geometry of bifurcations in the circle of Willis (glass model studies). Stroke. 1972 May-Jun; 3(3): 255-67

64. Tateshima S, Murayama Y, Villablanca JP, Morino T, Nomura K, Tanishita K and Vinuela F. In vitro measurement of fluid-induced wall shear stress in unruptured cerebral aneurysms harboring blebs. Stroke. 2003 Jan; 34(1): 187-92

65. Tateshima S, Tanishita K, Omura H, Villablanca JP and Vinuela F. Intra-aneurysmal hemodynamics during the growth of an unruptured aneurysm: in vitro study using longitudinal CT angiogram database. AJNR Am J Neuroradiol. 2007 Apr; 28(4): 622-7

66. Ahn S, Shin D, Tateshima S, Tanishita K, Vinuela F and Sinha S. Fluid-induced wall shear stress in anthropomorphic brain aneurysm models: MR phase-contrast study at 3 T. J Magn Reson Imaging. 2007 Jun; 25(6): 1120-30

67. Mantha A, Karmonik C, Benndorf G, Strother C and Metcalfe R. Hemodynamics in a cerebral artery before and after the formation of an aneurysm. AJNR Am J Neuroradiol. 2006 May; 27(5): 1113-8

68. Meng H, Feng Y, Woodward SH, Bendok BR, Hanel RA, Guterman LR and Hopkins LN. Mathematical model of the rupture mechanism of intracranial saccular aneurysms through daughter aneurysm formation and growth. Neurol Res. 2005 Jul; 27(5): 459-65

69. Feng Y, Wada S, Tsubota K and Yamaguchi T. The application of computer simulation in the genesis and development of intracranial aneurysms. Technol Health Care. 2005; 13(4): 281-91

70. Kroon M and Holzapfel GA. A model for saccular cerebral aneurysm growth by collagen fibre remodelling. J Theor Biol. 2007 Aug 21; 247(4): 775-87

71. Massoud TF, Guglielmi G, Ji C and et al. Experimental saccular aneurysms I. Review of surgically-constructed models and their laboratory applications. Neuroradiology. 1994; 36: 537-546

72. Kojima M, Handa H, Hashimoto N, Kim C and Hazama F. Early changes of experimentally induced cerebral aneurysms in rats: scanning electron microscopic study. Stroke. 1986 Sep-Oct; 17: 835-41

73. Meng H, Wang Z, Hoi Y, Gao L, Metaxa E, Swartz DD and Kolega J. Complex hemodynamics at the apex of an arterial bifurcation induces vascular remodeling resembling cerebral aneurysm initiation. Stroke. 2007 Jun; 38(6): 1924-31

74. Coutard M and Osborne-Pellegrin M. The rat testicular artery: a model of spontaneous aneurysmal-like structure formation. Am J Pathol. 1992 Nov; 141(5): 1053-61

75. Coutard M and Osborne-Pellegrin M. Effect of defective connective tissue on the formation of aneurysmal-like structures in the rat testicular artery. Int J Exp Pathol. 1996 Apr; 77(2): 53-62

76. Miskolczi L, Guterman LR, Flaherty JD and Hopkins LN. Saccular aneurysm induction by elastase digestion of the arterial wall: a new animal model. Neurosurgery. 1998 Sep; 43(3): 595-600

77. Altes TA, Cloft HJ, Short JG, DeGast A, Do HM, Helm GA and Kallmes DF. Creation of saccular aneurysms in the rabbit: a model suitable for testing endovascular devices. AJR Am J Roentgenol. 2000 Feb; 174(2): 349-54

78. Kadirvel R, Ding YH, Dai D, Zakaria H, Robertson AM, Danielson MA, Lewis DA, Cloft HJ and Kallmes DF. The influence of hemodynamic forces on biomarkers in the walls of elastase-induced aneurysms in rabbits. Neuroradiology. 2007 Sep; 49: 1041-53

79. Fujiwara NH, Cloft HJ, Marx WF, Short JG, Jensen ME and Kallmes DF. Serial angiography in an elastase-induced aneurysm model in rabbits: evidence for progressive aneurysm enlargement after creation. AJNR Am J Neuroradiol. 2001 Apr; 22(4): 698-703

80. Ding YH, Dai D, Layton KF, Lewis DA, Danielson MA, Kadirvel R, Cloft HJ and Kallmes DF. Vascular anatomic variation in rabbits. J Vasc Interv Radiol. 2006 Jun; 17(6): 1031-5

81. Onizuka M, Miskolczi L, Gounis MJ, Seong J, Lieber BB and Wakhloo AK. Elastase-induced aneurysms in rabbits: effect of postconstruction geometry on final size. AJNR Am J Neuroradiol. 2006 May; 27(5): 1129-31

82. Miskolczi L, Gounis MJ, Onizuka M, Cesar L, Lieber BB, Wakhloo AK and Anaya CA. Elastase-induced saccular aneurysms in rabbits: Instructions 'for the rest of us'. Proceedings of the 42nd Annual Meeting American Society of Neuroradiology. 2004; 352

83. Doerfler A, Becker W, Wanke I, Goericke S, Oezkan N, Forsting M and MRA and CTA. Multimodal imaging in the elastase-induced aneurysm model in rabbits: a comparative study using serial DSA. Rofo. 2004 Apr; 176(4): 590-6

84. Seong J, Sadasivan C, Onizuka M, Gounis MJ, Christian F, Miskolczi L, Wakhloo AK and Lieber BB. Morphology of elastase-induced cerebral aneurysm model in rabbit and rapid prototyping of elastomeric transparent replicas. Biorheology. 2005; 42: 345-61

85. Ding YH, Dai D, Lewis DA, Danielson MA, Kadirvel R, Cloft HJ and Kallmes DF. Long-term patency of elastase-induced aneurysm model in rabbits. AJNR Am J Neuroradiol. 2006 Jan; 27: 139-41

86. Short JG, Fujiwara NH, Marx WF, Helm GA, Cloft HJ and Kallmes DF. Elastase-induced saccular aneurysms in rabbits: comparison of geometric features with those of human aneurysms. AJNR Am J Neuroradiol. 2001 Nov-Dec; 22(10): 1833-7

87. Abruzzo T, Shengelaia GG, Dawson RC 3rd, Owens DS, Cawley CM and Gravanis MB. Histologic and morphologic comparison of experimental aneurysms with human intracranial aneurysms. AJNR Am J Neuroradiol. 1998 Aug; 19(7): 1309-14

88. Thiex R, Hans FJ, Krings T, Moller-Hartmann W, Brunn A, Scherer K, Gilsbach JM and Thron A. Haemorrhagic tracheal necrosis as a lethal complication of an aneurysm model in rabbits via endoluminal incubation with elastase. Acta Neurochir (Wien). 2004; 146: 285-9

89. Prestigiacomo CJ. Historical perspectives: the microsurgical and endovascular treatment of aneurysms. Neurosurgery. 2006 Nov; 59(5 Suppl 3): S39-47

90. Molyneux AJ, Kerr RS, Yu LM, Clarke M, Sneade M, Yarnold JA, Sandercock P and International Subarachnoid Aneurysm Trial (ISAT) Collaborative Group. International subarachnoid aneurysm trial (ISAT) of neurosurgical clipping versus endovascular coiling in 2143 patients with ruptured intracranial aneurysms: a randomised comparison of effects on survival, dependency, seizures, rebleeding, subgroups, and aneurysm occlusion. Lancet. 2005 Sep 3-9; 366(9488): 809-17

91. Pelz DM, Levy EI and Hopkins LN. Advances in interventional neuroradiology 2007. Stroke. 2008 Feb; 39: 268-72

92. Murayama Y, Nien YL, Duckwiler G, Gobin YP, Jahan R, Frazee J, Martin N and Vinuela F. Guglielmi detachable coil embolization of cerebral aneurysms: 11 years' experience. J Neurosurg. 2003 May; 98(5): 959-66

93. Fernandez Zubillaga A, Guglielmi G, Vinuela F and Duckwiler GR. Endovascular occlusion of intracranial aneurysms with electrically detachable coils: correlation of aneurysm neck size and treatment results. AJNR Am J Neuroradiol. 1994 May; 15(5): 815-20

94. Lieber BB, Sadasivan C, Gounis MJ and Wakhloo AK. The role of blood impulse in cerebral aneurysm coil compaction: effect of aneurysm neck size. IMECE 03; 2003 ASME International Mechanical Engineering Congress & Exposition. 2003

95. Turjman F, Massoud TF, Ji C, Guglielmi G, Vinuela F and Robert J. Combined stent implantation and endosaccular coil placement for treatment of experimental wide-necked aneurysms: a feasibility study in swine. AJNR Am J Neuroradiol. 1994 Jun; 15(6): 1087-90

96. Higashida RT, Smith W, Gress D, Urwin R, Dowd CF, Balousek PA and Halbach VV. Intravascular stent and endovascular coil placement for a ruptured fusiform aneurysm of the basilar artery. Case report and review of the literature. J Neurosurg. 1997 Dec; 87(6): 944-9

97. Higashida RT, Halbach VV, Dowd CF, Juravsky L and Meagher S. Initial clinical experience with a new self-expanding nitinol stent for the treatment of intracranial cerebral aneurysms: the Cordis Enterprise stent. AJNR Am J Neuroradiol. 2005 Aug; 26(7): 1751-6

98. Fiorella D, Albuquerque FC, Deshmukh VR and McDougall CG. Usefulness of the Neuroform stent for the treatment of cerebral aneurysms: results at initial (3-6-mo) follow-up. Neurosurgery. 2005 Jun; 56(6): 1191-201

99. Koebbe CJ, Veznedaroglu E, Jabbour P and Rosenwasser RH. Endovascular management of intracranial aneurysms: current experience and future advances. Neurosurgery. 2006 Nov; 59(5 Suppl 3): S93-102

100. Qureshi AI, Janardhan V, Hanel RA and Lanzino G. Comparison of endovascular and surgical treatments for intracranial aneurysms: an evidence-based review. Lancet Neurol. 2007 Sep; 6(9): 816-25

101. Lanzino G, Kanaan Y, Perrini P, Dayoub H and Fraser K. Emerging concepts in the treatment of intracranial aneurysms: stents, coated coils, and liquid embolic agents. Neurosurgery. 2005 Sep; 57(3): 449-59

102. Wakhloo AK, Shellhammer F, de Vries J and Schumacher J. Coated and non-coated stents for vessel reconstruction and treatment of aneurysms and av-fistulas: An experimental study. ESNR 92; XVIIIth Congress of the European Society of Neuroradiology. 1992; 34 (Suppl 1): S24

103. Turjman F, Acevedo G, Moll T, Duquesnel J, Eloy R and Sindou M. Treatment of experimental carotid aneurysms by endoprosthesis implantation: preliminary report. Neurol Res. 1993 Jun; 15(3): 181-4

104. Wakhloo AK, Schellhammer F, de Vries J, Haberstroh J and Schumacher M. Self-expanding and balloon-expandable stents in the treatment of carotid aneurysms: an experimental study in a canine model. AJNR Am J Neuroradiol. 1994 Mar; 15(3): 493-502

105. Geremia G, Haklin M and Brennecke L. Embolization of experimentally created aneurysms with intravascular stent devices. AJNR Am J Neuroradiol. 1994 Aug; 15(7): 1223-31

106. Doerfler A, Wanke I, Egelhof T, Stolke D and Forsting M. Double-stent method: therapeutic alternative for small wide-necked aneurysms. J Neurosurg. 2004 Jan; 100(1): 150-4

107. Han PP, Albuquerque FC, Ponce FA, MacKay CI, Zabramski JM, Spetzler RF and McDougall CG. Percutaneous intracranial stent placement for aneurysms. J Neurosurg. 2003 Jul; 99(1): 23-30

108. Lylyk P, Cohen JE, Ceratto R, Ferrario A and Miranda C. Endovascular reconstruction of intracranial arteries by stent placement and combined techniques. J Neurosurg. 2002 Dec; 97(6): 1306-13

109. Szikora I, Berentei Z, Kulcsar Z, Barath K, Berez A, Bose A and Nyary I. Endovascular treatment of intracranial aneurysms with parent vessel reconstruction using balloon and self expandable stents. Acta Neurochir (Wien). 2006 Jul; 148(7): 711-23

110. Vanninen R, Manninen H and Ronkainen A. Broad-based intracranial aneurysms: thrombosis induced by stent placement. AJNR Am J Neuroradiol. 2003 Feb; 24(2): 263-6

111. Zenteno MA, Murillo-Bonilla LM, Guinto G, Gomez CR, Martinez SR, Higuera-Calleja J, Lee A and Gomez-Llata S. Sole stenting bypass for the treatment of vertebral artery aneurysms: technical case report. Neurosurgery. 2005 Jul; 57(1 Suppl): E208

112. Zenteno M, Santos-Franco J, Aburto-Murrieta Y, Modenesi-Freitas JM, Ramirez-Guzman G, Gomez-Llata S and Lee A. Superior cerebellar artery aneurysms treated using the sole stenting approach. J Neurosurg. 2007 Oct; 107(4): 860-4

113. Marks MP, Dake MD, Steinberg GK, Norbash AM and Lane B. Stent placement for arterial and venous cerebrovascular disease: preliminary experience. Radiology. 1994 May; 191: 441-6

114. Fiorella D, Albuquerque FC, Deshmukh VR, Woo HH, Rasmussen PA, Masaryk TJ and McDougall CG. Endovascular reconstruction with the Neuroform stent as monotherapy for the treatment of uncoilable intradural pseudoaneurysms. Neurosurgery. 2006 Aug; 59(2): 291-300

115. Mase M, Banno T, Yamada K and Katano H. Endovascular stent placement for multiple aneurysms of the extracranial internal carotid artery: technical case report. Neurosurgery. 1995 Oct; 37: 832-5

116. Sadasivan C, Lieber BB, Gounis MJ, Lopes DK and Hopkins LN. Angiographic quantification of contrast medium washout from cerebral aneurysms after stent placement. AJNR Am J Neuroradiol. 2002 Aug; 23(7): 1214-21

117. Lanzino G, Wakhloo AK, Fessler RD, Hartney ML, Guterman LR and Hopkins LN. Efficacy and current limitations of intravascular stents for intracranial internal carotid, vertebral, and basilar artery aneurysms. J Neurosurg. 1999 Oct; 91(4): 538-46

118. Benndorf G, Herbon U, Sollmann WP and Campi A. Treatment of a ruptured dissecting vertebral artery aneurysm with double stent placement: case report. AJNR Am J Neuroradiol. 2001 Nov-Dec; 22(10): 1844-8

119. Lieber BB, Stancampiano AP and Wakhloo AK. Alteration of hemodynamics in aneurysm models by stenting: influence of stent porosity. Ann Biomed Eng. 1997 May-Jun; 25(3): 460-9

120. Aenis M, Stancampiano AP, Wakhloo AK and Lieber BB. Modeling of flow in a straight stented and nonstented side wall aneurysm model. J Biomech Eng. 1997 May; 119: 206-12

121. Liou TM, Liou SN and Chu KL. Intra-aneurysmal flow with helix and mesh stent placement across side-wall aneurysm pore of a straight parent vessel. J Biomech Eng. 2004 Feb; 126: 36-43

122. Seong J, Wakhloo AK and Lieber BB. In vitro evaluation of flow divertors in an elastase-induced saccular aneurysm model in rabbit. J Biomech Eng. 2007 Dec; 129: 863-72

123. Yu SC and Zhao JB. A steady flow analysis on the stented and non-stented sidewall aneurysm models. Med Eng Phys. 1999 Apr; 21: 133-41

124. Ohta M, Wetzel SG, Dantan P, Bachelet C, Lovblad KO, Yilmaz H, Flaud P and Rufenacht DA. Rheological changes after stenting of a cerebral aneurysm: a finite element modeling approach. Cardiovasc Intervent Radiol. 2005 Nov-Dec; 28(6): 768-72

125. Lieber BB, Livescu V, Hopkins LN and Wakhloo AK. Particle image velocimetry assessment of stent design influence on intra-aneurysmal flow. Ann Biomed Eng. 2002 Jun; 30(6): 768-77

126. Barath K, Cassot F, Rufenacht DA and Fasel JH. Anatomically shaped internal carotid artery aneurysm in vitro model for flow analysis to evaluate stent effect. AJNR Am J Neuroradiol. 2004 Nov-Dec; 25(10): 1750-9

127. Rhee K, Han MH and Cha SH. Changes of flow characteristics by stenting in aneurysm models: influence of aneurysm geometry and stent porosity. Ann Biomed Eng. 2002 Jul-Aug; 30(7): 894-904

128. Kim M, Levy EI, Meng H and Hopkins LN. Quantification of hemodynamic changes induced by virtual placement of multiple stents across a wide-necked basilar trunk aneurysm. Neurosurgery. 2007 Dec; 61: 1305-12

129. Barath K, Cassot F, Fasel JH, Ohta M and Rufenacht DA. Influence of stent properties on the alteration of cerebral intra-aneurysmal haemodynamics: flow quantification in elastic sidewall aneurysm models. Neurol Res. 2005; 27 Suppl 1: S120-8

130. Mandrusov E, Puszkin E, Vroman L and Leonard EF. Separated flows in artificial organs. A cause of early thrombogenesis? ASAIO J. 1996 Sep-Oct; 42(5): M506-13

131. Maxwell MJ, Westein E, Nesbitt WS, Giuliano S, Dopheide SM and Jackson SP. Identification of a 2-stage platelet aggregation process mediating shear-dependent thrombus formation. Blood. 2007 Jan 15; 109: 566-76

132. Spaeth EE, Roberts GW, Yadwadkar SR, Ng PK and Jackson CM. The influence of fluid shear on the kinetics of blood coagulation reactions. Trans Am Soc Artif Intern Organs. 1973; 19: 179-87

133. Brownlee RD, Tranmer BI, Sevick RJ, Karmy G and Curry BJ. Spontaneous thrombosis of an unruptured anterior communicating artery aneurysm. An unusual cause of ischemic stroke. Stroke. 1995 Oct; 26(10): 1945-9

134. Lopes D and Sani S. Histological postmortem study of an internal carotid artery aneurysm treated with the Neuroform stent. Neurosurgery. 2005 Feb; 56(2): E416

135. Palmaz JC. Intravascular stents in the last and the next 10 years. J Endovasc Ther. 2004 Dec; 11 Suppl 2: II200-206

136. Palmaz JC. Intravascular stents: tissue-stent interactions and design considerations. AJR Am J Roentgenol. 1993 Mar; 160(3): 613-8

137. Palmaz JC. The 2001 Charles T. Dotter lecture: understanding vascular devices at the molecular level is the key to progress. J Vasc Interv Radiol. 2001 Jul; 12(7): 789-94

138. Simon C, Palmaz JC and Sprague EA. Protein interactions with endovascular prosthetic surfaces. J Long Term Eff Med Implants. 2000; 10: 127-41

139. Basmadjian D, Sefton MV and Baldwin SA. Coagulation on biomaterials in flowing blood: some theoretical considerations. Biomaterials. 1997 Dec; 18(23): 1511-22

140. Edelman ER and Rogers C. Pathobiologic responses to stenting. Am J Cardiol. 1998 Apr; 81(7A): 4E-6E

141. Indolfi C, Mongiardo A, Curcio A and Torella D. Molecular mechanisms of in-stent restenosis and approach to therapy with eluting stents. Trends Cardiovasc Med. 2003 May; 13(4): 142-8

142. Rousseau H, Puel J, Joffre F, Sigwart U, Duboucher C, Imbert C, Knight C, Kropf L and Wallsten H. Self-expanding endovascular prosthesis: an experimental study. Radiology. 1987 Sep; 164(3): 709-14

143. Virmani R and Farb A. Pathology of in-stent restenosis. Curr Opin Lipidol. 1999 Dec; 10: 499-506

144. Davies MJ, Ballantine SJ, Robertson WB and Woolf N. The ultrastructure of organizing experimental mural thrombi in the pig aorta. J Pathol. 1975 Oct; 117(2): 75-81

145. Bai H, Masuda J, Sawa Y, Nakano S, Shirakura R, Shimazaki Y, Ogata J and Matsuda H. Neointima formation after vascular stent implantation. Spatial and chronological distribution of smooth muscle cell proliferation and phenotypic modulation. Arterioscler Thromb. 1994 Nov; 14(11): 1846-53

146. Virmani R, Kolodgie FD, Farb A and Lafont A. Drug eluting stents: are human and animal studies comparable? Heart. 2003 Feb; 89(2): 133-8

147. Stemerman MB, Spaet TH, Pitlick F, Cintron J, Lejnieks I and Tiell ML. Intimal healing. The pattern of reendothelialization and intimal thickening. Am J Pathol. 1977 Apr; 87: 125-42

148. Schatz RA, Palmaz JC, Tio FO, Garcia F, Garcia O and Reuter SR. Balloon-expandable intracoronary stents in the adult dog. Circulation. 1987 Aug; 76: 450-7

149. Richter GM, Palmaz JC, Noeldge G and Tio F. Blood flow and thrombus formation determine the development of stent neointima. J Long Term Eff Med Implants. 2000; 10(1-2): 69-77

150. Sprague EA, Luo J and Palmaz JC. Endothelial cell migration onto metal stent surfaces under static and flow conditions. J Long Term Eff Med Implants. 2000; 10(1-2): 97-110

151. Schwartz RS and Holmes DR. Pigs, dogs, baboons, and man: Lessons for stenting from animal studies. J Interv Cardiol. 1994; 7(4): 355-368

152. Edelman ER and Rogers C. Stent-versus-stent equivalency trials: are some stents more equal than others? Circulation. 1999 Aug 31; 100(9): 896-8

153. Harnek J, Zoucas E, Carlemalm E and Cwikiel W. Differences in endothelial injury after balloon angioplasty, insertion of balloon-expanded stents or release of self-expanding stents: An electron microscopic experimental study. Cardiovasc Intervent Radiol. 1999 Jan; 22(1): 56-61

154. Rogers C and Edelman ER. Endovascular stent design dictates experimental restenosis and thrombosis. Circulation. 1995 Jun 15; 91(12): 2995-3001

155. Garasic JM, Edelman ER, Squire JC, Seifert P, Williams MS and Rogers C. Stent and artery geometry determine intimal thickening independent of arterial injury. Circulation. 2000 Feb 22; 101(7): 812-8

156. LaDisa JF Jr, Olson LE, Molthen RC, Hettrick DA, Pratt PF, Hardel MD, Kersten JR, Warltier DC and Pagel PS. Alterations in wall shear stress predict sites of neointimal hyperplasia after stent implantation in rabbit iliac arteries. Am J Physiol Heart Circ Physiol. 2005 May; 288(5): H2465-75

157. Wakhloo AK, Tio FO, Lieber BB, Schellhammer F, Graf M and Hopkins LN. Self-expanding nitinol stents in canine vertebral arteries: hemodynamics and tissue response. AJNR Am J Neuroradiol. 1995 May; 16(5): 1043-51

158. Schultz JS, Lindenauer SM, Penner JA and Barenberg S. Determinants of thrombus formation on surfaces. Trans Am Soc Artif Intern Organs. 1980; 26: 279-83

159. Wentzel JJ, Krams R, Schuurbiers JC, Oomen JA, Kloet J, van Der Giessen WJ, Serruys PW and Slager CJ. Relationship between neointimal thickness and shear stress after Wallstent implantation in human coronary arteries. Circulation. 2001 Apr 3; 103(13): 1740-5

160. Eto K, Goto S, Shimazaki T, Sakakibara M, Yoshida M, Isshiki T and Handa S. Two distinct mechanisms are involved in stent thrombosis under flow conditions. Platelets. 2001 Jun; 12: 228-35

161. Baim DS and Carrozza JP Jr. Stent thrombosis. Closing in on the best preventive treatment. Circulation. 1997 Mar 4; 95(5): 1098-100

162. Duprat G Jr, Wright KC, Charnsangavej C, Wallace S and Gianturco C. Self-expanding metallic stents for small vessels: an experimental evaluation. Radiology. 1987 Feb; 162(2): 469-72

163. Turk AS, Niemann DB, Ahmed A and Aagaard-Kienitz B. Use of self-expanding stents in distal small cerebral vessels. AJNR Am J Neuroradiol. 2007 Mar; 28(3): 533-6

164. Roguin A and Grenadier E. Stent-based percutaneous coronary interventions in small coronary arteries. Acute Card Care. 2006; 8(2): 70-4

165. Gyongyosi M, Yang P, Khorsand A and Glogar D. Longitudinal straightening effect of stents is an additional predictor for major adverse cardiac events. J Am Coll Cardiol. 2000 May; 35(6): 1580-9

166. Schwartz RS. Neointima and arterial injury: dogs, rats, pigs, and more. Lab Invest. 1994 Dec; 71(6): 789-91

167. Marinkovic SV and Gibo H. The surgical anatomy of the perforating branches of the basilar artery. Neurosurgery. 1993 Jul; 33: 80-7

168. Marinkovic S, Gibo H, Brigante L, Nikodijevic I and Petrovic P. The surgical anatomy of the perforating branches of the anterior choroidal artery. Surg Neurol. 1999 Jul; 52: 30-6

169. Lopes DK, Ringer AJ, Boulos AS, Qureshi AI, Lieber BB, Guterman LR and Hopkins LN. Fate of branch arteries after intracranial stenting. Neurosurgery. 2003 Jun; 52(6): 1275-8

170. Masuo O, Terada T, Walker G, Tsuura M, Matsumoto H, Tohya K, Kimura M, Nakai K and Itakura T. Study of the patency of small arterial branches after stent placement with an experimental in vivo model. AJNR Am J Neuroradiol. 2002 Apr; 23(4): 706-10

171. Cho GY, Lee CW, Hong MK, Kim JJ, Park SW and Park SJ. Effects of stent design on side branch occlusion after coronary stent placement. Catheter Cardiovasc Interv. 2001 Jan; 52(1): 18-23

172. Levy EI, Hanel RA, Howington JU, Nemes B, Boulos AS, Tio FO, Paciorek AM, Amlani S, Kagan-Hallett KS, Fronckowiak MD, Guterman LR and Hopkins LN. Sirolimus-eluting stents in the canine cerebral vasculature: a prospective,

randomized, blinded assessment of safety and vessel response. J Neurosurg. 2004 Apr; 100(4): 688-94

173. Lieber BB, Sadasivan C, Gounis MJ, Seong J, Miskolczi L and Wakhloo AK. Functional angiography. Crit Rev Biomed Eng. 2005; 33(1): 1-102

174. Meier P and Zierler KL. On the theory of the indicator-dilution method for measurement of blood flow and volume. J Appl Physiol. 1954 Jun; 6(12): 731-44

175. Hilal SK. Determination of the blood flow by a radiographic technique. Physical considerations and experimental results. Am J Roentgenol Radium Th er Nucl Med. 1966; 96: 896–906

176. Silverman NR and Rosen L. Arterial blood flow measurement: assessment of velocity estimation methods. Invest Radiol. 1977 Jul-Aug; 12(4): 319-24

177. Shpilfoygel SD, Close RA, Valentino DJ and Duckwiler GR. X-ray videodensitometric methods for blood flow and velocity measurement: a critical review of literature. Med Phys. 2000 Sep; 27(9): 2008-23

178. Bursch JH, Hahne HJ, Brennecke R, Gronemeier D and Heintzen PH. Assessment of arterial blood flow measurements by digital angiography. Radiology. 1981 Oct; 141(1): 39-47

179. Kedem D, Smith CW, Dean RH and Brill AB. Velocity distribution and blood flow measurements using videodensitometric methods. Invest Radiol. 1978 Jan-Feb; 13(1): 46-56

180. Bassingthwaighte JB, Ackerman FH and Wood EH. Applications of the lagged normal density curve as a model for arterial dilution curves. Circ Res. 1966 Apr; 18(4): 398-415

181. Tenjin H, Asakura F, Nakahara Y, Matsumoto K, Matsuo T, Urano F and Ueda S. Evaluation of intraaneurysmal blood velocity by time-density curve analysis and digital subtraction angiography. AJNR Am J Neuroradiol. 1998 Aug; 19(7): 1303-7

182. Asakura F, Tenjin H, Sugawa N, Kimura S and Oki F. Evaluation of intra-aneurysmal blood flow by digital subtraction angiography: blood flow change after coil embolization. Surg Neurol. 2003 Apr; 59(4): 310-9

183. Rudin S, Wang Z, Kyprianou I, Hoffmann KR, Wu Y, Meng H, Guterman LR, Nemes B, Bednarek DR, Dmochowski J and Hopkins LN. Measurement of flow modification in phantom aneurysm model: comparison of coils and a longitudinally and axially asymmetric stent--initial findings. Radiology. 2004 Apr; 231(1): 272-6

184. Szikora I, Marosfoi M, Nelson PK, Berez A, Zsolt B, Zsolt K, Lee W and Nyary I. Treatment of intracranial saccular aneurysms using high mesh density vascular endoprosthesis: the Pipeline vascular reconstruction system. 2007; 71

185. Kallmes DF, Ding YH, Dai D, Kadirvel R, Lewis DA and Cloft HJ. A new endoluminal, flow-disrupting device for treatment of saccular aneurysms. Stroke. 2007 Aug; 38(8): 2346-52

186. Ahlhelm F, Roth C, Kaufmann R, Schulte-Altedorneburg G, Romeike BF and Reith W. Treatment of wide-necked intracranial aneurysms with a novel self-expanding two-zonal endovascular stent device. Neuroradiology. 2007 Dec; 49(12): 1023-8

187. Lieber BB, Sadasivan C, Miskolczi L, Cesar L, Seong J and Wakhloo AK. Flow divertors to treat cerebral aneurysms: preliminary results in the rabbit elastase-induced aneurysm model. Proceedings of the 2006 Summer Bioengineering Conference. 2006

188. Yu C, Liu Z, McKenna T, Reisner AT and Reifman J. A method for automatic identification of reliable heart rates calculated from ECG and PPG waveforms. J Am Med Inform Assoc. 2006 May-Jun; 13: 309-20

189. Meijering EH, Niessen WJ and Viergever MA. Retrospective motion correction in digital subtraction angiography: a review. IEEE Trans Med Imaging. 1999 Jan; 18: 2-21

190. Bullitt E, Muller KE, Jung I, Lin W and Aylward S. Analyzing attributes of vessel populations. Med Image Anal. 2005 Feb; 9: 39-49

191. Yimman S, Hinjit W, Sriboonsong S, Puangpool M and Dejhan K. IIR notch filter design with modified pole-zero placement algorithm. Proceedings of the 3rd IEEE International Symposium on Signal Processing and Information Technology (ISSPIT). 2003 Dec; 822-25

192. Massey FJ. The Kolmogorov-Smirnov test for goodness of fit. J Am Stat Assoc. 1951 Mar; 46: 68-78

193. Lilliefors HW. On the Kolmogorov-Smirnov test for normality with mean and variance unknown. J Am Stat Assoc. 1967 Jun; 62: 399-402

194. Figliola RS and Beasley DE. Theory and design for mechanical measurements. 1995

195. Lylyk P, Ferrario A, Pasbon B, Miranda C and Doroszuk G. Buenos Aires experience with the Neuroform self-expanding stent for the treatment of intracranial aneurysms. J Neurosurg. 2005 Feb; 102(2): 235-41

196. Hanel RA, Levy EI, Guterman LR and Hopkins LN. Advances in stent-assisted management of intracranial occlusive disease and cerebral aneurysms. Tech Vasc Interv Radiol. 2004 Dec; 7(4): 202-9

197. Geremia G, Brack T, Brennecke L, Haklin M and Falter R. Occlusion of experimentally created fusiform aneurysms with porous metallic stents. AJNR Am J Neuroradiol. 2000 Apr; 21: 739-45

198. Wakhloo AK, Lanzino G, Lieber BB and Hopkins LN. Stents for intracranial aneurysms: the beginning of a new endovascular era? Neurosurgery. 1998 Aug; 43(2): 377-9

199. Stewart GN. Researches on the circulation time and on the influences which affect it. J Physiol. 1897 Nov; 22: 159-83

200. Wang ZJ, Hoffmann KR, Wang Z, Rudin S, Guterman LR and Meng H. Contrast settling in cerebral aneurysm angiography. Phys Med Biol. 2005 Jul; 50: 3171-81

201. Wang Z, Ionita C, Rudin S, Hoffmann KR, Paxton AB and Bednarek DR. Angiographic analysis of blood flow modification in cerebral aneurysm models with a new asymmetric stent. Proc SPIE. 2004; 5369: 307-18

202. Sadasivan C, Cesar L and Lieber BB. Mixing of angiographic contrast with blood during injections in the cerebral circulation. Proceedings of the Summer Bioengineering Conference. 2008

203. Perry RH, Green DW and Maloney JO. Perry's Chemical engineers' handbook. Seventh Edition. 1997; 5.48

204. Hart WE, Goldbaum M, Cote B, Kube P and Nelson MR. Measurement and classification of retinal vascular tortuosity. Int J Med Inform. 1999 Feb-Mar; 53: 239-52

205. Kallmes DF, Fujiwara NH, Berr SS, Helm GA and Cloft HJ. Elastase-induced saccular aneurysms in rabbits: a dose-escalation study. AJNR Am J Neuroradiol. 2002 Feb; 23: 295-8

206. Rakian AIV. Scanning electron microscopy and histological evaluation of flow divertors. MS Thesis. 2007 Dec

207. Fiorella D, Albuquerque FC, Woo H, Rasmussen PA, Masaryk TJ and McDougall CG. Neuroform in-stent stenosis: incidence, natural history, and treatment strategies. Neurosurgery. 2006 Jul; 59(1): 34-42

208. Raymond J, Guilbert F, Metcalfe A, Gevry G, Salazkin I and Robledo O. Role of the endothelial lining in recurrences after coil embolization: prevention of recanalization by endothelial denudation. Stroke. 2004 Jun; 35(6): 1471-5

209. Raymond J, Sauvageau E, Salazkin I, Ribourtout E, Gevry G and Desfaits AC. Role of the endothelial lining in persistence of residual lesions and growth of recurrences after endovascular treatment of experimental aneurysms. Stroke. 2002 Mar; 33: 850-5

210. Moldovan NI and Asahara T. Role of blood mononuclear cells in recanalization and vascularization of thrombi: past, present, and future. Trends Cardiovasc Med. 2003 Oct; 13(7): 265-9

211. Darsaut T, Bouzeghrane F, Salazkin I, Lerouge S, Soulez G, Gevry G and Raymond J. The effects of stenting and endothelial denudation on aneurysm and branch occlusion in experimental aneurysm models. J Vasc Surg. 2007 Jun; 45(6): 1228-35

212. Byrne JV, Hope JK, Hubbard N and Morris JH. The nature of thrombosis induced by platinum and tungsten coils in saccular aneurysms. AJNR Am J Neuroradiol. 1997 Jan; 18(1): 29-33

213. Prati F, Zimarino M, Stabile E, Pizzicannella G, Fouad T, Rabozzi R, Filippini A, Pizzicannella J, Cera M and De Caterina R. Does optical coherence tomography identify arterial healing after stenting? An in vivo comparison with histology, in a rabbit carotid model. Heart. 2008 Feb; 94: 217-21

214. Hans FJ, Krings T, Moller-Hartmann W, Thiex R, Pfeffer J, Scherer K, Brunn A, Dreeskamp H, Stein KP, Meetz A, Gilsbach JM and Thron A. Endovascular treatment of experimentally induced aneurysms in rabbits using stents: a feasibility study. Neuroradiology. 2003 Jul; 45(7): 430-4

215. Krings T, Busch C, Sellhaus B, Drexler AY, Bovi M, Hermanns-Sachweh B, Scherer K, Gilsbach JM, Thron A and Hans FJ. Long-term histological and scanning electron microscopy results of endovascular and operative treatments of experimentally induced aneurysms in the rabbit. Neurosurgery. 2006 Oct; 59(4): 911-23

216. Krings T, Hans FJ, Moller-Hartmann W, Brunn A, Thiex R, Schmitz-Rode T, Verken P, Scherer K, Dreeskamp H, Stein KP, Gilsbach J and Thron A. Treatment of experimentally induced aneurysms with stents. Neurosurgery. 2005 Jun; 56(6): 1347-59

APPENDIX 1

This appendix includes tables of results obtained from the experiments and analyses. Corresponding table captions explain the listed information.

Table A1.1: Dimensions of the 40 created aneurysms and the averages per group. The mean (standard error) over all the 40 animals was 4.1(0.2)×3.7(0.1)×7.9(0.3) mm.

Rabbit ID	Aneurysm dimensions (mm)			Mean (Standard Error)		
	Neck	Width	Height	Neck	Width	Height
#B_021_1	4.8	5.1	9.3			
#B_021_2	4.3	4.3	6.3			
#B_021_3	2.5	3.2	8.3			
#B_090_1	3.1	2.9	6.9			
#B_090_2	5.7	3.6	5.5	4.3	3.7	7.6
#B_090_3	4.4	3.7	7.8	(0.4)	(0.2)	(0.5)
#B_180_1	3.7	3.1	9.7			
#B_180_2	3.1	3.3	7.1			
#B_180_3	7.1	3.6	5.7			
#B_180_4	4.2	4.4	9.2			
#C_021_1	3.3	3.4	8.1			
#C_021_2	2.0	3.2	6.5			
#C_021_3	3.3	3.4	5.3			
#C_090_1	5.7	3.7	10.3			
#C_090_2	4.7	3.7	7.2	4.4	3.6	7.5
#C_090_3	8.7	3.1	5.8	(0.6)	(0.2)	(0.4)
#C_180_1	5.0	3.5	7.9			
#C_180_2	3.5	3.6	8.2			
#C_180_3	4.3	3.7	7.6			
#C_180_4	3.6	4.9	7.7			
#E_021_1	5.6	4.7	10.3			
#E_021_2	2.5	3.5	7.7			
#E_021_3	3.0	3.5	9.3			
#E_090_1	2.1	3.0	8.4			
#E_090_2	2.1	3.5	7.4	3.7	3.6	9.0
#E_090_3	3.5	2.4	7.5	(0.4)	(0.2)	(0.4)
#E_180_1	3.6	3.6	9.7			
#E_180_2	5.1	3.4	8.7			
#E_180_3	4.4	4.2	11.3			
#E_180_4	5.5	4.5	9.9			
#O_021_1	1.8	2.9	4.2			
#O_021_2	4.8	3.9	7.2			
#O_021_3	2.6	2.9	4.8			
#O_090_1	3.8	4.1	8.2			
#O_090_2	4.2	4.2	9.9	3.8	3.8	7.7
#O_090_3	3.7	3.7	5.2	(0.3)	(0.2)	(0.9)
#O_180_1	4.5	3.4	6.6			
#O_180_2	3.2	3.5	8.1			
#O_180_3	4.5	3.3	9.3			
#O_180_4	4.9	5.6	13.5			

Table A1.2. Dates (in *yyyymmdd* format) of treatment (initial angiography for controls) and follow-up giving the average number of days to follow-up for each animal.

Rabbit ID	Implant Date	Follow-up Date	Follow-up time (days)	Mean	Standard Error
#B_021_1	20060630	20060724	24		
#B_021_2	20060906	20060927	21	23.0	1.0
#B_021_3	20060808	20060901	24		
#B_090_1	20060630	20060929	91		
#B_090_2	20060630	20060929	91	91.7	0.7
#B_090_3	20060701	20061002	93		
#B_180_1	20060425	20061024	182		
#B_180_2	20060522	20061120	182	183.3	1.3
#B_180_3	20060522	20061120	182		
#B_180_4	20060705	20070108	187		
#C_021_1	20060406	20060426	20		
#C_021_2	20060406	20060428	22	21.0	0.6
#C_021_3	20060906	20060927	21		
#C_090_1	20060425	20060725	91		
#C_090_2	20060523	20060823	92	92.0	0.6
#C_090_3	20060701	20061002	93		
#C_180_1	20060424	20061024	183		
#C_180_2	20060424	20061024	183	183.8	1.5
#C_180_3	20060523	20061120	181		
#C_180_4	20060705	20070109	188		
#E_021_1	20060719	20060809	21		
#E_021_2	20060719	20060809	21	21.0	0.0
#E_021_3	20060906	20060927	21		
#E_090_1	20060304	20060609	97		
#E_090_2	20060304	20060609	97	95.3	1.7
#E_090_3	20060309	20060609	92		
#E_180_1	20060304	20060905	185		
#E_180_2	20060524	20061127	187	186.5	0.5
#E_180_3	20060524	20061127	187		
#E_180_4	20060524	20061127	187		
#O_021_1	20060522	20060612	21		
#O_021_2	20060524	20060612	19	20.0	0.6
#O_021_3	20060705	20060725	20		
#O_090_1	20060808	20061108	92		
#O_090_2	20061122	20070222	92	92.0	0.0
#O_090_3	20061122	20070222	92		
#O_180_1	20060705	20070108	187		
#O_180_2	20060902	20070302	181	183.0	1.4
#O_180_3	20060902	20070302	181		
#O_180_4	20061120	20070522	183		

Table A1.3. Histomorphometry of the luminal surface of the devices; average (standard error) values of neointimal thickness (in μm) in each animal based on 4 or 5 sections along the device and the average (standard error) diameter of the parent artery (mm) based on the same sections. The sub-group averages (standard error) are also included.

Rabbit ID	Neointimal Thickness (μm)	Mean (Standard Error)	Artery Diameter (mm)	Mean (Standard Error)
#B_021_3	204 (40)	204 (40)	3.6 (0.2)	3.6 (0.2)
#B_090_1	214 (21)		4.1 (0.1)	
#B_090_2	184 (21)	177 (14)	3.9 (0.3)	3.9 (0.1)
#B_090_3	121 (7))		3.8 (0.1)	
#B_180_1	180 (15)	175 (13)	3.8 (0.2)	3.7 (0.1)
#B_180_2	168 (26)		3.5 (0.2)	
#C_021_3	151 (13)	151 (13)	3.3 (0.2)	3.3 (0.2)
#C_090_1	126 (9)	181 (24)	3.2 (0.2)	3.4 (0.2)
#C_090_3	236 (32)		3.7 (0.2)	
#C_180_1	160 (8)		3.7 (0.2)	
#C_180_2	196 (23)	168 (10)	3.8 (0.2)	3.6 (0.1)
#C_180_3	149 (10)		3.3 (0.2)	
#E_021_1	115 (11)	118 (9)	2.6 (0.1)	2.5 (0.1)
#E_021_3	120 (14)		2.5 (0.1)	
#E_090_1	144 (17)		2.9 (0.1)	
#E_090_2	98 (6)	133 (11)	2.9 (0.1)	3.0 (0.1)
#E_090_3	156 (21)		3.4 (0.1)	
#E_180_1	109 (14)	129 (16)	2.9 (0.1)	3.1 (0.2)
#E_180_2	155 (24)		3.4 (0.2)	

Table A1.4. Histomorphometry of aneurysms; semi-quantitative scores of the extent of aneurysm occlusion and the degree of organization of aneurysm contents.

Rabbit ID	Aneurysm Occlusion Score	Mean (Standard Error)	Degree of Organization	Mean (Standard Error)
#B_021_3	3		3	
#B_090_1	2		2	
#B_090_2	2	2.2 (0.2)	2	2.0 (0.3)
#B_090_3	2		1	
#B_180_1	2		2	
#C_021_3	3		3	
#C_090_1	0		–	
#C_090_3	0	1.8 (0.6)	–	2.5 (0.5)
#C_180_1	3		3	
#C_180_2	2		1	
#C_180_3	3		3	
#E_021_1	2		1	
#E_021_3	2		2	
#E_090_1	3		3	
#E_090_2	2	2.0 (0.4)	3	2.3 (0.3)
#E_090_3	0		–	
#E_180_1	3		3	
#E_180_2	2		2	

Aneurysm occlusion score: 0 – Aneurysm lumen essentially empty; 1 – Aneurysm lumen slightly filled; 2 – Aneurysm lumen at least half filled; 3 – Aneurysm lumen essentially filled

Degree of organization of aneurysm contents score: 1 – Clot with little organization; 2 – Clot with more organization; 3 – Organized with recanalization

Table A1.5. Frame number at which contrast was first visualized in the ascending aorta representing the delay in contrast injection and the calculated respiratory periods (in frames) for each animal. "PRE", "POST", and "FU" denote angiograms taken before device implant, immediately after device implant and at follow-up. No "POST" angiograms for controls. Acquisition rate was 30 frames per second.

Rabbit ID	Time to contrast visualization (frames)			Respiratory periods (frames)		
	PRE	POST	FU	PRE	POST	FU
#B_021_1	115	102	100	54	52	29
#B_021_2	88	101	129	48	47	62
#B_021_3	90	142	159	49	51	51
#B_090_1	130	104	121	41	43	24
#B_090_2	100	99	118	49	58	90
#B_090_3	92	81	102	43	55	25
#B_180_1	72	80	117	41	45	48
#B_180_2	91	75	153	50	49	43
#B_180_3	85	65	120	56	59	61
#B_180_4	114	93	102	60	60	43
#C_021_1	79	59	105	37	34	49
#C_021_2	102	79	78	52	44	43
#C_021_3	100	118	108	50	47	44
#C_090_1	81	71	104	35	41	32
#C_090_2	73	101	123	37	35	28
#C_090_3	113	90	75	46	63	49
#C_180_1	79	77	167	41	43	55
#C_180_2	89	58	204	57	57	108
#C_180_3	68	81	178	55	43	44
#C_180_4	113	93	160	43	64	40
#E_021_1	100	100	92	36	66	38
#E_021_2	117	97	134	68	65	67
#E_021_3	105	110	148	27	28	53
#E_090_1	85	73	98	20	32	32
#E_090_2	75	63	130	55	35	35
#E_090_3	67	32	90	33	31	32
#E_180_1	76	91	137	55	38	60
#E_180_2	82	95	93	43	58	27
#E_180_3	75	128	169	40	41	44
#E_180_4	75	71	120	53	59	41
#O_021_1	109	–	74	46	–	53
#O_021_2	84	–	93	80	–	65
#O_021_3	107	–	81	41	–	28
#O_090_1	99	–	105	42	–	48
#O_090_2	193	–	71	33	–	34
#O_090_3	156	–	77	35	–	29
#O_180_1	91	–	121	69	–	53
#O_180_2	96	–	96	29	–	35
#O_180_3	96	–	98	41	–	41
#O_180_4	132	–	110	51	–	56

Table A1.6. Percentage aneurysm occlusion based on angiography. POST implies percent occlusion of the aneurysm measured immediately after device implantation; FU implies percent occlusion of the aneurysm measured at follow-up; POST to FU is the calculated occlusion during the follow-up period.

Rabbit ID	POST %	FU %	POST to FU %	Mean (Standard Error)
#B_021_1	30.9	99.0	98.6	
#B_021_2	56.7	100.0	100.0	POST: 34.0%
#B_021_3	62.0	100.0	100.0	(5.5%)
#B_090_1	29.8	99.2	98.9	
#B_090_2	17.1	84.4	81.2	FU: 83.0%
#B_090_3	32.1	89.4	84.4	(8.8%)
#B_180_1	37.5	97.5	96.0	
#B_180_2	41.8	97.8	96.2	POST – FU: 78.2%
#B_180_3	31.3	23.8	-10.9	(11.6%)
#B_180_4	1.2	38.5	37.7	
#C_021_1	53.0	78.5	54.3	
#C_021_2	6.1	62.7	60.3	POST: 38.8%
#C_021_3	42.6	100.0	100.0	(6.6%)
#C_090_1	39.0	80.8	68.5	
#C_090_2	55.1	51.4	-8.3	FU: 80.7%
#C_090_3	44.7	52.5	14.0	(6.2%)
#C_180_1	46.2	100.0	100.0	
#C_180_2	14.6	100.0	100.0	POST – FU: 66.7%
#C_180_3	72.5	100.0	100.0	(12.1%)
#C_180_4	14.5	81.5	78.3	
#E_021_1	66.5	97.2	91.6	
#E_021_2	44.8	100.0	100.0	POST: 35.5%
#E_021_3	43.0	95.8	92.6	(7.7%)
#E_090_1	41.4	100.0	100.0	
#E_090_2	29.0	100.0	100.0	FU*: 97.0%
#E_090_3	11.2	93.5	92.7	(1.1%)
#E_180_1	72.5	100.0	100.0	
#E_180_2	14.4	91.5	90.1	POST – FU*: 95.5%
#E_180_3	31.9	95.1	92.8	(1.4%)
#E_180_4	0.6	15.7	15.2*	
#O_021_1		51.3		
#O_021_2		4.8		
#O_021_3		7.9		
#O_090_1		7.4		
#O_090_2		2.0		FU: 9.4%
#O_090_3		6.4		(4.7%)
#O_180_1		1.9		
#O_180_2		8.8		
#O_180_3		1.3		
#O_180_4		2.0		

*The proximal diameter of the parent vessel in this case was larger than the open diameter of the device as a result of which, flow went around the device and into the aneurysm. This animal is excluded from the percentage aneurysm occlusion calculations at follow-up.

Table A1.7. Arc and chord lengths (pixels) and arc-to-chord ratios of the treated vessel segments used an index of the change in curvature of the segment after device implantation. The ratios obtained after device implantation (POST) are listed as a percentage of the corresponding ratios before device implantation (PRE).

Rabbit ID	PRE			POST			% of PRE	Mean (Standard Error) %
	Arc (pix)	Chord(pix)	Arc / Chord	Arc (pix)	Chord(pix)	Arc / Chord		
#B_021_1	82	64	1.3	73	73	1.0	78.7	
#B_021_2	79	71	1.1	79	79	1.0	90.6	
#B_021_3	80	70	1.1	79	79	1.0	87.7	
#B_090_1	94	81	1.2	77	77	1.0	86.4	
#B_090_2	84	74	1.1	86	80	1.1	94.6	79.8 (3.0)
#B_090_3	85	60	1.4	85	85	1.0	71.8	
#B_180_1	94	64	1.5	80	80	1.0	68.6	
#B_180_2	81	62	1.3	88	88	1.0	76.4	
#B_180_3	66	50	1.3	84	83	1.0	75.8	
#B_180_4	89	60	1.5	80	80	1.0	67.8	
#C_021_1	81	73	1.1	92	91	1.0	89.4	
#C_021_2	96	74	1.3	98	98	1.0	77.7	
#C_021_3	61	55	1.1	70	70	1.0	90.1	
#C_090_1	88	64	1.4	96	95	1.0	72.8	
#C_090_2	106	81	1.3	88	88	1.0	76.8	83.9 (2.8)
#C_090_3	89	68	1.3	88	88	1.0	76.2	
#C_180_1	80	63	1.3	68	68	1.0	79.3	
#C_180_2	65	63	1.0	84	84	1.0	98.0	
#C_180_3	77	73	1.1	86	86	1.0	94.7	
#C_180_4	75	63	1.2	65	65	1.0	83.8	
#E_021_1	64	58	1.1	65	64	1.0	92.1	
#E_021_2	70	56	1.3	70	70	1.0	80.1	
#E_021_3	77	70	1.1	80	80	1.0	92.2	
#E_090_1	79	73	1.1	70	70	1.0	93.0	
#E_090_2	83	67	1.2	88	85	1.0	83.9	84.8 (1.9)
#E_090_3	90	73	1.2	86	85	1.0	82.0	
#E_180_1	84	71	1.2	83	82	1.0	84.4	
#E_180_2	84	68	1.2	77	77	1.0	81.3	
#E_180_3	81	68	1.2	84	84	1.0	84.1	
#E_180_4	79	59	1.3	85	84	1.0	75.0	

Table A1.8. Values of the optimized model parameters and the washout curve amplitudes at different treatment phases (PRE: before device implant, POST: immediately after device implant, FU: at follow-up) for device B.

Device	Phase	ρ_{conv} (%)	$\%\rho_{diff}$ (%)	τ_{diff} (s)	σ (s)	μ (s)	τ_{conv} (s)	Washout curve amplitude
#B_021_1	PRE	83.80	16.20	73.91	0.51	1.16	1.15	0.26
	POST	51.12	48.88	1916.00	1.17	2.70	2.91	0.12
#B_021_2	PRE	74.17	25.83	12.87	0.55	1.62	0.81	0.47
	POST	33.59	66.41	1985.00	0.68	1.57	4.78	0.06
#B_021_3	PRE	55.08	44.92	22.33	0.77	1.77	0.43	0.14
	POST	72.81	27.19	1810.00	1.10	2.54	14.08	0.08
#B_090_1	PRE	62.39	37.61	50.17	0.51	1.17	1.24	0.13
	POST	84.44	15.56	1848.00	0.89	2.05	17.74	0.08
#B_090_2	PRE	78.09	21.91	1385.00	0.89	2.10	0.10	0.15
	POST	53.38	46.62	262.34	0.79	1.85	1.95	0.10
	FU	18.31	81.69	203.67	0.69	1.59	0.01	0.03
#B_090_3	PRE	67.69	32.31	40.36	0.65	1.56	0.37	0.15
	POST	45.09	54.91	1954.00	0.70	1.61	2.42	0.07
	FU	27.36	72.64	123.01	0.79	1.81	0.01	0.04
#B_180_1	PRE	62.79	37.21	36.02	0.53	1.39	0.69	0.16
	POST	52.10	47.90	1989.00	1.69	3.92	0.18	0.04
#B_180_2	PRE	70.53	29.47	30.65	0.56	1.30	0.66	0.08
	POST	16.45	83.55	55.01	0.59	1.36	0.01	0.08
#B_180_3	PRE	61.63	38.37	43.95	0.85	1.96	0.10	0.10
	POST	73.59	26.41	1700.00	0.93	2.16	0.10	0.12
	FU	88.42	11.58	1857.00	0.71	1.64	0.11	0.16
#B_180_4	PRE	72.91	27.09	22.16	0.85	1.97	0.16	0.13
	POST	66.36	33.64	1947.00	0.52	1.20	3.66	0.11
	FU	76.30	23.70	1106.00	0.64	1.86	0.03	0.14

Table A1.9. Values of the optimized model parameters and the washout curve amplitudes at different treatment phases (PRE: before device implant, POST: immediately after device implant, FU: at follow-up) for device C.

Device	Phase	ρ_{conv} (%)	$\%\rho_{diff}$ (%)	τ_{diff} (s)	σ (s)	μ (s)	τ_{conv} (s)	Washout curve amplitude
#C_021_1	PRE	51.24	48.76	17.47	0.43	0.99	1.19	0.09
	POST	50.38	49.62	1697.00	0.79	1.91	0.15	0.06
	FU	27.95	72.05	34.79	0.60	1.37	1.40	0.05
#C_021_2	PRE	68.21	31.79	29.27	0.66	1.61	1.34	0.17
	POST	29.94	70.06	1978.00	0.47	1.07	8.23	0.07
	FU	54.99	45.01	1938.00	0.55	1.26	7.99	0.10
#C_021_3	PRE	55.91	44.09	20.84	0.69	1.95	0.31	0.14
	POST	15.44	84.56	106.34	1.13	2.60	0.01	0.06
#C_090_1	PRE	77.84	22.16	33.12	0.66	1.78	0.05	0.15
	POST	26.37	73.63	1970.00	0.59	1.35	3.39	0.08
	FU	73.09	26.91	32.21	0.89	2.05	0.08	0.10
#C_090_2	PRE	66.46	33.54	56.51	0.69	1.85	0.20	0.13
	POST	28.68	71.32	1987.00	0.61	1.39	6.32	0.07
	FU	73.30	26.70	1964.00	0.53	1.25	0.19	0.10
#C_090_3	PRE	67.71	32.29	39.18	0.73	1.69	0.16	0.10
	POST	43.08	56.92	154.04	0.71	1.63	1.46	0.07
	FU	60.03	39.97	1954.00	0.73	2.05	0.01	0.07
#C_180_1	PRE	77.11	22.89	18.27	0.66	1.51	0.17	0.11
	POST	8.93	91.07	222.10	0.89	2.05	0.01	0.06
#C_180_2	PRE	67.90	32.10	25.95	0.50	1.14	1.01	0.14
	POST	36.38	63.62	139.09	0.92	2.12	2.61	0.08
#C_180_3	PRE	70.04	29.96	56.76	0.89	2.05	0.06	0.16
	POST	14.55	85.45	58.91	0.63	1.44	0.01	0.07
#C_180_4	PRE	75.53	24.47	1914.00	0.52	1.20	2.19	0.13
	POST	58.38	41.62	1978.00	0.77	1.78	5.52	0.08
	FU	42.42	57.58	173.57	0.47	1.08	12.80	0.08

Table A1.10. Values of the optimized model parameters and the washout curve amplitudes at different treatment phases (PRE: before device implant, POST: immediately after device implant, FU: at follow-up) for device E.

Device	Phase	ρ_{conv} (%)	%ρ_{diff} (%)	τ_{diff} (s)	σ (s)	μ (s)	τ_{conv} (s)	Washout curve amplitude
#E_021_1	PRE	77.36	22.64	10.41	0.51	1.16	0.88	0.26
	POST	81.30	18.70	1870.00	0.79	1.82	7.28	0.07
#E_021_2	PRE	80.47	19.53	1867.00	0.67	1.54	9.98	0.13
	POST	47.12	52.88	1931.00	0.78	1.80	13.47	0.06
#E_021_3	PRE	90.38	9.62	28.85	0.64	1.48	0.27	0.57
	POST	48.13	51.87	26.51	0.82	1.88	0.15	0.07
	FU	18.65	81.35	102.77	0.60	1.38	0.01	0.03
#E_090_1	PRE	67.50	32.50	1934.00	0.59	1.35	0.63	0.08
	POST	38.01	61.99	1980.00	0.62	1.43	6.27	0.06
#E_090_2	PRE	59.19	40.81	40.26	0.46	1.06	2.50	0.10
	POST	36.67	63.33	216.00	0.64	1.48	3.51	0.11
#E_090_3	PRE	79.29	20.71	1975.00	0.50	1.14	6.06	0.11
	POST	25.41	74.59	1981.00	0.40	0.91	7.16	0.07
	FU	36.17	63.83	39.90	0.92	2.13	0.56	0.04
#E_180_1	PRE	67.75	32.25	28.19	0.46	1.04	0.86	0.12
	POST	53.27	46.73	1980.00	0.60	1.38	0.70	0.05
#E_180_2	PRE	73.71	26.29	24.19	0.50	1.15	0.69	0.16
	POST	62.25	37.75	1987.00	0.50	1.14	2.14	0.11
	FU	12.91	87.09	20.98	0.27	0.61	0.01	0.02
#E_180_3	PRE	65.40	34.60	37.94	0.55	1.35	2.73	0.13
	POST	56.03	43.97	1749.00	0.69	1.85	11.83	0.08
	FU	12.08	87.92	1569.00	0.20	0.45	0.01	0.02
#E_180_4	PRE	82.56	17.44	91.25	0.81	1.94	0.09	0.37
	POST	57.90	42.10	113.35	0.73	1.68	1.21	0.23
	FU	81.15	18.85	41.02	0.76	1.94	0.50	0.32

Table A1.11. The Pearson correlation coefficient (*r*) and the Kolmogorov-Smirnov statistic (*D*) for each of the model-fits. The critical value of D at 5% significance is 0.866.

Rabbit ID	PRE		POST		FU	
	r	*D*	*r*	*D*	*r*	*D*
#B_021_1	0.98	2.00	0.95	0.61		
#B_021_3	0.97	0.52	0.93	0.61		
#B_090_1	0.95	1.02	0.90	0.70		
#B_090_2	0.94	1.42	0.92	0.66	0.54	0.99
#B_090_3	0.95	1.12	0.80	0.43	0.36	0.64
#B_180_1	0.97	0.61	0.78	0.60		
#B_180_2	0.93	0.43	0.91	0.61		
#B_180_3	0.89	1.36	0.92	1.00	0.92	0.80
#B_180_4	0.97	0.60	0.94	0.70	0.97	1.02
#C_021_1	0.93	0.53	0.66	0.69	0.74	0.60
#C_021_2	0.99	0.60	0.87	0.47	0.93	0.65
#C_021_3	0.94	0.82	0.78	0.76		
#C_090_1	0.93	1.11	0.93	0.78	0.90	0.95
#C_090_2	0.95	0.82	0.71	0.60	0.89	0.63
#C_090_3	0.91	0.50	0.81	0.78	0.83	0.47
#C_180_1	0.96	0.75	0.90	0.52		
#C_180_2	0.96	0.67	0.89	0.60		
#C_180_3	0.96	0.75	0.64	0.62		
#C_180_4	0.96	0.59	0.90	0.66	0.89	0.78
#E_021_1	0.99	0.86	0.85	0.60		
#E_021_2	0.94	0.52	0.71	0.80		
#E_090_1	0.93	0.57	0.86	0.60		
#E_090_2	0.96	0.59	0.95	0.73		
#E_090_3	0.96	0.93	0.74	1.36	0.50	0.55
#E_180_1	0.95	1.18	0.60	0.95		
#E_180_2	0.96	1.07	0.91	0.58	0.16	0.44
#E_180_3	0.98	0.50	0.93	0.46	0.11	0.68

Table A1.12. Ratios of proximal device diameter to distal device diameter.

Rabbit ID	Proximal Diameter (pixels)	Distal Diameter (pixels)	Proximal/ Distal Diameter	Mean (Standard Error)
#B_021_1	42	20	2.1	
#B_021_2	42	21	2.0	
#B_021_3	46	22	2.1	
#B_090_1	48	36	1.3	
#B_090_2	46	28	1.6	1.6 (0.1)
#B_090_3	47	38	1.2	
#B_180_1	46	34	1.4	
#B_180_2	46	32	1.4	
#B_180_3	51	40	1.3	
#B_180_4	46	32	1.4	
#C_021_1	44	32	1.4	
#C_021_2	52	34	1.5	
#C_021_3	45	35	1.3	
#C_090_1	47	34	1.4	
#C_090_2	42	30	1.4	
#C_090_3	47	33	1.4	1.5 (0.0)
#C_180_1	44	28	1.6	
#C_180_2	43	30	1.5	
#C_180_3	45	27	1.6	
#C_180_4	46	30	1.5	
#E_021_1	37	30	1.3	
#E_021_2	39	25	1.6	
#E_021_3	31	23	1.4	
#E_090_1	38	20	1.9	
#E_090_2	44	30	1.5	1.5 (0.1)
#E_090_3	41	30	1.4	
#E_180_1	44	25	1.8	
#E_180_2	47	39	1.2	
#E_180_3	42	29	1.5	
#E_180_4	37	24	1.5	

Highlighted ratios indicate animals in which delayed filling of the subclavian artery is visualized at follow-up angiography, suggesting partial occlusion of the distal segment of the device

APPENDIX 2

This appendix includes the angiograms showing the maximum opacification of the region of interest (aneurysm) for all 40 animals and the aneurysmal washout curves and corresponding curve-fits for the 30 animals implanted with devices. The first 30 pages relating to the treated animals are formatted identically as per the sketch shown below (Fig A2.1). The last 3 pages show the angiograms from the control animals obtained at initial angiography (marked as "PRE") and at follow-up (marked as "FU"). The values of the optimized parameters corresponding to the curve-fits are listed in Appendix I. The naming system for the animals is the same as in the text.

Animal # Pre-treatment angiogram	Post-treatment angiogram	Follow-up angiogram	Notch-filtered aneurysm washout curves; before treatment (solid black lines), immediately after treatment (solid white lines), and, if aneurysm remains, at follow-up (thin dashed black lines)
Curve-fit for the pre-treatment washout curve Normalized washout curve (dots), model-fit (solid lines), convective component (dotted lines) and diffusive component (dashed lines)	Curve-fit for the post-treatment washout curve Labeling of curves same as for Pre-treatment case	Curve-fit for the follow-up washout curve Labeling of curves same as for Pre-treatment case If aneurysm remnant does not exist, this space is left blank	

Figure A2.1. Format of the angiograms and plots in the following 30 pages corresponding to the 30 treated animals; each page contains information from 1 animal.

#B_021_3
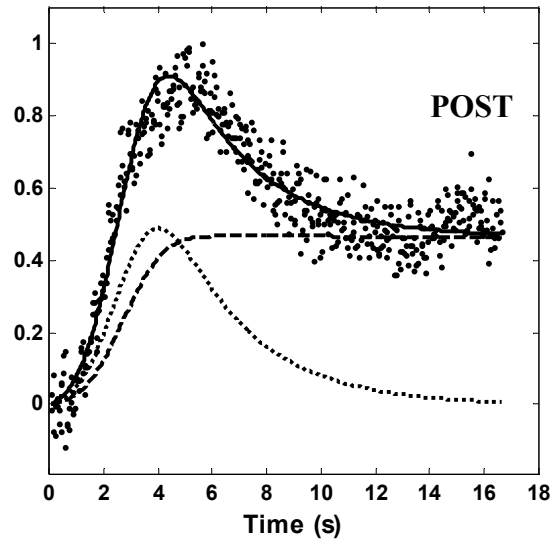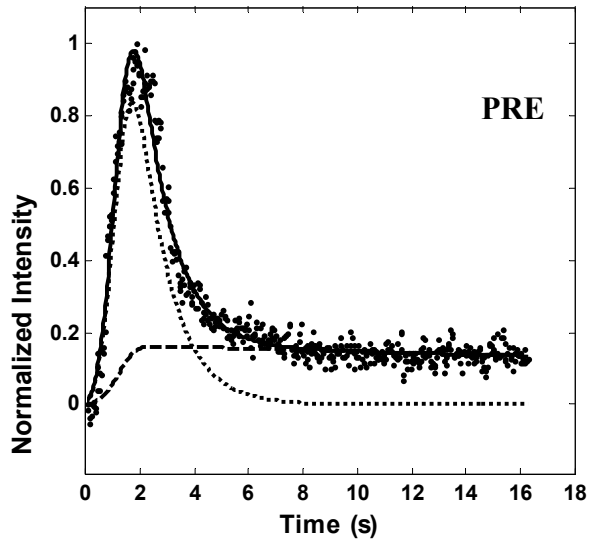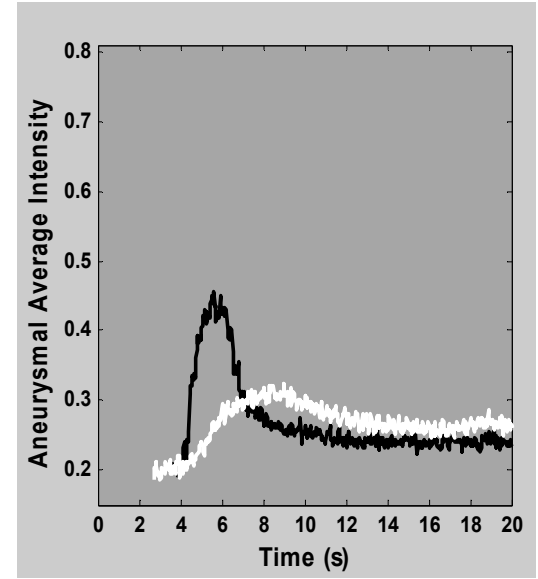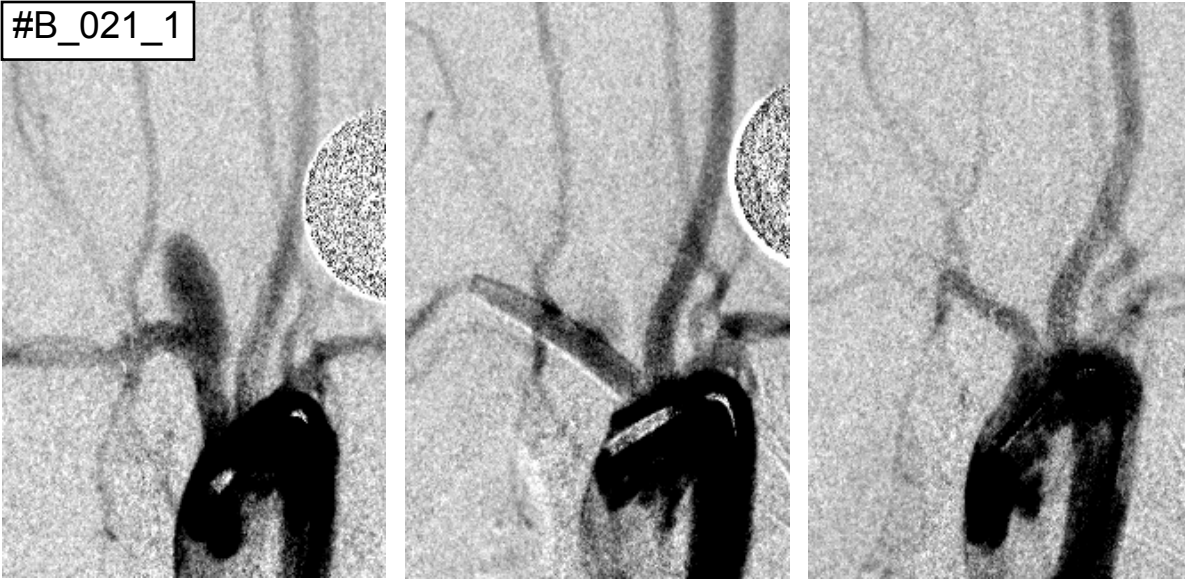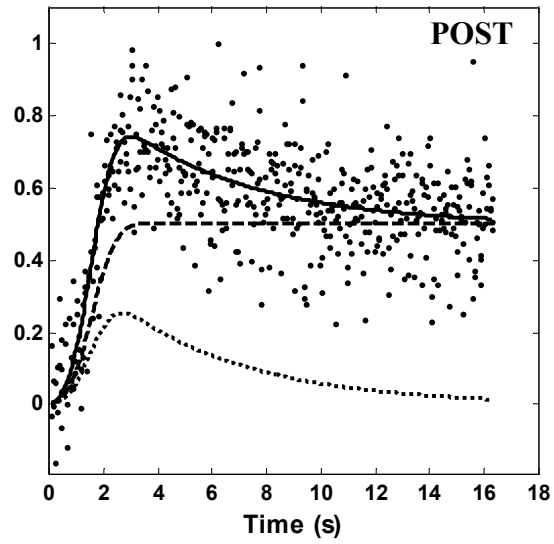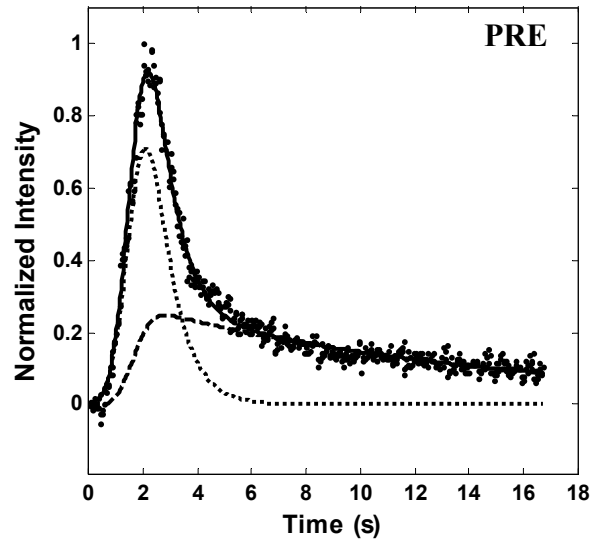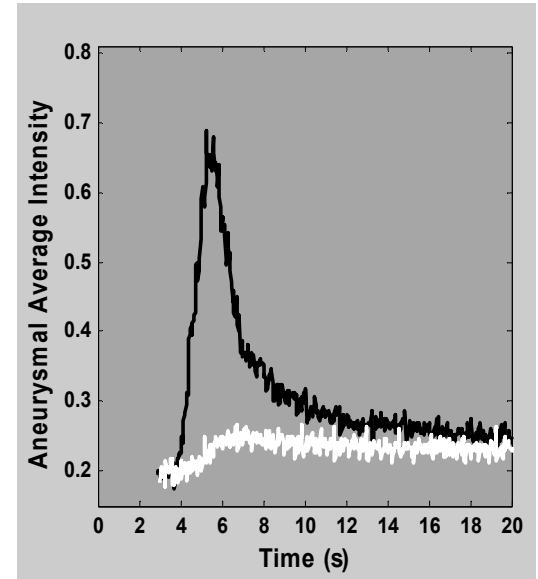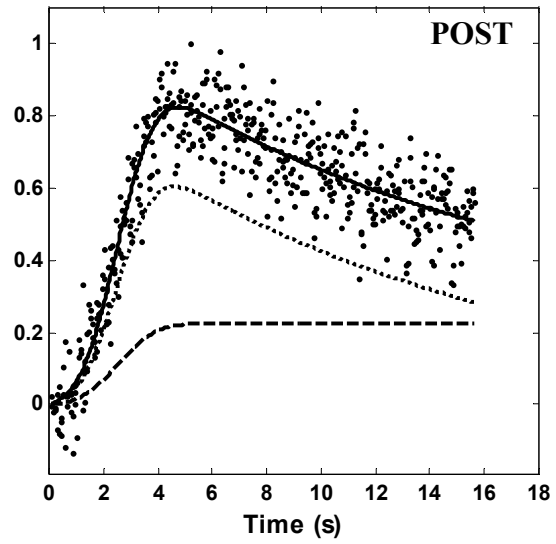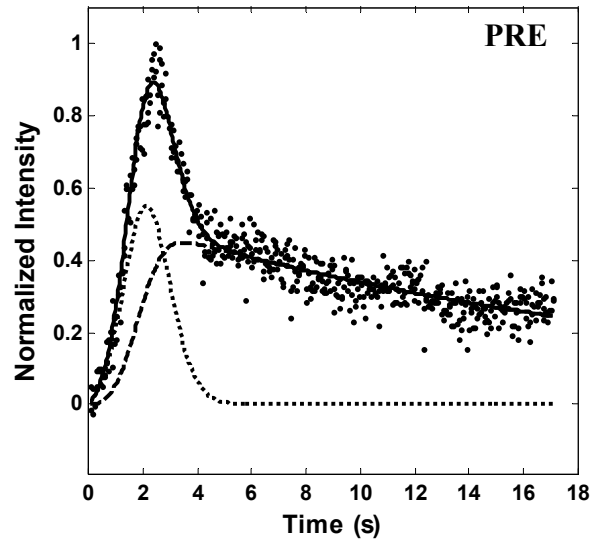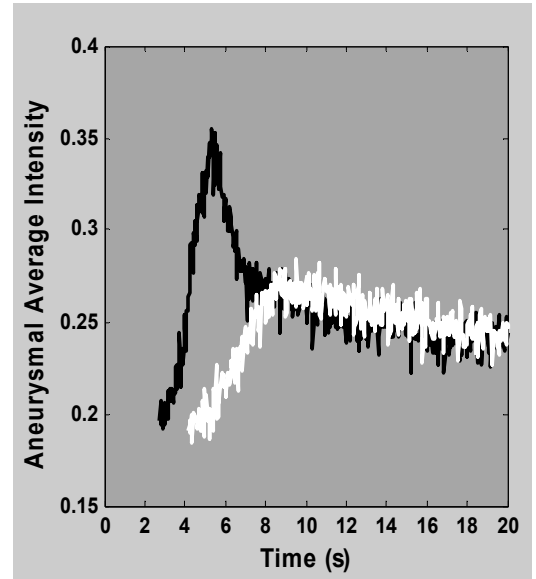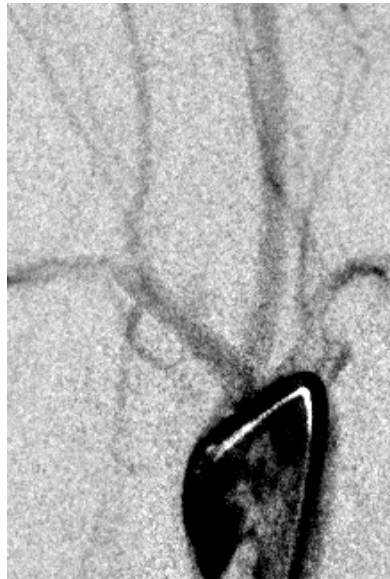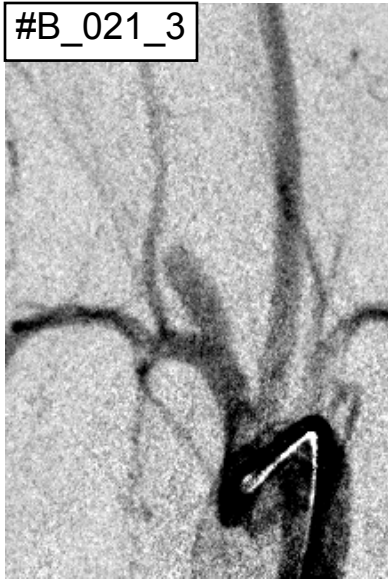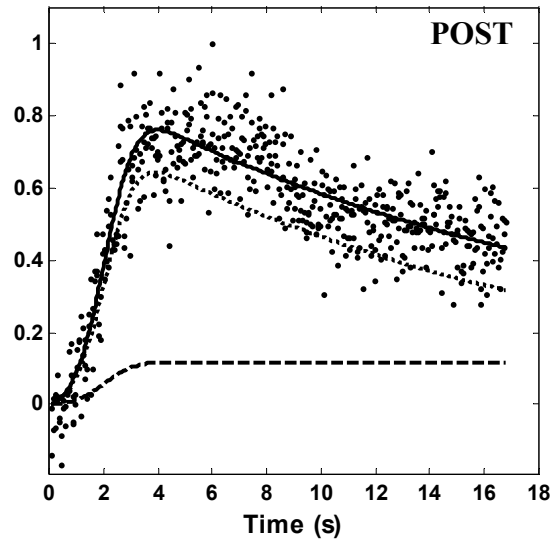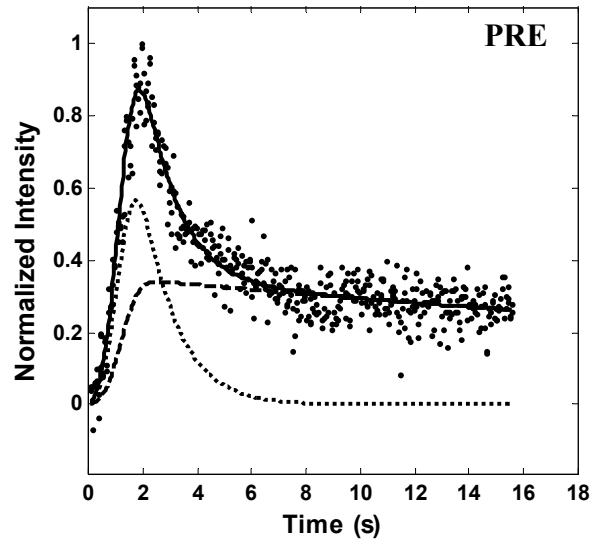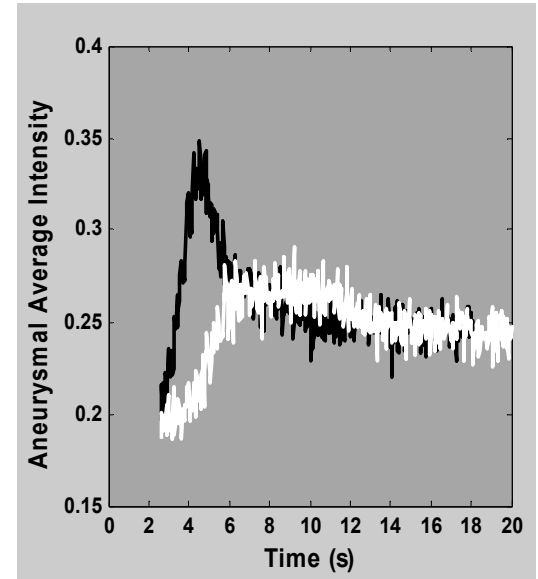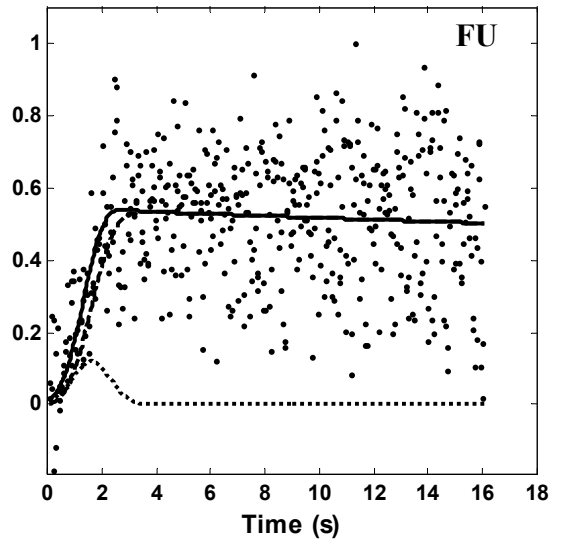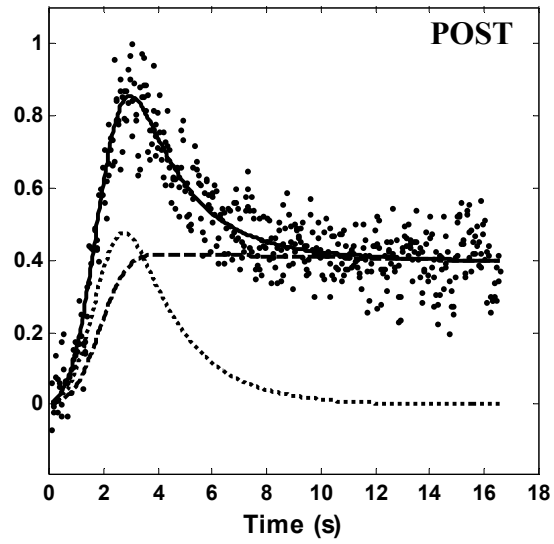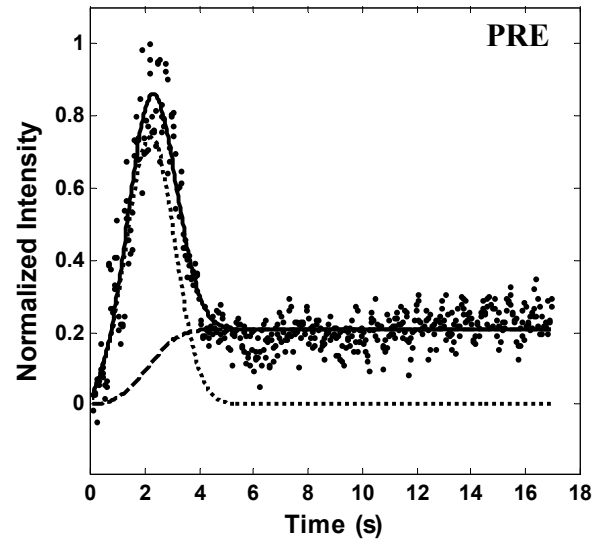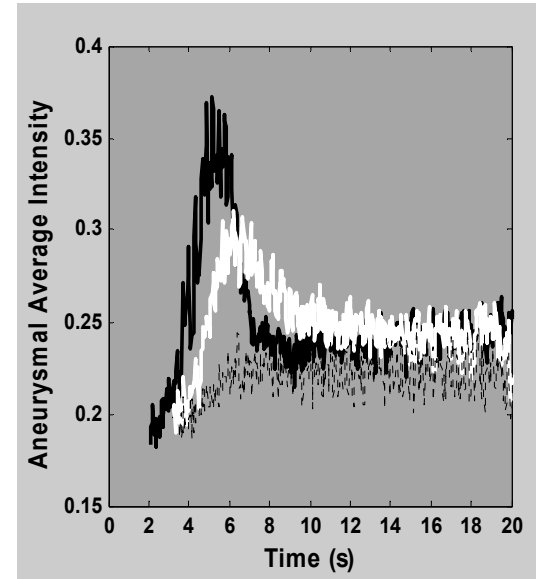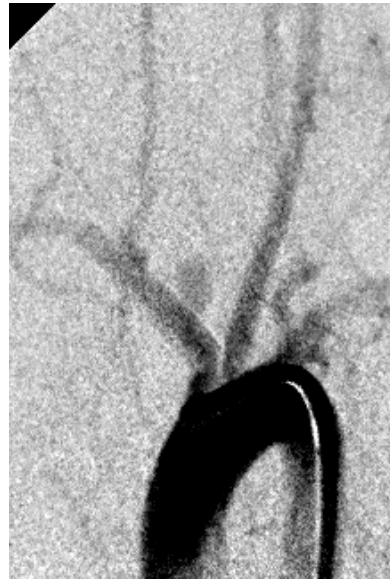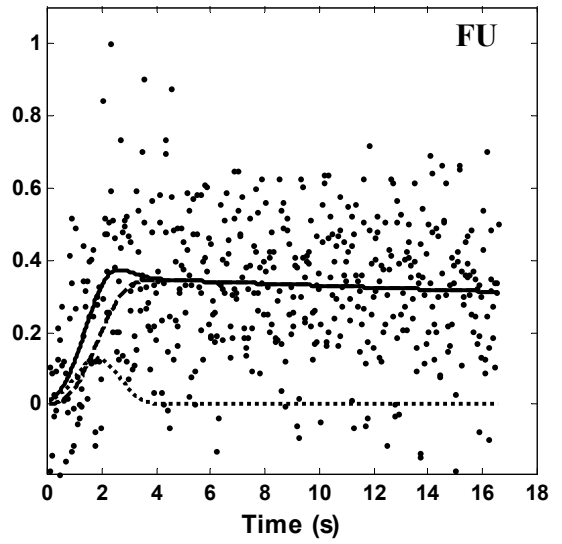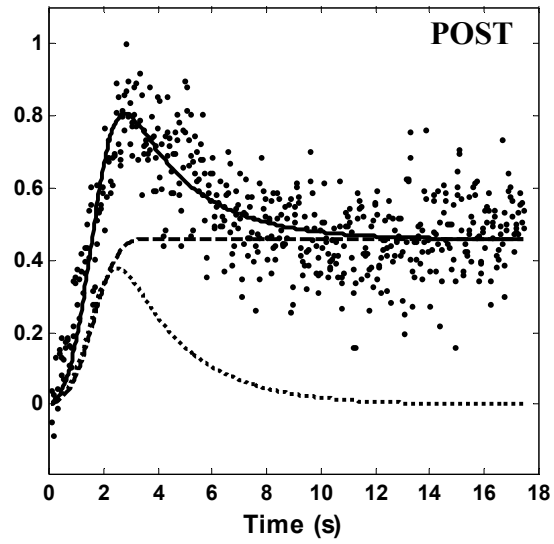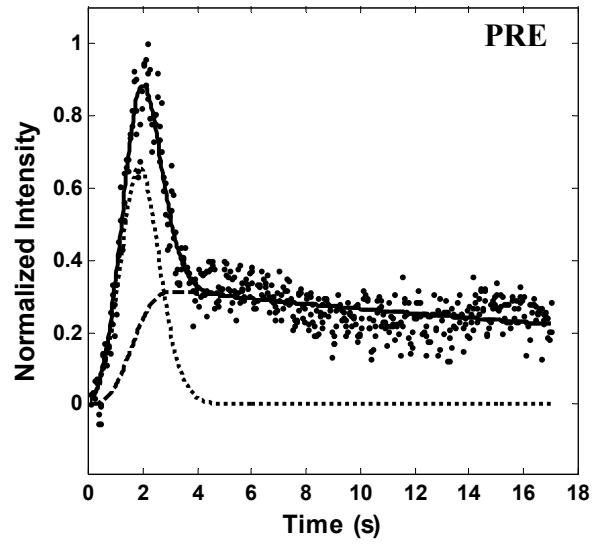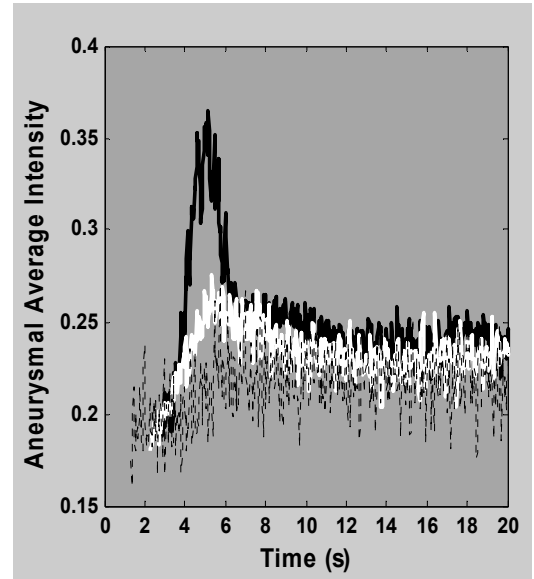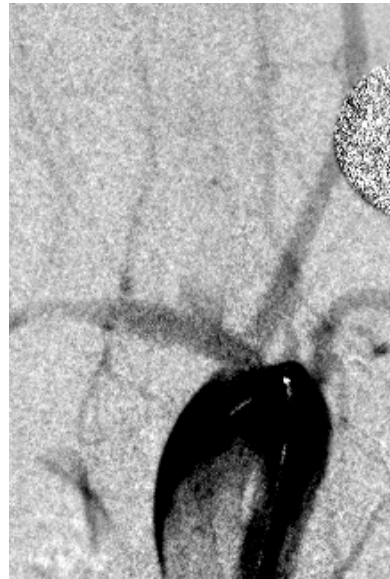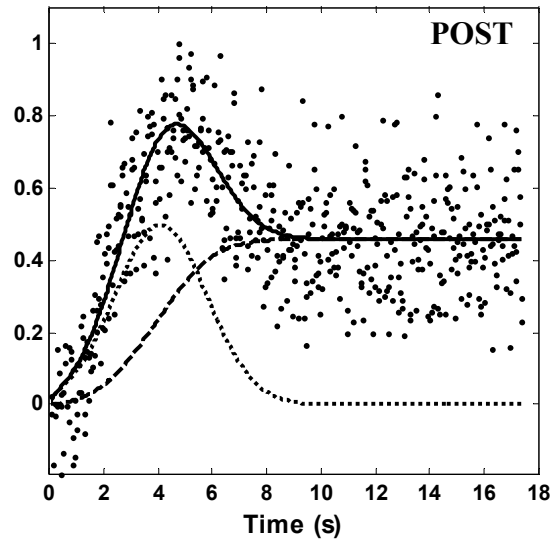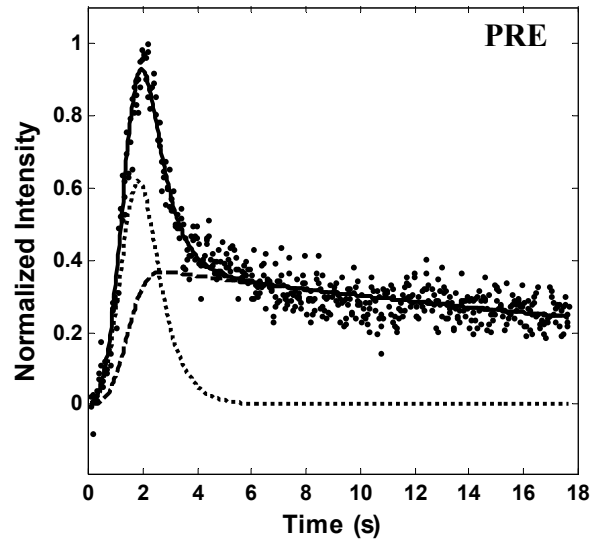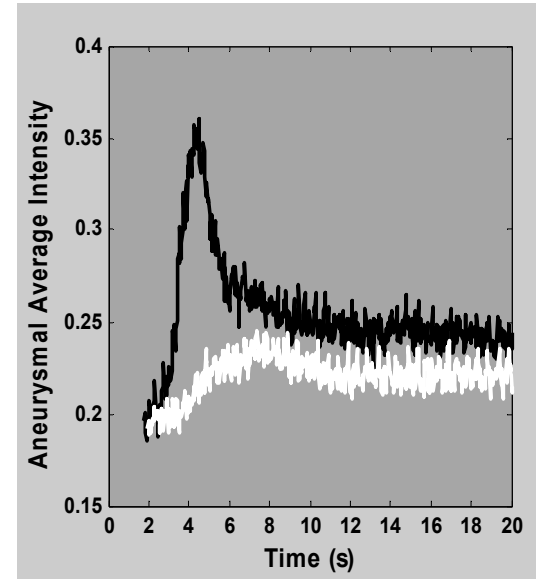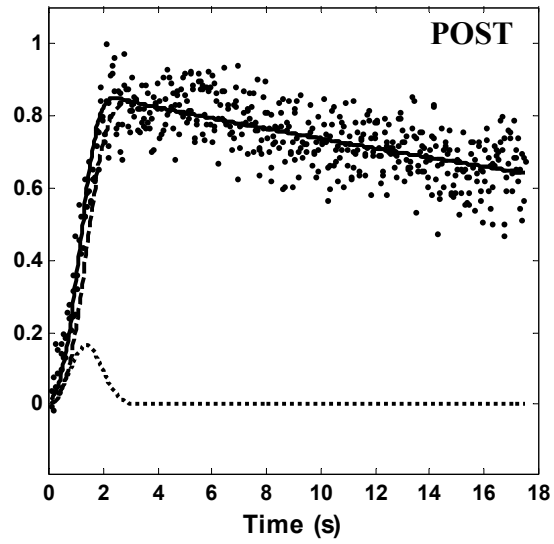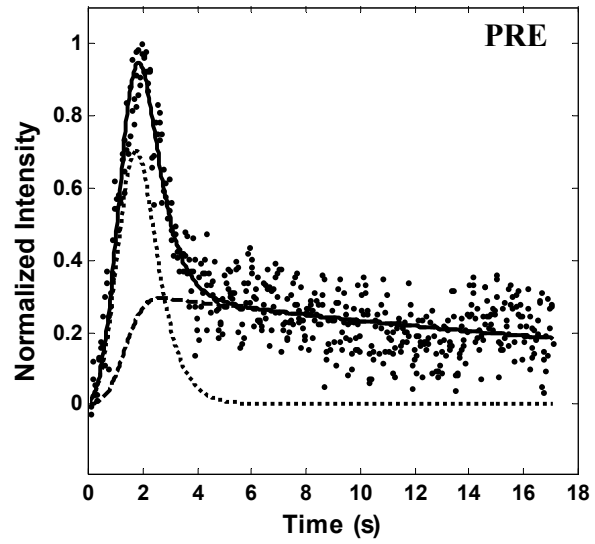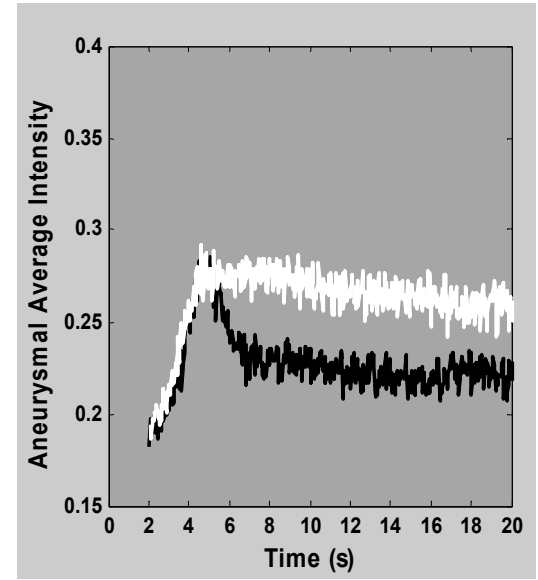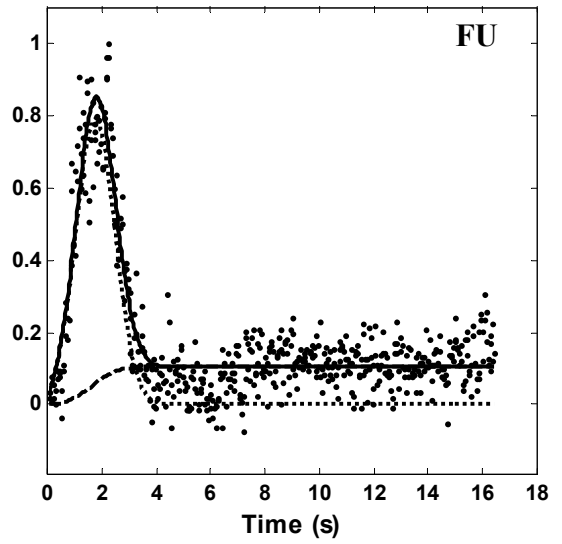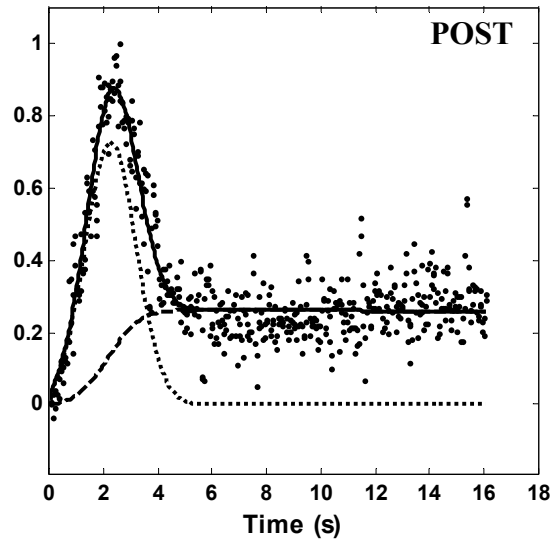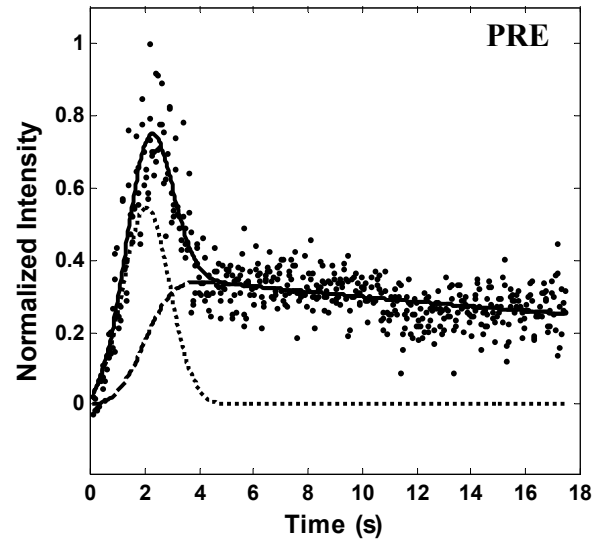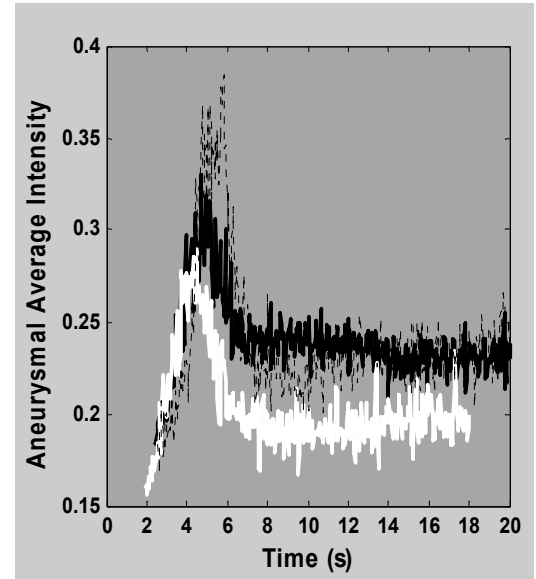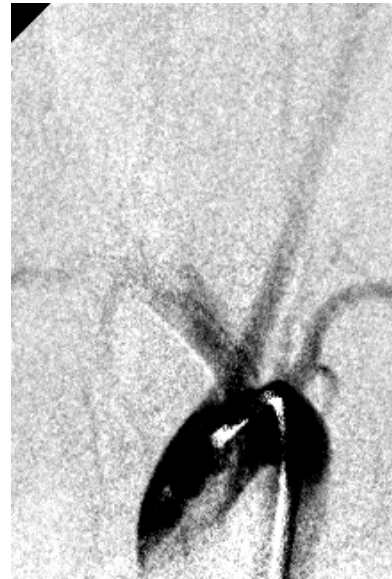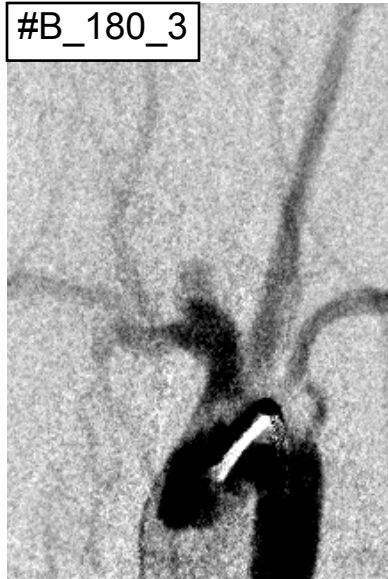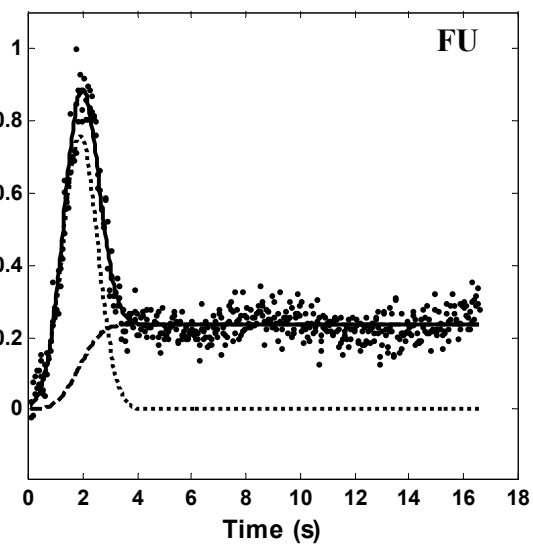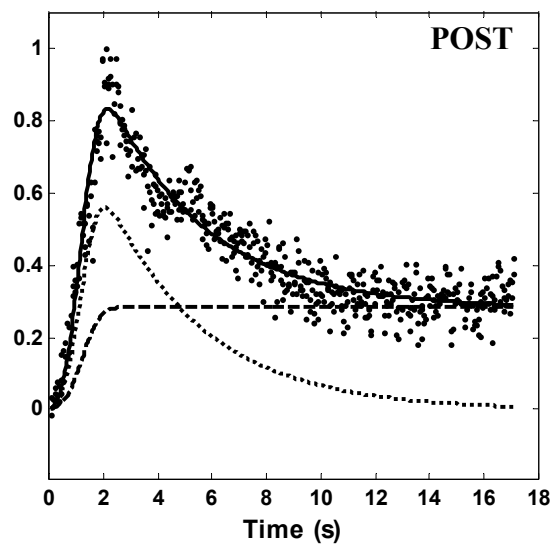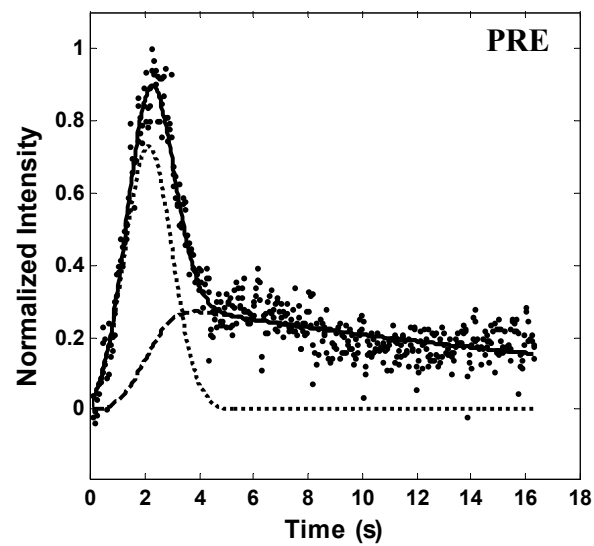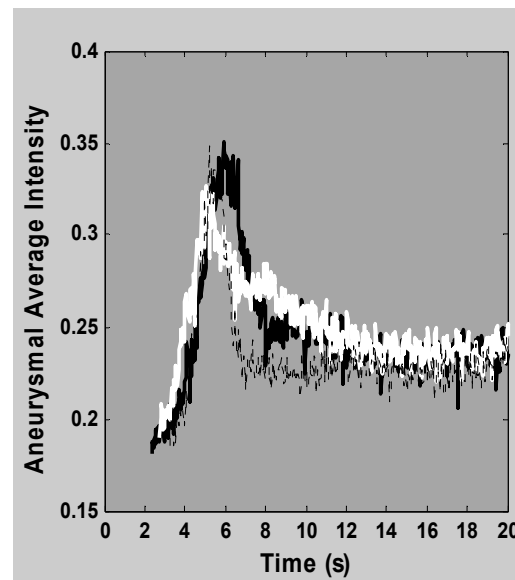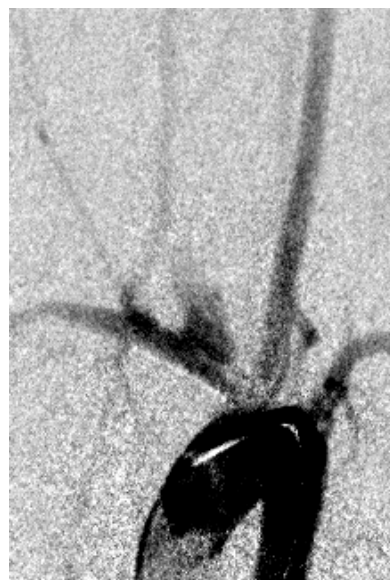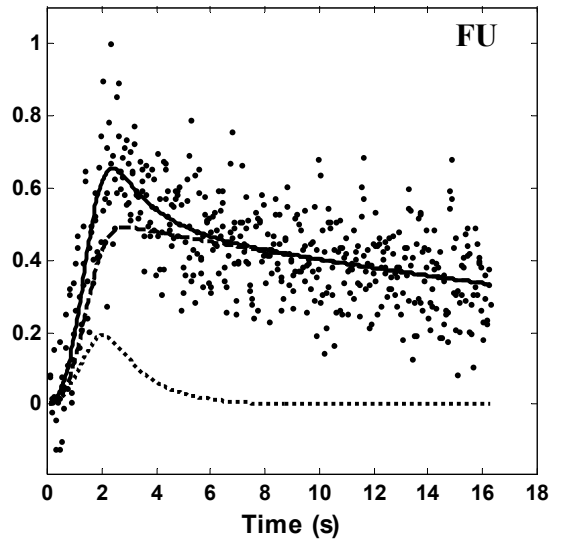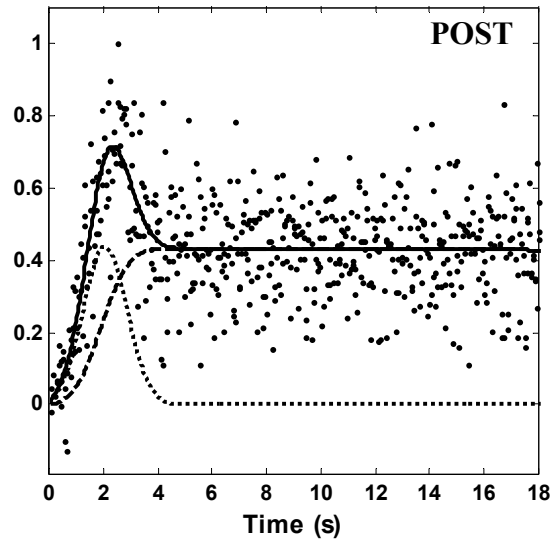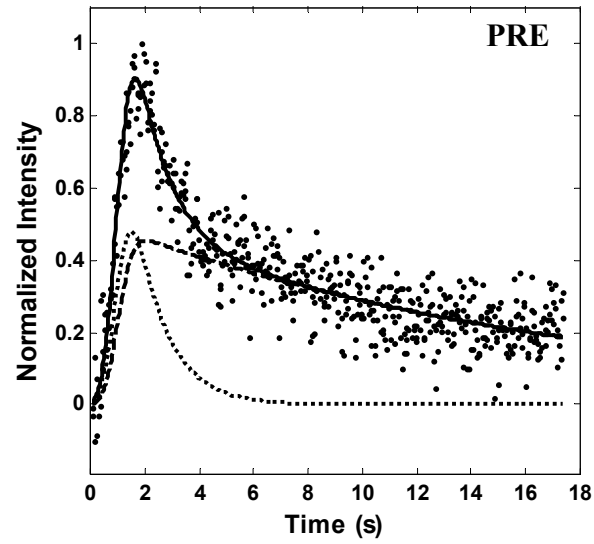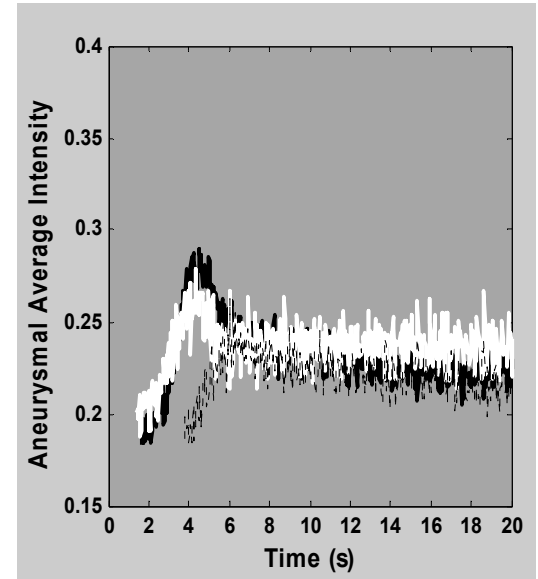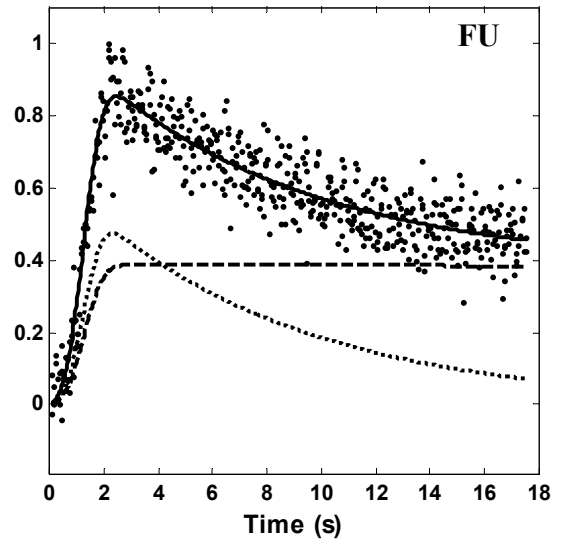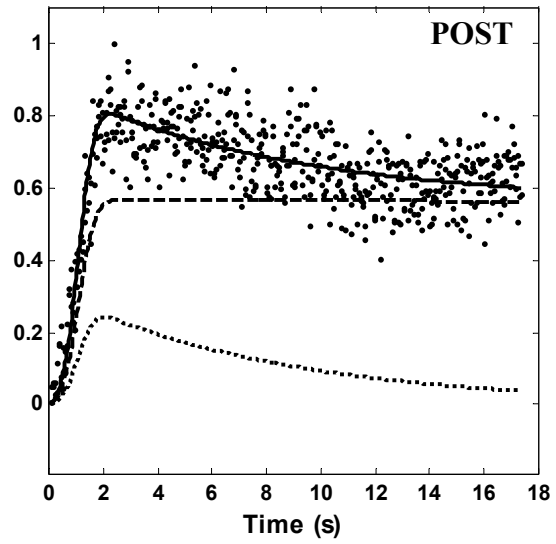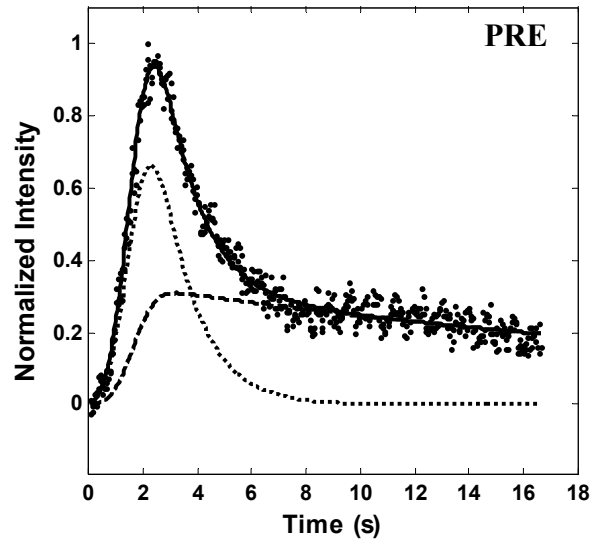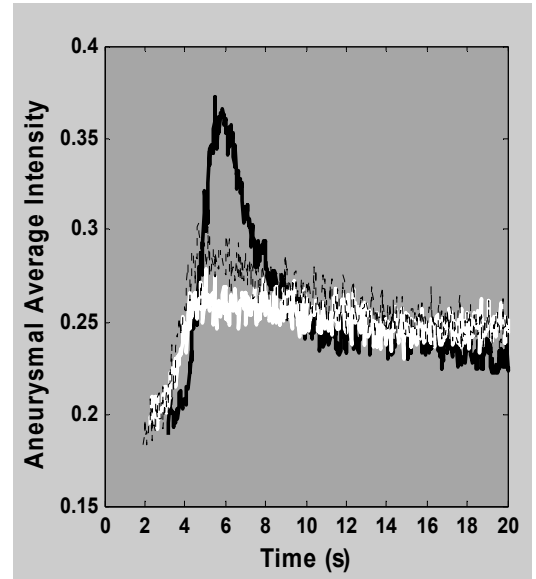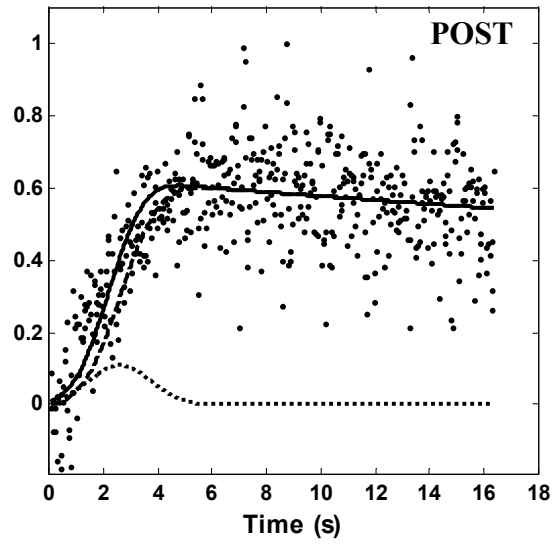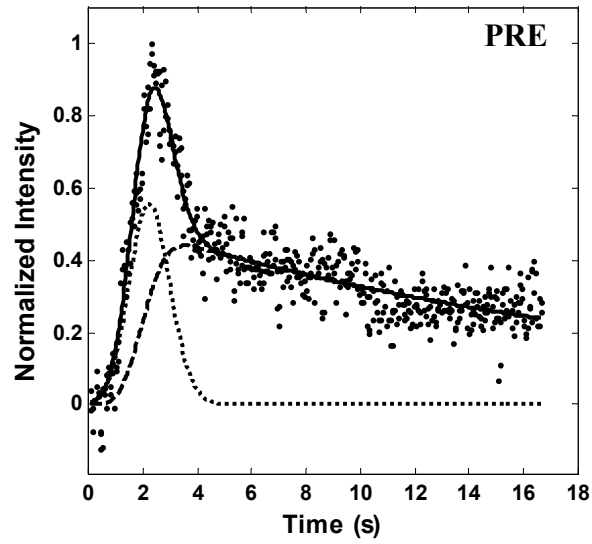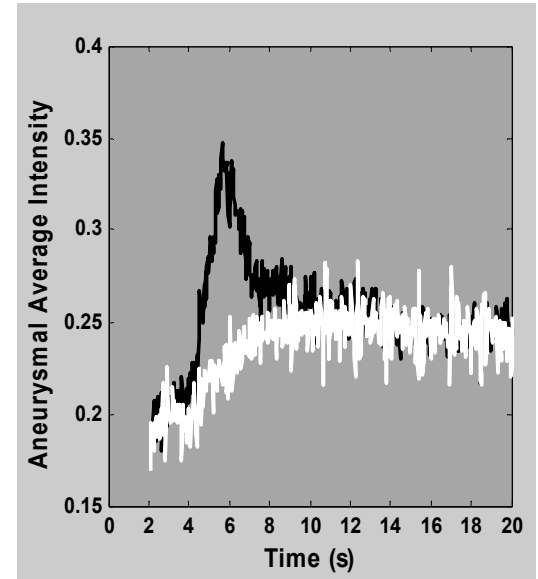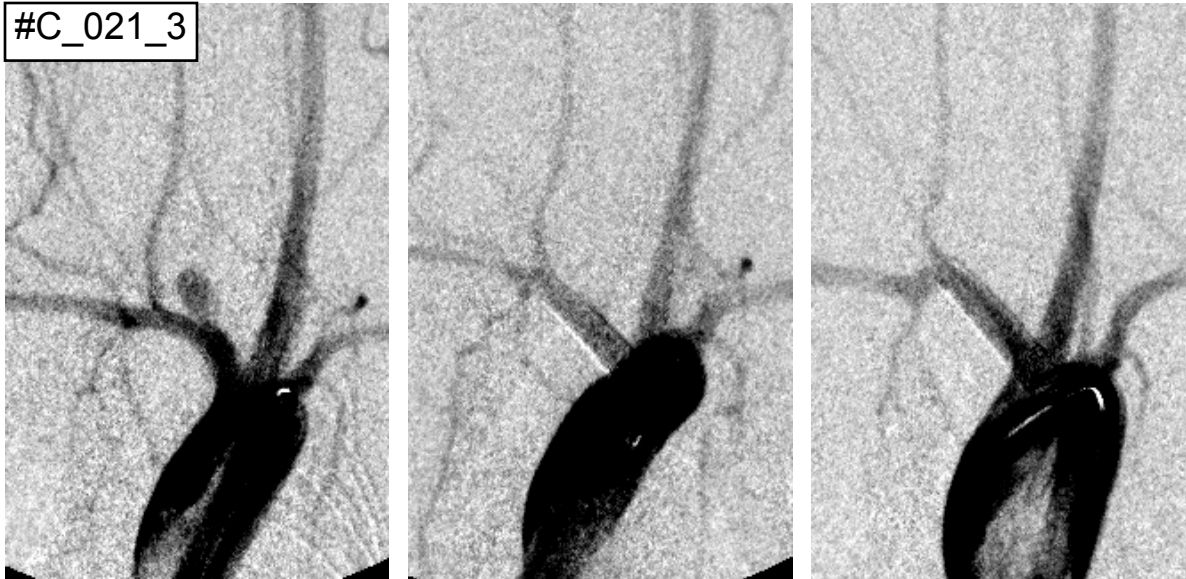
PRE

POST

148

#C_180_1

PRE

POST

#E_021_1

PRE

POST

#O_090_1 PRE FU

#O_090_2 PRE FU

#O_090_3 PRE FU

#O_180_1   PRE   FU

#O_180_2   PRE   FU
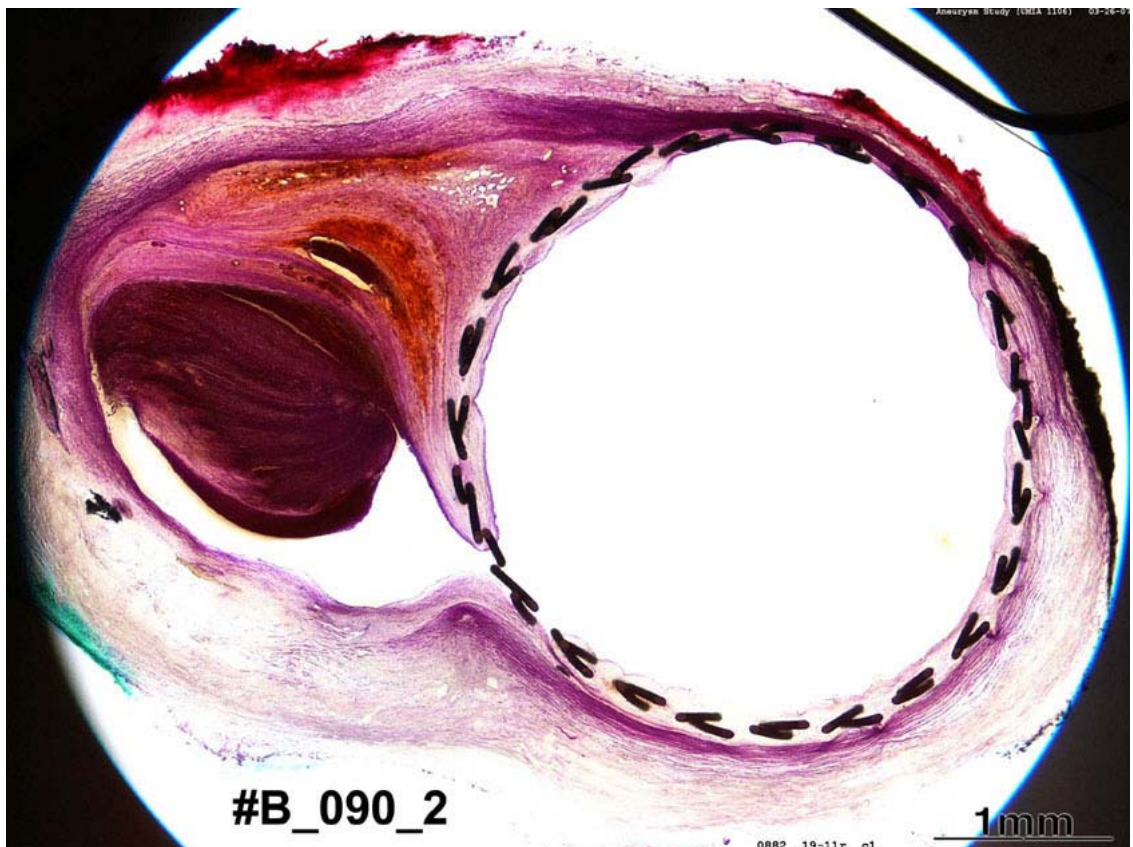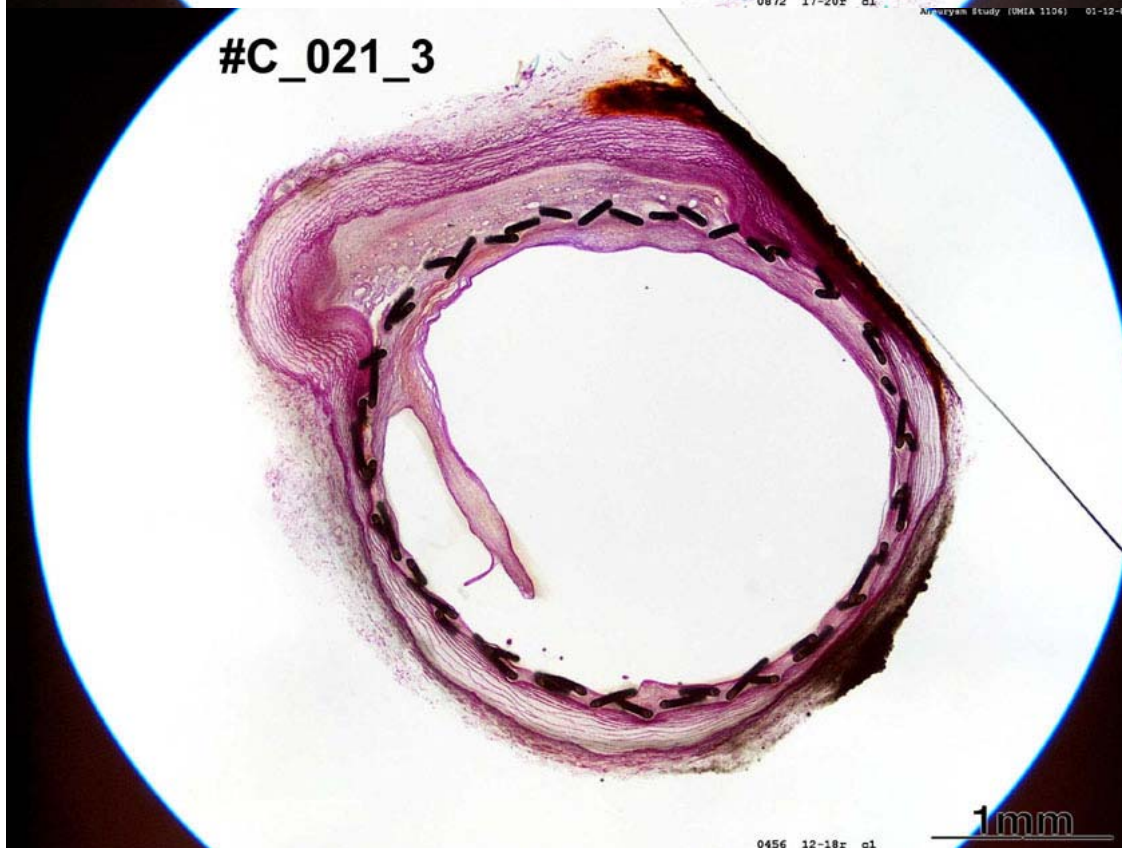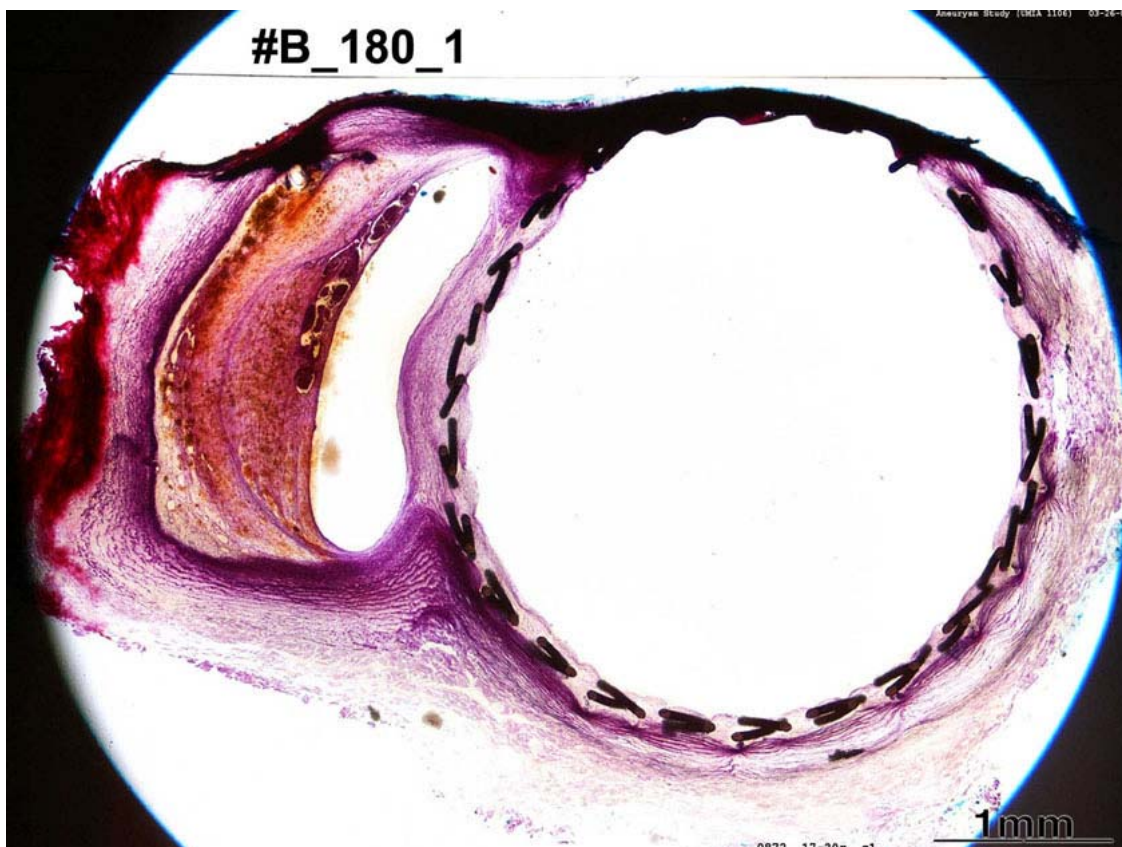
#O_180_3   PRE   FU

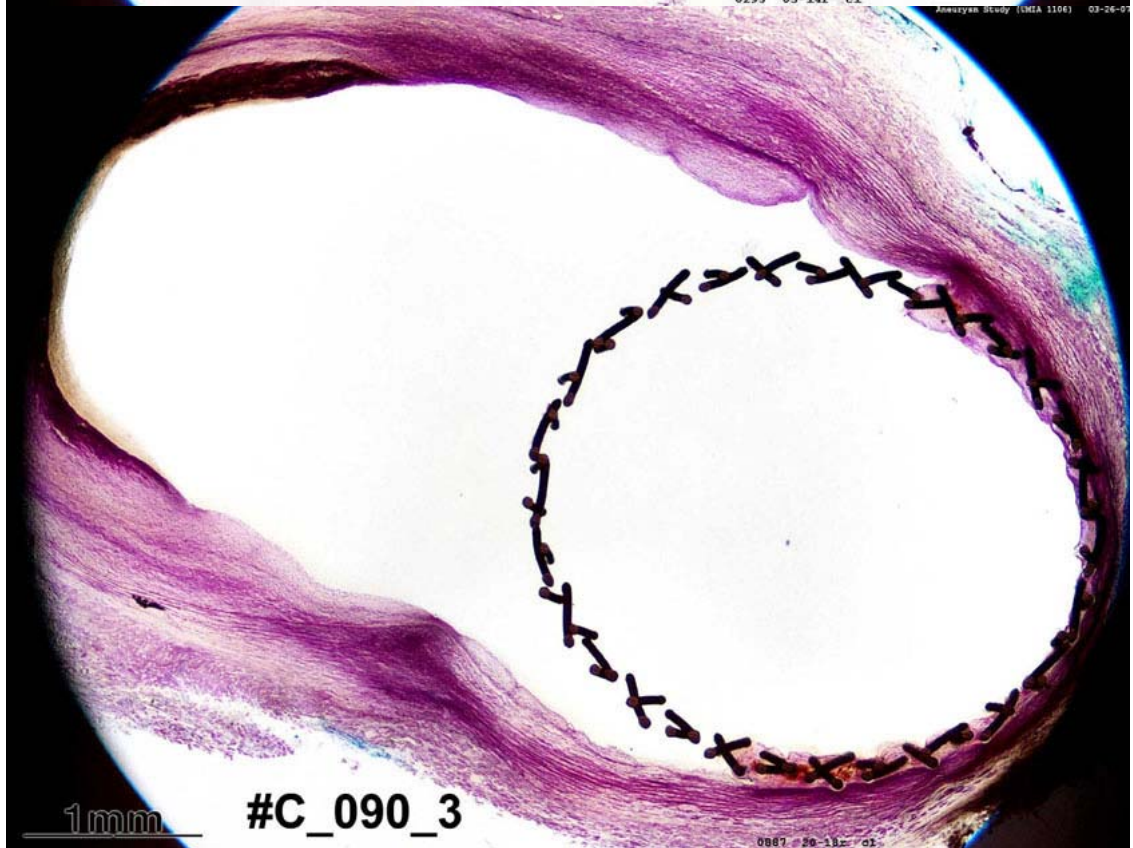#O_180_4   PRE   FU
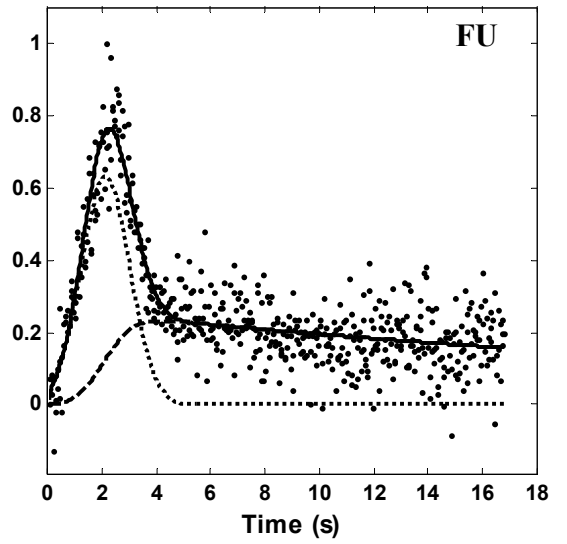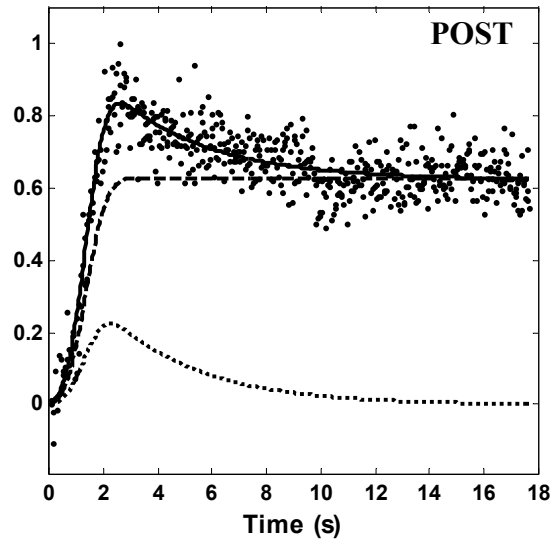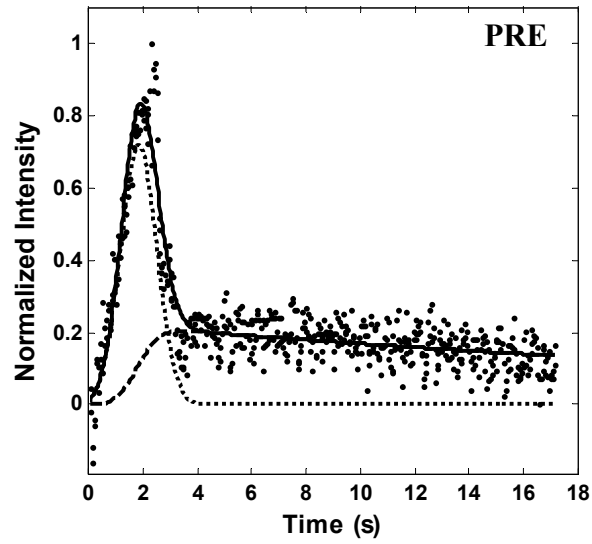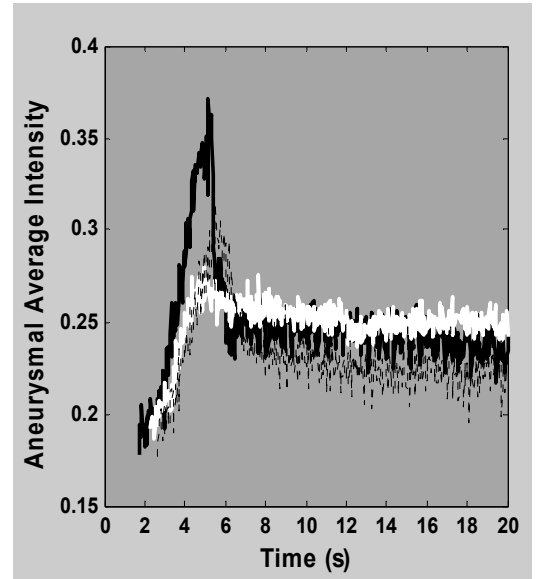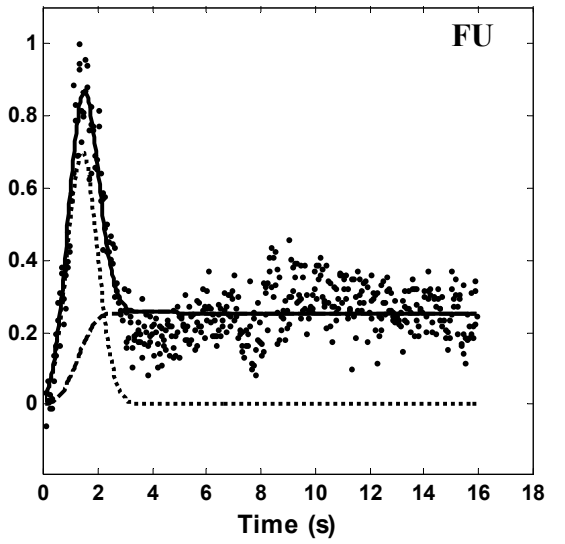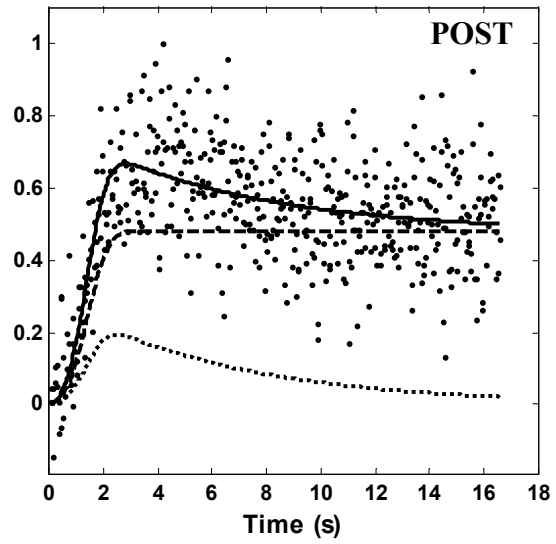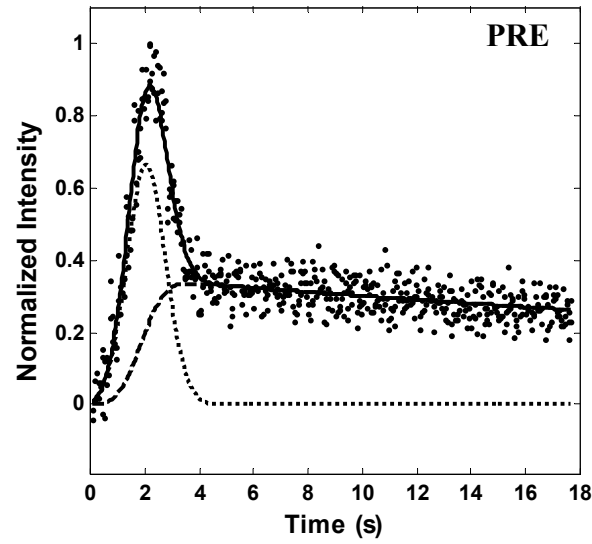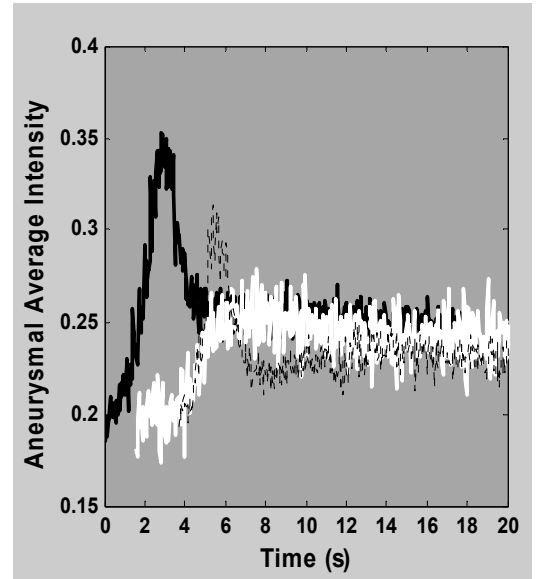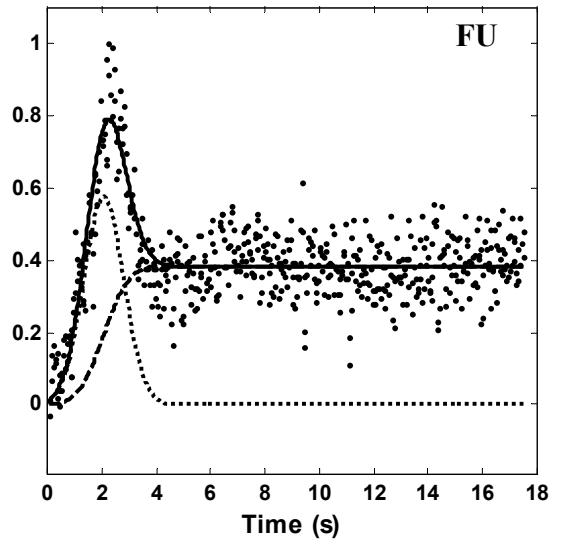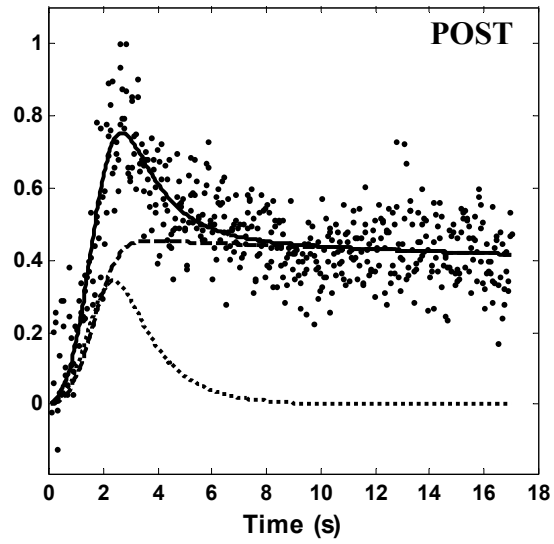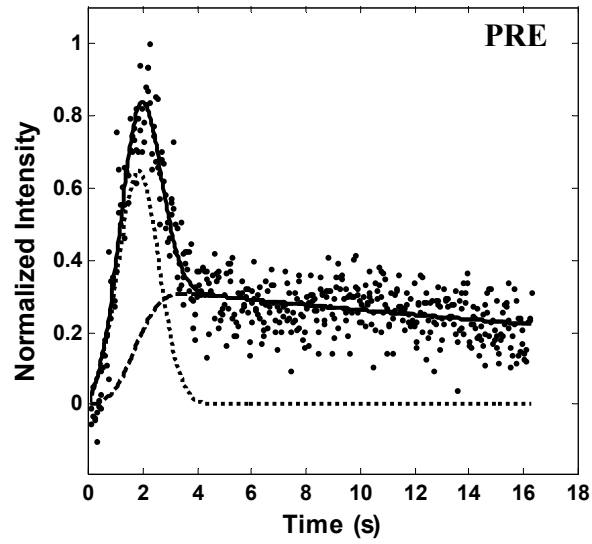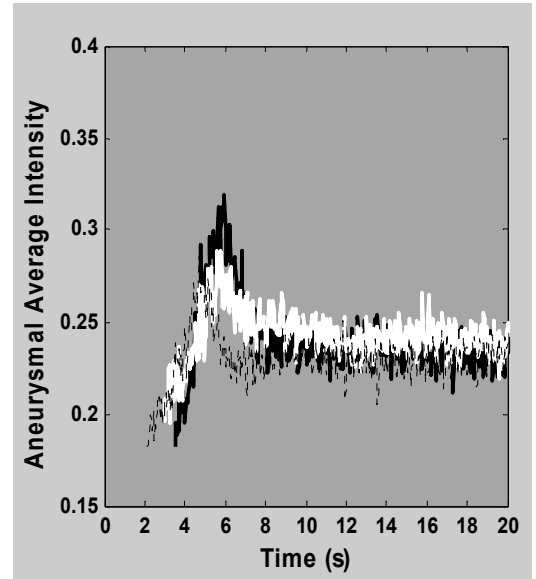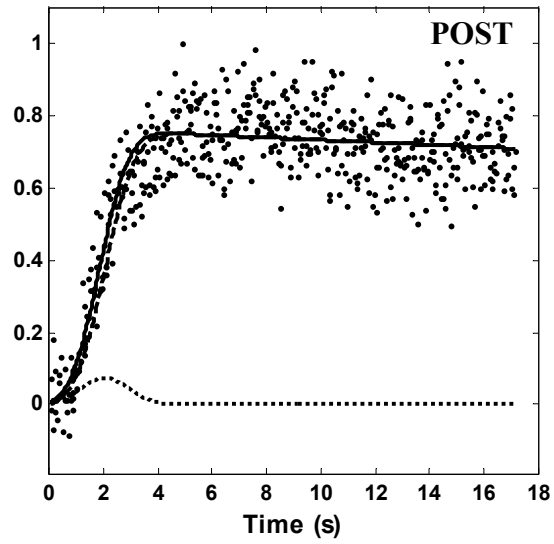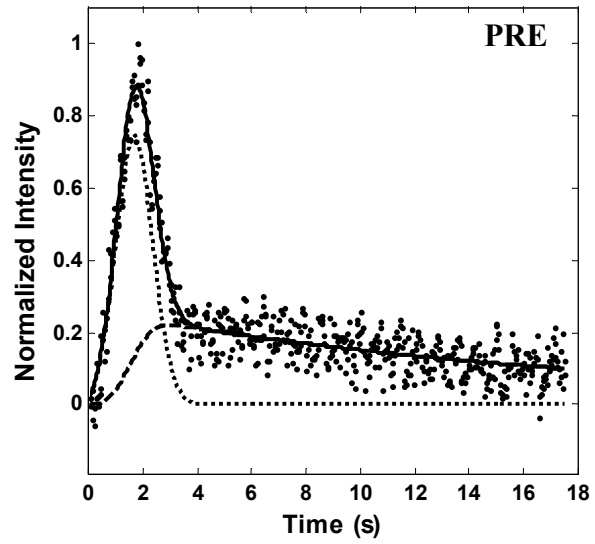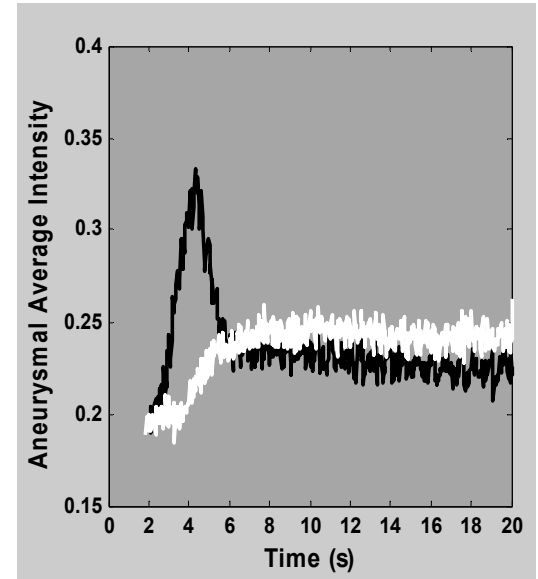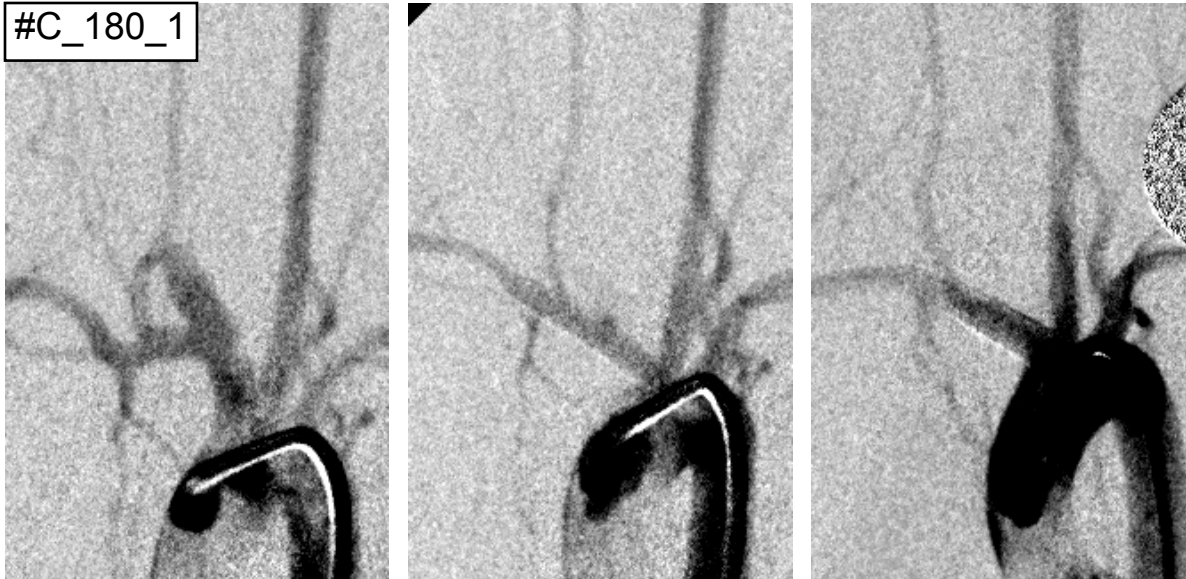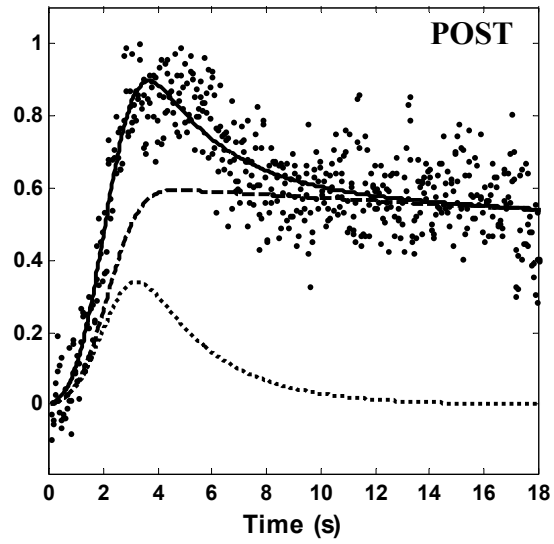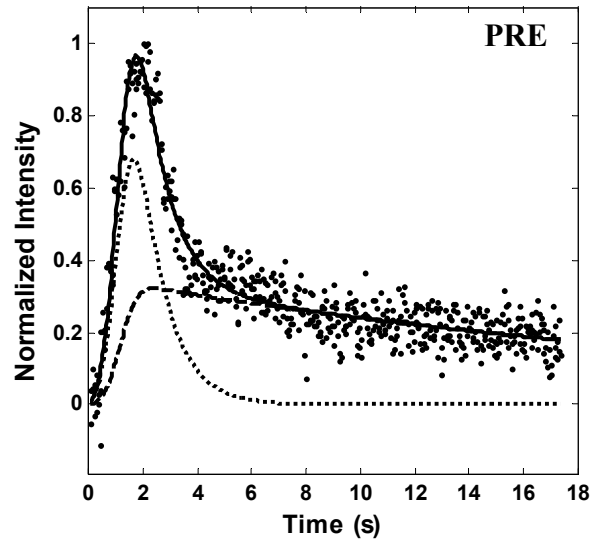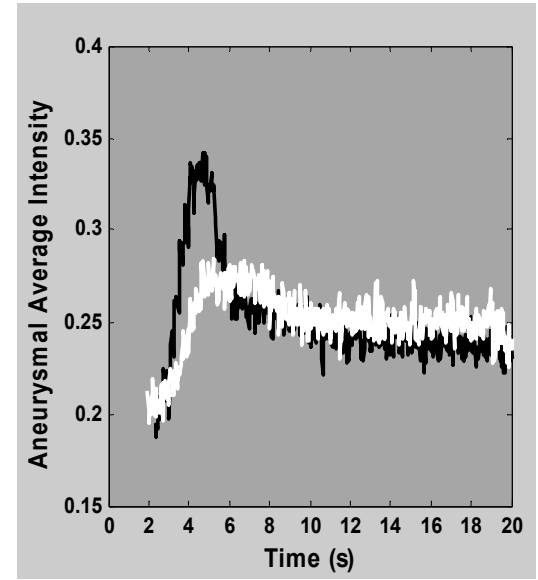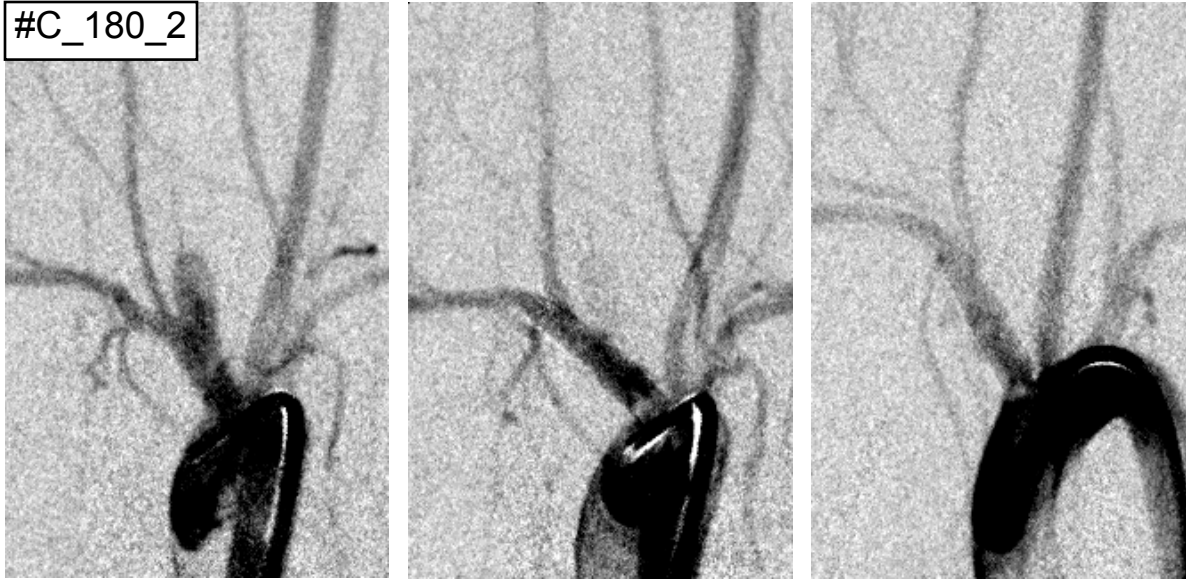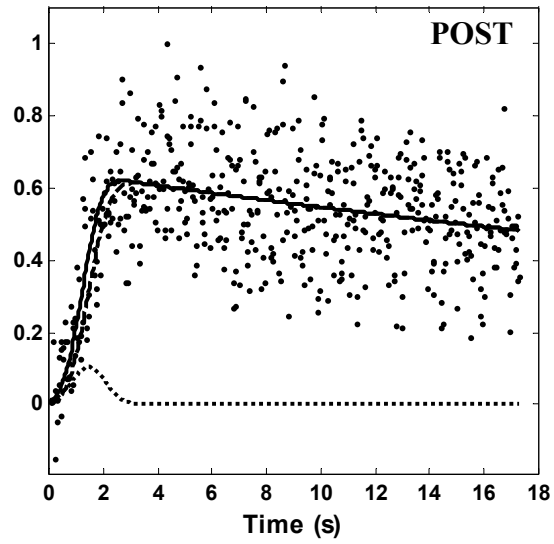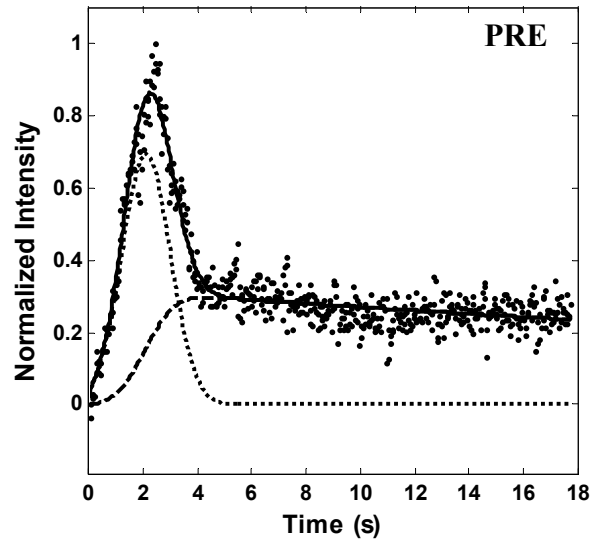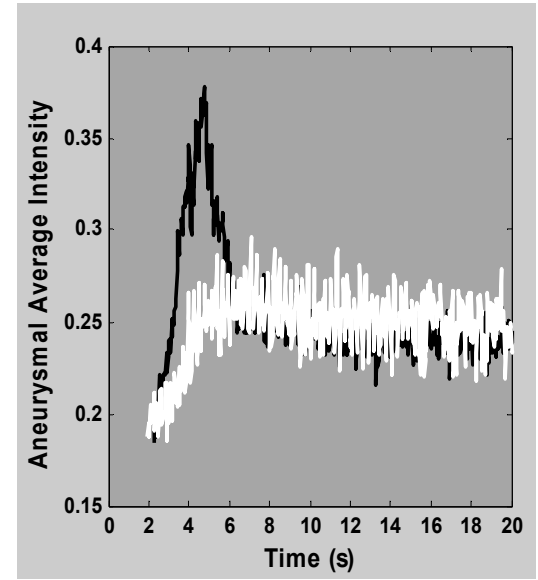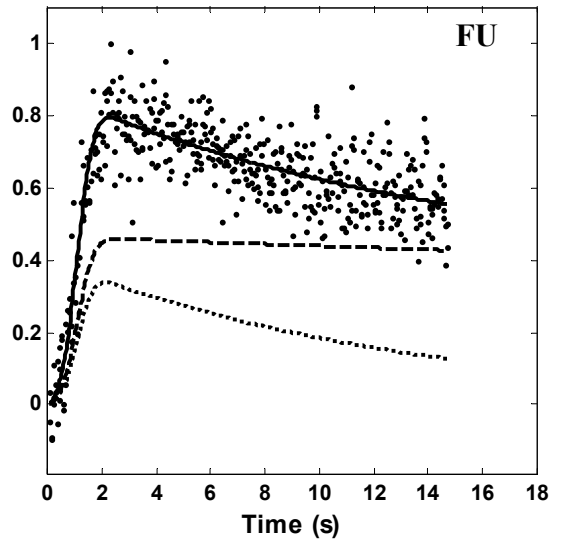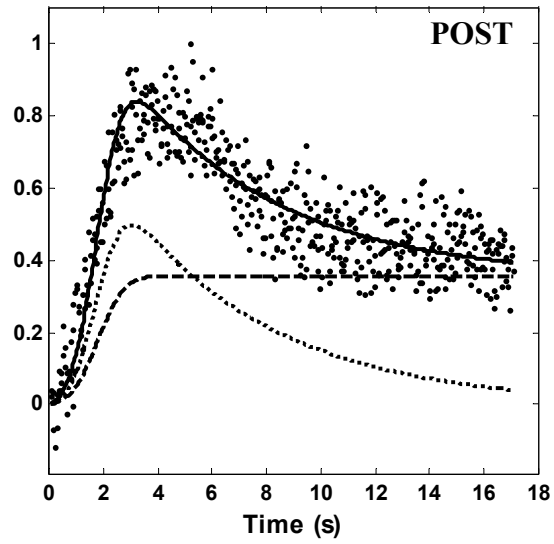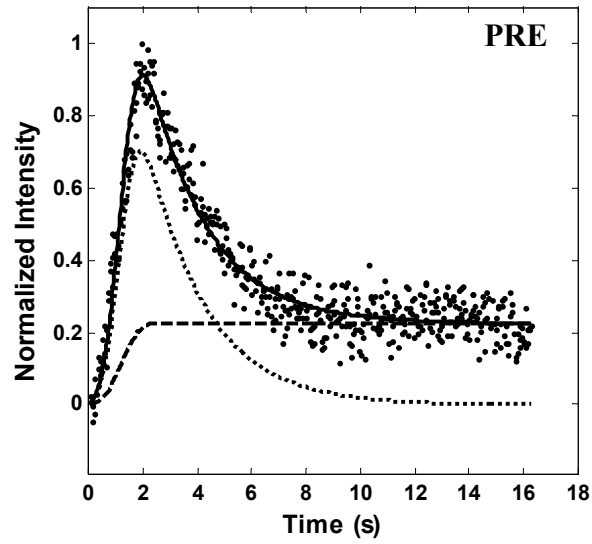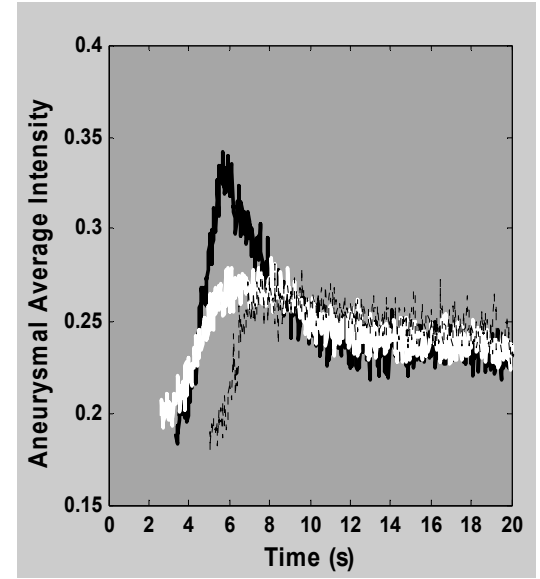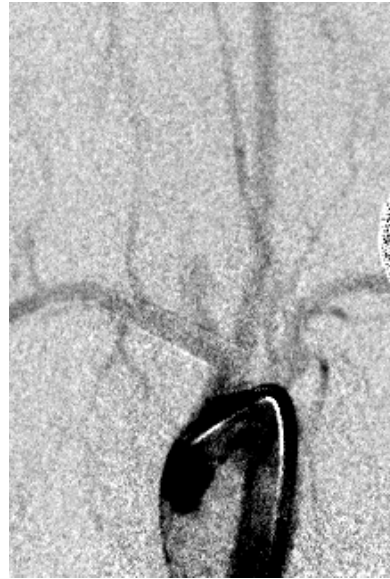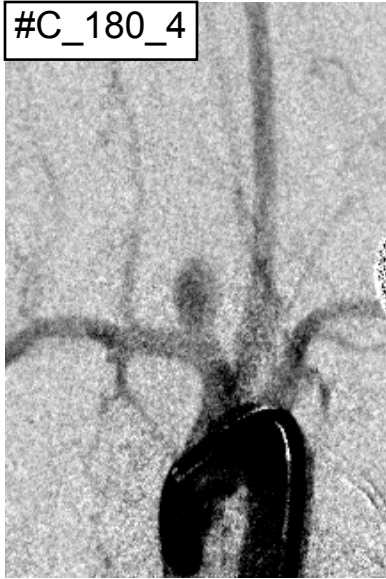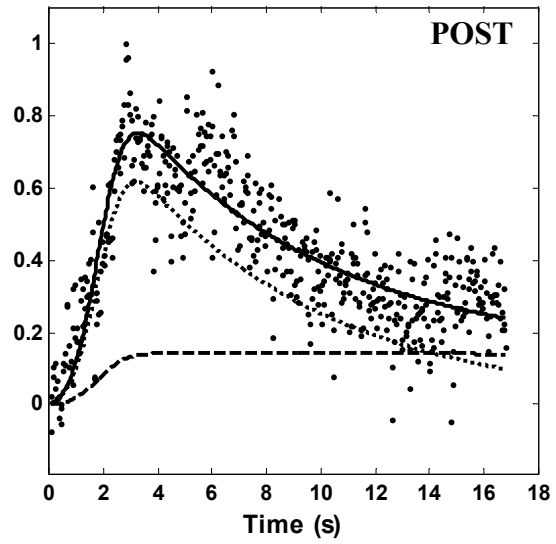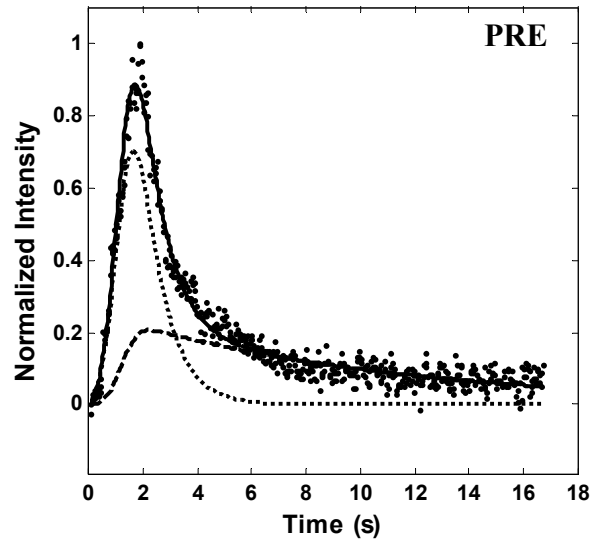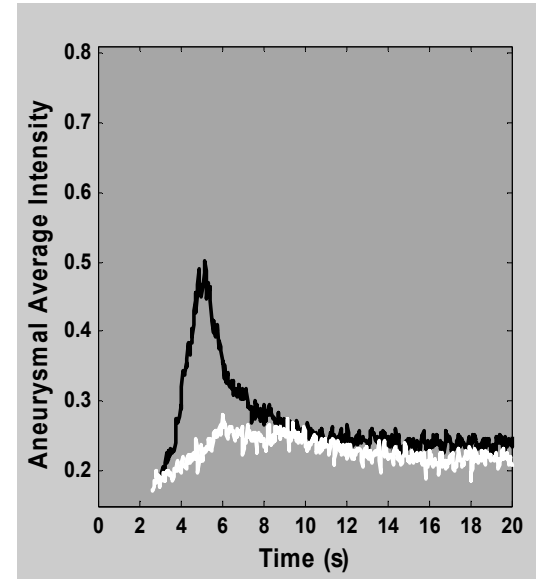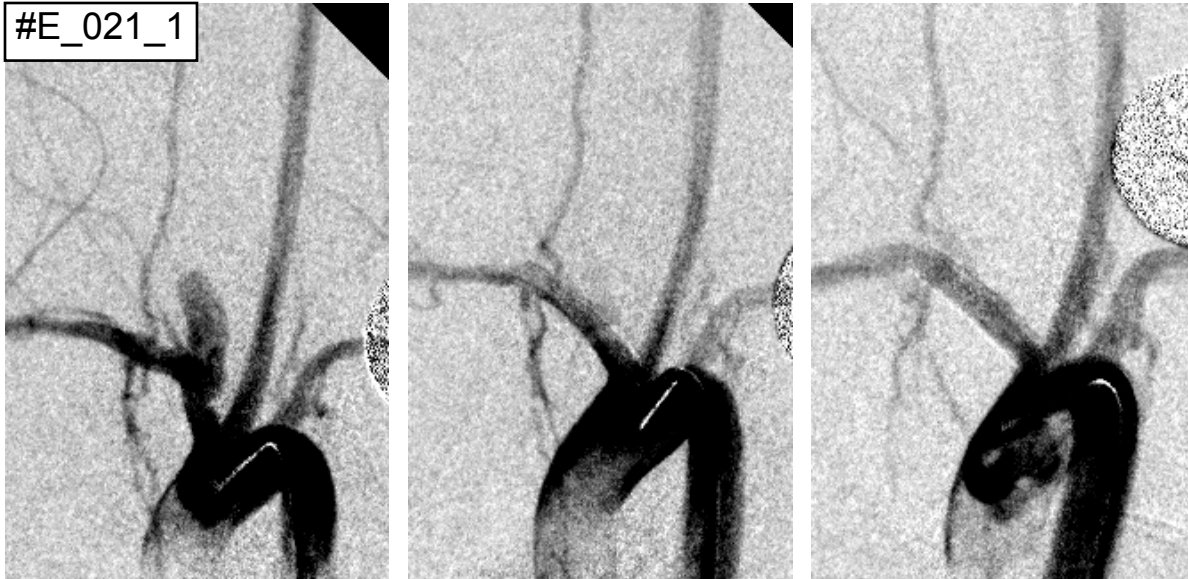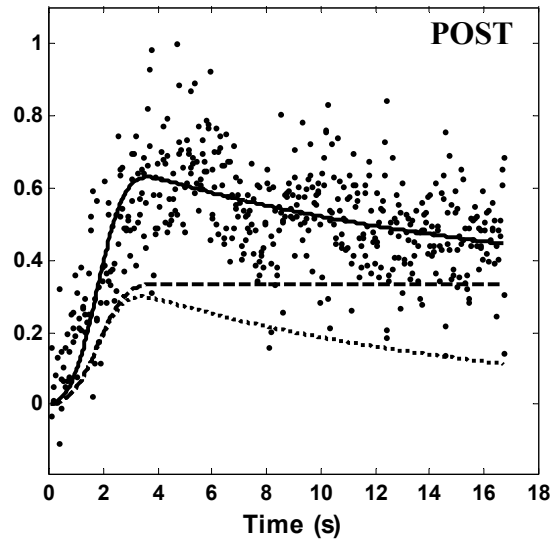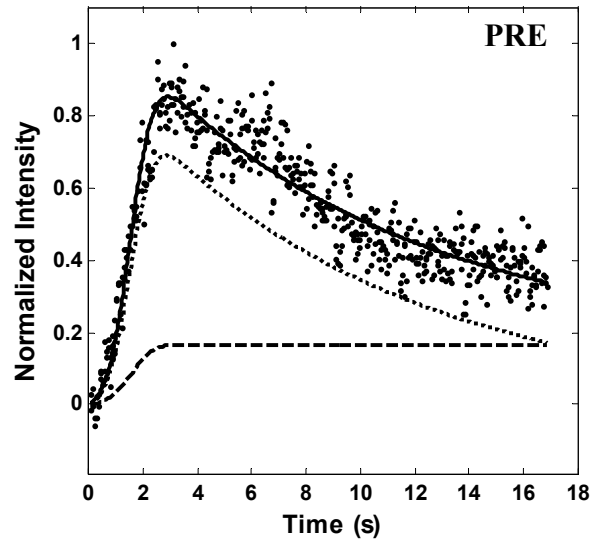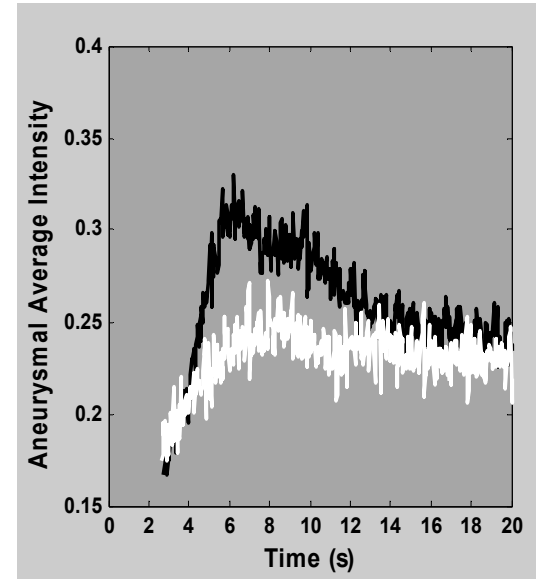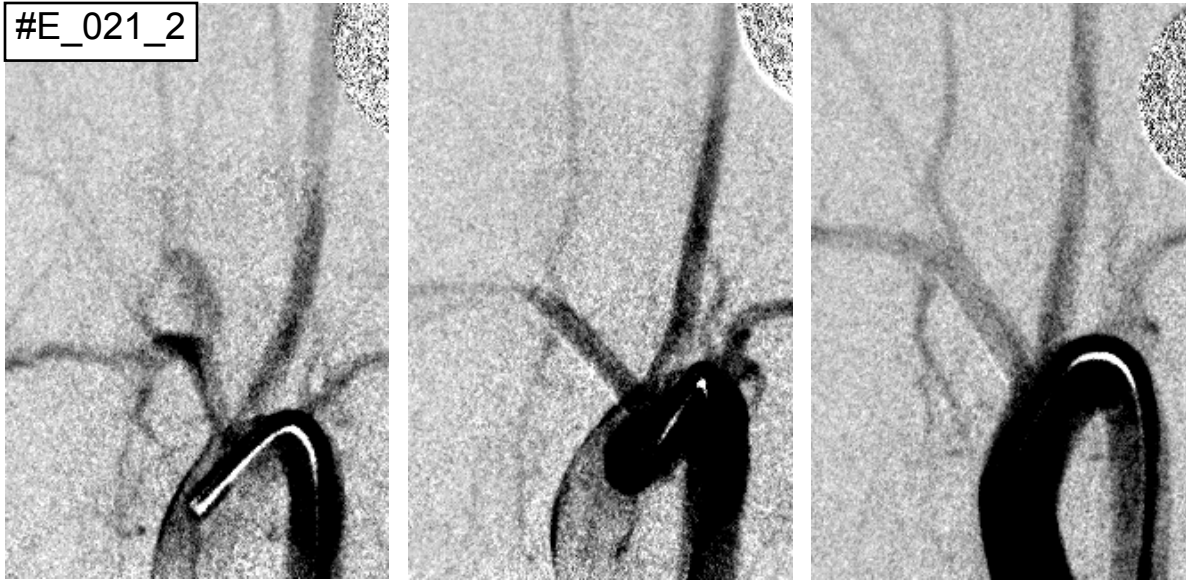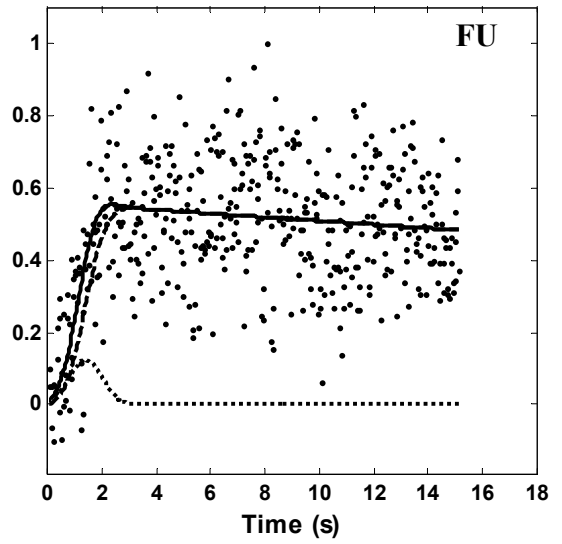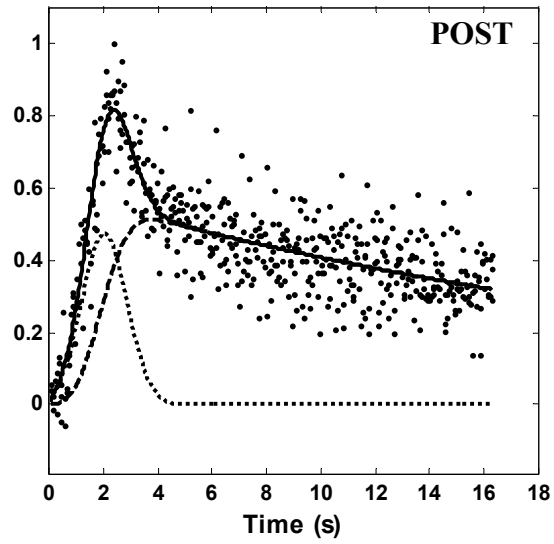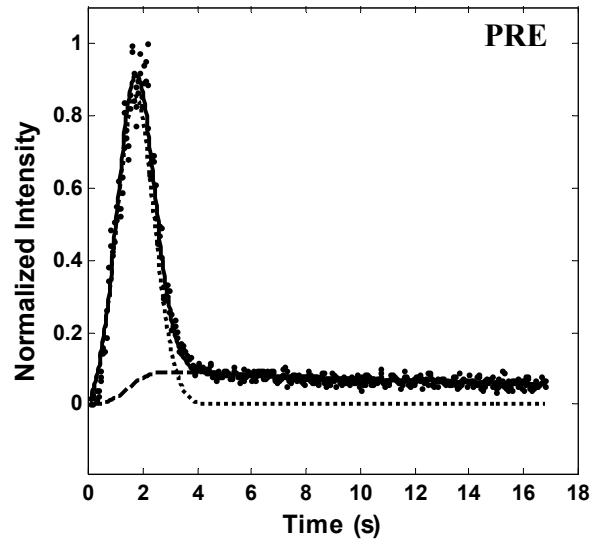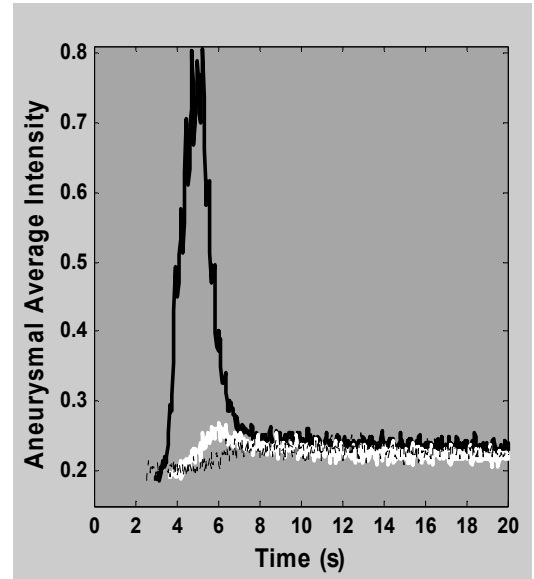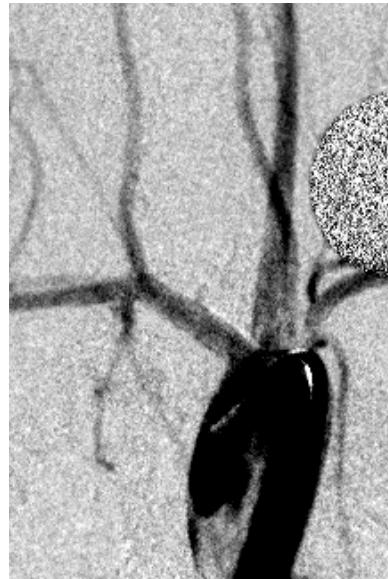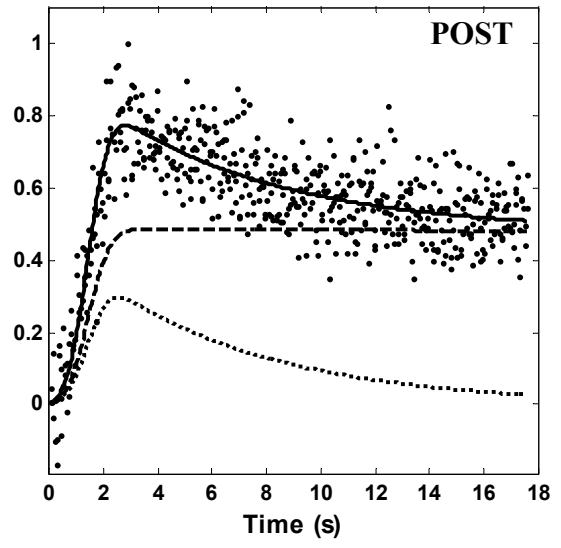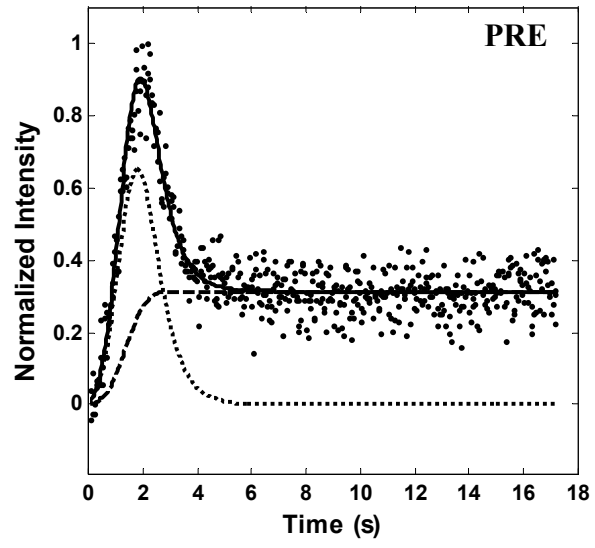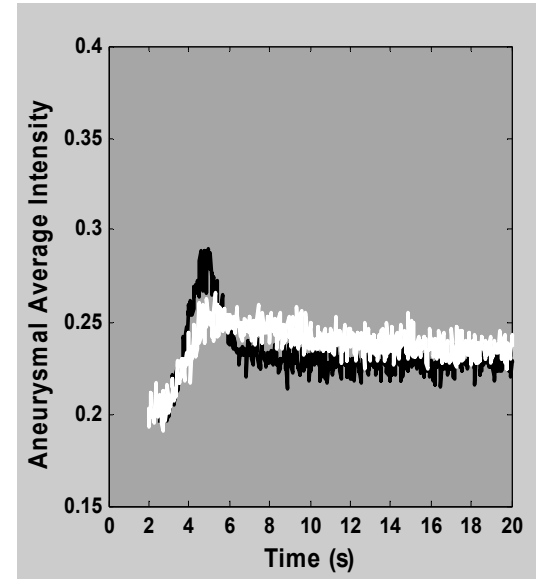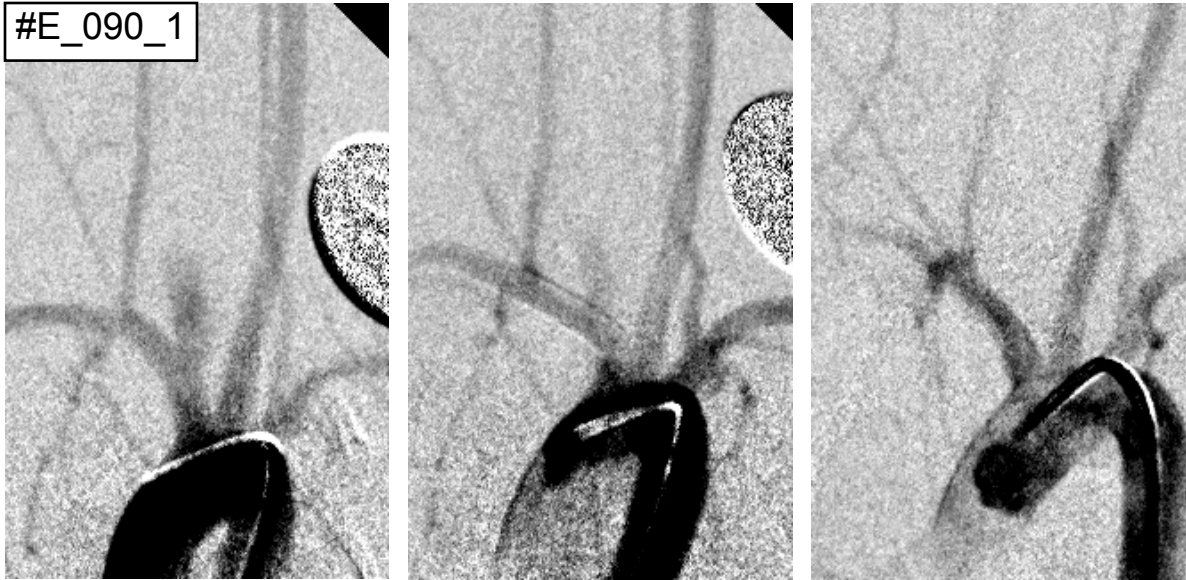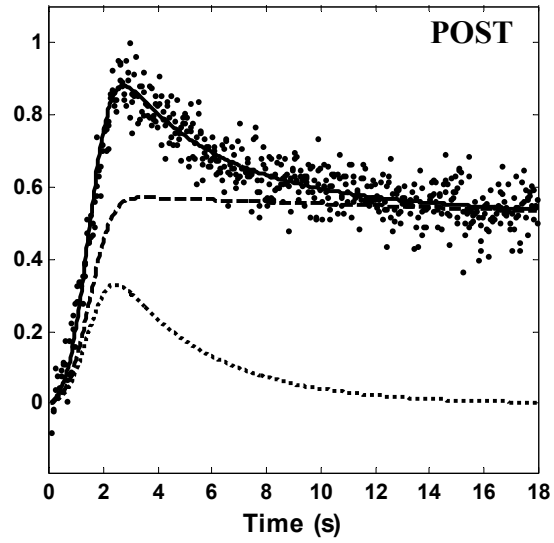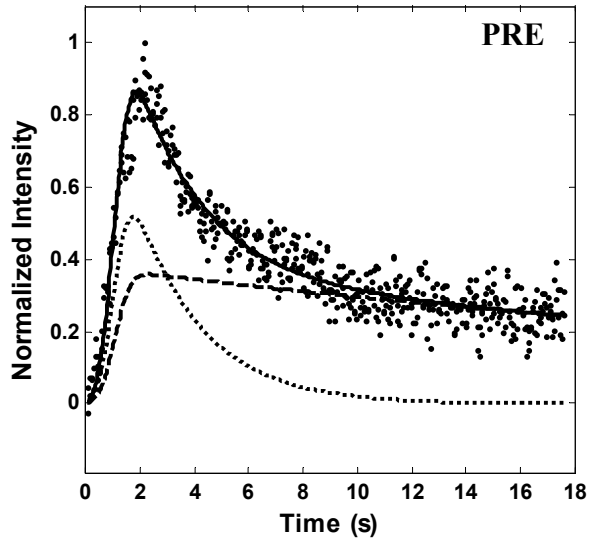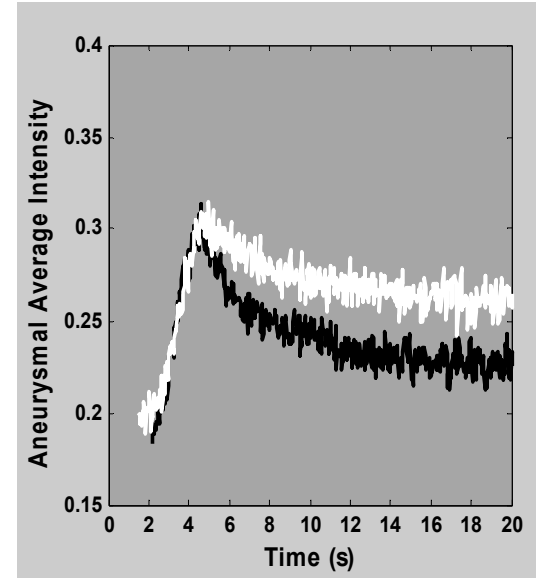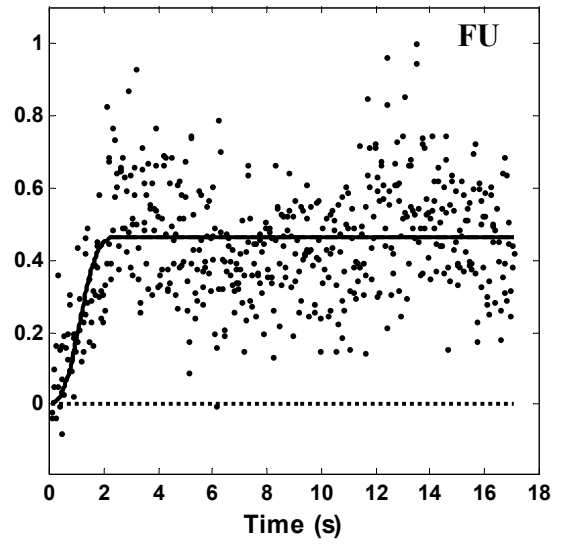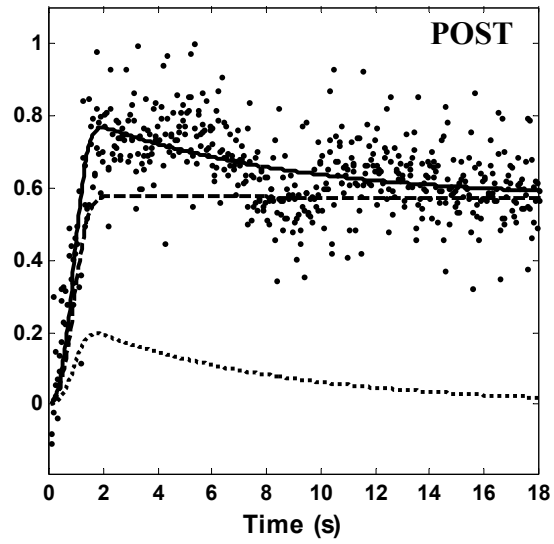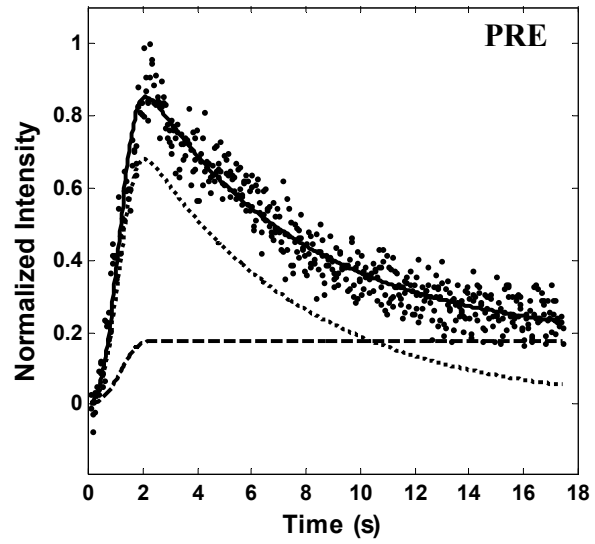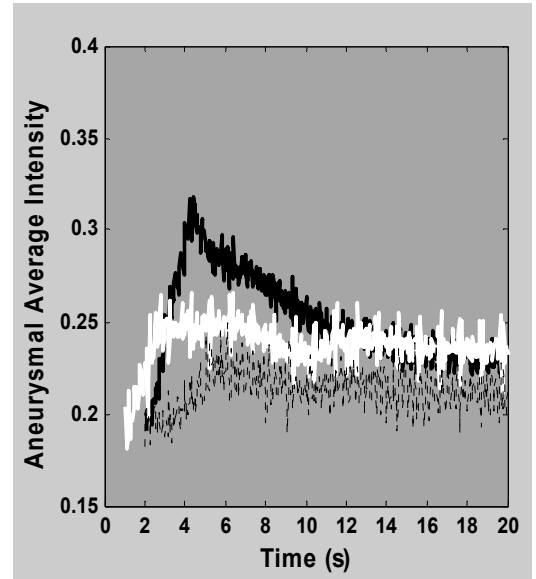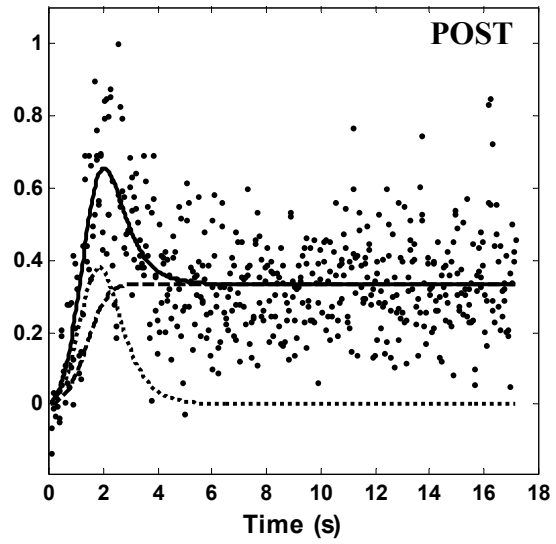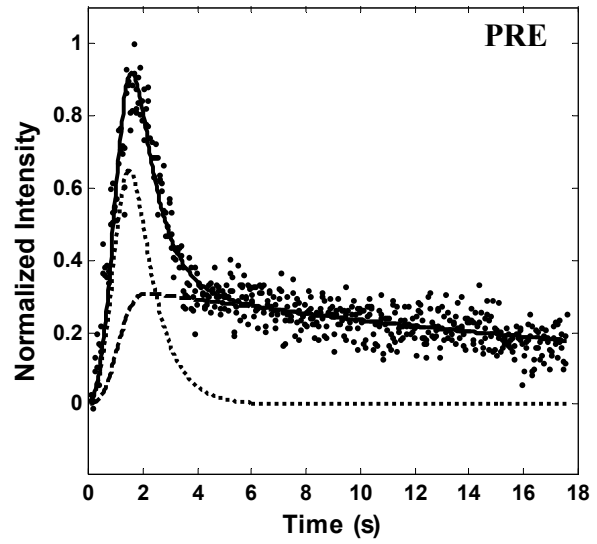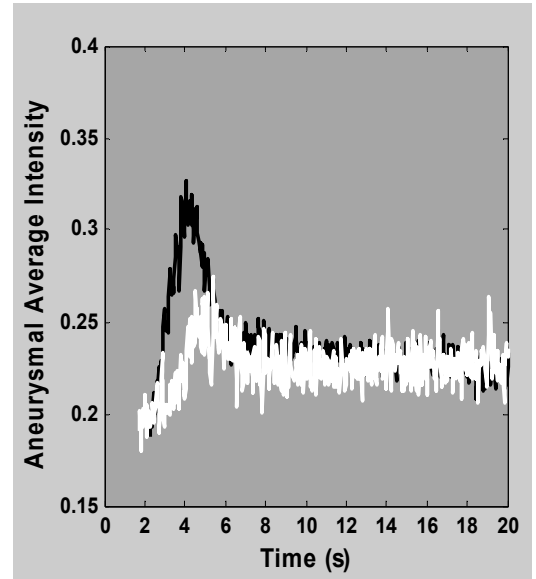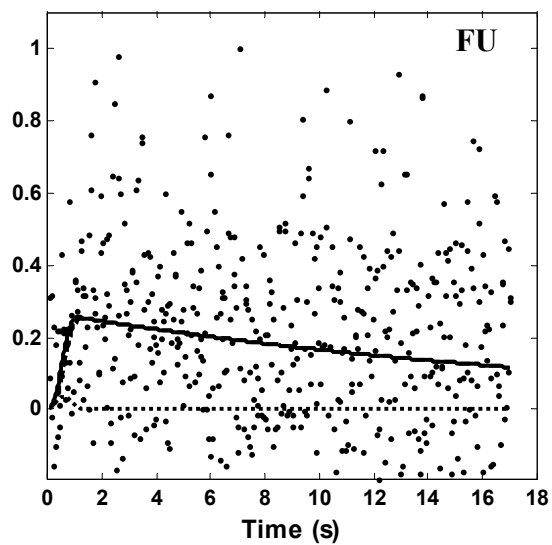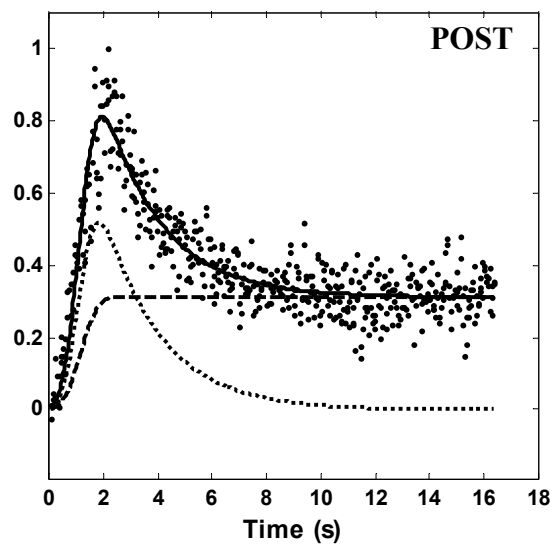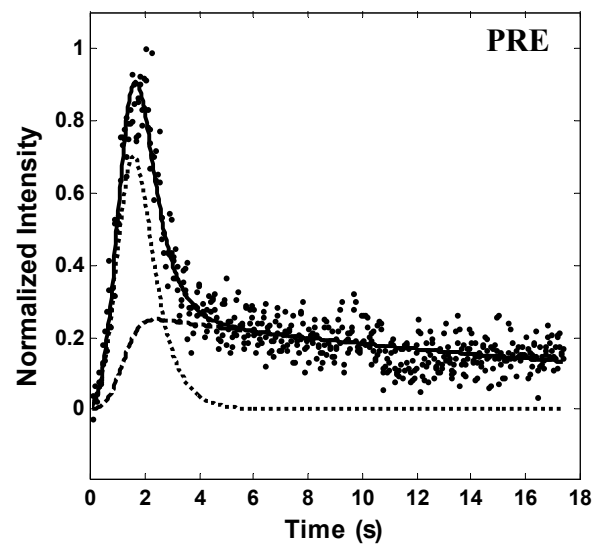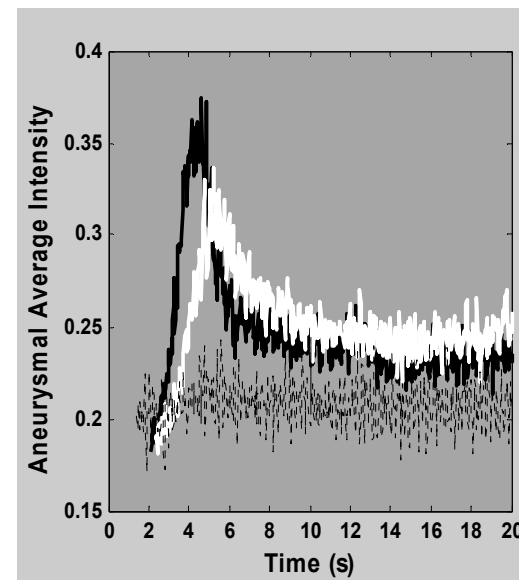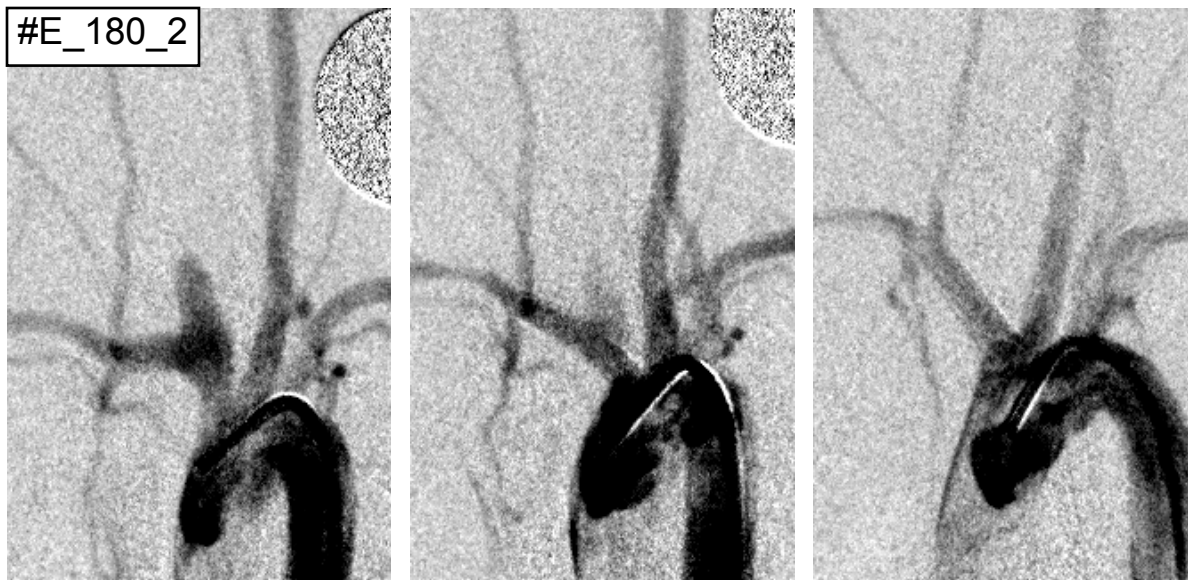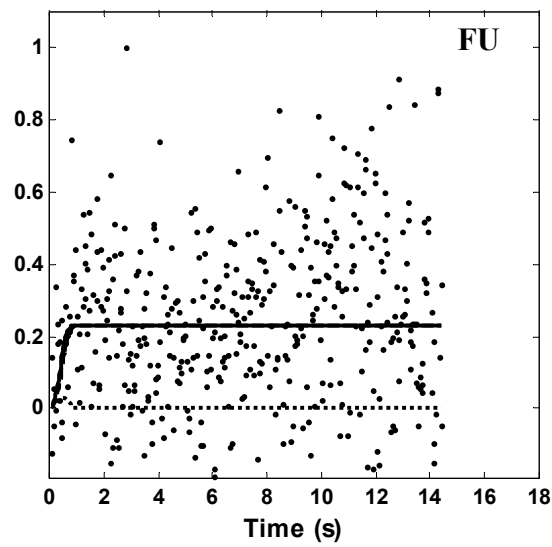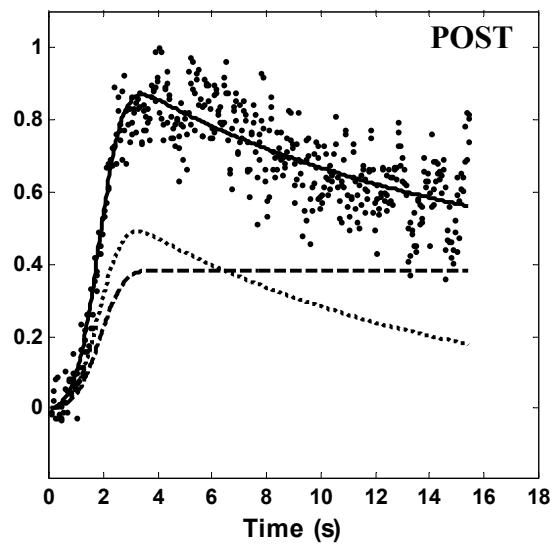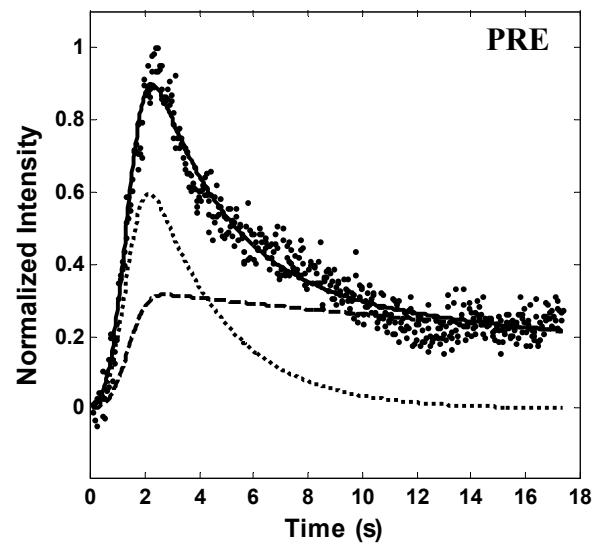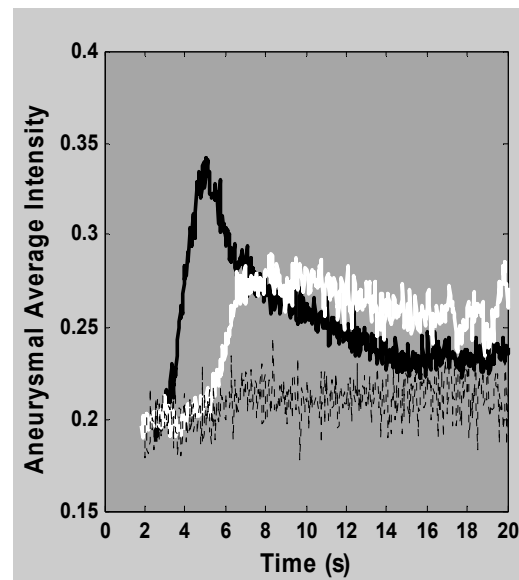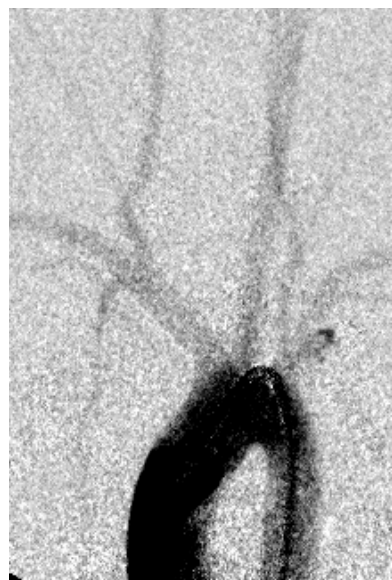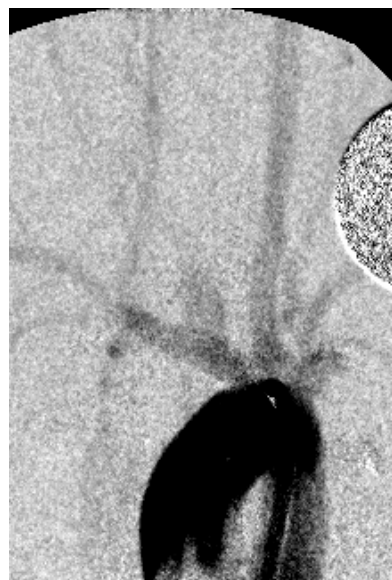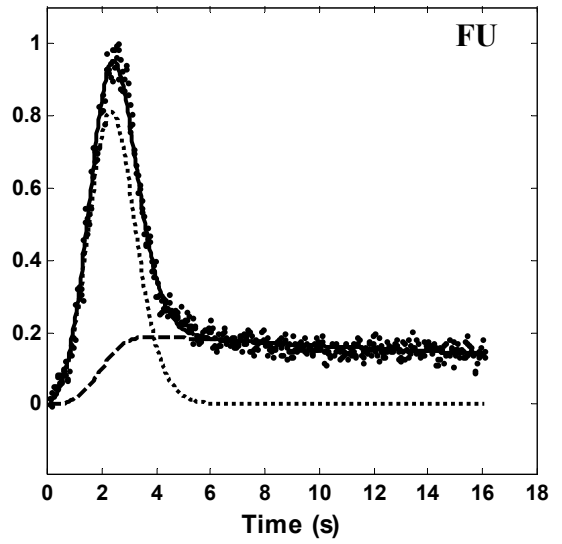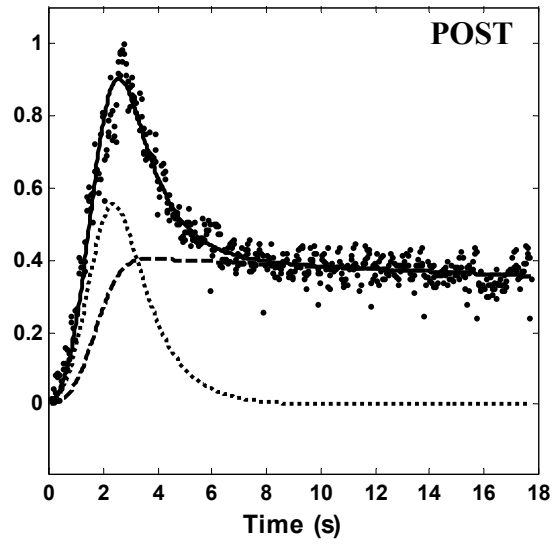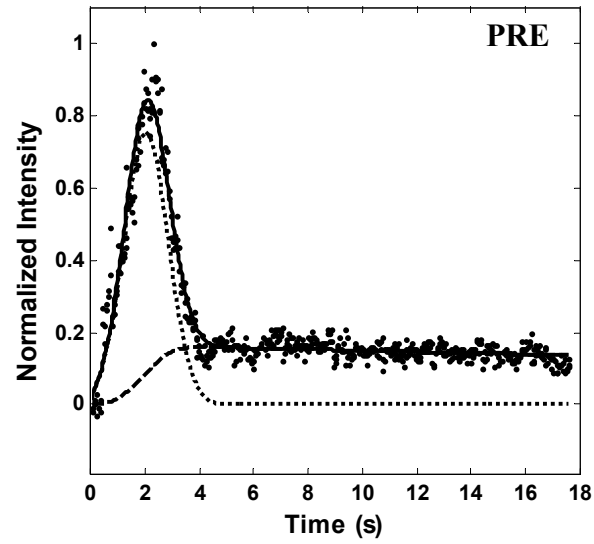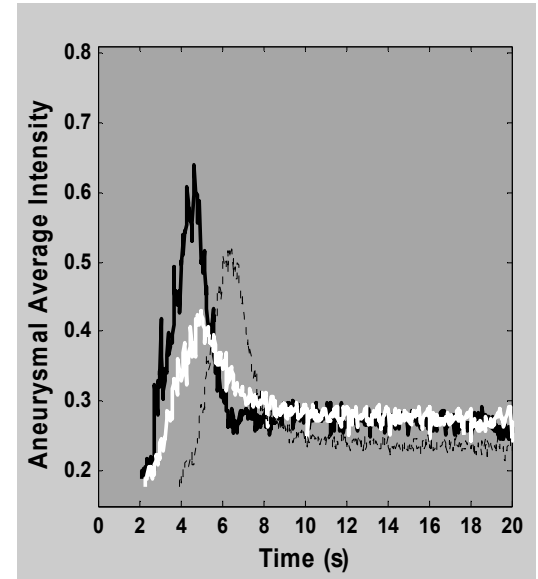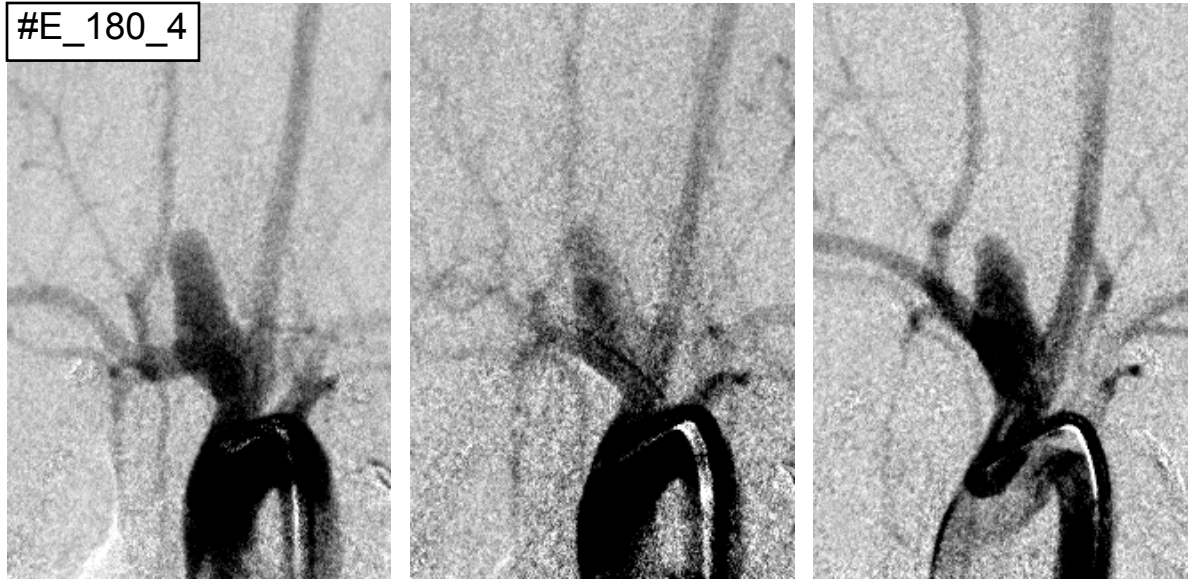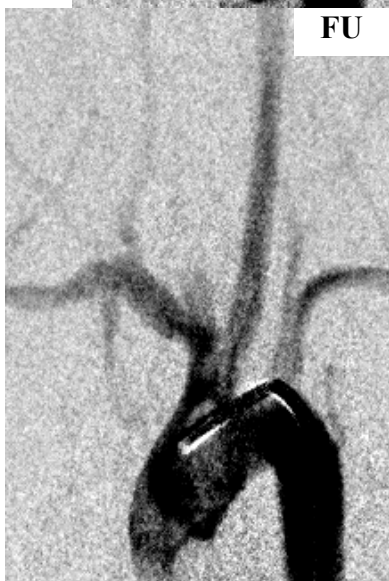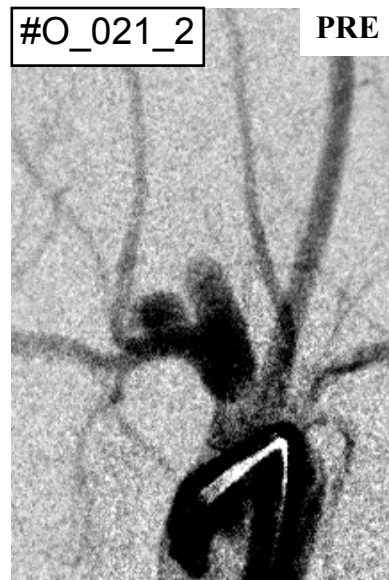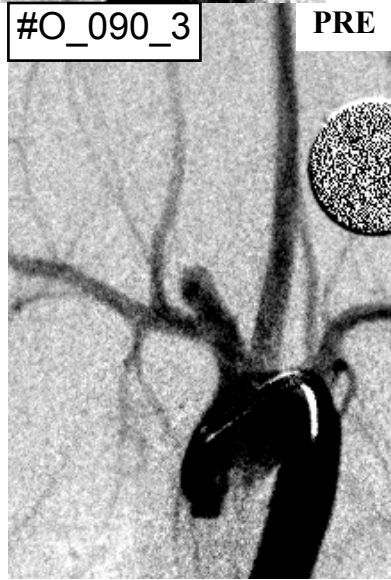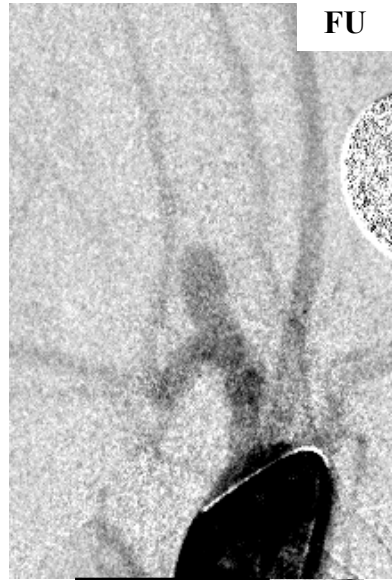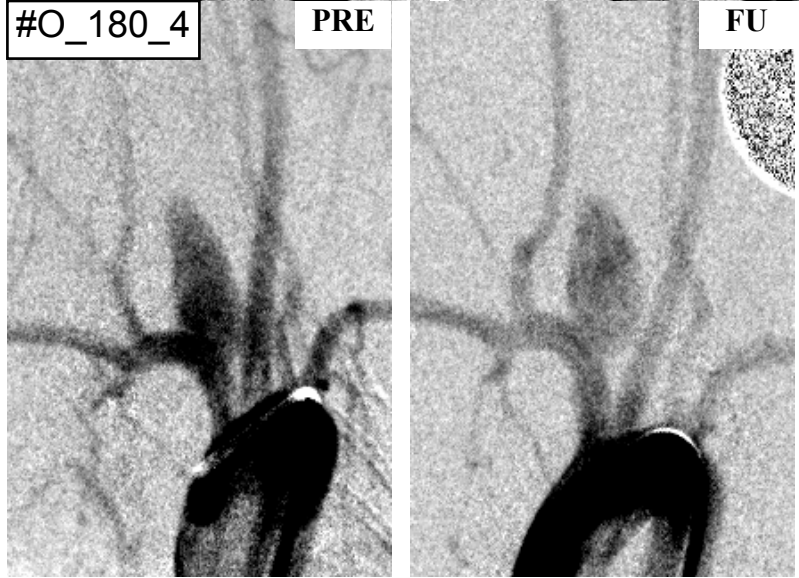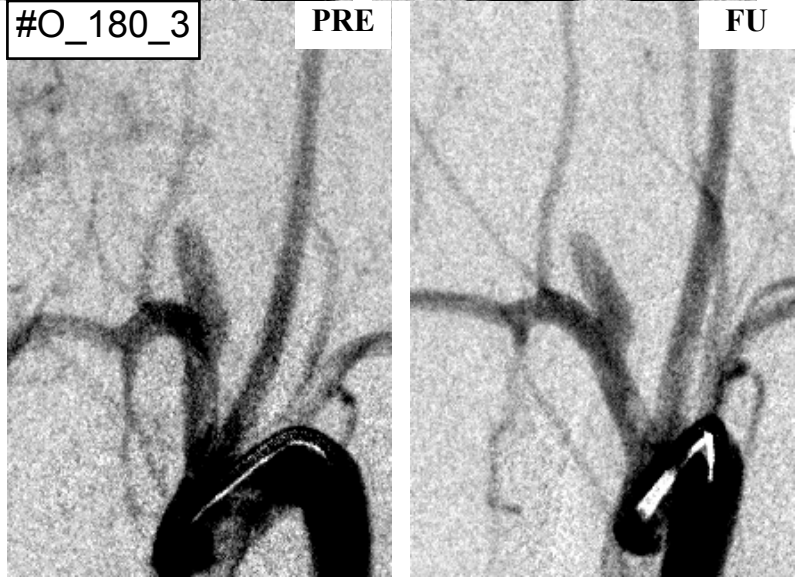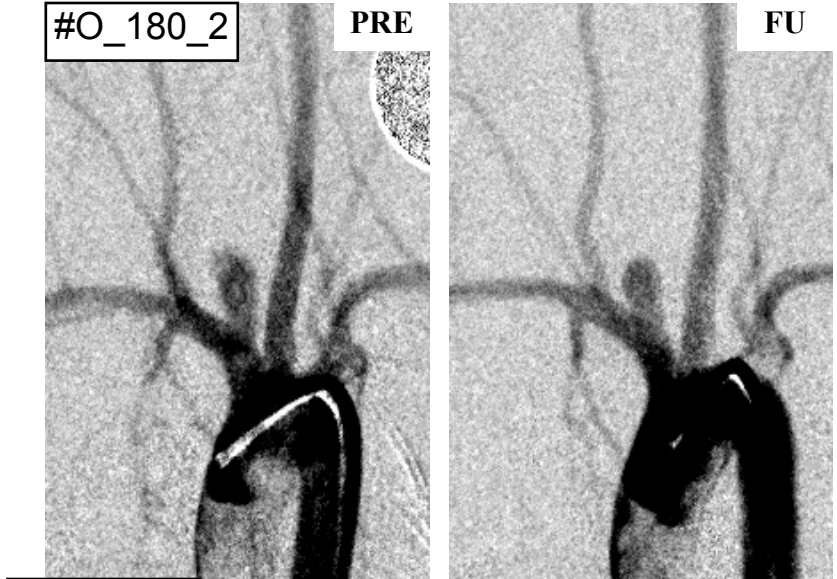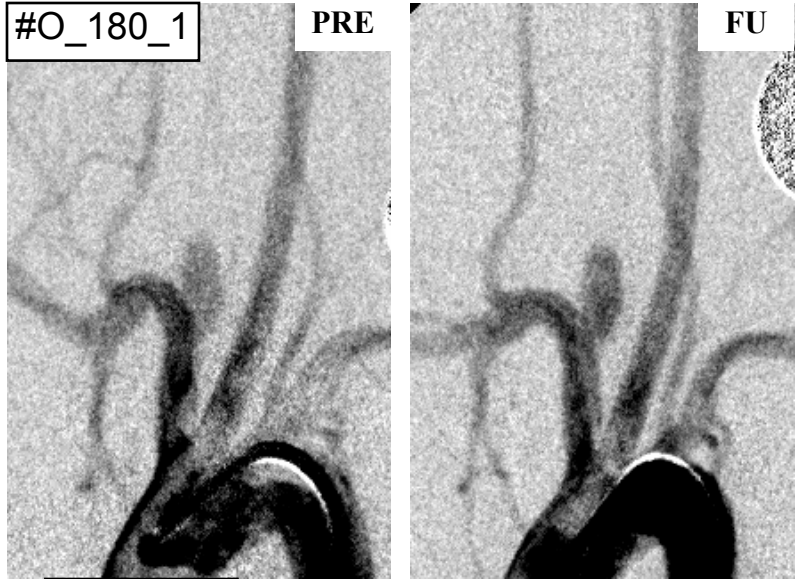
APPENDIX 3

This appendix includes histological sections at the aneurysm from 18 animals.[*]
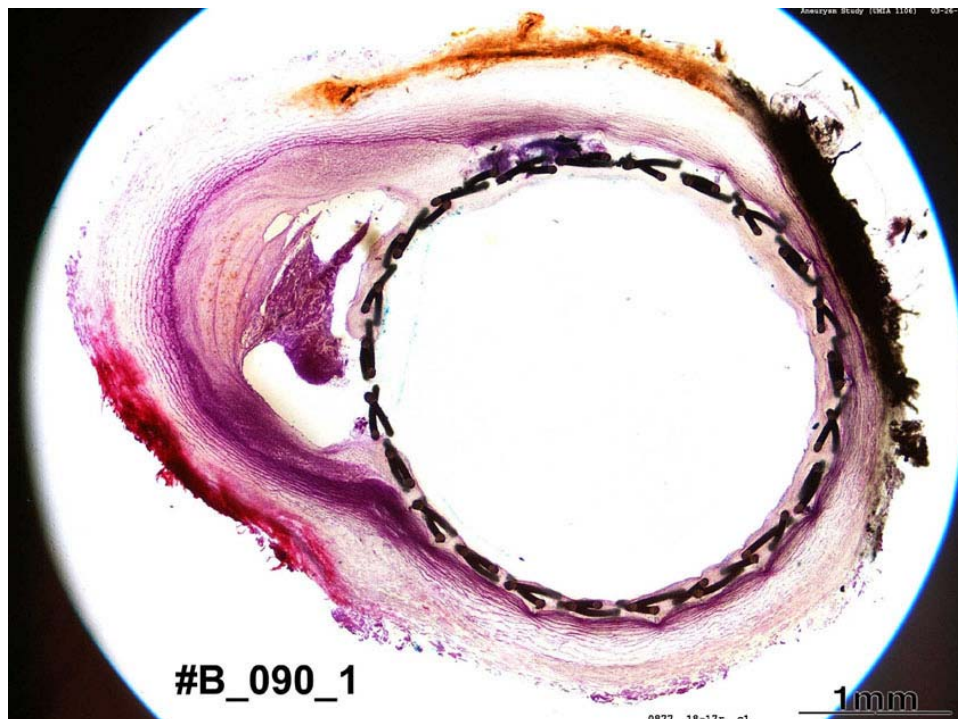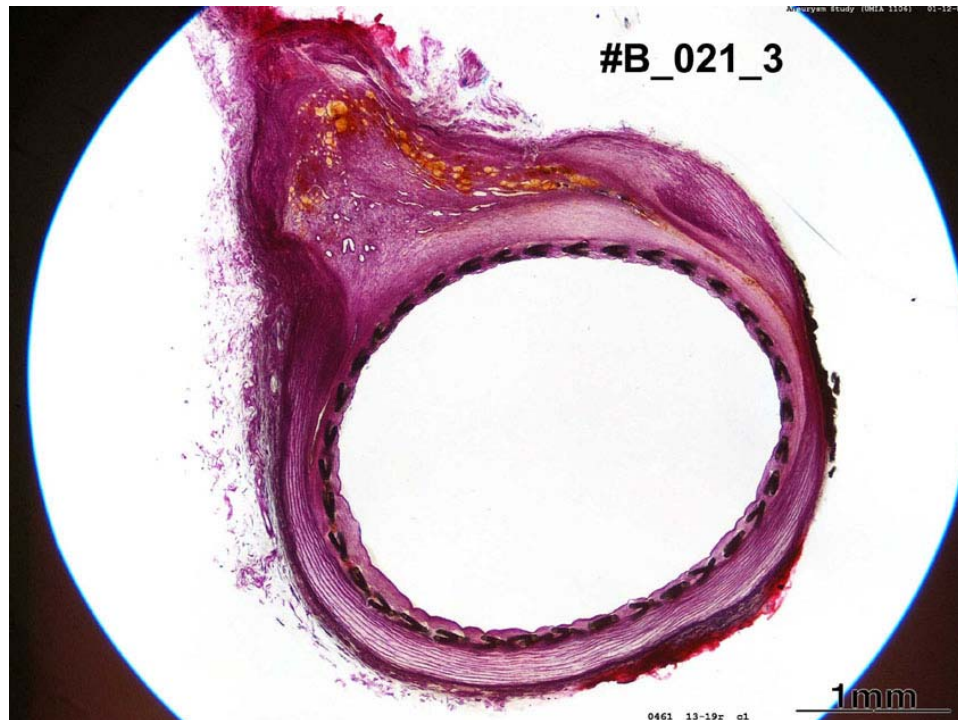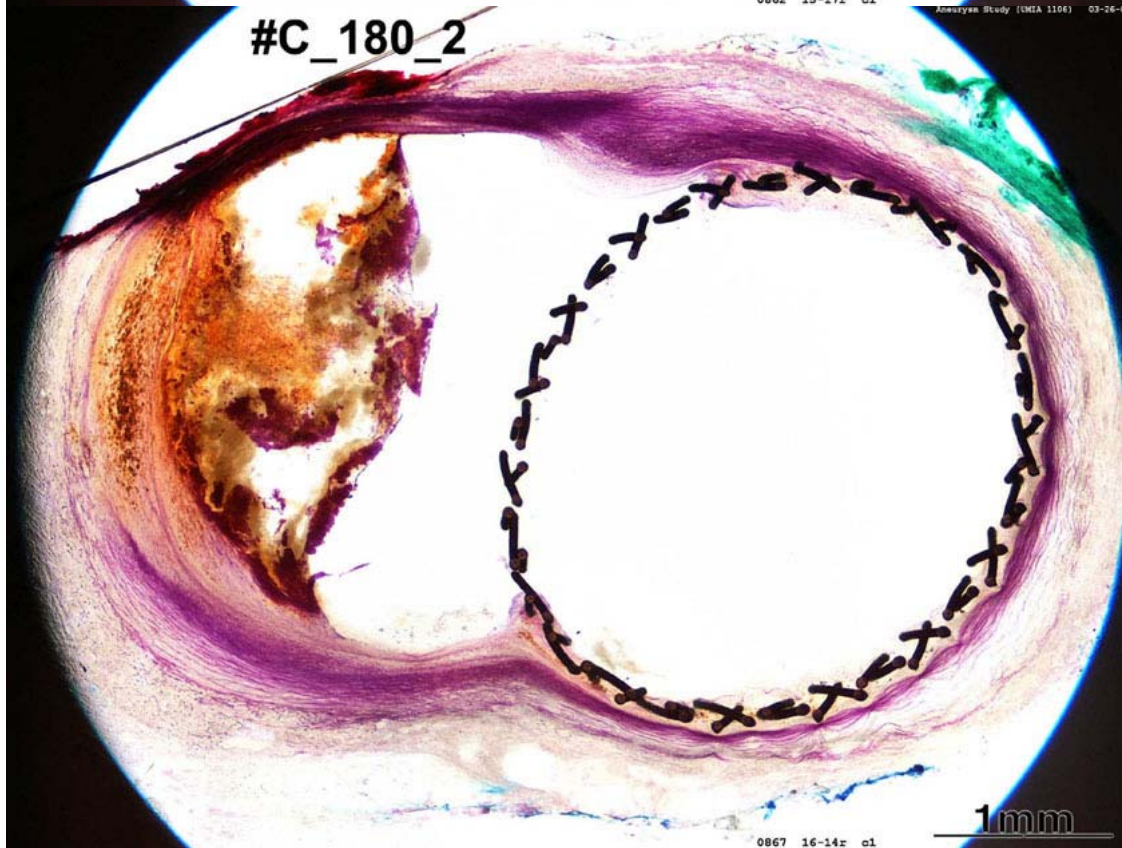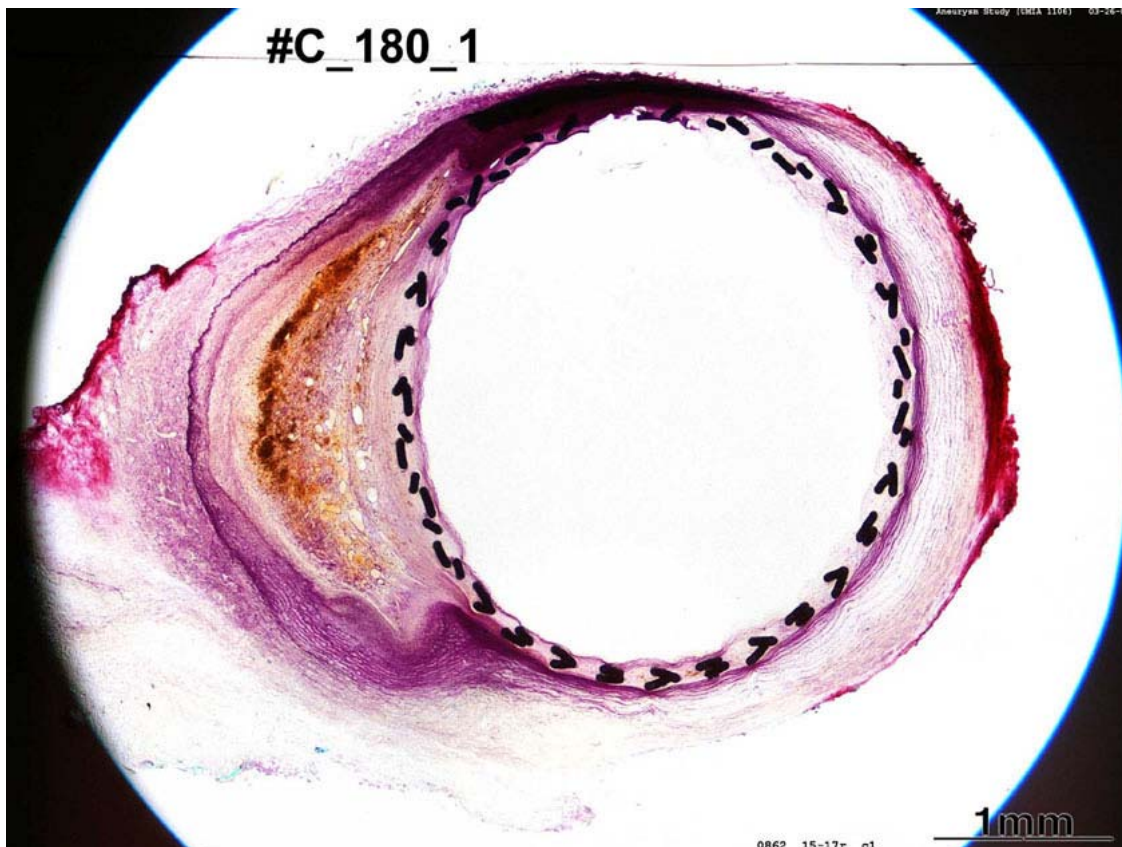

* These histological images were acquired by Dr. Fermin Tio at the Department of Veterans Affairs, South Texas Veterans Health Care System, San Antonio, TX.
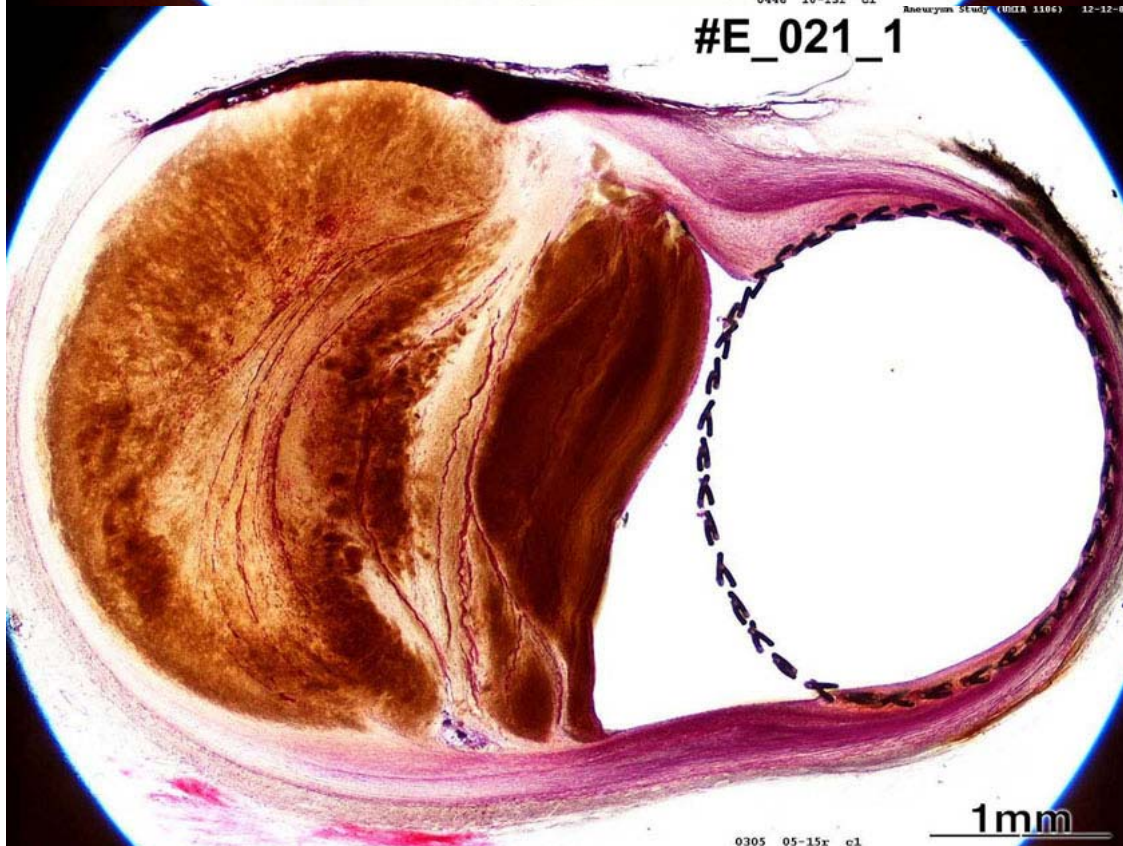
#B_090_2

1mm

#B_090_3

1mm

#B_180_1

#C_021_3

#C_090_1

1mm

#C_090_3

1mm

#C_180_1

1mm

#C_180_2

1mm

#C_180_3

1mm

#E_021_1

1mm

#E_021_3

1mm

#E_090_1

1mm

#E_090_2

1mm

0290 02-17r c1

#E_090_3

1mm

0857 14-19r c1

#E_180_1

1mm

#E_180_2

1mm